DEVELOPMENT OF A MEMS PIEZOELECTRIC MICROPHONE FOR AEROACOUSTIC APPLICATIONS

By

MATTHEW D. WILLIAMS

A DISSERTATION PRESENTED TO THE GRADUATE SCHOOL
OF THE UNIVERSITY OF FLORIDA IN PARTIAL FULFILLMENT
OF THE REQUIREMENTS FOR THE DEGREE OF
DOCTOR OF PHILOSOPHY

UNIVERSITY OF FLORIDA

2011

© 2011 Matthew D. Williams

To my wife, Laura, who came with me to Gainesville
for four years but stuck with me for six

ACKNOWLEDGMENTS

The Interdisciplinary Microsystems Group (IMG) at University of Florida has been an outstanding place to earn two graduate degrees, and there are many people to thank. My advisor, Mark Sheplak, deserves tremendous praise for the incredible research group he put together and now maintains together with David Arnold, Lou Cattafesta, Toshi Nishida, Hugh Fan, Huikaie Xie and YK Yoon. Over the last six years, Mark has pushed me well beyond any imagined limitations I had when I arrived, and he has done it with a mix of bluster, compassion, acumen, and generosity that is unique only to him. I will owe Mark immensely for any future success that I enjoy. For a young father like myself, he has also been a terrific role model.

I have benefited significantly from my contact with the other IMG professors as well, most notably David Arnold and Lou Cattafesta, who are at once tremendous researchers, teachers, and men. They both served as members of my committee and it was a pleasure working with them in many different capacities. David Arnold taught me, whether he knows it or not, about vision; I admire his unique ability to cut through the weeds. I aspire to Lou Cattafesta's level of precision in all that I do.

I have enjoyed many fruitful conversations with my other committee members, Nam-Ho Kim and Bhavani Sankar, as well. Both have always been extremely helpful and cordial, and I thank them wholeheartedly for all of their support. I also owe David Norton a debt of thanks for serving on my committee and for granting, as associate dean, additional flexibility in my funding situation for my final semester.

I entered graduate school with a National Science Foundation Graduate Fellowship for which I am exceedingly grateful, not just for the funding it supplied but for the doors that it opened. Boeing Corporation was the sponsor for my dissertation work; I owe them for the funding they provided and for the privilege of working on a problem of such importance to them. Jim Underbrink of Boeing always kept a watchful eye on my progress, and it was our close contact late in the project that really solidified my

understanding of the big picture. I benefited immensely from working with him and cannot thank Jim enough for being so giving of his time and so willing to teach. His commitment to improve the technology of aeroacoustic measurements is inspiring.

My colleagues within IMG deserve high praise. Ben Griffin has been a mentor to me since the moment I stepped on the University of Florida campus. I can only hope that I have contributed a fraction as much to his development as he has to mine. My other senior colleagues who have since gone on to industry, Vijay Chandrasekharan and Brian Homeijer, were always tremendously supportive as well. Finally, Jess Meloy is easily the most simultaneously helpful and knowledgeable person I have ever known; I offer my sincerest apologies to her for so regularly asking for her circuit expertise.

A bond is formed between graduate students who work on their proposals or dissertations at the same time, and so it is with fond memories that I will look back on my time in the trenches with Alex Phipps in the summer of 2008 and Jeremy Sells and Drew Wetzel in the spring of 2011. I will not soon forget our mutual support (or all the work).

The combined social and intellectual aspect of IMG cannot be ignored, and so it is in that spirit that I thank Brandon Bertolucci, Chris Bahr, Dylan Alexander, David Mills, Erin Patrick, Nik Zawodny, Jessica Sockwell, Miguel Palaviccini, Matias Oyarzun, and honorary IMGer Richard Parker. Whether at 80's night, a football tailgate, happy hour, or a frisbee game, I have been privileged to share their company.

I have worked with many outstanding undergradraduates on this project who deserve recognition: Tiffany Reagan, Anup Parikh, Adam Ecker, Kaleb Erwin, and Kyle Hughes. In particular, it is Tiffany Reagan's relentlessness that has most directly contributed to the success of this project. Her fingerprints are all over this dissertation.

Thanks are due to David Martin, Osvaldo Buccafusca, and Atul Goel at Avago Technologies for always working with me on the piezoelectric microphone project in good

faith and with expectations for its success. They deserve much credit for the results that were achieved.

Customer service continues to decline in today's world, but the people at Brüel and Kjær, Polytec, and TMR Engineering have not heard. Jim Wyatt and Joe Chou always came through my answers to my microphone questions when their competitors did not; Arend von der Lieth and John Foley worked tirelessly to ensure IMG's laser vibrometer system stayed running at least until I graduated; and Ken Reed always turned up with high-quality mechanical parts in record time.

Thanks are due to my undergraduate advisor, Paul Joseph, for turning me on to research in the first place. In addition, my parents David and Anna made all that I have accomplished possible. Long before Mark Sheplak was preaching the wisdom of setting his students up for success and getting out of the way, my parents were doing just that with their son.

The latter parts of graduate school can be hard on a family, but my wife Laura was a rock. Words cannot thank her enough for the sacrifices she made to make this dissertation possible. I did it all for her and our daughter, Callahan.

TABLE OF CONTENTS

page

ACKNOWLEDGMENTS . . . 4

LIST OF TABLES . . . 11

LIST OF FIGURES . . . 13

ABSTRACT . . . 18

CHAPTER

1 INTRODUCTION . . . 20

1.1 Motivation . . . 20
1.2 Research Objectives . . . 25
1.3 Dissertation Overview . . . 27

2 MICROPHONE FUNDAMENTALS . . . 29

2.1 Sound and Pseudo Sound . . . 29
2.2 The Realities of Microphone Design . . . 31
2.3 Microphone Performance Metrics . . . 36
2.3.1 Frequency Response and Sensitivity . . . 37
2.3.2 Noise Floor and Minimum Detectable Pressure . . . 38
2.3.3 Linearity and Maximum Pressure . . . 42
2.3.4 Dynamic Range . . . 44
2.3.5 Summary of Microphone Performance Metrics . . . 44
2.4 Summary . . . 45

3 PRIOR ART . . . 46

3.1 Review of MEMS Piezoelectric and Aeroacoustic Microphones . . . 46
3.2 Summary . . . 58

4 MEMS PIEZOELECTRIC MICROPHONE . . . 62

4.1 Piezoelectricity . . . 62
4.2 Design for Fabrication . . . 66
4.3 Summary . . . 70

5 MODELING . . . 71

5.1 Lumped Element Modeling Overview . . . 71
5.2 Lumped Element Model of a Piezoelectric Microphone . . . 73
5.2.1 Elements . . . 76
5.2.1.1 Transduction . . . 76
5.2.1.2 Structural elements . . . 78

5.2.1.3 Acoustic elements . . . 80
5.2.1.4 Electrical elements . . . 83
5.2.2 Diaphragm Mechanical Model . . . 83
5.2.3 Frequency Response . . . 88
5.2.3.1 Sensor . . . 90
5.2.3.2 Actuator . . . 92
5.2.4 Electrical impedance . . . 93
5.2.5 Validation . . . 94
5.2.5.1 Diaphragm model validation . . . 95
5.2.5.2 Lumped element model validation . . . 97
5.3 Interface Circuitry . . . 98
5.3.1 Voltage Amplifier . . . 99
5.3.2 Charge Amplifier . . . 102
5.3.3 Noise Models . . . 104
5.3.3.1 Noise model with voltage amplifier . . . 105
5.3.3.2 Noise model with charge amplifier . . . 108
5.3.4 Selection . . . 110
5.4 Summary . . . 112

6 OPTIMIZATION . . . 113

6.1 Design Overview . . . 113
6.1.1 Design Variables . . . 113
6.1.2 Objective . . . 115
6.2 Formulation . . . 117
6.3 Approach . . . 119
6.4 Results and Discussion . . . 121
6.5 Summary . . . 126

7 REALIZATION AND PACKAGING . . . 128

7.1 Realization . . . 128
7.1.1 Geometry . . . 128
7.1.2 Fabrication Results . . . 128
7.2 Dicing . . . 130
7.2.1 Dicing Process . . . 131
7.2.2 Dicing Results . . . 134
7.3 Packaging . . . 134
7.4 Summary . . . 140

8 EXPERIMENTAL CHARACTERIZATION . . . 141

8.1 Experimental Setup . . . 141
8.1.1 Die Selection Setup . . . 141
8.1.2 Diaphragm Topography Measurement Setup . . . 144
8.1.3 Acoustic Characterization Setup . . . 145
8.1.3.1 Frequency response measurement setup . . . 145

8.1.3.2 Linearity measurement setup . . . 150
8.1.4 Electrical Characterization Setup . . . 153
8.1.4.1 Noise floor measurement setup . . . 154
8.1.4.2 Impedance measurement setup . . . 156
8.1.4.3 Parasitic capacitance extraction setup . . . 158
8.1.5 Electroacoustic Parameter Extraction . . . 159
8.1.5.1 Compliance and mass measurement setup . . . 160
8.1.5.2 Frequency response measurement setup . . . 165
8.1.5.3 Effective piezoelectric coefficient measurement setup . . . 167
8.2 Experimental Results . . . 168
8.2.1 Die Selection . . . 168
8.2.2 Diaphragm Topography . . . 173
8.2.3 Acoustic Characterization . . . 175
8.2.3.1 Frequency response . . . 175
8.2.3.2 Linearity . . . 176
8.2.4 Electrical Characterization . . . 180
8.2.4.1 Noise floor . . . 180
8.2.4.2 Impedance . . . 183
8.2.4.3 Parasitic capacitance extraction . . . 184
8.2.5 Electroacoustic Parameter Extraction . . . 187
8.3 Summary . . . 195

9 CONCLUSION . . . 196

9.1 Recommendations for Future Piezoelectric Microphones . . . 198
9.2 Recommendations for Future Work . . . 202

APPENDIX

A DIAPHRAGM MECHANICAL MODEL . . . 204

A.1 Strain-Displacement Relations . . . 205
A.2 Kirchhoff Hypothesis . . . 207
A.3 Equations of Motion . . . 208
A.4 Constitutive Equation . . . 214
A.5 Displacement Differential Equations of Motion . . . 217
A.6 Equations of Equilibrium . . . 219
A.6.1 Nonlinear . . . 219
A.6.2 Linear . . . 221
A.7 Problem Solutions . . . 222
A.7.1 Linear . . . 223
A.7.1.1 General solutions . . . 223
A.7.1.2 Particular solutions . . . 224
A.7.1.3 Inner region: tension ($x^{(1)} > 0$) . . . 226
A.7.1.4 Inner region: $x^{(1)} = 0$ . . . 226
A.7.1.5 Inner region: compression ($x^{(1)} < 0$) . . . 227

A.7.1.6 Outer region: tension ($x^{(2)} > 0$) . . . 228
A.7.1.7 Outer region: $x^{(2)} = 0$ . . . 229
A.7.1.8 Outer region: compression ($x^{(2)} = 0$) . . . 230
A.7.2 Nonlinear . . . 231
A.8 Closing . . . 234

B BOUNDARY CONDITION INVESTIGATION . . . 235

C UNCERTAINTY ANALYSIS . . . 237

C.1 Approach . . . 237
C.2 Frequency Response Function . . . 238
C.3 Noise Floor . . . 238
C.3.1 Spectra . . . 239
C.3.2 Narrow Band . . . 240
C.3.3 Integrated . . . 240
C.4 Impedance . . . 240
C.5 Parasitic Capacitance Extraction . . . 240
C.6 Parameter Extraction . . . 241

D MATERIAL PROPERTIES . . . 242

REFERENCES . . . 243

BIOGRAPHICAL SKETCH . . . 260

LIST OF TABLES

Table		page
1-1	Fuselage array application requirements.	27
2-1	Performance characteristics of common aeroacoustic microphones.	45
3-1	Summary of MEMS microphones.	59
4-1	Typical properties of piezoelectric materials in MEMS.	66
5-1	Geometric dimensions of an example device.	95
5-2	Comparison of voltage and charge amplifier topologies	110
6-1	Microphone dimensions fixed by the fabrication process.	114
6-2	Design variable bounds.	118
6-3	Constant values used in the optimization.	121
6-4	Target thin-film residual stresses.	121
6-5	Optimal layer thicknesses.	124
6-6	Optimization results.	124
7-1	Design dimensions.	129
7-2	Film properties.	129
7-3	Tape and substrate thicknesses.	132
7-4	Dicer settings.	133
7-5	Epoxy dispenser settings.	137
7-6	Wire bond settings.	137
8-1	Die selection laser vibrometer settings.	143
8-2	Scanning white light interferometer software settings.	145
8-3	Settings for microphone frequency response measurements in PULSE.	148
8-4	Frequency response measurement settings used at Boeing.	151
8-5	Total harmonic distortion measurement settings used at Boeing.	153
8-6	Noise floor measurement settings.	155
8-7	Impedance measurement settings.	157

8-8 Pressure coupler measurement settings. 163
8-9 Settings for sensitivity measurement of pressure coupler microphones. 166
8-10 Wafer statistics. 172
8-11 Pre- and post-packaging LV measurements. 172
8-12 Microphone frequency response characteristics at 1 kHz in air. 176
8-13 THD measurements performed at Boeing Corporation. 180
8-14 Minimum detectable pressure metrics. 183
8-15 Extracted electrical parameters. 185
8-16 Open-circuit sensitivity estimates. 187
8-17 Extracted mechanoacoustic parameters. 191
8-18 Extracted electroacoustic parameters. 193
9-1 Realized MEMS piezoelectric microphone performance. 197
9-2 Performance characteristics of MEMS piezoelectric microphone 138-1-J3-F. . . . 199
C-1 Parasitic capacitance extraction uncertainties. 241
D-1 Properties of microphone diaphragm materials. 242
D-2 Properties of gases. 242

LIST OF FIGURES

Figure page

1-1 Boeing 777 fuselage instrumented with an array of microphones. 22

1-2 Aeroacoustic phased arrays deployed as part of the QTD2 program. 23

2-1 Force-displacement characteristics for a perfect spring. 32

2-2 Frequency response of a second-order system. 33

2-3 Constitutive behavior for a Duffing spring. 35

2-4 Various cavity configurations. 35

2-5 Typical aeroacoustic microphone frequency response. 38

2-6 Noise model for a resistor. 40

2-7 Noise model for a resistor in parallel with a capacitor. 40

2-8 Low-pass filtering of thermal noise. 41

2-9 Voltage noise spectrum for an LTC6240 amplifier. 41

2-10 Ideal and actual response of a microphone. 43

2-11 Operational space of an aeroacoustic microphone. 45

3-1 Piezoelectric (ZnO) microphone with integrated buffer amplifier. 47

3-2 Piezoelectric (ZnO) microphone utilizing multiple concentric electrodes. 48

3-3 Piezoelectric microphone utilizing aromatic polyurea. 48

3-4 Piezoelectric (ZnO) microphone with cantilever sensing element. 49

3-5 Cross section of the first aeroacoustic MEMS microphone. 50

3-6 Piezoresistive MEMS microphone for aeroacoustic measurements. 51

3-7 Second-generation aeroacoustic MEMS microphone. 52

3-8 A dual-backplate capacitive MEMS microphone. 53

3-9 Early PZT-based piezoelectric microphone. 53

3-10 Piezoelectric (ZnO) microphone with two concentric electrodes. 54

3-11 Measurement-grade MEMS condenser microphone developed at Brüel and Kjær. 55

3-12 Piezoelectric (PZT) microphone for aeroacoustic applications. 56

3-13 Top-view of microphone structures from Fazzio et al. (2007). 57
3-14 Cross section of a second-generation AlN double-cantilever microphone. 58
4-1 Venn diagram for piezoelectric, pyroelectric, and ferroelectric materials. 63
4-2 FBAR-variant process film stack. 67
4-3 Potential circular diaphragm piezoelectric/metal film stack configurations. . . . 69
4-4 Outline of fabrication steps. 70
5-1 Illustration of the electrical-mechanical analogy. 73
5-2 Piezoelectric microphone structure. 74
5-3 Piezoelectric microphone lumped element model. 75
5-4 Two-port piezoelectric transduction element. 77
5-5 Laminated composite plate representation of the thin-film diaphragm. 84
5-6 Deflection of a radially non-uniform composite plate with residual stress. 88
5-7 Boundary conditions applied to a radially non-uniform piezoelectric composite. . 89
5-8 Lumped element model with collected impedances. 90
5-9 Impedance ratios appearing in the open circuit frequency response expression. . 91
5-10 Comparison of open-circuit sensitivity expressions. 92
5-11 Lumped element model of the piezoelectric microphone as an actuator. 93
5-12 Finite element model for validation exercise. 96
5-13 Analytical and FEA predictions of $w_{inc}(0)$ (pressure loading case). 96
5-14 Relative error between analytical and FEA predictions of $w_{inc}(0)$. 97
5-15 Analytical and FEA predictions of $w_{inc}(0)$ (voltage loading case). 97
5-16 Lumped element model and FEA predictions of frequency response function. . 98
5-17 Non-ideal operational amplifier model. 100
5-18 Lumped element model with voltage amplifier. 100
5-19 Non-ideal charge amplifier model. 102
5-20 Lumped element model with charge amplifier. 103
5-21 Noise model for the microphone with voltage amplifier circuitry. 105

5-22 Output-referred noise floor for the microphone with a voltage amplifier. 107
5-23 Noise model for the microphone with charge amplifier circuitry. 108
5-24 Output-referred noise floor for the microphone with charge amplifier. 109
6-1 Cross-section of the piezoelectric microphone with notable dimensions. 114
6-2 Pareto front example. 117
6-3 Optimization approach. 120
6-4 Pareto front associated with minimization of MDP and maximization of PMAX. 122
6-5 Normalized design variable values for each optimization. 123
6-6 Sensitivity of MDP to $\pm 10\,\%$ perturbations in the design variables. 125
6-7 Sensitivity of PMAX to $\pm 10\,\%$ perturbations in the design variables. 126
6-8 Sensitivity of MDP to in-plane stress variations. 126
7-1 Wafer of piezoelectric microphones fabricated at Avago Technologies. 130
7-2 Dicing blade and sample orientation. 131
7-3 Dicing process for MEMS piezoelectric microphone die. 133
7-4 Micrographs of microphone die (designs A-G). 135
7-5 Exploded view of the laboratory test package. 136
7-6 Microphone endcap. 137
7-7 Closeup photograph of a packaged MEMS piezoelectric microphone. 138
7-8 Voltage amplifier circuitry included in the microphone package. 139
7-9 Voltage amplifier circuit board layout. 139
7-10 Charge amplifier circuit diagram. 140
7-11 Complete packaged MEMS piezoelectric microphone. 140
8-1 Experimental setup for die selection. 143
8-2 Predicted frequency response magnitude in air and helium. 147
8-3 Plane wave tube setup for acoustic characterization. 148
8-4 Microphone switching procedure. 149
8-5 Infinite tube measurement setup. 151

8-6 Linearity measurement setup at Boeing Corporation. 153
8-7 Triple Faraday cage setup for noise floor characterization. 155
8-8 Noise floor measurements spans, frequency resolution, and averages. 156
8-9 Impedance measurement setup using a probe station. 157
8-10 Pressure coupler assembly. 162
8-11 Closeup depiction of a microphone die in the pressure coupler setup. 163
8-12 Experimental setup for extraction of acoustic mass and compliance. 164
8-13 Laser vibrometer scan grid overlayed on design E micrograph. 164
8-14 Experimental setup for pressure coupler calibration. 165
8-15 Experimental setup for microphone calibration in the pressure coupler. 166
8-16 Experimental setup for extraction of effective piezoelectric coefficient. 167
8-17 Maps of diced section of wafer 116 (all designs). 168
8-18 Maps of diced section of wafer 138 (all designs). 169
8-19 Resonant frequency maps for wafer 116. 169
8-20 Center displacement sensitivity maps for wafer 116. 170
8-21 Resonant frequency maps for wafer 138. 171
8-22 Center displacement sensitivity maps for wafer 138. 171
8-23 Changes in resonant frequency and displacement sensitivity due to packaging. . 173
8-24 Static deflection profiles of several microphone diaphragms. 174
8-25 Static deflection differences for pre- and post-packaged microphones. 174
8-26 Microphone frequency responses in helium. 175
8-27 Piezoelectric microphone frequency response functions at low frequencies. 177
8-28 Linearity measurements. 178
8-29 Linearity measurements showing unusual nonlinear behavior. 178
8-30 THD measurements. 179
8-31 Output-referred noise floors. 181
8-32 Minimum detectable pressure spectra. 182

8-33 Noise floor spectra for 116-1-J7-A. 182
8-34 Admittance measurements and fits for microphone B5-E. 184
8-35 Frequency response function of microphone 116-1-J7-A. 186
8-36 Parasitic capacitance extraction for microphone 116-1-J7-A. 186
8-37 Comparison of pressure at test and reference locations in pressure coupler. . . . 188
8-38 Frequency response of piezoelectric microphones in pressure coupler. 189
8-39 Displacement per pressure plots. 190
8-40 Displacement per voltage plots. 192
8-41 Comparison of measured and theoretical trends for extracted parameters. 194
8-42 Corrected frequency response magnitude of microphones in pressure coupler. . . 195
9-1 A MEMS piezoelectric microphone die on a playing card. 196
A-1 Laminated composite plate representation of the thin-film diaphragm. 204
A-2 Layer coordinates for an arbitrary composite layup. 216
B-1 Finite element model for investigation of boundary compliancy. 235
B-2 Deflection profiles from FEA with clamped and compliant boundary conditions. 236
B-3 FEA results for models with clamped and compliant boundary conditions. . . . 236
C-1 Noise spectra 95% confidence intervals. 239
C-2 MDP spectra 95% confidence intervals. 239

Abstract of Dissertation Presented to the Graduate School
of the University of Florida in Partial Fulfillment of the
Requirements for the Degree of Doctor of Philosophy

DEVELOPMENT OF A MEMS PIEZOELECTRIC MICROPHONE FOR AEROACOUSTIC APPLICATIONS

By

Matthew D. Williams

May 2011

Chair: Mark Sheplak
Major: Mechanical Engineering

Passenger expectations for a quiet flight experience coupled with concern about long-term noise exposure of flight crews drive aircraft manufacturers to reduce cabin noise in flight. During the aircraft component design or redesign process, aeroacousticians use advanced experimental techniques to help guide these noise-reduction efforts. Chief among their available tools are arrays, distributed collections of microphones that spatially sample pressure fluctuations. Different array configurations are deployed in flight tests on the exterior of aircraft, enabling characterization of the turbulent boundary layer, identification of noise sources, and/or assessment of the effectiveness of candidate noise-reduction technologies.

The requirements for microphones used in aircraft fuselage arrays are demanding. They should be small, thin, and passive; respond linearly to a large maximum pressure; possess audio bandwidth and moderate noise floor; be robust to moisture and freezing; and exhibit stability to large variations in temperature and humidity. Microelectromechanical systems (MEMS) microphones show promise for meeting the stringent performance needs for this application at reduced cost, made possible using batch fabrication technology. This research study represents the first stage in the development of a microphone that meets these needs.

The developed microphone utilized piezoelectric transduction via an integrated aluminum nitride layer in a thin-film composite diaphragm. A theoretical lumped element

model and associated noise model of the complete microphone system was developed and utilized in a formal design-optimization process. Seven optimal microphone designs with 515-910 μm diaphragm diameters and 500 μm-thick substrate were fabricated using a variant of the film bulk acoustic resonator (FBAR) process at Avago Technologies. Laboratory test packaging was developed to enable thorough acoustic and electrical characterization of nine microphones. Measured performance was in line with sponsor specifications, including sensitivities in the range of 30-40 μV/Pa, minimum detectable pressures in the range of 75-80 dB(A), 70 Hz to greater than 20 kHz bandwidths, and maximum pressures up to 172 dB. With this performance in addition to their small size, these microphones were shown to be a viable enabling technology for the kind of low-cost, high resolution fuselage array measurements that aircraft designers covet.

CHAPTER 1
INTRODUCTION

Microphones are among the most fundamental of physical tools in the aeroacoustician's toolbox for locating, understanding, and ultimately reducing noise sources in aircraft. The expense of measurement-grade aeroacoustic microphones suitable for high pressure level measurements places restrictions on even the most richly funded aeroacoustician's experimental plans. Size also remains an issue in some applications. Options are needed, and a new class of high-performance, reduced-size microphones manufactured using low-cost batch fabrication technology may be the answer. The goal of this research is development and demonstration of just such a microphone.

This chapter opens with the motivation for the development of a microelectromechanical systems (MEMS)-based aeroacoustic microphone. Research objectives and contributions are then given, followed by an outline for the remainder of this study.

1.1 Motivation

With the worldwide airline fleet estimated to double in the next 15 years [1], aircraft manufacturers increasingly face regulatory and market driven pressures to reduce aircraft noise. Prolonged exposure to aircraft noise — a recognized form of pollution — in areas surrounding airports is known to have adverse effects on animal behavior and can lead to increase in blood pressure, stress, and fatigue in humans [2]. In the United States, the Federal Aviation Administration (FAA) dictates noise standards that aircraft must meet in order to receive airworthiness certification in terms of effective perceived noise level (EPNL). The EPNL of an aircraft is a measure of the subjective impact of its noise on humans, taking into account the sound level, frequency content, and duration [3]. Noise standards also continue to grow more stringent abroad [1].

Passenger expectations for a quiet flight experience [4] coupled with concern about long-term noise exposure of flight crews [5] also drive aircraft manufacturers to reduce cabin noise in flight. Cabin noise has traditionally been limited using insulating panels

and skin dampers on the fuselage. Practical restrictions on the size and weight of these thin panels limit their effectiveness in reducing low-frequency (long-wavelength) noise [4]. Treating the noise at its source is a promising method for reduction of low-frequency noise with weight savings compared to insulating panels.

During the aircraft component design process, aeroacousticians use advanced experimental techniques to help guide noise-reduction efforts. Chief among their available tools are microphone arrays, distributed collections of microphones that spatially sample pressure fluctuations. Different arrays with different purposes are deployed: dynamic pressure arrays capture hydrodynamic pressure fluctuations associated with a turbulent boundary layer (in addition to any incident acoustic fluctuations), while aeroacoustic phased arrays are used to resolve noise sources.

In 2005–2006 the Quiet Technology Demonstrator 2 (QTD2) program brought together a consortium of aerospace industry leaders for a series of tests to evaluate noise-reduction technologies. A goal of the tests was to determine the effectiveness of various engine inlet and exhaust configurations at reducing noise transmitted to the cabin or radiated to the community below. One noise source that received particular attention was shockcell noise[1] , "a major component of aft interior cabin noise" at cruise conditions that propagates aft of the engine [6]. A dynamic pressure array deployed in flight tests is pictured in Figure 1-1 and was composed of 84 microphones. The array enabled spectral mapping of pressure fluctuations associated with boundary layer and shockcell noise along the fuselage, comparison of levels before and after engine treatments, and identification of axial fuselage locations subjected to the highest shockcell noise levels [7]. A similar array was deployed forward of the engines for characterization of buzzsaw noise[2] [6].

[1] Shockcell noise is "generated by the interaction between the downstream-propagating turbulence structures and the quasi-periodic shockcells in the jet plume" [6].

[2] Buzzsaw noise is "multiple-pure-tone noise generated by high-speed turbofans under conditions of supersonic fan tip speeds" [8].

Figure 1-1. Boeing 777 fuselage instrumented with an array of microphones. [Courtesy Boeing Corporation]

Aeroacoustic phased arrays enable other sophisticated noise-assessment capabilities via an important family of processing techniques known as beamforming algorithms. These schemes allow aeroacousticians to selectively "listen" to regions in space. Maps of the acoustical power reaching the array from a selected spatial region can be generated, and acousticians use this information to locate noise sources or to justify experimental/numerical studies of specific noise generation mechanisms. In addition, array measurements obtained from different test configurations can be compared to assess the effectiveness of noise treatments.

Figure 1-2A shows linear and elliptic phased arrays composed of 132 and 181 microphones, respectively, deployed as part of the static engine test component of the

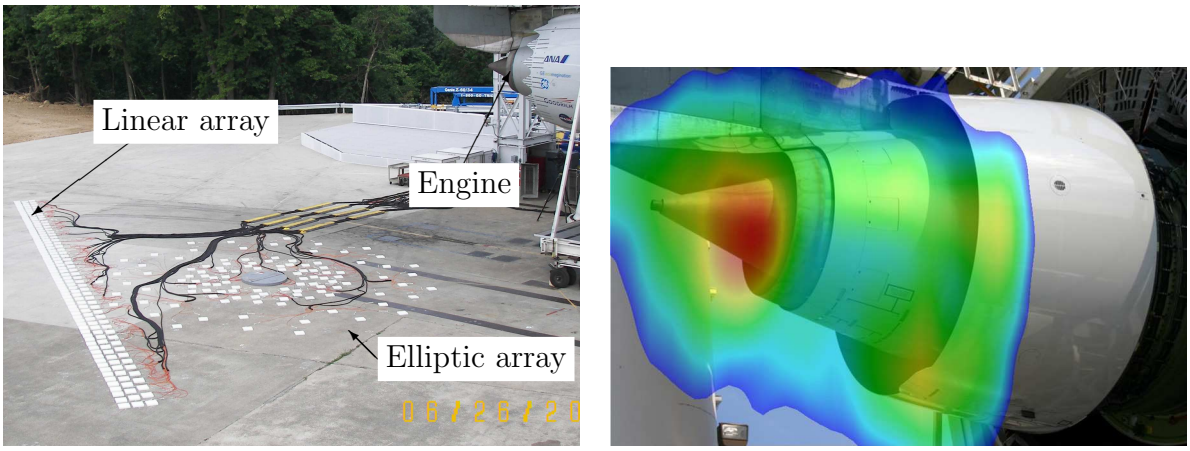

A B

Figure 1-2. Aeroacoustic phased arrays deployed as part of the QTD2 program [9]. A) Linear and elliptic phased arrays located aft of an aircraft engine. B) Relative sound power level map created via beamforming. [Courtesy Boeing Corporation]

QTD2 program [9]. Static engine tests, with their lower cost and complexity compared to flight tests, enable a more comprehensive assessment of noise reduction technologies via inclusion of more engine configurations and instrumentation. The elliptic array in Figure 1-2A was designed to enable discrimination between fan and core sources of engine noise, while the linear array was used primarily to identify noise sources along the jet axis. An example map of the relative sound pressure levels associated with a particular engine configuration, found via beamforming with the elliptic array, is shown in Figure 1-2B.

Array performance is a function of the number and arrangement of microphones that comprise it, in addition to the individual microphone characteristics. A dynamic pressure array for turbulent boundary layer measurements must have adequately small sensors with high bandwidth and close spacing in order to resolve the smallest length and time scales of interest in the flow. Two relevant representative length scales are the Kolmogorov length scale and viscous length scale [10]. The ratio of the Kolmogorov microscale η to the boundary layer thickness δ, for example, scales as [11, 12]

$$\frac{\eta}{\delta} \sim \mathrm{Re}_{\delta}^{-3/4}, \tag{1–1}$$

where $\mathrm{Re}_\delta = u\delta/\nu$ is the eddy Reynolds number that characterizes the turbulent boundary layer and ν is the kinematic viscosity. The eddy velocity u and boundary layer thickness δ serve as the velocity and length scales in Re_δ, respectively. Dynamic pressure array design for turbulent boundary layers thus becomes more challenging as the Reynolds number increases [13].

Phased arrays used for beamforming also have stringent requirements of their own. Developments in aperiodic phased array design [14] have helped to relax the sensor-to-sensor spacing and channel-count requirements, but the need for higher channel counts at lower cost remains. The dynamic range of a phased array, for example, improves with the number of microphones [14, 15]. In a book chapter he wrote on phased array measurements in wind tunnels, James Underbrink of Boeing Corporation — a foremost expert in aeroacoustic phased array technology — wrote this of his experiences designing phased arrays: "In dozens of phased array tests, no matter how many measurement channels were available, more would have always been better" [14]. Achieving high channel counts is particularly challenging for high frequency arrays, in which small apertures are used in order to accurately capture directive sources. Small-aperture arrays with high channel counts require small sensors.

Limitations exist in the deployment of high-channel-count arrays, including the cost per channel, data collection and storage capabilities, and compatibility with existing test facilities [15]. In addition, microphones suitable for use in aeroacoustic array measurements must often meet demanding requirements, including sensing of high sound pressure levels (>160 dB) with low distortion (<3 %) and high sensitivity stability (hundredths of a dB). Depending on the scale of the test, large bandwidths (up to 90 kHz for 1/8 scale [14]) may also be necessary. Measurement-grade sensors that meet these criteria are expensive, often costing upwards of $2k. With unavoidable equipment loss in aeroacoustic testing, where measurements may be done in high pressure wind tunnels,

outdoors, or in full-scale flight tests, the large initial investment gives way to significant recurring costs as well.

MEMS microphones show promise for meeting the stringent performance needs of aeroacoustic applications at reduced cost, made possible using batch fabrication technology [16–21]. At reduced cost per channel, higher density arrays with better performance become possible. In addition, there is an obvious relationship between sensor cost and the need for time-consuming protective measures; made cheap enough (<$50/channel), "disposable" sensors would eliminate dozens of man-hours from moderate sensor-count (50–100) tests or even more from very large installations.

Perhaps most importantly, the small size of MEMS microphones position them as an enabling technology for more advanced measurements, particularly in full-scale flight tests where sensors must be extremely thin and robust. One reason the Kulite microphone array on the Boeing 777 fuselage in Figure 1-1 are sparsely distributed — other than cost constraints — is because sensor locations must be carefully chosen to avoid flow disturbances caused by upstream sensors affecting those downstream. With these sensor density restrictions, deployed arrays have not yet been sufficient for beamforming [22]. Thinner sensors requiring smaller packaging may be more densely packed, enabling both higher-resolution maps of the fluctuating pressure field on the fuselage and eventually, beamforming of in-flight data to identify dominant noise sources for actual — not simulated — flight conditions.

1.2 Research Objectives

The goal of this research is the design, fabrication, and characterization of a MEMS microphone appropriate for use in aeroacoustic arrays. Among the application areas are flyover arrays [23–25], static engine test arrays [9, 26, 27], and fuselage arrays [4, 7, 22], each with its own set of requirements. The primary application for this work is the fuselage array; static engine test arrays, with less stringent specifications in many respects, are viewed as a secondary application.

The demanding set of requirements for fuselage array microphones may only be met by careful engineering decisions even in the early design stages. To overcome fuselage instrumentation challenges already discussed, size — particularly thickness — is extremely important; only microfabricated sensors are capable of achieving the small sizes needed. The microphones must be robust, particularly to moisture. Microphones with low complexity that fully leverage existing data acquisition equipment are highly desirable for flight tests at remote locations involving thousands of sensors. Specifically, low power consumption, characteristic of passive sensors in which only interface electronics need be powered, enables the use of compact data acquisition systems with integrated standard 4 mA constant-current sources. Among the transduction mechanisms available for microfabricated microphones are capacitive, piezoresistive, optical, and piezoelectric, but only piezoelectric transduction offers the right mix of robustness, simplicity, performance, and passivity. A review of MEMS microphones from the academic literature in Chapter 3 shows the promise of piezoelectric microphones for meeting fuselage array application requirements.

The project sponsor, Boeing Corporation, specified design requirements for the fuselage array application that are found in Table 1-1. These requirements were derived from the sponsor's desire to meet or exceed existing measurement capabilities. The current sensor in use, the Kulite LQ-1-750-25SG, is a custom-packaged version of the commercially-available Kulite LQ line of pressure transducers. Its performance characteristics, as provided by Boeing, are collected as well in Table 1-1.[3] Perhaps the most difficult competing specifications in Table 1-1 to be met are the maximum pressure of 172 dB (400 times the threshold of pain for humans) and minimum detectable pressure of 93 dB overall sound pressure level (OASPL). The relationship between these

[3] Definitions of the important microphone performance metrics are found in Chapter 2.

specifications and a variety of other design trade-offs are discussed at length in Chapters 5 and 6.

Table 1-1. Fuselage array application requirements.

Metric	MEMS Requirement	Kulite LQ-1-750-25SG
Sensing element size	$\phi \leq 1.9\,\text{mm}$	$864\times864\,\mu\text{m}^2$
Sensitivity	$500\,\mu\text{V/Pa}^{\dagger}$	$1.1\,\mu\text{V/Pa}$
Minimum detectable pressure	$\leq 48.5\,\text{dB}^{\ddagger}$	$48.5\,\text{dB}^{\ddagger}$
	$\leq 93\,\text{dB OASPL}^{\#}$	$93\,\text{dB OASPL}^{\#}$
Maximum pressure*	$\geq 172\,\text{dB}$	$172\,\text{dB}$
Bandwidth	$20\,\text{Hz–}20\,\text{kHz}^{\S}$	$<20\,\text{Hz–}20\,\text{kHz}+$
Packaged thickness	$0.05\,\text{in}$	$0.07\,\text{in}$

† With on-board gain ‡ 1 Hz bin centered at 1 kHz $^{\#}$ 20 Hz–20 kHz * 3% distortion
§ ±2 dB

The scope of this study is the design, fabrication, and laboratory characterization of a piezoelectric MEMS microphone that reaches the design specifications of Table 1-1. A number of additional needs, including stability over a wide range of temperatures ($-60\,^{\circ}\text{F}$ to $150\,^{\circ}\text{F}$), robustness to the harsh high-altitude environment and moisture, and ultra-thin packaging, fall outside of this scope. These items represent future research and development work.

1.3 Dissertation Overview

This chapter established the need for an aeroacoustic MEMS microphone suitable for aeroacoustic array measurements. Design goals were defined for microphone deployment in full-scale flight-test fuselage arrays. In Chapter 2 microphone fundamentals and performance metrics are defined, then in Chapter 3 previous work in the area of MEMS microphones is reviewed. The choice of piezoelectric material, fabrication process, and basic microphone geometry are addressed in Chapter 4. A system-level lumped element model and a novel piezoelectric composite plate model are developed in Chapter 5 and then used for design optimization in Chapter 6. In Chapter 7, the fabrication results and packaging process are discussed. Chapter 8 presents characterization and parameter

extraction results for the realized piezoelectric MEMS microphones, and Chapter 9 concludes with final observations and suggestions for future work.

CHAPTER 2
MICROPHONE FUNDAMENTALS

This chapter covers the fundamentals of microphones. First, the concepts of sound and pseudo sound are introduced. Next, the realities of designing a microphone to sense sound, including inherent limitations in physical systems and common characteristics, are discussed. The various performance metrics for microphones are then addressed. At the conclusion of the chapter, microphone performance is summarized in a holistic way in terms of sound pressure and frequency.

2.1 Sound and Pseudo Sound

A wave, as defined by Blackstock [28], is "a disturbance or deviation from a pre-existing condition." Sound waves, in particular, are a disturbance in pressure. This pressure disturbance is characterized via the pressure decomposition

$$P = p_0 + p, \tag{2–1}$$

where P is the instantaneous absolute pressure, p_0 is the static pressure, and p is the fluctuating pressure. This fluctuation is known as the acoustic pressure and is reported in units of Pascal (Pa). Sound waves propagate as longitudinal waves via a molecular collision process, in which individual particle motion occurs in the same direction as wave propagation [28].

The field of aeroacoustics is concerned with the generation of sound by moving flows and the propagation of sound from them. In the study of aerodynamically generated sound, is it important to distinguish sound, which propagates as a wave and is a compressibility-based phenomenon, from pseudo sound, which decays rapidly away from its source and is hydrodynamic in nature [29, 30]. Both sound and pseudo sound are present in the turbulent boundary layer associated with flow over an aircraft fuselage. Pseudo sound does not propagate in air away from the airplane but can transmit to the

interior via induced vibration on the fuselage skin. As a result, pseudo sound does not contribute to ground level noise, but does play a role in cabin noise [30].

Because sound pressures vary over a wide range, they are quantified on a logarithmic scale. Sound pressure level (SPL) is defined in units of decibels (dB) as [28, 31]

$$\mathrm{SPL} = 20 \log_{10} \left(\frac{p_{rms}}{p_{ref}} \right), \tag{2–2}$$

where p_{rms} is the rms pressure level and p_{ref} is a reference pressure. In air, it is standard for p_{ref} to be taken as $20\,\mu$Pa, the approximate threshold of hearing in the 1–4 kHz range for young persons [28]. Typical sound pressure levels therefore vary from 0 dB (at the threshold of hearing) to 120 dB (at the threshold of pain) [28]. Sound pressure levels associated with, for example, aircraft engines can exceed this threshold by orders of magnitude.

Given the human ear's nonlinear and frequency dependent behavior, various psychoacoustic measures of sound are used to quantify noise levels in a human-oriented way. Frequency-weighting is often used to obtain sound pressure levels that more accurately reflect human judgements of loudness. Three such schemes are known as A-, B-, and C-weighting, with each accounting for frequency-dependent hearing characteristics in humans at different sound pressure levels. A-weighting is appropriate for the lowest sound pressure levels and its use is the most prevalent. Sound pressure levels that have been weighted are traditionally denoted in dB(A), etc. As sound energy may be distributed over a broad range of frequencies, integrating sound pressure over frequency (usually the range of human hearing) produces another useful measure, the overall sound pressure level (OASPL). The OASPL may also be obtained from a frequency-weighted spectrum. The effective perceived noise level (EPNL), mentioned briefly in Chapter 1, is an overall sound pressure metric used for aircraft certification that accounts for frequency/tonal content and duration [32, 33].

2.2 The Realities of Microphone Design

A transducer is a device that uses an input in one energy domain to produce a corresponding output in another energy domain. A microphone is a particular kind of transducer that converts an input acoustic signal into an output electrical signal. To perform this conversion, the microphone possesses a mechanical element, usually a diaphragm, that displaces under an incident acoustic pressure wave. An electromechanical transduction mechanism serves to either convert this mechanical reaction to an output electrical signal or use it to modulate an existing electrical signal.

The ideal mechanical element for this electromechanical system is a linear, massless spring, i.e. one that obeys the constitutive relationship

$$f_a(t) = kx(t), \tag{2–3}$$

where f_a is the applied force (input) analogous to pressure, k is the spring stiffness, and x is the displacement (output) analogous to an electrical signal. Because the spring is perfectly linear, this relationship continues to hold regardless of the magnitude of the input f_a. The frequency response of this ideal, massless spring is [34]

$$\frac{X(f)}{F_a(f)} = \frac{1}{k}, \tag{2–4}$$

where X and F_a are the Fourier transforms of x and f_a. Regardless of the excitation frequency f, the input F_a and output X are related by the constant $1/k$ (the gain factor) and are always perfectly in phase (zero phase factor). The perfect spring thus responds to an input of any magnitude at any frequency with perfect fidelity. These response characteristics are reflected in Figure 2-1. If a massless spring by itself could serve as a microphone, it could detect the quiest whisper or the loudest explosion at infrasonic, sonic, or ultrasonic frequencies and reproduce it perfectly.

Mechanical systems in the real world necessarily possess mass as well as damping, so it should come as no surprise that the frequency response of a real "spring" differs

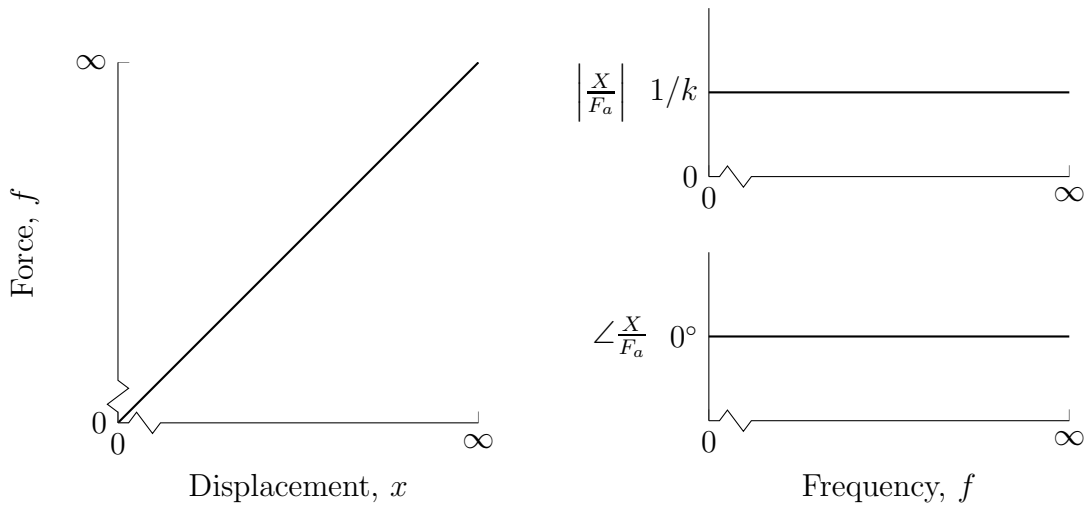

Figure 2-1. Force-displacement characteristics for a perfect spring.

markedly from the ideal spring. The governing equation for a representative single degree of freedom mass (m)-spring (k)-damper (b) system is

$$m\ddot{x} + b\dot{x} + kx = f_a, \tag{2–5}$$

where each $\dot{\square}$ symbolizes differentiation with respect to time, d/dt. Equation 2–5 is the classical equation for a second-order system. The frequency response function is then

$$\frac{X(f)}{F_a(f)} = \frac{1/k}{1 - \left(\frac{f}{f_n}\right)^2 + j2\zeta\left(\frac{f}{f_n}\right)}, \tag{2–6}$$

where the natural frequency $f_n = 1/2\pi\sqrt{k/m}$ and the damping ratio $\zeta = b/2m\omega_n = b/4\pi m f_n$ [34]. The frequency response function of the mass-spring-damper system is now a function of frequency as shown in Figure 2-2 for various values of the damping ratio. An under-damped ($\zeta < 1$) second-order system has a maximum gain at the resonance or damped natural frequency, $f_r = f_n\sqrt{1 - 2\zeta^2}$. If this system alone served as a microphone, the signal components with frequencies near f_r would be amplified considerably compared to those at other frequencies and the original signal could not be recovered exactly without accurate knowledge of the entire frequency response function. Figure 2-2 also shows that under-damped systems have excellent phase response over a wide frequency

range, but as the damping ratio is increased, significant phase lag in the output results. When working with real mechanical systems that behave this way, an engineer must decide what kind of gain and phase error are acceptable and over what frequency range they are achievable.

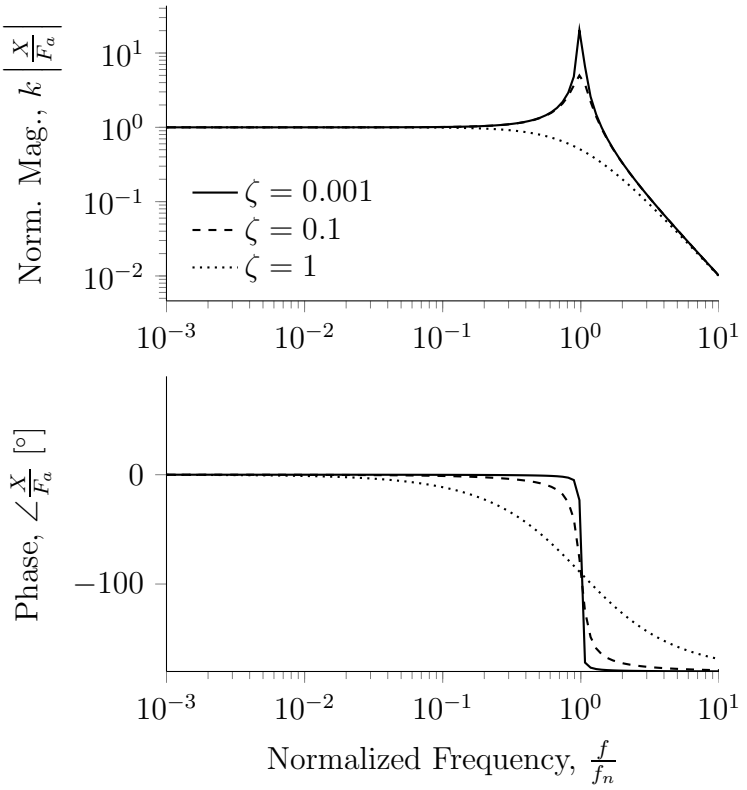

Figure 2-2. Frequency response of a second-order system.

A perfectly linear spring — even one that accounts for mass and damping — also does not exist, as physical systems respond linearly at best over a limited range of inputs. The elastic limit is a well-known threshold beyond which many materials transition from linear elastic to nonlinear plastic behavior. However, in many mechanical systems, the linear/nonlinear threshold is actually dictated by the onset of geometric nonlinearity, which occurs when displacements become sufficiently large that their relationship to strain is no longer approximately linear. The Duffing spring is a well-known single-degree-of-freedom representation of a geometrically nonlinear mechanical system, and it is governed by the

equation

$$m\ddot{x} + b\dot{x} + k_1 x + k_3 x^3 = f_a. \tag{2–7}$$

For sufficiently small values of the input f_a (corresponding to a sufficiently small output x), the nonlinear term does not significantly contribute. Nonlinear spring-hardening behavior ($k_3 > 0$) is shown in Figure 2-3 together with the linearization about $x = 0$. Input waveform $f_a(t)$ is increasingly distorted at the output $x(t)$ as its amplitude exceeds the approximately linear region of the sensitivity curve in Figure 2-3.

Consider, for example, the input-output relationship expressed as a Taylor series over a limited domain as [35]

$$x(t) = b_1 f_a(t) + b_3 f_a^3(t), \tag{2–8}$$

where a f_a^2 term is not included such that x is an odd function of f_a. For an input $f_a(t) = a_1 \sin(\omega t)$, the output becomes, after making use of trigonometric identities,

$$x(t) = \left(a_1 b_1 + \frac{3}{4} a_1^3 b_3\right) \sin(\omega t) - \frac{1}{4} a_1^3 b_3 \sin(3\omega t). \tag{2–9}$$

Due to the nonlinear input-output relationship, the response x contains a signal component at frequency 3ω despite the presence of only a signal component at frequency ω at the input. This nonlinear phenomenon is in contrast to that of an idealized linear system, for which magnitude and phase of the input signal are modified but the frequencies of the input signal are preserved [34]. It is thus important for a microphone designer to know the range of inputs for which the assumption of linearity is valid.

In order to promote a pressure difference across the mechanical sensing element of a microphone in an acoustic field, acoustic propagation between the front and back of the sensing element must be impeded. In general, the sensing element (for example, a diaphragm) is suspended over a back cavity, with one side exposed to the acoustic field and the other exposed to the cavity. The composition of the back cavity must then be determined; obvious choices are that it can be sealed at vacuum or contain a fluid. For the

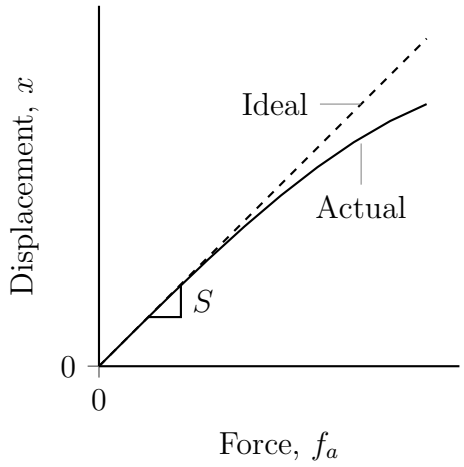

Figure 2-3. Constitutive behavior for a Duffing spring.

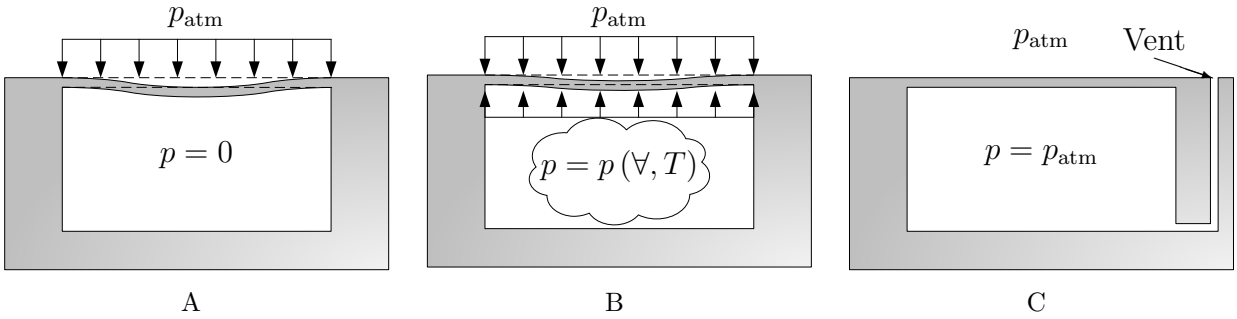

Figure 2-4. Various cavity configurations. A) Vacuum sealed. B) Fluid isolated. C) Vented.

latter, the fluid can be isolated from or vented to the measurement medium. Each of these configurations are shown in Figure 2-4.

There are consequences to each of these choices. A vacuum-sealed cavity as in Figure 2-4A enables measurement of static pressure changes, but as a consequence leaves the diaphragm always subjected to atmospheric pressure loading. Acoustic signals then cause the diaphragm to oscillate about a statically-deflected configuration. In order for this static deflection to not exceed the approximately linear regime of operation, the diaphragm must be very stiff and thus less sensitive to acoustic perturbations, which even in high SPL aeroacoustic applications are one or more orders of magnitude smaller than the equivalent 194 dB atmospheric pressure. Alternatively, the microphone can be

operated about the nonlinearly-deflected operating point, but sensitivity becomes highly dependent on atmospheric pressure and dynamic range is likely sacrificed. For all of these reasons, the vacuum-sealed cavity configuration of Figure 2-4A is typically only utilized as an absolute static pressure sensor and not as a microphone.

Meanwhile, a fluid medium inside a cavity acts as an additional spring and thus has its own impact on the overall dynamics of the system [28]. The configuration of Figure 2-4B — in which the reference pressure is set — enables measurement of differential static and dynamic pressure and is typical of dynamic pressure sensors. One downside is that unintended changes in the reference pressure impact the measurement. For example, at zero pressure there is sensitivity to temperature change in the cavity fluid due to expansion, particularly if the cavity is sealed.

Microphones are usually vented — the cavity is connected to the ambient environment by a thin channel as in Figure 2-4C — to avoid the effects of static pressure. The channel allows static pressure equilibration between the front and back of the diaphragm, but more rapid pressure changes associated with acoustic waves still cause the diaphragm to vibrate [36]. As a result, a vented microphone is less responsive to sound waves below a certain design frequency. In addition, since the cavity is connected to the operating environment, it is filled with the associated gas (usually air).

Thus, microphones generally share the traits shown in the cross section of Figure 2-4C: a diaphragm (the typical mechanical sensing element); a cavity, which isolates the front and back of the diaphragm and provides room for it to deflect; and a vent, which allows static pressure equilibration between the front and back of the diaphragm. A transduction mechanism (not shown) is responsible for producing electrical output.

2.3 Microphone Performance Metrics

In Section 2.2, the realities of microphone design were addressed from the perspective of a classical second-order system. Common features of microphones and their roles in

determining microphone performance were established. In this section, the various metrics used to characterize the performance of a microphone are discussed in turn.

2.3.1 Frequency Response and Sensitivity

The typical frequency response of an under-damped aeroacoustic microphone is shown in Figure 2-5. The region of the frequency response that is approximately constant is known as the flat band and its corresponding magnitude value is called the sensitivity, S. The sensitivity has units of V/Pa (or often dB re 1 V/Pa) and relates output voltage to input pressure for frequencies in the flat band. Microphone manufacturers quote the sensitivity on specification sheets at a particular flat-band frequency; for Danish company Brüel and Kjær, a prominent supplier of measurement quality microphones, this is usually 250 Hz [31]. The total frequency range over which the frequency response is equal to this sensitivity to within some tolerance, usually ± 3 dB (or sometimes ± 2 dB) , is known as the bandwidth [31]. The lower end of the bandwidth at $f_{-3\ dB}$ is the *cut-on frequency*, while $f_{+3\ dB}$ is the *cut-off frequency*. The vent structure, transduction mechanism, and/or interface electronics dictate the low frequency response of the microphone, and thus the cut-on frequency. The resonance behavior of the diaphragm (or the roll-off for overdamped microphones) dictates the cut-off frequency. Although only the first (or fundamental) resonance is shown in Figure 2-5, microphones in reality exhibit an infinite number of additional resonances because they are continuous system with infinite degrees of freedom [37].

Also illustrated in Figure 2-5, the phase of an ideal microphone in the flat band is zero, meaning there is no lag between input and output. In commercial condenser microphones, the damping is often tuned to reduce the resonant peak to within the ± 3 dB limits or eliminate it entirely, which extends the bandwidth but causes early phase roll-off as discussed in Section 2.2 (Figure 2-2) [31].

It would seem that achieving a high microphone sensitivity is a primary design goal. Increasing the sensitivity, after all, ensures a higher (and presumably easier to measure)

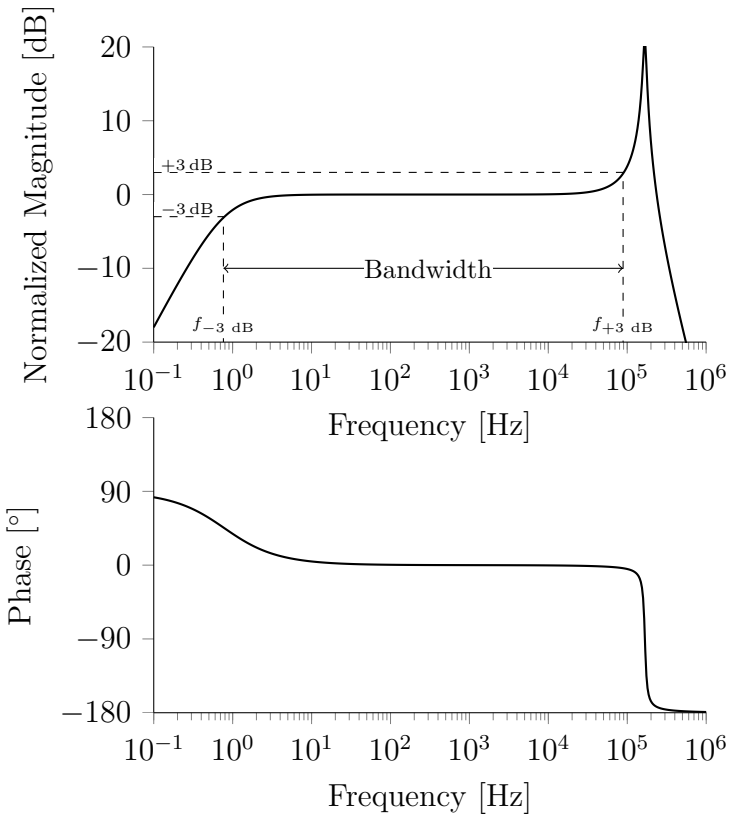

Figure 2-5. Typical aeroacoustic microphone frequency response (magnitude normalized by flat-band sensitivity and phase).

output signal for the same input signal. However, amplification of the output signal can achieve much the same effect. In the next section, it will be shown that while a high sensitivity is beneficial, it is not of primary importance.

2.3.2 Noise Floor and Minimum Detectable Pressure

Noise, in a general sense, is the output signal of a device in the absence of an intended input. Noise may be classified as intrinsic noise, a truly random output in the absence of input, and extrinsic noise, which is due to pickup of unwanted external signals. In a microphone, an input pressure that yields an output voltage lower than the noise of the microphone (the noise floor) cannot be easily detected; a microphone's minimum detectable pressure is therefore defined as the pressure that produces an output signal equivalent to the noise floor.

The most common intrinsic noise source is thermal noise, which is present in electrical and mechanical/acoustic systems in thermodynamic equilibrium. In the electrical domain, this form of noise is called Johnson or Nyquist noise and is due to random thermal motion of charge carriers [38, 39]; the mechanical/acoustic analog is Brownian motion, the random thermal motion of particles [40]. The fluctuation-dissipation theorem [41] establishes the relationship between thermal noise and dissipation in a system. Gabrielson summarizes the fluctuation-dissipation theorem thusly [42]: "If there is a path by which energy can leave a system, then there is also a route by which molecular-thermal motion in the surroundings can introduce fluctuations into that system." As a result, any source of dissipation is also a source of noise [42]. Thermal noise has uniform power at all frequencies[1] and is conveniently defined in terms of power spectral density (PSD) as [39, 43]

$$S_n = 4k_B T R, \tag{2–10}$$

where k_B is the Boltzmann constant, T is the temperature, and R is the dissipation or damping. For an electrical system, R is in units of Ω and thus S_n is in units of V^2/Hz; the use of Equation 2–10 in other energy domains is discussed further in Section 5.3.3. An equivalent noise model for a resistor consistent with the fluctuation-dissipation theorem is shown in Figure 2-6. Here, a "noisy" resistor has been replaced with a perfect noiseless resistor in series with a noise source v_n with spectral density function defined in Equation 2–10.

Equation 2–10 implies that thermal noise always increases with dissipation; this is only partially true. In reality, the placement of the dissipative element in the circuit plays a role. Taking a resistor in parallel with a capacitor as an example and measuring output

[1] In reality, thermal noise has uniform noise power at frequencies for which $hf/k_BT \ll 1$, where h is Planck's constant. This condition holds to approximately the microwave band [39].

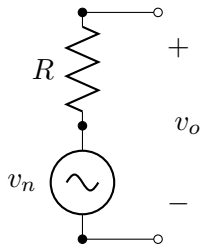

Figure 2-6. Noise model for a resistor.

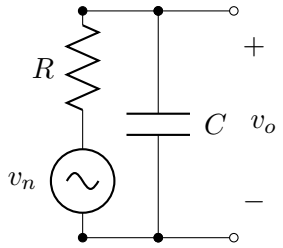

Figure 2-7. Noise model for a resistor in parallel with a capacitor.

noise voltage across the capacitor, as in Figure 2-7, a low pass filter is formed. As a result, the shunt capacitance actually serves to attenuate the noise at high frequencies. As R increases, the filter cutoff frequency ($f_c = 1/2\pi RC$) is correspondingly reduced and noise power is shifted to lower and lower frequencies, as illustrated in Figure 2-8. This form of thermal noise is sometimes called k_BT/C noise because when the output noise PSD is integrated over an infinite bandwidth, the squared rms output noise voltage is equal to k_BT/C [39]. The concept of k_BT/C noise is shown to be important in the context of a piezoelectric microphone in Chapter 5.

Non-equilibrium noise sources also exist in solid state devices when direct current is present (for example, in operational amplifiers). One such noise source, flicker noise, has an inverse frequency dependence and is often called $1/f$ *noise*. It is dominant at low frequencies, but at a sufficiently high frequency, called the *corner frequency*, thermal noise [43] becomes dominant. In the context of microphones, for example, $1/f$ noise is present in piezoresistive microphones [38] and is common in interface electronics used in microphones. Figure 2-9 shows the transition from $1/f$ noise to thermal noise for the voltage noise of the LTC6240 amplifier [44] utilized in this study (see Chapter 7).

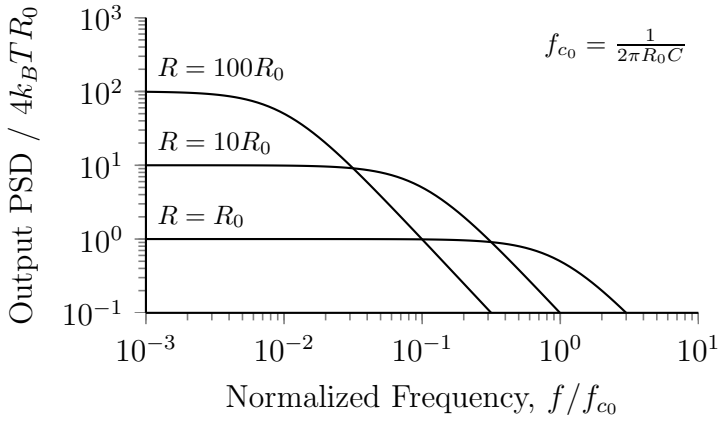

Figure 2-8. Low-pass filtering of thermal noise.

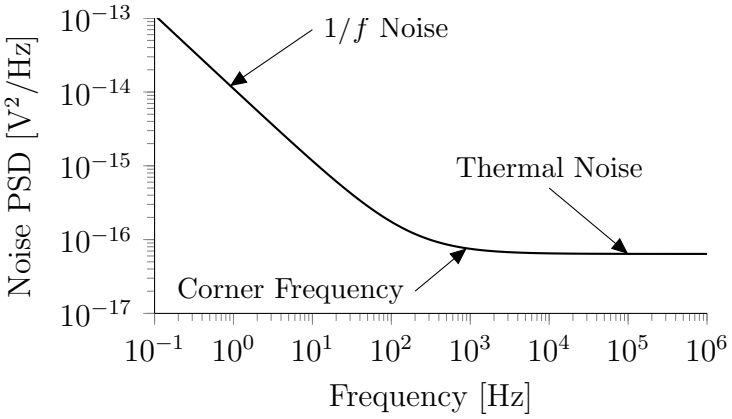

Figure 2-9. Voltage noise spectrum for an LTC6240 amplifier [44].

Extrinsic noise is altogether different, in that it originates external to the sensor and is typically deterministic in nature [45]. Avoidance of pickup of omnipresent electromagnetic signals radiated from everyday electronics (at 50 Hz to 60 Hz and harmonics) is important for an audio sensor and can be a particular challenge for sensors with high electrical impedance [46]. In general, the impact of extrinsic noise can be mitigated at the package-level using careful circuit layout and shielding techniques [43], though shielding of microscale sensors becomes more difficult at low frequencies when the skin depth of electromagnetic radiation becomes large and thicker conductive shields become necessary [45].

The minimum detectable pressure is the input-referred noise of a microphone integrated over a bandwidth of interest,

$$p_{min} = \sqrt{\int_{f_1}^{f_2} \frac{S_o^v(f)}{|S|^2} df}, \tag{2–11}$$

where $S_o^v(f)$ is the output-referred noise PSD [V^2/Hz] and S is the microphone frequency response function. Minimum detectable pressure is often reported as a SPL, i.e.

$$\text{MDP} = 20 \log_{10} \left(\frac{p_{min}}{p_{ref}} \right). \tag{2–12}$$

Equation 2–11 clarifies why sensitivity alone is not the primary design metric of interest. Although high sensitivity naturally leads to a low minimum detectable pressure, the noise characteristics of the microphone and its associated electronics also play an important role.

Several variations of the minimum detectable pressure metric exist with different physical and psychoacoustic focuses. Integration over a narrow bandwidth in Equation 2–11 yields "narrow band MDP"; for an aeroacoustic microphone, the integration is commonly over a 1 Hz bin centered at 1 kHz. This narrow band definition provides information at an important frequency to which human sound sensitivity is high [28] and is easy to compare and compute. However, it says little about the overall microphone noise characteristics. Integration over the bandwidth of the device in Equation 2–11 (e.g. the audio band), meanwhile, gives the minimum detectable broadband rms pressure level. In this case, MDP is reported in units of dB OASPL (overall sound pressure level). Finally, it is also common for the noise spectrum to be A-weighted in order to mimic the overall human sound perception; MDP is then given in units of dB(A).

2.3.3 Linearity and Maximum Pressure

It was established in Section 2.2 that a perfectly linear mechanical sensing element does not exist. As a result, the actual response of a microphone can only be approximated as linear for sufficiently small pressure inputs. When the pressure becomes "large,"

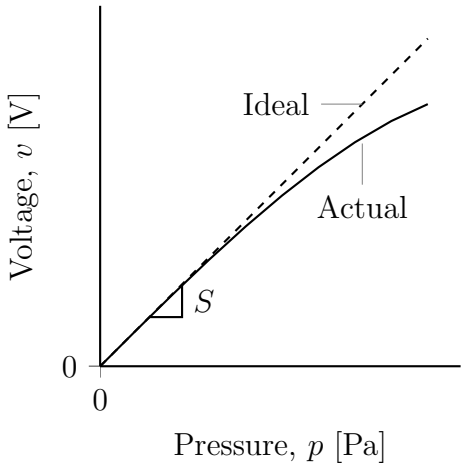

Figure 2-10. Ideal and actual response of a microphone.

higher-order effects, often geometric nonlinearity of the diaphragm or transduction nonlinearities, become important. The typical characteristics of an actual microphone response are compared to the ideal linear response in Figure 2-10. The local slopes of the lines correspond to the ideal and actual microphone sensitivity.

Waveform distortion is always present in real, nonlinear systems. As discussed in Section 2.2, an input waveform $A\sin(\omega t)$ does not emerge from a nonlinear system purely as an output $B\sin(\omega t + \phi)$; the output signal also contains frequencies at integer multiples of the fundamental frequency, called harmonics. In typical nomenclature, a signal component with frequency $n\omega$ is referred to as the nth harmonic. The assumption of linearity implies that the power distributed to the second and higher harmonics is negligibly small with respect to the first.

To quantify the extent of nonlinearity in the response of a microphone for a particular input pressure level, the total harmonic distortion metric is used. Many variants on this metric exist [35, 47, 48] and thus great care must be taken when it is used to compare different microphones. The definition of total harmonic distortion used here is [47, 49],

$$\mathrm{THD} = \sqrt{\frac{\sum_{n=2}^{\infty} {v_o}^2(f_n)}{{v_o}^2(f_1)}} \times 100\%, \tag{2–13}$$

which represents the ratio of the rms output voltage in all higher harmonics (f_n, $n = 2 \ldots \infty$) to that in the first for a single tone input pressure signal at f_1. The maximum pressure p_{max} for a microphone is the pressure at which the THD reaches a prescribed value (often 3-10%). The maximum pressure may be reported in units of Pa or dB with the nomenclature PMAX used for the latter case.

2.3.4 Dynamic Range

Together, MDP and PMAX define the operating pressure range for a microphone, called the *dynamic range*. It is defined in units of dB as

$$\mathrm{DR} = 20 \log_{10} \left(\frac{p_{max}}{p_{min}} \right) = \mathrm{PMAX} - \mathrm{MDP}. \tag{2–14}$$

Because there are several variations on the definition of MDP, the dynamic range metric is often written as a range of two numbers (e.g. MDP – PMAX) rather than in dB. When Equation 2–14 is used, clarifying language is often included.

2.3.5 Summary of Microphone Performance Metrics

Microphone performance can be condensed into the concept of an operational "space" in the frequency and pressure domains, pictured in Figure 2-11. The bounds of this "space," are related to each of the performance metrics discussed in Section 2.3.1–Section 2.3.3. Note that although the "space" is shown in Figure 2-11 as rectangle for simplicity, both MDP and PMAX are in general frequency dependent.

To provide context for each of the presented performance metrics, the properties of well-known aeroacoustic microphones from Brüel and Kjær (B&K) and Kulite are collected in Table 2-1. All of these microphones are high-frequency instruments appropriate for model-scale measurements. Sensitivities of the Brüel and Kjær 4138 and 4938 pressure-field microphones (1/8" and 1/4" diameters, respectively) are on the order of 1 mV/Pa, while the smaller Kulite microphone (.093") has a lower sensitivity on the order of 1 μV/Pa. As a result, the Kulite microphone also has a significantly higher noise

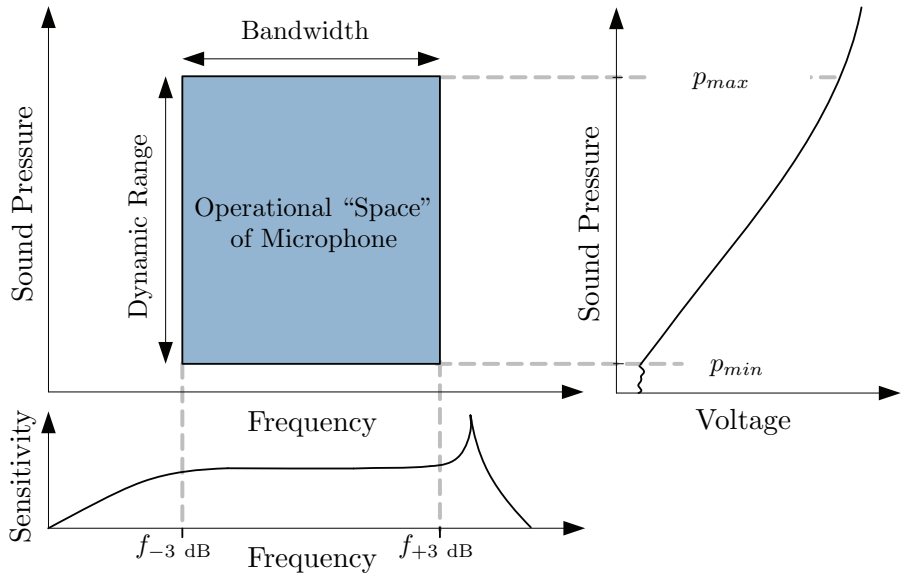

Figure 2-11. Operational space of an aeroacoustic microphone.

Table 2-1. Performance characteristics of common aeroacoustic microphones.

Metric	B&K 4138 [50]	B&K 4938 [51]	Kulite MIC-093 [52]
Sensitivity [mV/Pa]	1	1.6	.004
Bandwidth	6.5 Hz – 140 kHz†	4 Hz – 70 kHz†	<125 kHz$^{\#}$
MDP [dB]	52	30‡	100‡
PMAX [dB]	168*	172*	194
Dynamic Range [dB]	116	142	94

† ±2 dB $^{\#}$ Resonant frequency ‡ A-weighted * 3% distortion

floor (100 dB(A)) compared to the Brüel and Kjær microphones. Every microphone in Table 2-1 possesses PMAX > 160 dB.

2.4 Summary

The fundamentals of microphones, including the physical structure and performance metrics, were addressed in this chapter. Knowledge of these topics sets the stage for a review of the state-of-the-art of MEMS microphones in Chapter 3 and microphone design in Chapters 5 and 6.

CHAPTER 3
PRIOR ART

In this chapter, a review of realized microelectromechanical systems (MEMS) microphones provides context for the development efforts of this study. The literature on MEMS microphones is extensive, with most efforts focused on microphones for consumer audio applications. The requirements associated with audio microphones differ significantly from those of an aeroacoustic measurement microphone. In the former application area, the minimum detectable pressure requirements are particularly stringent (usually $< 30\,\mathrm{dB(A)}$), while requirements for bandwidth (10–15 kHz) and maximum pressure (typically $< 120\,\mathrm{dB}$) are less important. Maximum pressure and bandwidth requirements for microphones targeted at aeroacoustic measurements vary with the specific measurement, sometimes reaching or exceeding 160 dB and 100 kHz, respectively. The noise floor, meanwhile, is less critical than for audio microphones.

The review in this chapter is restricted to MEMS microphones utilizing piezoelectric transduction and MEMS microphones targeted at aeroacoustic applications. MEMS microphones of these classifications form a portrait of the state-of-the-art from which the piezoelectric microphone developed in this study emerges. A general review of MEMS microphones was written by Scheeper (1994) [53] and more recent but unpublished reviews were completed by Martin (2007) [21] and Homeijer (2008) [54].

3.1 Review of MEMS Piezoelectric and Aeroacoustic Microphones

The first microfabricated piezoelectric microphone, depicted in Figure 3-1, was developed by Royer et al. (1983) [55]. It was composed of a sputtered zinc oxide (ZnO) layer atop a thin circular silicon diaphragm. Some devices featured an integrated on-chip MOS buffer amplifier, though the highest sensitivity of $250\,\mu\mathrm{V/Pa}$ was reported for a non-integrated device.

In 1987, Kim et al. [56] of the Berkeley Integrated Sensor Center presented the second piezoelectric MEMS microphone fabricated using ZnO thin film, this time on

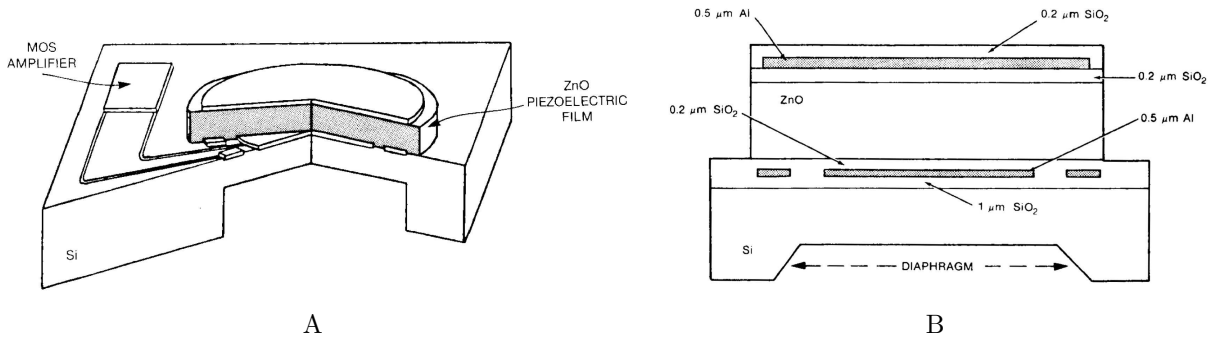

A B

Figure 3-1. Piezoelectric (ZnO) microphone with integrated buffer amplifier [55]. A) Structure. B) Layer composition. [Reprinted from Sensors and Actuators, vol 4, Royer et al., ZnO on Si Integrated Acoustic Sensor, pgs. 357–362, Copyright 1983, with permission from Elsevier.]

a silicon nitride diaphragm. Silicon nitride was cited as having more easily controlled stress and thickness than silicon. The 3 mm × 3 mm × 2 μm square diaphragm featured multiple concentric segmented aluminum top electrodes, as shown in Figure 3-2A, and polysilicon bottom electrodes. The obtained frequency response was not flat; the sensitivity was 50 μV/Pa to within 9 dB from 4 kHz to 20 kHz. A patent was issued in 1988 [57]. Later, through a partnership with Orbit Semiconductor, Kim et al. (1989) [58] were able to integrate the same basic microphone design with a complementary metal-oxide-semiconductor (CMOS) amplifier on-chip. In 1991 [59], a number of improvements were made to the microphone design that resulted in a factor of 5 improvement in sensitivity, though a flat frequency response was still not obtained. The cross-section of the microphone with integrated amplifier from that work is found in Figure 3-2B.

A 1988 German language dissertation by Franz [60], of Darmstadt University of Technology, featured a piezoelectric microphone design utilizing aluminum nitride (AlN). This work was not published, but according to Schellin et al., also from Darmstadt University, the microphone had a sensitivity of 25 μV/Pa [61]. Those authors introduced a piezoelectric microphone of their own in 1992 (shown in Figure 3-3), which used the organic film aromatic polyurea as the piezoelectric. A maximum sensitivity of 126 μV/Pa

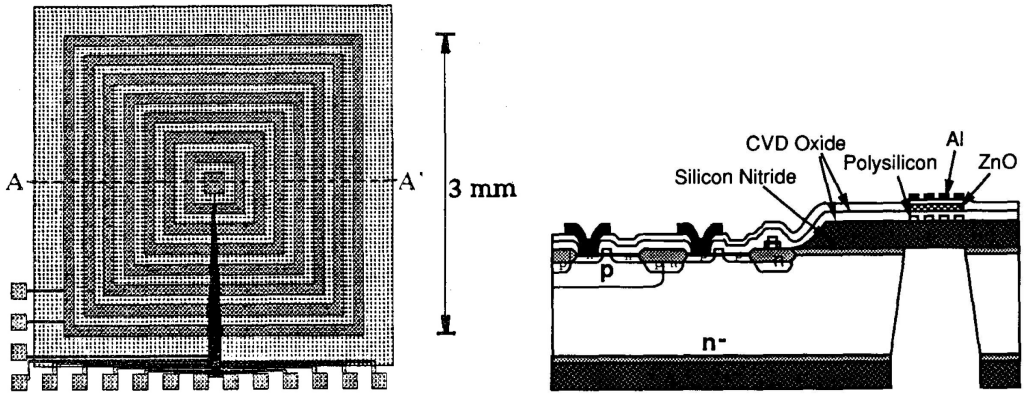

Figure 3-2. Piezoelectric (ZnO) microphone utilizing multiple concentric electrodes [56, 58, 59]. A) Multiple concentric electrode configuration [56]. [© 1987 IEEE. Reprinted, with permission, from Kim et al., IC-Processed Piezoelectric Microphone, IEEE Electron Device Letters, Oct. 1987.] B) Cross-sectional view, including integrated amplifier [59]. [© 1991 IEEE. Reprinted, with permission, from Kim et al., Improved IC-Compatible Piezoelectric Microphone and CMOS Process, Proceedings of 1991 International Conference on Solid-State Sensors and Actuators, Jun. 1991.]

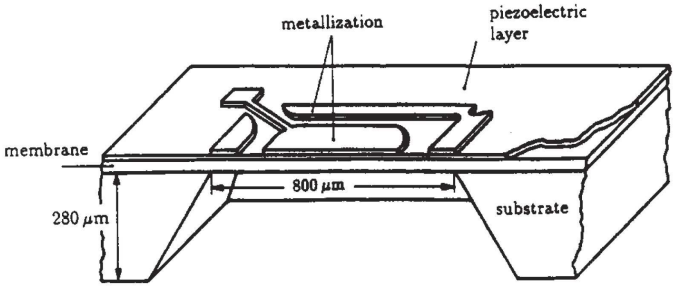

Figure 3-3. Piezoelectric microphone utilizing aromatic polyurea [61]. [© 1992 IEEE. Reprinted, with permission, from Schellin et al., Silicon Subminiature Microphones with Organic Piezoelectric Layers: Fabrication and Acoustical Behaviour, IEEE Transactions on Electrical Insulation, Aug. 1992.]

was achieved (though the typical response was $4\,\mu$V/Pa to $30\,\mu$V/Pa). The microphone exhibited a non-flat frequency response due to a damped mechanical resonance in the audio band. A second incarnation of the microphone in 1994 [62] featured another organic film, P(VDF/TrFE), as the piezoelectric. An improved sensitivity of $150\,\mu$V/Pa was achieved but the frequency response was still not flat in the audio band.

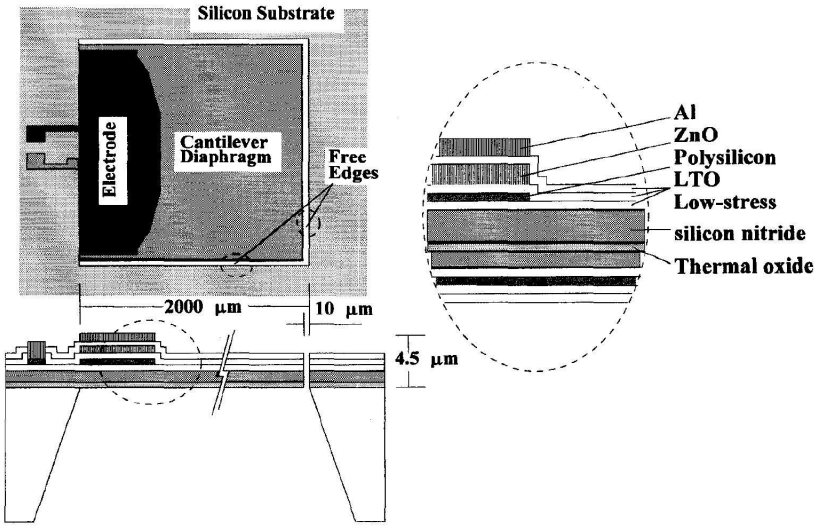

Figure 3-4. Piezoelectric (ZnO) microphone with cantilever sensing element [64]. [© 1996 IEEE. Reprinted, with permission, from Lee et al., Piezoelectric Cantilever Microphone and Microspeaker, Journal of Microelectromechanical Systems, Dec. 1996.]

In 1993, Ried et al. of the Berkeley Sensor and Actuator Center extended the work of Kim [56–59]. The new iteration [63] made use of a 2.5 mm × 2.5 mm × 3.5 μm silicon nitride structural layer with improved stress control. This layer was designed to be thick relative to other diaphragm layers, which were fabricated at corporate partner Orbit Semiconductor and not controlled for stresses. ZnO was again used as the piezoelectric and large-scale integrated CMOS circuits were included on-chip. A flat frequency response was obtained from 100 Hz–18 kHz, with a sensitivity of 0.92 mV/Pa. In 1996, Lee et al. [64] of the same research group presented a new piezoelectric microphone with ZnO on a low pressure chemical vapor deposition (LPCVD), low-stress silicon nitride cantilever sensing element, pictured in Figure 3-4. The enhanced compliance of this "cantilever diaphragm" resulted in a high sensitivity of 30 mV/Pa. However, with the more compliant diaphragm also came a low resonant frequency and a resulting bandwidth of only 100 Hz to 890 Hz. A later iteration [65] improved the bandwidth to 1.8 kHz while maintaining the same sensitivity.

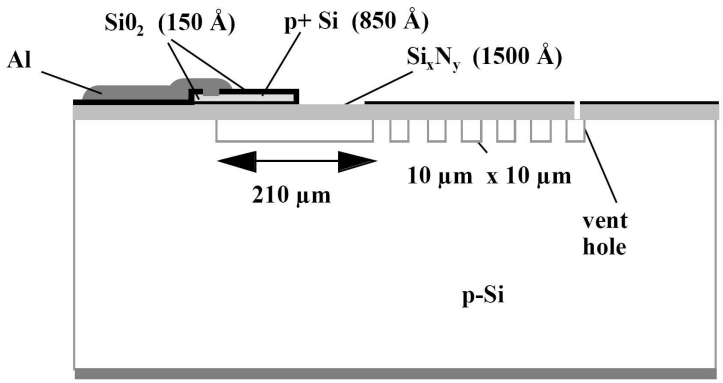

Figure 3-5. Cross section of the first aeroacoustic MEMS microphone [17]. [Reprinted with permission of the American Institute of Aeronautics and Astronautics.]

In 1998, Sheplak et al. [16, 17] introduced the first MEMS microphone designed specifically for aeroacoustics applications (Figure 3-5). The microphone included four dielectrically isolated piezoresistors on top of a 210 μm diameter, 0.15 μm thick silicon nitride diaphragm for sensing of diaphragm deflection. Lumped element modeling was used to predict performance. A sensitivity of 2.24 μV/Pa/V was measured to within $\pm$3 dB from 200 Hz to the testing limit of 6 kHz, though the frequency response was predicted to be flat up to 300 kHz. A linear response was obtained up to the testing limit of 155 dB. The device noise floor was 92 dB/$\sqrt{\text{Hz}}$ at 250 Hz.

In 1999, Naguib et al. [66, 67] introduced two square diaphragm (510 μm to 710 μm on a side) piezoresistive microphone designs for use in measuring jet screech noise. Sensitivities of 1.2 mV/Pa/V to 1.8 mV/Pa/V were measured over a frequency range of 1.5 kHz–5 kHz. The dynamic range was not reported. In 2002, Huang et al. [68] improved the performance of the 710 μm design through the use of an improved fabrication process. The new microphone, for which a depiction is found in Figure 3-6, yielded the highest reported maximum linear pressure for a MEMS microphone yet reported in the literature, 174 dB. The authors were only able to confirm a flat frequency response up to 10 kHz because of testing limitations.

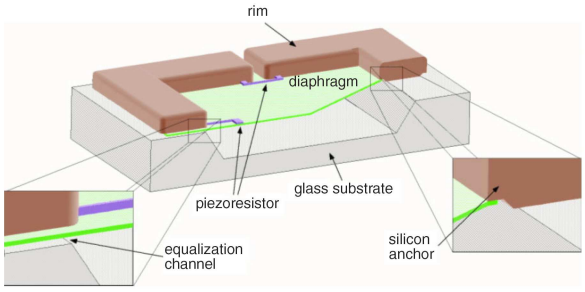

Figure 3-6. Piezoresistive MEMS microphone for aeroacoustic measurements [68]. [Reprinted, with permission, from Huang et al., A Silicon Micromachined Microphone for Fluid Mechanics Research, Journal of Micromechanics and Microengineering, 2002.]

Starting in 2001, researchers at the Interdisciplinary Microsystems Group (IMG) at the University of Florida presented a number of MEMS microphones specifically designed for aeroacoustic measurement purposes. In 2001, Arnold et al. [18] made several modifications to the piezoresistive microphone design of Sheplak et al. [16, 17] in order to improve performance, particularly the MDP: the device was enlarged in order to limit misalignment effects; noise in the piezoresistors was reduced via a reduction in resistance and the use of higher quality wafers; a higher doping concentration was used for the piezoresistors; and finally, a plasma-enhanced chemical vapor deposition (PECVD) silicon nitride passivation layer was added to protect the device from moisture and reduce drift. A micrograph of the microphone is shown in Figure 3-7. The MDP was indeed lowered to 52 dB (1 Hz bin centered at 1 kHz) and a linear response was measured up to the testing limit of 160 dB, though the sensitivity was reduced by nearly a factor of 3. The frequency response of this microphone was later characterized up to very high frequencies at Boeing Corporation; it showed a flat response to within ± 1 dB out to 100 kHz [19].

Aeroacoustic microphones were developed at IMG utilizing other transduction methods as well. In 2004, Kadirvel et al. [70] described the design, fabrication, and testing of an intensity-modulated optical MEMS microphone. The intensity noise in the light source contributed to a high MDP of 70 dB and the device was linear only to 132 dB. In 2007, Martin et al. [71, 72] discussed a dual-backplate capacitive MEMS

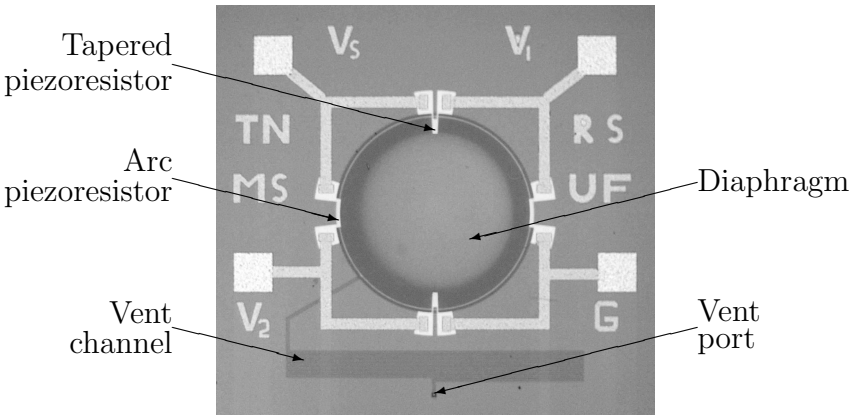

Figure 3-7. Second-generation aeroacoustic MEMS microphone [18]. [Reprinted from [69] with permission from author.]

microphone design, depicted in Figure 3-8. The dual backplates formed two capacitors with the microphone diaphragm, allowing a sensitivity-increasing differential capacitance measurement. The microphone was fabricated using the Sandia Ultra-planar, Multi-level MEMS Technology 5 (SUMMiT V) fabrication process and the interface electronics included an off-package charge amplifier. The authors reported excellent agreement between lumped element model predictions and experiment. A dynamic range of 41 dB to 164 dB and bandwidth of 300 Hz–20 kHz were measured, with the upper end of the bandwidth limited by testing capabilities. Later improvements in packaging and interface electronics (namely the use of a low-noise voltage amplifier instead of a charge amplifier) resulted in a significant reduction of MDP to 22.7 dB. The sensitivity was also reduced to 166 μV/Pa [73].

In 2002, Zhang et al. [74] used lead zirconate titanate (PZT) in a MEMS microphone for the first time. The sensitivity of the cantilever-based microphones were reported to vary from 10 mV/Pa to 40 mV/Pa for square geometries 200 μm to 2 mm on a side, though no details were given of the measurement setup. Later iterations from Zhao et al. [75, 76] moved away from the cantilever geometry to that pictured in Figure 3-9, with square diaphragms from 600 μm to 1 mm on a side. They achieved a remarkably flat frequency response from 10 Hz to 20 kHz, with a sensitivity of 38 mV/Pa.

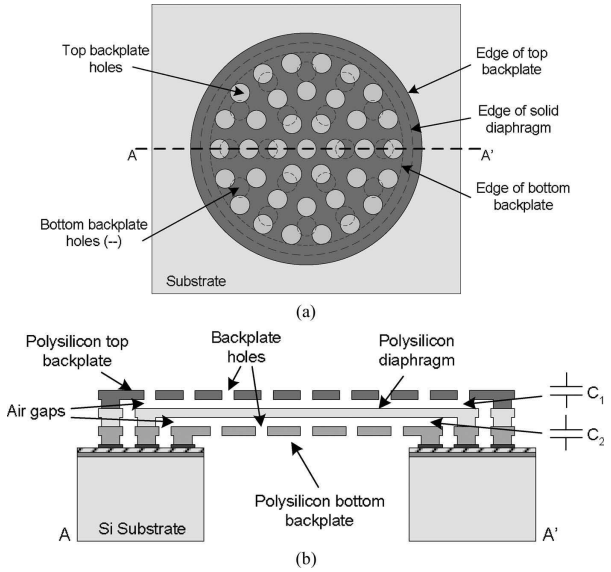

Figure 3-8. A dual-backplate capacitive MEMS microphone [71]. [©2007 IEEE. Reprinted, with permission, from Martin et al., A Micromachined Dual-Backplate Capacitive Microphone for Aeroacoustics Measurements, Journal of Microelectromechanical Systems, Dec. 2007.]

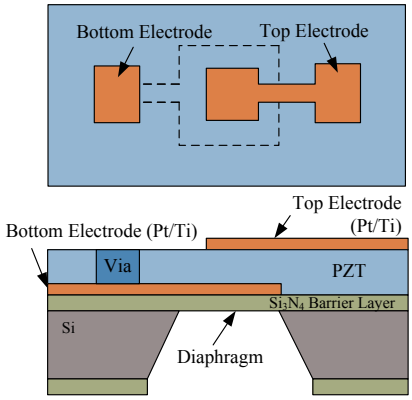

Figure 3-9. Early PZT-based piezoelectric microphone (adapted from Zhao et al. 2003 [75, 76]).

The next piezoelectric microphone, pictured in Figure 3-10, was presented by Ko et al. in 2003 [77]. The square diaphragm was formed from ZnO sandwiched between two concentric segmented aluminum electrodes on LPCVD silicon nitride. The microphone had a sensitivity of approximately 30 μV/Pa and a resonance at 7.3 kHz.

In order to avoid residual stress issues omnipresent in silicon nitride diaphragms, Niu and Kim [78] proposed a novel bimorph structure in 2003. The film stack was composed

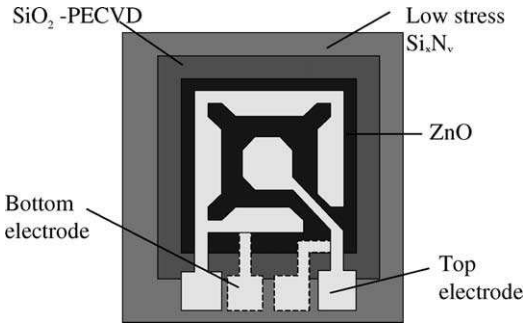

Figure 3-10. Piezoelectric (ZnO) microphone with two concentric electrodes [77]. [Reprinted from Sensors and Actuators A, vol. 103, Ko et al., Micromachined Piezoelectric Membrane Acoustic Device, pgs. 130–134, Copyright 2003, with permission from Elsevier.]

of ZnO, aluminum (Al) electrodes, and parylene D as the structural layer. Concentric segmented electrodes were also used as in [56, 58, 59]. A sensitivity of 520 μV/Pa was achieved, which was an improvement over [56, 58] but not [59].

In 2003, efforts at Brüel and Kjær [79] yielded a measurement quality MEMS condenser microphone, depicted in Figure 3-13. The design goal for the mic was to achieve a 1/4" measurement microphone with noise characteristics near that of a traditional 1/2" Brüel and Kjær 4134 microphone (18 dB(A)). A number of stability issues were also considered, including sensitivity to temperature, relative humidity, and static pressure. The design featured a 1.95 mm octagonal LPCVD silicon nitride diaphragm with chrome/gold electrodes mounted in a titanium housing. The microphone had a dynamic range of 23 dB(A)–141 dB and bandwidth of 251 Hz – 20 kHz.

In 2004, Polcawich [80] shared development details for a PZT MEMS microphone targeted for use in a MEMS photoacoustic spectrometer or remote acoustic sensor. The circular diaphragm diameters ranged from 500 μm to 2000 μm and were fabricated in designs with 80 % PZT coverage in the center of the diaphragm and 20 % PZT coverage on the outside edge of the diaphragm. Sensitivities of 97.9 nV/Pa to 920 nV/Pa were reported and resonant frequencies were O (100 kHz). No indication of the bandwidth or dynamic range was given for these microphones.

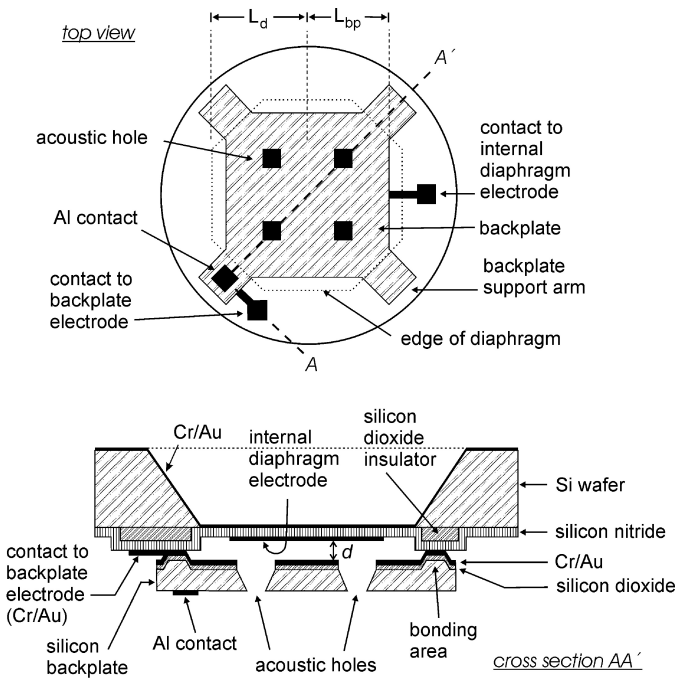

Figure 3-11. Measurement-grade MEMS condenser microphone developed at Brüel and Kjær [79]. [©2003 IEEE. Reprinted, with permission, from Scheeper et al., A New Measurement Microphone Based on MEMS Technology, Journal of Microelectromechanical Systems, Dec. 2003.]

Also in 2004, Hillenbrand et al. [81] suggested the use of charged cellular polypropylene (commercially known as VHD40) as the piezoelectric material in a microphone. They presented results for two structures formed from single and five layer glued stacks of metallized VHD40, which had sensitivities of 2 mV/Pa and 10.5 mV/Pa, respectively. A total harmonic distortion of only 1% at 164 dB was reported, though it is not clear to which of the two designs the measurement applied or how the measurement was performed. This large maximum pressure, in addition to a large reported bandwidth up to nearly 140 kHz for the single film design, makes this microphone potentially appealing for use in aeroacoustic applications. However, the microphone was not batch fabricated and concerns about the temperature stability of the charged film were noted.

Horowitz et al. (2007) [20] of IMG introduced the first — and prior to this study, only — piezoelectric MEMS microphone designed specifically for aeroacoustic applications. The circular microphone diaphragm was a piezoelectric (PZT) unimorph with an annular

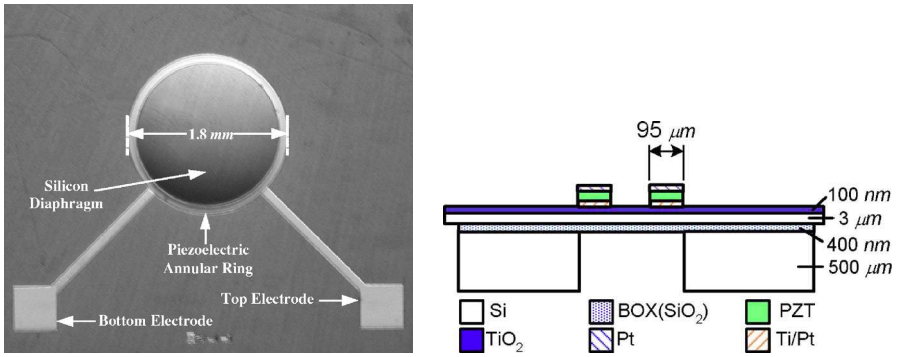

A B

Figure 3-12. Piezoelectric (PZT) microphone for aeroacoustic applications [20]. [Reprinted with permission from S. Horowitz et al., Development of a micromachined piezoelectric microphone for aeroacoustics applications, Journal of the Acoustical Society of America, vol. 122, pp. 34283436, Dec. 2007. © 2007, Acoustic Society of America.]

piezoelectric film stack on a silicon layer, as shown in Figure 3-12. Lumped element modeling was used to predict device performance. The reported maximum pressure of 169 dB exceeded the design goal of 160 dB. The frequency response could not be measured beyond 6.7 kHz due to equipment limitations, though the resonant frequency of the microphone diaphragm was found via a laser vibrometer measurement to be 59 kHz. This suggested a usable bandwidth nearly sufficient for 1/4 scale model aeroacoustic measurement applications.

Also in 2007, Fazzio et al. of Avago Technologies [82] described several microphones produced using a variant of the FBAR (film bulk acoustic resonator) process. The circular diaphragm was composed of AlN with molybdenum (Mo) electrodes in one of three configurations: annular ring, inner disk, or a combination of the two. Few performance specifications were included in the paper. The fabrication process was outlined separately by Lamers and Fazzio [83].

Lee and Lee (2008) presented a ZnO microphone utilizing a circular diaphragm with annular ZnO/Mo film stack. Limited characterization work was conducted. The frequency response was not flat, with the sensitivity varying from around 1 μV/Pa at 400 Hz to

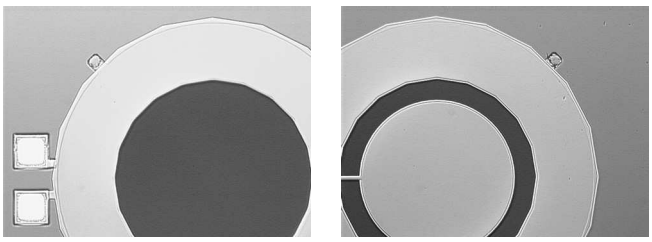

A B

Figure 3-13. Top-view of microphone structures from Fazzio et al. (2007) [84]. A) Annular outer electrode. B) Combined circular inner and annular outer electrodes. [© 2003 IEEE. Reprinted, with permission, from Fazzio et al., Design and Performance of Aluminum Nitride Piezoelectric Microphones, 14th International Conference on Solid-State Sensors, Actuators, and Microsystems, Jun. 2007.]

around 100 μV/Pa at 10 kHz. The resonance was reported to be 54.8 kHz, so the source of the variation was not clear.

In his 2010 doctoral dissertation from the University of Michigan, Robert Littrell described two generations of piezoelectric microphones based on double-layered AlN/Mo cantilevers [85]. The goal of the work was to demonstrate a low noise piezoelectric microphone. In the first generation, an array of 20 cantilevers were used as the microphone sensing elements, with model predictions leading to the selection of 0.5 μm AlN layers. The resulting microphones were found to have higher than expected noise floor (58 dB(A)) due to poor film quality and thus high dielectric loss. In addition, stress in the thin films resulted in slightly curved cantilevers that reduced the vent resistance. The second generation, with cross-section shown in Figure 3-14, featured thicker AlN layers (1 μm) for which better film quality was known to be achievable, modifications to the fabrication process that enabled individual patterning of AlN and Mo, and reduction of the number of cantilevers to 2 (395 μm long by 790 μm wide) in an effort to reduce the gap around them and thus increase the acoustic resistance. A tested microphone had a sensitivity of 1.82 mV/Pa, minimum detectable pressure of 37 dB(A), and 3 % THD at 128 dB. The non-standard method used to calculate THD involved summation of harmonic amplitudes rather than harmonic powers [47, 86, 87] and thus the distortion at 128 dB was likely

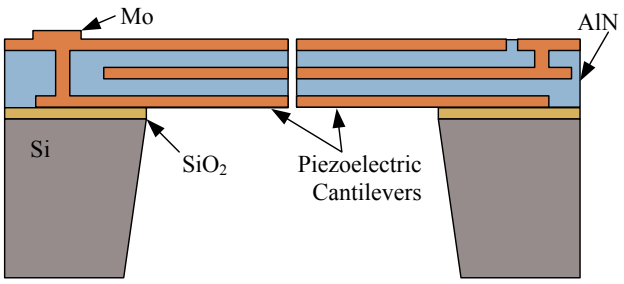

Figure 3-14. Cross section of a second-generation AlN double-cantilever microphone (adapted from Littrell 2010 [85].)

over-predicted. Some stress remaining in the bottom Mo layer resulted in curvature of the cantilever sensing elements and thus a low vent resistance that necessitated packaging the microphones with large cavity volumes. Packaged in this way, the frequency response was shown to be flat at least to 8 kHz, near which the plane wave tube calibration procedure broke down due to cut-on of non-planar acoustic modes. The microphone was reported to have a resonant frequency of 18 kHz.

Table 3-1 provides a chronological summary of piezoelectric MEMS microphones discussed in this section, including performance data not given in the text. Due to the myriad ways researchers present data, performance specifications collected in Table 3-1 often required interpretation; consultation of the original source is thus necessary in order to judge the true performance of any particular microphone.

3.2 Summary

Since the first MEMS piezoelectric and aeroacoustic microphones in 1983 and 1998, respectively, significant progress has been achieved. MEMS piezoelectric microphones have been fabricated using a number of different materials (ZnO, AlN, polyurea, PZT, etc.) and geometries (square and circular membranes, novel electrode configurations, etc.). Development of MEMS aeroacoustic microphones has included the use of piezoresistive, capacitive, optical, and piezoelectric transduction techniques and has seen steady increases in dynamic range and bandwidth. Sufficient evidence exists to suggest that meeting the aggressive performance specifications for a fuselage microphone is achievable.

Table 3-1. Summary of MEMS microphones.

Author	Transduction Method	Sensing Element Size	Sensitivity	Dynamic Range	Bandwidth (Predicted)
Royer et al. 1983 [55]	Piezoelectric (ZnO)	1.5 mm* ×30 μm	250 μV/Pa	66 dB– N/R	10 Hz–10 kHz (0.1 Hz-10 kHz)
Kim et al. 1987 [56]	Piezoelectric (ZnO)	3 mm† × 3.6 μm	0.5 mV/Pa	72 dB– N/R	20 Hz–5 kHz
Franz 1988 [60]	Piezoelectric (AlN)	0.72 mm^2 × 1 μm#	25 μV/Pa#	68 dB(A)#– N/R	N/R–45 kHz#
Kim et al. 1989 [58]	Piezoelectric (ZnO)	2 mm† × ↑1.4 μm	80 μV/Pa	N/R	3 kHz–30 kHz
Kim et al. 1991 [59]	Piezoelectric (ZnO)	3.04 mm† × 3 μm	1000 μV/Pa	50 dB(A)– N/R	200 Hz–16 kHz
Schellin et al. 1992 [61]	Polyurea	0.8 mm† × 1 μm	4–30 μV/Pa	N/R	100 Hz–20 kHz
Ried et al. 1993 [63]	Piezoelectric (ZnO)	2.5 mm† × 3.5 μm	920 μV/Pa	57 dB(A)– N/R	100 Hz–18 kHz
Schellin et al. 1994 [62]	Piezoelectric (P(VDF/TrFE))	1 mm† × 3 μm	150 mV/Pa	60 dB(A)– N/R	50 Hz–16 kHz.
Lee et al. 1996 [64]	Piezoelectric (ZnO)	2 mm‡ × 4.5 μm	3 mV/Pa	N/R	100 Hz–890 Hz
Lee et al. 1998 [65]	Piezoelectric (ZnO)	2 mm‡ × 1.5–4.7 μm	30 mV/Pa	N/R	50 Hz–1.8 kHz
Sheplak et al. 1998 [16, 17]	Piezoresistive	105 μm* × 0.15 μm	2.24 μV/Pa·V	92 dB§– 155 dB	200 Hz–6 kHz (100 Hz–300 kHz)
Naguib et al. 1999 [66, 67]	Piezoresistive	510 μm† × 0.4 μm	1.2 μV/Pa·V	N/R	1.5 kHz–5 kHz
Arnold et al. 2001 [18]	Piezoresistive	500 μm* × 1 μm	0.6 μV/Pa·V	52 dB§– 160 dB	1 kHz–20 kHz (10 Hz–40 kHz)
Huang et al. 2002 [68]	Piezoresistive	710 μm† × 0.38 μm	1.1 mV/Pa·V	53 dB§– 174 dB	100 Hz–10 kHz
Scheeper et al. 2003 [79]	Capacitive	1.9 mm* × 0.5 μm	22.4 mV/Pa	23 dB(A)– 141 dB	251 Hz–20 kHz
Ko et al. 2003 [77]	Piezoelectric (ZnO)	3 mm† × 3 μm	30 μV/Pa	N/R	1 kHz–7.3 kHz
Niu et al. 2003 [78]	Piezoelectric (ZnO)	3 mm† × 3.2 μm	520 μV/Pa	N/R	100 Hz–3 kHz
Zhao et al. 2003 [75]	Piezoelectric (PZT)	0.6–1 mm† × N/R	38 mV/Pa	N/R	10 Hz–20 kHz
Kadirvel et al. 2004 [70]	Optical	500 μm* × 1 μm	0.5 mV/Pa	70 dB§– 132 dB	300 Hz–6.5 kHz (1 Hz–100 kHz)
Polcawich 2004 [80]	Piezoelectric (PZT)	250 μm–1 mm* × 2.18 μm	97.9– 920 nV/Pa	N/R	N/R

* Radius of circular diaphragm. † Side length of square diaphragm. ‡ Side length of cantilever.
§ 1 Hz bin. # Per references [62, 88]

Table 3-1. Continued.

Author	Transduction Method	Sensing Element Size	Sensitivity	Dynamic Range	Bandwidth (Predicted)
Hillenbrand et al. 2004 [81]	Piezoelectric (VHD40)	0.3 cm^2 area × 55 μm	2.2 mV/Pa	37 dB(A)–164 dB	20 Hz–140 kHz
		0.3 cm^2 area × 275 μm	10.5 mV/Pa	26 dB(A)–164 dB	20 Hz–28 kHz
Martin et al. 2007 [71, 72, 89]	Capacitive	230 μm^* × 2.25 μm	390 mV/Pa	41 dB[§]–164 dB	300 Hz–20 kHz
Horowitz et al. 2007 [20]	Piezoelectric (PZT)	900 μm^* × 3 μm	1.66 μV/Pa	35.7 dB[§] (95.3 dB(A)) – 169 dB	100 Hz–6.7 kHz (100 Hz–50 kHz)
Fazzio et al. 2007 [82]	Piezoelectric (AlN)	350 μm^* × 1.44 μm	N/R	60 dB–155 dB	1 kHz-6 kHz
Lee et al. 2008[90]	Piezoelectric (ZnO)	1 mm × 1 μm	1 μV to 100 μV	N/R	<1 kHz
Martin et al. 2008 [73]	Capacitive	230 μm^* × 2.25 μm	166 μV/Pa	22.7 dB[§]–164 dB	300 Hz–20 kHz
Littrell 2010 [85]	Piezoelectric (AlN)	0.62 mm^2[¶] 2.3 μm	1.82 mV/Pa	37 dB(A)–128 dB	50 Hz–8 kHz (18.4 kHz)

[*] Radius of circular diaphragm. [§] 1 Hz bin. [¶] 2 cantilevers

Referring to Table 3-1, the performance of several prior microphone designs approach the benchmarks set for this study. The microphones of Martin et al. [21, 72, 73] and Hillenbrand et al. [81] possessed strong performance but the fundamental ability of the underlying technologies to withstand the harsh high-altitude environment on an airplane fuselage is questionable. In the case of Martin et al., the capacitive transduction method is highly susceptible to failure from moisture shorting the electrodes, in addition to not being a passive technology. Meanwhile, the charged cellular polypropylene film utilized by Hillenbrand et al. has noted temperature stability problems that require further material development [81]; it was also not batch-fabricated [91].

The microphones of Huang et al. [68] and Horowitz et al. [20] also come close to meeting the design goals for this work with better promise of robustness. The former has the highest reported maximum linear pressure (174 dB) but also a correspondingly high noise floor (53 dB/$\sqrt{\text{Hz}}$); meanwhile, the latter has a lower noise floor (47.8 dB/$\sqrt{\text{Hz}}$) but the maximum pressure (169 dB) obtained from measurements is also lower than

desired. Neither frequency response was experimentally confirmed to be flat over the entire audio range. Kulite microphones already deployed in fuselage arrays utilize the same piezoresistive technology as Huang et al. [68], and thus the primary advantage of the piezoelectric microphone of Horowitz et al. [20] is its passivity.

The microphone of Horowitz et al. [20] proved a piezoelectric MEMS microphone is a viable technology for obtaining performance near that needed for deployment in a fuselage array. However, improvements are required to meet the performance objectives in Chapter 1. The microphone of [20] was not designed using optimization techniques and thus it is unlikely that performance was maximized. In this study, a system-level model of the piezoelectric fuselage microphone is developed in Chapter 5 and used to produce optimal microphone designs in Chapter 6. In addition, the choice of geometry and materials — particularly the piezoelectric material — provide additional avenues for improved performance. These choices are addressed in the next chapter, Chapter 4.

CHAPTER 4
MEMS PIEZOELECTRIC MICROPHONE

It was determined in Section 1.2 and confirmed in the literature review of Chapter 3 that a microphone utilizing piezoelectric transduction was the best choice for aircraft fuselage array applications. In this chapter, material and fabrication issues are discussed. First, the piezoelectric effect is reviewed, and possible piezoelectric material choices for the MEMS microphone are compared. Next, the commercial fabrication process used to produce the piezoelectric microphone is described and a compatible geometry is established.

4.1 Piezoelectricity

Piezoelectric materials are those which exhibit coupling between strain and electric field. A change in electric field resulting from strain in the material is referred to as the direct piezoelectric effect; meanwhile, the spontaneous straining of a material which results from an externally applied electric field is called the converse piezoelectric effect [92].

The presence of the piezoelectric effect in a material is intimately tied to its crystal structure. Only crystals which lack a center of symmetry, called noncentrosymmetric crystals, may be piezoelectric. Twenty out of 21 noncentrosymmetric crystal classes exhibit piezoelectricity [92, 93]. From those, some are polar and possess a net dipole moment in the unstrained state. These polar crystals also exhibit pyroelectricity, the coupling of temperature and electric field. Materials in which the orientation of the polarization may be changed under application of an external electric field, and for which the change remains after removal of the field, are called ferroelectric materials [93, 94]. See Figure 4-1 for a Venn diagram showing the interrelationships between piezoelectric, pyroelectric, and ferroelectric materials.

Many ferroelectric materials are polycrystalline and thus do not exhibit piezoelectricity on the macroscale. The random orientation of crystals means the materials are isotropic from a constitutive law perspective. These materials may be made piezoelectrically active

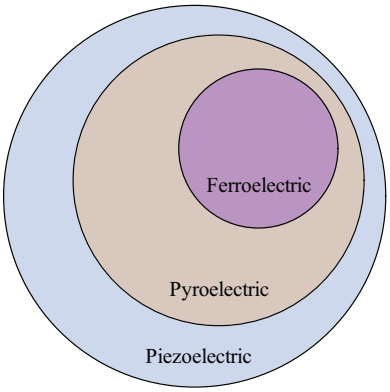

Figure 4-1. Venn diagram for piezoelectric, pyroelectric, and ferroelectric materials.

through a process called poling. In this process, the materials are heated, and a strong external electric field is applied that causes the polarization direction within the materials to reorient. After reduction of temperature and removal of the external field, the new polarization orientation remains and the piezoelectric effect is macroscopically active. During this process, symmetry in the direction of poling is destroyed and the resulting material is transversely isotropic [92]. The poled direction is referred to as the 3-direction in the local material coordinate system.

The constitutive equations of linear piezoelectricity are given in "compressed matrix" (or "abbreviated subscript") form in the nomenclature of the IEEE standard as [95, 96]

$$D_i = d_{iq} T_q + \varepsilon_{ij}^T E_j \tag{4–1}$$

and

$$S_p = s_{pq}^E T_q + d_{jp} E_j, \tag{4–2}$$

where $i, j = 1 \ldots 3$ and $p, q = 1 \ldots 6$. In these equations, D_i are the three components of the electric displacement, d_{iq} are the 18 piezoelectric strain constants, T_q are the six mechanical stresses, ε_{ij}^T are the six electrical permittivities, E_j are the three components of the electric field, S_p are the six engineering (not tensoral) strains, and s_{pq}^E are the 36 elastic compliance components. Symmetry considerations for a material reduce the number of independent d_{iq}, S_p, and s_{pq}^E. The superscripts T and E indicate that the material properties must be measured under conditions of constant stress and electric

field, respectively [96]. In the absence of piezoelectric coupling, all d coefficients are zero, and the constitutive equations reduce to those for purely dielectric [97] and linear elastic [92, 98] materials, respectively. A second convenient form of the linear constitutive equations is [92, 95, 96]

$$D_i = e_{iq} S_q + \varepsilon_{ij}^S E_j \tag{4–3}$$

and

$$T_p = c_{pq}^E S_q - e_{jp}^T E_j, \tag{4–4}$$

where

$$c_{pq}^E = s_{pq}^{E^{-1}} \tag{4–5}$$

are the 36 elastic stiffness components,

$$e_{iq} = d_{ip} c_{pq}^E \tag{4–6}$$

are the 18 piezoelectric stress constants [96], and

$$\varepsilon_{ij}^S = \varepsilon_{ij}^T - e_{iq} d_{jq} \tag{4–7}$$

are the permittivity components measured under constant strain [96].

Piezoelectric materials used in microsystems include lead zirconium titanate (PZT), zinc oxide (ZnO), aluminum nitride (AlN), aromatic polyurea, polyvinylidene fluoride (PVDF), and others. PZT is the most popular due to large piezoelectric coefficients. It is a ferroelectric material that requires poling and is available in polycrystalline, textured, and epitaxial thin films [93].

AlN and ZnO offer significantly lower piezoelectric coefficients than PZT, but their dielectric properties still make them attractive materials for some applications. In bending mode sensors that utilize the d_{31} coefficient, for instance, a figure of merit is the

piezoelectric "g" coefficient[1] [94],

$$g_{31} = \frac{d_{31}}{\varepsilon_{33,r}\varepsilon_0}, \tag{4–8}$$

which is representative of the open circuit electric field per applied mechanical stress. Because AlN and ZnO possess significantly lower permittivities than PZT, their g_{31} coefficients are actually both superior.

AlN and ZnO are both pyroelectric, but not ferroelectric, and thus cannot be poled [93, 94]; they must instead be oriented appropriately during deposition. ZnO has traditionally been the material of choice for MEMS piezoelectric microphones (see Section 3.1) due to the difficulty of depositing AlN films [99] and thus better availability of ZnO [100]. The situation has been rectified with the advent of modern magnetron sputtering tools [100–102], and it has been recognized that AlN holds several advantages over ZnO. Zinc is a fast-diffusing ion that presents problems for integration with silicon semiconductor processing [93, 100]. In addition, with a bandgap of 3 eV, ZnO is really a semiconductor and there is always risk that inadvertent doping could degrade its dielectric properties, i.e. result in a high dielectric loss [93, 100, 103]. It is thus difficult to obtain ZnO films with high resistivity [100].

The dissipation qualities of a piezoelectric are an important consideration when comparing material choices for piezoelectric sensors. Low resistivity (high dielectric loss) is especially crippling in low-frequency sensors, for instance below 10 kHz [100]. Lossiness is typically characterized via the electric loss tangent [97],

$$\tan\delta = \frac{\sigma}{\omega\varepsilon_{33,r}\varepsilon_0}, \tag{4–9}$$

where σ is the electrical conductivity and ω is the radial frequency. The loss tangent represents the ratio of dissipated power to stored power in a dielectric. The presence of

[1] Compare this to the expression for open circuit sensitivity for the pieozelectric microphone, Equation 5–35.

dissipation introduces noise, and thus $\tan\delta$ plays a role in determining the signal-to-noise ratio of piezoelectric sensors. A figure of merit is [100],

$$\frac{d_{31}}{(s_{11}^E + s_{12}^E)\sqrt{\varepsilon_0 \varepsilon_{33,r} \tan\delta}}, \tag{4–10}$$

which represents the intrinsic signal-to-noise ratio of the material. AlN outperforms ZnO in this regard, with both a lower loss tangent and higher intrinsic signal-to-noise ratio. A comparison of typical material properties and the discussed figures of merit for PZT, AlN, and ZnO are given in Table 4-1.

Table 4-1. Typical properties of piezoelectric materials in MEMS.[†]

		PZT[‡]	AlN	ZnO
Properties	E [GPa]	76	345	127
	ρ [10^3 kg/m^3] [20]	7.7	3.26	5.6
	d_{31} [pm/V]	-274	-2	-5.4
	d_{33} [pm/V]	593	5	11.7
	e_{31} [C/m^2]	-6.5	-0.6	-0.6
	e_{33} [C/m^2]	23.3	1.6	1.3
	$\varepsilon_{33,r}$	1470	8.5	9.2
	$\tan\delta$ [93, 100]	0.01–0.03	0.003	0.01–0.1
Figures of Merit	$\lvert g_{31}\rvert$ [V/m/Pa]	0.018	0.027	0.07
	$\lvert d_{31}\rvert/\left(s_{11}^E + s_{12}^E\right)\sqrt{\varepsilon_0 \varepsilon_{33,r} \tan\delta}$ [10^5 Pa$^{1/2}$]	11.7–20.3	21.4	4.3–13.5

[†] Material properties drawn from [104] unless otherwise noted [‡] PZT-5H [92, 96]

AlN was selected as the material for use in the piezoelectric microphone due to its relatively high g_{31} coefficient and best signal-to-noise ratio among the common thin-film piezoelectric materials. In the next section, the commercial process used to fabricate the microphones and the role it played in early design choices is discussed.

4.2 Design for Fabrication

A partnership was formed with Avago Technologies of Fort Collins, CO for fabrication of the piezoelectric MEMS microphone using a variant of their film bulk acoustic resonator (FBAR) process [82, 83, 105]. An FBAR is an electromechanical filter that utilizes the resonance of bulk acoustic waves excited in a thin piezoelectric film [106]. FBAR

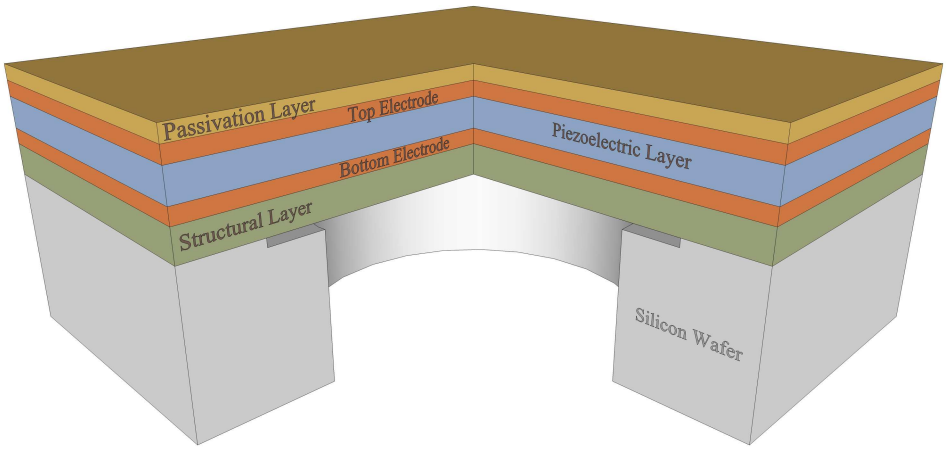

Figure 4-2. FBAR-variant process film stack.

duplexers and filters for cellular phones have been produced in volume using the FBAR process since 2002 [101] and Avago Technologies remains the world's only "high volume producer of thin-film AlN products" [83]. They are by far the most successful piezoelectric MEMS products on the market [103].

A depiction of the film stack used in the modified FBAR process of Avago Technologies is shown in Figure 4-2. It is composed of passivation, electrode, piezoelectric, and structural layers; all but the latter are components of the standard FBAR process. A key reason AlN was chosen over ZnO in the original FBAR process development was because of its better semiconductor process compatibility [101]. The electrode material in the film stack of Figure 4-2, molybdenum (Mo), was subsequently selected because it was a stiff, low-loss acoustic material with high conductivity and compatible etch chemistry with AlN [101, 106]. As proprietary features of the FBAR-variant process, the materials used in the passivation and structural layers are not disclosed. A deep reactive ion etch (DRIE) forms a cavity underneath the diaphragm in Figure 4-2.

The performance of microphones with thin film diaphragms is extremely sensitive to film stress, while the first priority in FBAR fabrication is piezoelectric film thickness uniformity [83]. Leveraging the FBAR process, therefore, requires renewed attention to film stress. Thin films are susceptible to developing both intrinsic and extrinsic residual

stresses. Thermal expansion mismatch between films, substrate, and package lead to thermal stress, the most common extrinsic stress. Intrinsic stresses can be caused by a variety of factors, including lattice mismatch, impurities, volume change processes (e.g. phase transformation or outgassing), or atoms being trapped in high-energy configurations [107, 108]. The amount of stress control varies by process; sputter deposition (common for AlN), for instance, is a complex process that does afford some flexibility to tailor stresses. Customization of the stress state is achieved via adjustment of bias power, argon pressure, sputtering gas mass, temperature, and/or deposition rate [108]. Avago Technologies is able to adjust film deposition parameters to target a large range of film stresses.

The FBAR-variant film stack provided some flexibility in the selection of microphone geometry. With a DRIE step already integrated into the FBAR-variant process — as opposed to an anisotropic release etch — the diaphragm was not limited to rectangular geometry [90, 109]. A circular diaphragm offers several advantages over rectangular geometries: it is easier to model/design since first-mode vibrations can be reduced to a 1-D axisymmetric problem, as opposed to a 2-D problem in the rectangular case; it lends itself to simpler electrode configurations over the rectangular case, in which high stress regions are not uniformly distributed along the boundary [90]; and the circular geometry does not inherently include lifetime-reducing stress concentrations.

Clamped circular diaphragms possess high stress/strain regions both along the circumference and at the center. The configuration of the piezoelectric/electrode films on the structural layer therefore presents another design choice [110]. A single stack of piezoelectric/electrode films presents the least complexity; two such configurations are shown in Figure 4-3. Figure 4-3A shows the piezoelectric/electrode stack in the middle of the diaphragm, called here the "central disc" configuration, while Figure 4-3B shows the stack as an "outer annulus." Concerns about the contribution of electrode traces running over the diaphragm in the former case, particularly their potential contribution to device

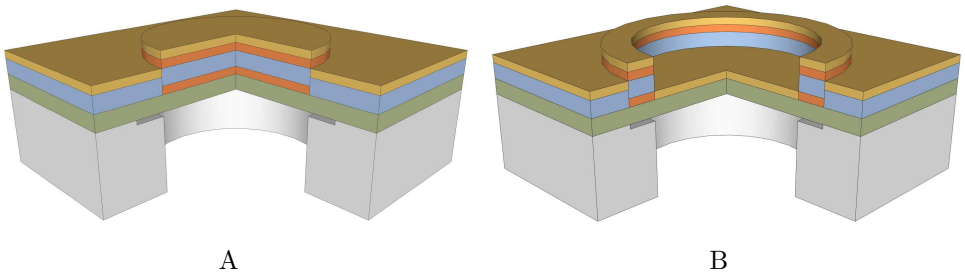

Figure 4-3. Potential circular diaphragm piezoelectric/metal film stack configurations. A) Central disc. B) Outer annulus.

stiffness and parasitic capacitance and the possibility that they could promote asymmetric modal vibrations [20, 111], led to the choice of the annular configuration.

Although exact FBAR process details are proprietary, a general outline of fabrication steps for a microphone structure was published by Avago Technologies [82, 83] and is summarized in Figure 4-4. The process involved both surface and bulk micromachining, starting with a 675 μm thick, 150 mm (6") silicon wafer (Figure 4-4A). First, a shallow cavity was etched and filled with sacrificial material, which served to define the diaphragm diameter and set an etch stop for subsequent backside processing. The wafer surface was thinned to 500 μm and planarized via chemical-mechanical polishing (CMP) as in Figure 4-4B. The structural, metal, piezoelectric, and passivation layers, in addition to the bond pads, were then deposited and patterned in a set of proprietary process steps (Figure 4-4C). What is known from the open literature about the film deposition is that AlN is typically sputter-deposited [100–103], often at low temperatures (<200 °C). Possible etch chemistries for AlN and Mo include chlorine and fluorine gas, respectively [101]. Projection step-and-repeat photolithography [43] was used to repeat the same 10 × 10 pattern of microphones (with die 2 mm on a side) over the entire wafer. A DRIE from the backside of the wafer formed the back cavity (Figure 4-4D) and the sacrificial material was removed to release the diaphragm (Figure 4-4E).

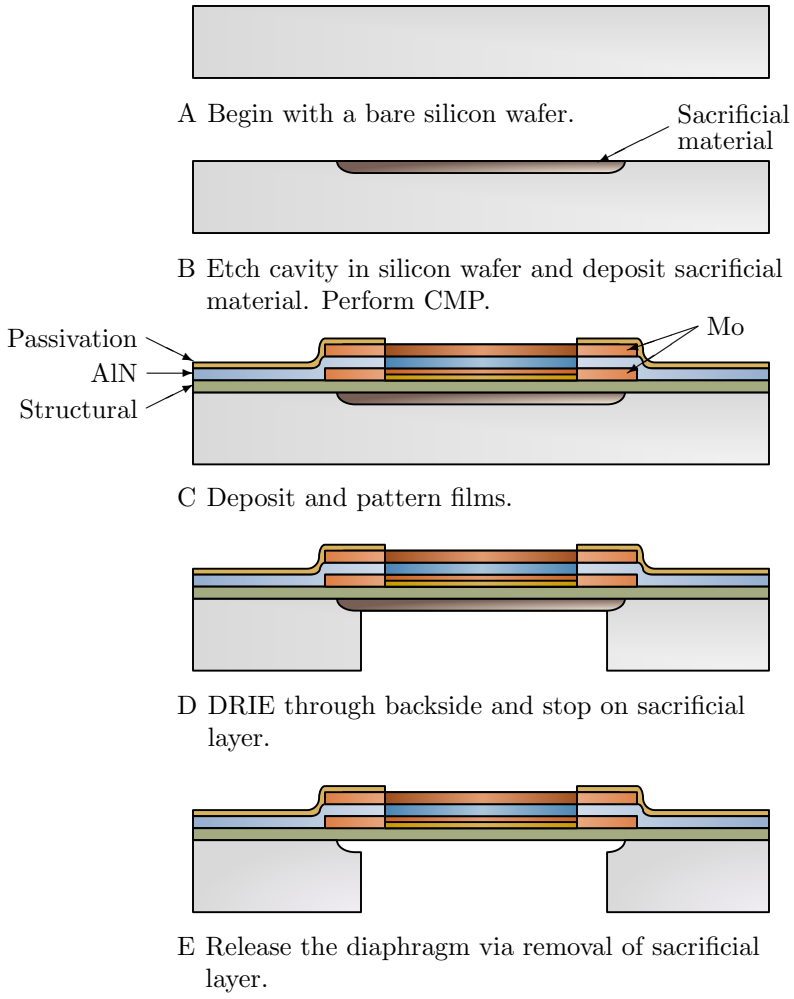

Figure 4-4. Outline of fabrication steps.

4.3 Summary

In this chapter, material and fabrication-related issues relevant to the piezoelectric MEMS microphone were discussed. First, the relative merits of common thin-film piezoelectric materials were reviewed, and the material choice of AlN was established. Next, a microphone geometry utilizing an annular piezoelectric film stack and compatible with the selected fabrication process was chosen. Finally, the proprietary FBAR-variant fabrication process was described via reference to open literature on the subject. With the microphone geometry and composition firmly established, the next chapter focuses on the development of a model to predict its performance.

CHAPTER 5
MODELING

In this chapter, a multiple-energy-domain dynamic model of the piezoelectric microphone is developed that allows computation of performance metrics such as sensitivity, bandwidth, and minimum detectable pressure. First, an overview of the lumped element modeling technique is given. Next, an overall lumped element model of the microphone is introduced and predictive models for its component parts are discussed in turn. With the lumped element model established, several important quantities, including the open circuit frequency response function of the microphone and the overall electrical impedance, are derived. The need for interface electronics and their impact on system response is then addressed. Finally, two architectures for interface electronics — a voltage amplifier and charge amplifier — are integrated with the lumped element model and their relative merits are discussed in terms of sensitivity and minimum detectable pressure.

5.1 Lumped Element Modeling Overview

A piezoelectric microphone converts energy between the acoustic and electrical energy domains. Accurate prediction of its behavior requires physics-based models that capture the underlying transport of energy. Unfortunately, exact analytical solutions to governing differential equations coupling multiple energy domains are rarely available [112]. Numerical solutions to these equations using techniques such as the finite element method are possible, but are often computationally intensive and do not readily provide physical insight [43]. Therefore, a compromise in fidelity in exchange for efficient and physically insightful models is warranted; this is the overriding reason for the use of the lumped element modeling technique.

When the wavelength of a physical phenomenon being measured is much greater than the characteristic length scale ($\lambda \gg L$) of the sensor itself, spatial and temporal variations of the physical phenomenon may be decoupled [113]. A microphone, for instance, which

has a sensing element much smaller than the wavelength of incident acoustic waves sees a distribution of pressure which is essentially uniform. Although the pressure continues to change with time, the changes are effectively felt everywhere on the microphone diaphragm at the same instant [35]. For an acoustic signal at a frequency of 20 kHz, $\lambda = 17\,\text{mm}$ in air and the diaphragm diameter must be much less than λ.

Under the condition $\lambda \gg L$, the distributed energy storage mechanisms of the true system may be lumped into equivalent energy storage elements, called "lumped elements." In the mechanical domain, this means a distributed system with infinite degrees of freedom may be represented by an equivalent single-degree-of-freedom mass-spring-damper system. Generalized kinetic energy is stored in a lumped mass, generalized potential energy is stored in a lumped compliance (inverse of spring stiffness), and energy is dissipated in a lumped damper. The lumped elements may be found via a truncated series expansion of the complex impedance [28]. Alternatively, they may be found from equating the energy storage of the true system (using the static solution to approximate the dynamic one) with the energy storage in the ideal lumped elements. The resulting single-degree-of-freedom representation is then valid up to and just beyond the first resonant frequency of the true system [114].

Convenient analogies exist between the mechanical/acoustic domains and the electrical domain. A mass-spring-damper system may be represented by an equivalent LCR circuit in which an inductor is analogous to a mass, a capacitance is analogous to a compliance, and a resistor is analogous to a damper [43]. This analogy is illustrated in Figure 5-1. The conjugate power variables in the electrical domain, voltage (an "effort variable") and current (a "flow variable"), are then analogous to force and velocity in the mechanical domain or pressure and volume velocity in the acoustic domain. These so-called conjugate power variables may be defined in each energy domain [43].

The circuit analogy, in conjunction with lumped element modeling, may be employed to produce a system-level model in which the lumped elements, including those

Figure 5-1. Illustration of the electrical-mechanical analogy. A) Mass-spring-damper system. B) Inductor-capacitor-resistor circuit.

representative of different energy domains, are all interconnected in a way that captures the energy exchange of components in the true system. Techniques developed for circuit analysis then become available, as well as the intuitive understanding of circuit diagrams that many engineers share. The end result is an insightful, efficient, and acceptably accurate model of a multiple-energy-domain system.

The lumped element modeling technique and equivalent circuit representations have historically been used in the field of electroacoustics [35, 114, 115] and have found use in the design of microelectromechanical systems (MEMS) transducers [17, 20, 21, 116]. The technique is utilized in this study to perform model-based design.

5.2 Lumped Element Model of a Piezoelectric Microphone

In this section, a system-level lumped element model of the piezoelectric MEMS microphone is produced. The development is similar to Horowitz et al. (2007) [20], with extensions to the underlying mechanical modeling. The cross section of the piezoelectric microphone structure considered in this study is shown in Figure 5-2. It includes a diaphragm, which deflects under an incident acoustic pressure; a cavity, which allows the diaphragm to move; and a vent, which connects the cavity to the ambient environment and thereby eliminates sensitivity to static pressure changes. As the diaphragm deflects, strain in the piezoelectric layer yields an electric field due to the direct piezoelectric effect. The electric field is sensed as a voltage difference across the electrodes — this is the microphone output.

In a general design setting, much flexibility exists in the selection of piezoelectric microphone geometry and film stack composition, but a piezoelectric microphone diaphragm must at minimum include a set of electrodes and a piezoelectric layer. The microphone in this study is composed of thin-film materials dictated by the FBAR-variant fabrication process as described in Section 4.2; these include an aluminum nitride (AlN) piezoelectric layer, molybdenum (Mo) electrodes, and structural and passivation layers for which the proprietary material choices are not disclosed.

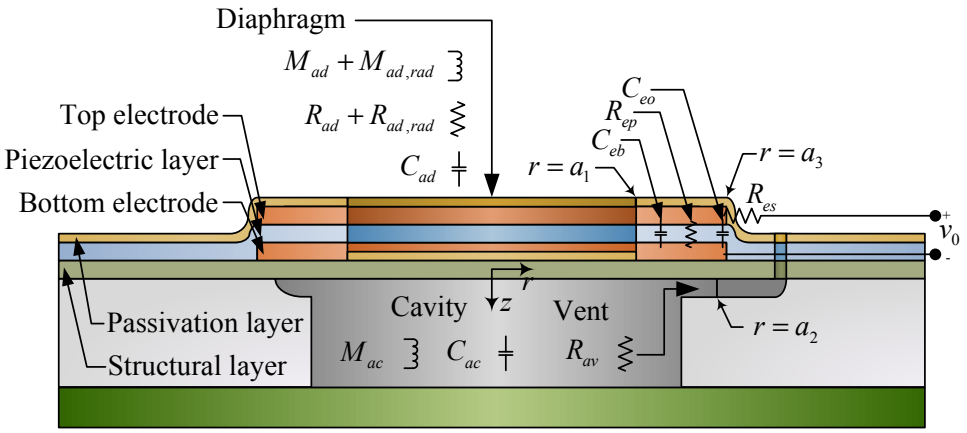

Figure 5-2. Piezoelectric microphone structure.

Lumped element modeling was introduced as an efficient and simple technique for estimating the behavior of transducers. In Figure 5-2, the lumped elements that represent each of the microphone's major components are identified based on the underlying physics of each. To avoid confusion, the convention used here is that the first subscript on an element stands for the domain (**a**coustic or **e**lectrical) and the second subscript provides identification. For instance, M_{ad} is the lumped diaphragm mass in the acoustic domain.

Each of the elements found in Figure 5-2 are connected in an equivalent circuit as shown in Figure 5-3. The diaphragm is modeled as a lumped mass and compliance, M_{ad} and C_{ad}, respectively [113]. Damping is included as a resistance, R_{ad}, that accounts for loss mechanisms such as thermoelastic dissipation [117] and anchor/support loss [118]. Coupling between the diaphragm and the air on the free side is modeled using a

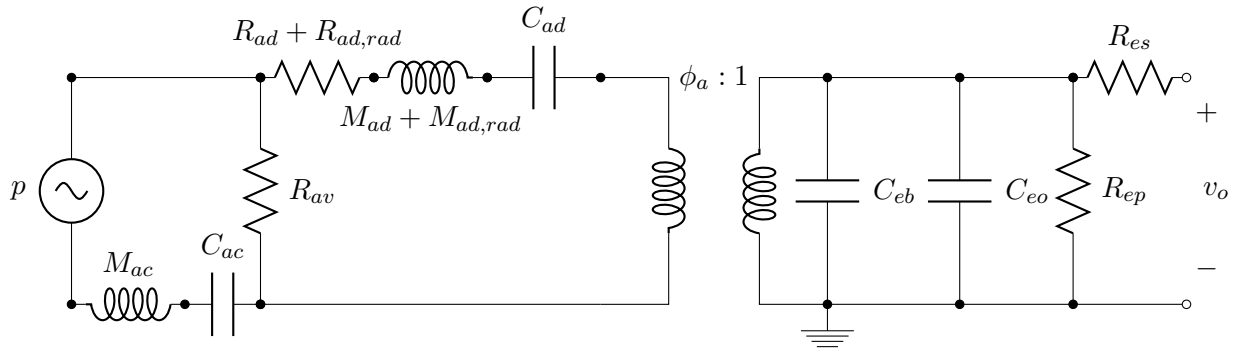

Figure 5-3. Piezoelectric microphone lumped element model.

radiation mass $M_{ad,rad}$ and resistance $R_{ad,rad}$ that are connected in series with C_{ac} and M_{ad} because they all experience the same volume velocity. The cavity is modeled as a mass and compliance, M_{ac} and C_{ac}, respectively. The vent is represented as a resistance R_{av}. Just as in Figure 5-2, the placement of R_{av} in Figure 5-3 provides an alternate path for volume velocity, and thus a pressure drop, between the ambient environment and the back cavity. Coupling between the acoustical and electrical domains is captured using a transformer with turns ratio ϕ_a. Electrical elements are connected on the right side of Figure 5-3 and include the sense capacitance C_{eb}, the parasitic capacitance due to electrode overhang beyond the diaphragm C_{eo}, piezoelectric loss resistance R_{ep}, and series resistance R_{es}. The "b" in C_{eb} stands for "blocked," meaning it is the capacitance that remains when the piezoelectric is blocked from motion (and thus no volume velocity flows into the transformer). The element R_{es} represents the resistance of any leads or wires on or connecting to the microphone. The microphone output is the voltage v_o.

Although the impedances of each component of the microphone are introduced here as combinations of masses/ inductances, compliances/ capacitances, and dampers/ resistances, it is sufficient at this stage to recognize that each component possesses an impedance and that the form of the impedance is dictated by the associated physics. The origins of each impedance are discussed in the next sections.

5.2.1 Elements

In this section, the various elements included in the lumped element model for the piezoelectric MEMS microphone are discussed in turn. First, modeling of the piezoelectric transduction is discussed. Next, structural elements that represent the diaphragm are defined and the associated underlying diaphragm mechanical model is outlined. Acoustical and electrical elements are then examined.

5.2.1.1 Transduction

Modeling the transduction of the piezoelectric microphone requires a knowledge of the constitutive behavior of piezoelectric materials. The 3-D constitutive equations [95, 96] were discussed in Section 4.1 and may be written compactly, denoting vectors and matrices with bold symbols, as

$$\begin{Bmatrix} \boldsymbol{D} \\ \boldsymbol{S} \end{Bmatrix} = \begin{bmatrix} \boldsymbol{\varepsilon^T} & \boldsymbol{d} \\ \boldsymbol{d}^T & \boldsymbol{s^E} \end{bmatrix} \begin{Bmatrix} \boldsymbol{E} \\ \boldsymbol{T} \end{Bmatrix}. \tag{5–1}$$

The 1-D, time-harmonic equivalent of Equation 5–1 is [20, 113]

$$\begin{Bmatrix} I \\ q \end{Bmatrix} = \begin{bmatrix} j\omega C_{ef} & j\omega d_a \\ j\omega d_a & j\omega C_{ad} \end{bmatrix} \begin{Bmatrix} V \\ p \end{Bmatrix}, \tag{5–2}$$

where I is current, $q = j\omega\Delta\forall$ is volume velocity, $\Delta\forall$ is volume displacement, V is voltage, and p is pressure. The quantities C_{ef}, d_a, C_{ad}, ϕ_a, and C_{eb} all serve as constitutive properties of the piezoelectric and are defined in turn in the coming paragraphs. It may be shown using circuit analysis techniques that a transformer in the configuration of Figure 5-4 is equivalent to Equation 5–2 given appropriate definitions for ϕ_a and C_{eb}. Thus, just as Equation 5–2 couples the acoustic and electrical domain, so too does the two-port electroacoustic circuit element of Figure 5-4. As used in the lumped element model of Figure 5-3, this element couples the diaphragm/cavity/vent response to the electrical response of the piezoelectric.

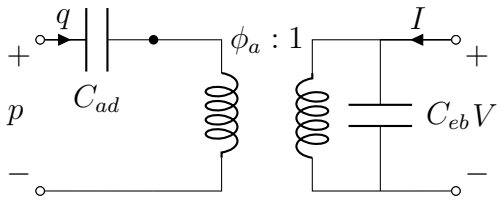

Figure 5-4. Two-port piezoelectric transduction element.

The capacitance of the annular film stack is composed of a sense capacitance that contributes to the transduction and a parasitic capacitance due to electrode overhang beyond the stressed diaphragm region. The electrical free capacitance C_{ef}, i.e. the capacitance observed when the diaphragm is free to move, is simply the parallel plate capacitance between the electrodes [35],

$$C_{ef} = \frac{\epsilon A_e}{h_p}. \tag{5–3}$$

Here, ϵ is the absolute permittivity of the piezoelectric layer, $A_e = \pi\left(a_2^2 - a_1^2\right)$ is the electrode area, and h_p is the distance the electrodes are separated by the piezoelectric layer. It is related to the electrical blocked capacitance C_{eb} as [35, 113]

$$C_{eb} = \left(1 - k^2\right) C_{ef}, \tag{5–4}$$

where k is the electromechanical coupling factor defined from

$$k^2 = \frac{d_a^2}{C_{ef} C_{ad}}, \tag{5–5}$$

which is representative of the efficiency of energy conversion from one domain to the other, though losses are not accounted for [35]. The diaphragm compliance C_{ad} is defined from Equation 5–2 as

$$C_{ad} = \frac{\Delta\forall|_{V=0}}{p}, \tag{5–6}$$

so the diaphragm compliance in the transduction representation of Figure 5-4 is the volume displacement per pressure under short-circuit conditions, called the short-circuit

compliance [35]. Calculation of C_{ad} from Equation 5–6 is related to the structural model of the diaphragm that is discussed further in Section 5.2.1.2.

Two definitions for the acoustic piezoelectric coefficient d_a may be extracted from Equation 5–2. The first is

$$d_a = \frac{Q|_{V=0}}{p}, \tag{5–7}$$

where Q is the electric charge, which is related to the current as $I = j\omega Q$. The second definition is

$$d_a = \frac{\Delta\forall|_{p=0}}{V}. \tag{5–8}$$

The choice of which of Equations 5–7 to 5–8 to use for calculation of d_a is dictated by the ease of calculating the quantities Q or $\Delta\forall$ from a mechanical model of the diaphragm; their equality, or reciprocity, is implied from the linear piezoelectric constitutive relations. Finally, the turns ratio of the transformer (or transduction factor) is defined as [20, 113]

$$\phi_a = -\frac{d_a}{C_{ad}}. \tag{5–9}$$

5.2.1.2 Structural elements

Using the lumped element method, the electromechanical behavior of the diaphragm is captured in a series of elements. The distributed mass and compliance of the diaphragm are collected, or "lumped" into an acoustic mass M_{ad} and compliance C_{ad} that together in series with the acoustic damping R_{ad} form the impedance of the diaphragm. Taken alone, these elements are sufficient to represent the diaphragm as a single-degree-of-freedom system. However, the piezoelectric transduction mechanism is integrated directly with the diaphragm and the effective piezoelectric coefficient d_a is also dependent on the diaphragm's electromechanical behavior. To determine the values of these elements for a given diaphragm configuration, predictive capabilities are needed.

First, however, it is expedient to define each of the elements under the assumption that a prediction for the static transverse diaphragm displacement, $w(r)$, due to a

pressure or voltage input is available. With $w\left(r\right)$ known, the volume displaced by the diaphragm is defined as its area integral, i.e.

$$\Delta\forall = \int_0^{a_2} w\left(r\right) 2\pi r dr. \tag{5–10}$$

Equation 5–10 may be used to compute the acoustic compliance C_{ad} or the acoustic piezoelectric coefficient d_a per Equations 5–6 and 5–8.

The lumped mass of the diaphragm in the acoustic domain is found from equating the kinetic energy of the lumped mass to the actual, distributed kinetic energy of the diaphragm. This equality is given as

$$\frac{1}{2} M_{ad} \left(j\omega\Delta\left.\forall\right|_{V=0}\right)^2 = \frac{1}{2}\int_{\forall} \rho \left[j\omega \left.w\left(r\right)\right|_{V=0}\right]^2 d\forall, \tag{5–11}$$

where the volume velocity q and actual plate velocity $\dot{w}\left(r\right)$ are assumed time harmonic. The stipulation that $V = 0$ is made because pressure, not voltage, is the effort variable for this element. Solving Equation 5–11 while making use of Equation 5–6 yields

$$M_{ad} = \frac{\int_0^{a_2} \rho_A \left.w\left(r\right)\right|_{V=0}^2 2\pi r dr}{\left.\Delta\forall\right|_{V=0}^2}, \tag{5–12}$$

where ρ_A [kg/m^2] is the aerial density of the diaphragm,

$$\rho_A(r) = \int_{z_b}^{z_t} \rho(r,z) dz, \tag{5–13}$$

and z_b and z_t are the top and bottom z-coordinates of the diaphragm, respectively. Making use of Equation 5–6, M_{ad} is equivalently written as [20, 113]

$$M_{ad} = \frac{2\pi}{C_{ad}^2}\int_0^{a_2} \rho_A \left(\frac{\left.w\left(r\right)\right|_{V=0}}{p}\right)^2 r dr, \tag{5–14}$$

which though awkwardly suggesting M_{ad} is directly dependent on compliance and pressure, is convenient for performing calculations.

Finally, the lumped resistance R_{ad} is related to the classical damping coefficient ζ as [34]

$$R_{ad} = 2\zeta\sqrt{\frac{M_{ad}}{C_{ad}}}. \tag{5–15}$$

The damping coefficient is usually determined experimentally because of the difficulty of both predicting what damping mechanisms are important and modeling their effects. In this study, $\zeta = 0.03$ — representative of an observed value for a similar device [119] — is assumed.

With the lumped elements associated with the diaphragm defined and the need for prediction of $w(r)$ motivated, Section 5.2.2 details the model implementation for this study. First, however, the remaining lumped elements are defined.

5.2.1.3 Acoustic elements

In this section, lumped elements capturing the impact of the presence of fluid in and around the microphone are defined. These include impedances associated with fluid external to the microphone, $R_{ad,rad}$ and $M_{ad,rad}$, fluid within the back cavity, C_{ac} and M_{ac}, and fluid in the vent, R_{av}. In each of these elements, the gas density ρ_0 and isentropic speed of sound c_0 appear regularly, in addition to the acoustic wave number $k = \omega/c_0$. The product $\rho_0 c_0$ is known as the characteristic impedance of the fluid medium, Z_0.

The diaphragm re-radiates sound to the surrounding fluid as it vibrates, and this interaction with the fluid impacts the diaphragm dynamics. The so-called Rayleigh integral [28] governs the relationship between the vibrations of a "piston" in a rigid baffle (representative of the microphone diaphragm) and the radiated pressure field. It may be solved numerically for an arbitrary piston modal vibration, but in the interest of simplicity and computational efficiency, the classical solution for a rigid circular piston moving with uniform velocity is leveraged to predict the effect of the fluid on the diaphragm. The diaphragm and a rigid circular piston as radiators are similar in character, with the fundamental difference being that the piston moves as a rigid body with a single velocity, while the diaphragm does not. The acoustic radiation impedance of a rigid circular piston

with an undetermined effective radius — not equal to the radius of the circular diaphragm — is [28]

$$Z = \frac{Z_0}{\pi a_{eff}^2}\left[1 - \frac{2J_1\left(2ka_{eff}\right)}{2ka_{eff}} + j\frac{2K_1\left(2ka_{eff}\right)}{2ka_{eff}}\right], \tag{5–16}$$

where J_1 is the first-order Bessel function of the first kind and K_1 is the first-order Struve function.

To find the effective radius a_{eff}, the volume velocity of the diaphragm,

$$q = j\omega\Delta\forall|_{V=0}\,, \tag{5–17}$$

is equated to the volume velocity of an equivalent circular piston moving with the center velocity of the diaphragm,

$$q = j\omega w\left(0\right)|_{V=0}\,\pi a_{eff}^2. \tag{5–18}$$

Solving for a_{eff} then yields

$$a_{eff} = \sqrt{\frac{1}{\pi}\frac{\Delta\forall|_{V=0}}{w\left(0\right)|_{V=0}}}, \tag{5–19}$$

from which the effective area $A_{eff} = \pi a_{eff}^2$ may also be calculated. For a given diaphragm geometry, a circular piston of radius a_{eff} and corresponding area A_{eff} therefore produces the same volume displacement and should have the same approximate radiative properties.

In the low-frequency approximation ($ka_{eff} \ll 1$), obtained by performing a Maclaurin series expansion of Equation 5–16 and dropping terms of order $\left(ka_{eff}\right)^3$ and higher, the radiation impedance of air reduces to a mass [28],

$$M_{a,rad} = \frac{8\rho_0}{3\pi^2 a_{eff}}, \tag{5–20}$$

and a resistance,

$$R_{a,rad} = \frac{\rho_0\omega^2}{2\pi c_0}. \tag{5–21}$$

These quantities capture the effects of air particles moving together with the diaphragm and the loss of acoustic energy into the surrounding medium. This low-frequency approximation of Equation 5–16 is valid to within 5% up to approximately $ka = 0.43$.

The fluid in the cavity behind the diaphragm also impacts its dynamics. The cavity impedance is derived from the classical acoustics solution for the acoustic impedance of a rigid-walled tube with a rigid termination [28],

$$Z_{ac} = -j\frac{Z_0}{A_c}\cot\left(kd_c\right), \tag{5–22}$$

where A_c is the cavity area and d_c is the cavity depth. When the acoustic wavelength is much less than the length of the tube, a truncated series expansion yields an acoustic compliance,

$$C_{ac} = \frac{\forall_c}{\rho_0 c_0^2}, \tag{5–23}$$

where $\forall_c = d_c A_c$ is the cavity volume, and an acoustic mass,

$$M_{ac} = \frac{\rho_0 \forall_c}{3A_c^2}. \tag{5–24}$$

For $kd_c \leq 0.3$, the contribution of M_{ac} to the cavity impedance is less than 3% of the contribution of C_{ac} and it may be neglected. However, it is retained because its inclusion adds little additional complication to the model. The FBAR-variant process makes use of silicon wafers that are 500 μm thick following the chemical-mechanical polish step, yielding $d_c = 500\,\mu$m. As an example, for this cavity at 20 kHz, $kd_c = 0.18$.

Finally, the flow through the vent channel is modeled as fully developed, pressure driven flow between two parallel surfaces [43, 120]. The canonical vent structure has a length L_v and a rectangular cross section of height h_v and width b_v, with $b_v \gg h_v$. This thin channel runs from the cavity underneath the diaphragm and emerges topside through a circular hole in the film stack. The impedance of the vent is simply the resistance, [43]

$$R_{av} = \frac{12\mu L_v}{b_v h_v^3}, \tag{5–25}$$

where μ is the viscosity of the fluid. For the FBAR-variant fabrication process, $L_v = 50\,\mu$m, $h_v = 2\,\mu$m, and $b_v = 25\,\mu$m.

5.2.1.4 Electrical elements

Electrical elements found in the lumped element model represent the capacitance of the piezoelectric film stack (C_{eb}), a parasitic capacitance associated with electrode overhang past the diaphragm (C_{eo}), the resistance of the piezoelectric (R_{ep}), and the resistance associated with leads (R_{es}). The electrical blocked capacitance C_{eb} was addressed in Section 5.2.1.1 as part of the transduction model.

The electrodes and piezoelectric overhang slightly past the free diaphragm region, acting as a parasitic capacitance. Using the parallel plate capacitance formula for predictive purposes, the result is

$$C_{eo} = \frac{\epsilon}{A_o} h_p, \tag{5–26}$$

where the electrode overhang area $A_o = \pi\left(a_3^2 - a_2^2\right)$.

A potential difference generated across a piezoelectric cannot remain indefinitely due to charge leakage across it. This effect is accounted for in the lumped element model using the piezoelectric loss resistance, R_{ep}. It is found via the well-known relationship between resistance and the material property resistivity (ρ_p for the piezoelectric) [97],

$$R_{ep} = \frac{\rho_p h_p}{A_e}. \tag{5–27}$$

Even in the absence of a vent, the presence of R_{ep} precludes a microphone output voltage v_o when a static pressure acts on the diaphragm.

The series resistance R_{es} represents leads and wire bonds connecting the microphone to external circuitry. It was estimated from impedance measurements of early prototype devices (with typical lead geometries for the FBAR-variant process) to be approximately 4 kΩ. The impact of this element is generally negligible but it is included for completeness.

5.2.2 Diaphragm Mechanical Model

As established in Section 5.2.1.2, displacement predictions for a piezoelectric microphone diaphragm under pressure and voltage loading are needed in order to calculate several lumped elements, including C_{ad} and M_{ad}, in addition to the effective piezoelectric

coefficient d_a. In this section, the prior art for modeling of such structures is summarized and the model implementation used in this study is described. The majority of model development, however, is found in Appendix A.

The microphone diaphragm is made up of composite layers, and thus it shares some common characteristics with macroscale laminated composites. Modeling of composite laminates is well-developed, and an appropriate theory for modeling of high aspect-ratio, thin-film composites such as the microphone diaphragm is the classical laminated plate theory (CLPT) [121, 122]. The simplified geometrical representation of Figure 5-5 shows the diaphragm as a circular laminated composite plate with an integrated piezoelectric layer and step discontinuity at $r = a_1$. In common vernacular, the diaphragm of Figure 5-5 is of "unimorph"[1] geometry, meaning there is a single piezoelectric layer [123]. Two common unimorph circular diaphragm configurations were shown in Figure 4-3.

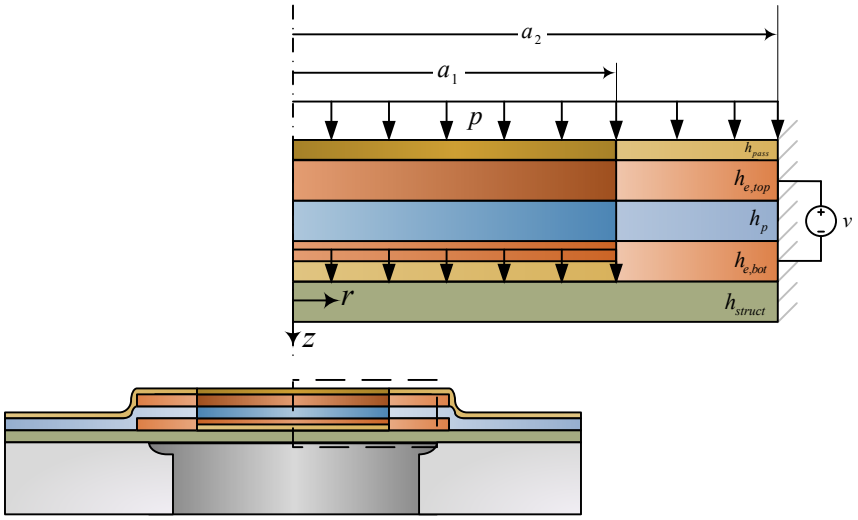

Figure 5-5. Laminated composite plate representation of the thin-film diaphragm under pressure and voltage loading.

The literature on piezoelectric composite plates, even narrowed to unimorphs of circular geometry, is extensive. Although unimorphs may contain piezoelectric and

[1] Similarly, the term "bimorph" refers to a structure with two piezoelectric layers, and so on [123].

structural layers of equal radii, those with radially nonuniform layer compositions as in Figure 5-5 are of the most interest in this study. Analytical investigations of this geometry appear to have roots in the Russian literature with Antonyak and Vassergiser (1982) [124], who presented a static model of a simply-supported two-layer circular unimorph transducer in which the radius of the piezoelectric layer was less than that of the structural layer. The governing equations were solved piecewise on either side of the step discontinuity, with matching conditions on moments and displacements applied at it. Simply-supported boundary conditions were used. An equivalent electroacoustic circuit was used to examine the variation of sensitivity and electromechanical coupling coefficient with changes in thickness and radius ratios. Evseichik et al. [125] performed a similar study in 1991, but solved the time harmonic governing equations. The impacts of clamped, free, and hinged boundary conditions were discussed. Chang and Du (2001) [126] investigated essentially the same problem but also formally determined optimized configurations for large electromechanical coupling factor and static deflection.

A static model of a clamped piezoelectric circular plate with radially nonuniform layers together with a two-port electroacoustic equivalent circuit representation was developed in a series of conference and journal papers from the Interdisciplinary Microsystems Group at the University of Florida [113, 127, 128] in the years 2002–2006. In Prasad et al. (2002, 2006) [113, 128], a compact, closed-form solution was offered for the problem of a clamped central disc unimorph. Layer composition was generalized in the provided solution via use of the stiffness matrices $\boldsymbol{A}$, $\boldsymbol{B}$, and $\boldsymbol{D}$, though the outer region was restricted to symmetric layups. The two-port electroacoustic equivalent circuit developed had the same form utilized by Antonyak and Vassergiser [124]. The model was validated experimentally and with finite element analysis [113]. Another version of the model presented in Wang et al. (2002) [127] included in-plane residual stress as an input, motivated by its significant impact in microfabricated structures. Validation against nonlinear finite element analysis was provided.

In 2003, Li and Chen [129] found the deflection profile of a simply-supported unimorph with inner-disc actuator and bond layer. Later, several papers from a group at the University of Pittsburgh addressed circular piezoelectric unimorphs. In 2005, Kim et. al. [130] presented models for a circular unimorph with uniform piezoelectric and structural-layer thicknesses but two different electrode configurations. In the first configuration, the electrodes fully covered the piezoelectric layer; in the second, the electrodes were segmented into inner and outer regions with reversed polarization. In 2006, Mo et al. [131] investigated a two layer unimorph with clamped, simply supported, and elastic edge conditions. Both radially uniform and nonuniform layer compositions were discussed. The authors focused on the variation of deflection profiles with a number of parameters, including thickness, radius, and elastic modulus ratios of the piezoelectric to structural layer. Experimental verification was also given. The next year, the same authors modified the model with a segmented electrode configuration [130] to include elastically restrained edge conditions. Experimental verification of the model was provided [132].

Deshpande and Saggere (2007) [133] provided a generalized model for prediction of the displacements of a circular piezoelectric plate with a single radial discontinuity. The ease with which aribitrary layer configurations could be included via avoidance of early simplifications to the $\boldsymbol{A}$, $\boldsymbol{B}$, and $\boldsymbol{D}$ stiffness matrices was emphasized. Finite element and experimental verification were given for a range of voltage and pressure loadings. Papila et al. (2008) [134] provided a similarly general formulation for a circular piezoelectric plate with two radial discontinuities.

Other papers acknowledged for their contribution to composite piezoelectric sensors and actuators — not just for circular geometries — include those of Lee [135, 136] and Reddy [137]. Each contains discussion of sensor and actuator forms for the governing piezoelectric plate equations.

In-plane residual stresses are nearly omnipresent byproducts of microfabrication processes and often dominate the behavior of thin-film mechanical structures [20]. Predicting the impact of stress on diaphragm performance is thus extremely important, and only the model of Wang et al. [127] sought to include these effects.

As a result, this study utilizes extended versions of that model, including both linear and nonlinear formulations. The linear model was extended to include arbitrary film stacks. The nonlinear version of the model was based on the von Kármán plate theory and was developed to assess the transition from linear to nonlinear response of the microphone diaphragm. In both linear and nonlinear cases, residual stresses are taken to be known inputs for the mechanical model. Their presence gives rise to a static transverse deflection even in the absence of an applied pressure or voltage, as shown in Figure 5-6A. It is the incremental deflection about this static profile — due to application of pressure or voltage — that characterizes the response of the microphone. Incremental deflection due to pressure loading is is illustrated in Figure 5-6B. Mathematically, the initial, incremental, and total deflection are related as

$$w_{inc}(r) = w_{tot}(r) - w_{ini}(r). \tag{5–28}$$

Here, the initial deflection, w_{ini} $(= w|_{V\&p=0})$, is purely due to residual stresses; the incremental deflection, w_{inc} is due to pressure or voltage loading; and the total deflection, w_{tot} $(= w|_{V|p\neq 0})$, is due to both residual stress and external loading. In Section 5.2.1.2, the diaphragm deflection w always refers to the incremental displacement, w_{inc}.

The model was derived using the same two-domain solution methodology that is prevalent in the literature, with the governing equations of the CLPT solved on either side of the radial discontinuity and matched via boundary conditions at the interface. Figure 5-7 depicts the idea of the boundary matching process, where at $r = a_1$ the displacements, in addition to the force and moment resultants N_r and M_r associated with each domain ($0 < r \leq a_1$ and $a_1 \leq r < a_2$) must be equal. The presence of the

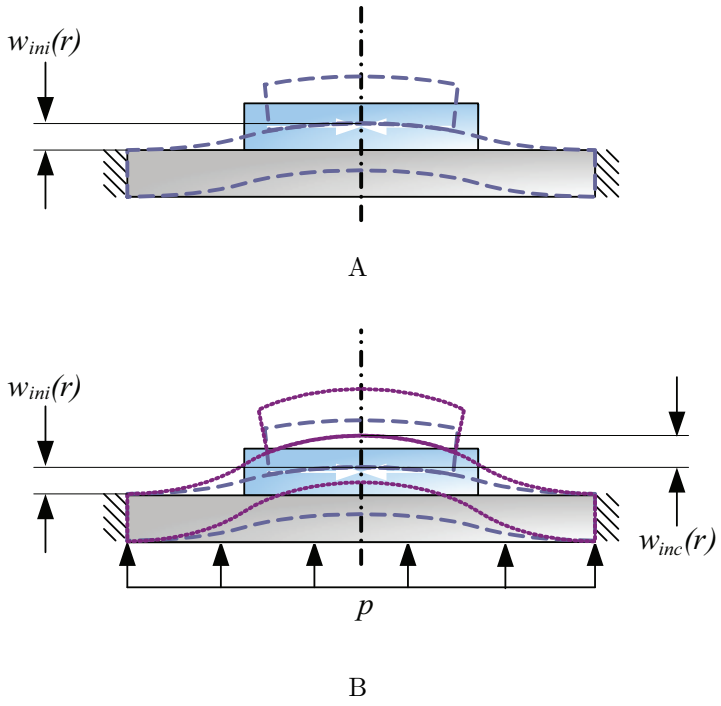

Figure 5-6. Deflection of a radially non-uniform composite plate with residual stress. A) Initial deflection, $w_{ini}(r)$. B) Incremental deflection due to pressure loading, $w_{inc}(r)$.

piezoelectric is communicated via equivalent piezoelectric force and moment resultants, N_p and M_p, appearing in these interface matching conditions. Loading of the plate includes both a uniform pressure and layer-wise voltage differences as originally depicted in Figure 5-5.

A detailed derivation of the linear and nonlinear piezoelectric composite plate models are found in Appendix A. Solution methodologies are also given in both cases; the linear model is solved using a semi-analytical approach where constants of integration are found numerically rather than explicitly, while the nonlinear model is formulated for solution via a boundary value problem solver package, for example `bvp4c` in MATLAB [138].

5.2.3 Frequency Response

With all of the individual lumped elements defined, the equivalent circuit model of Figure 5-3 is complete. Using standard circuit analysis techniques, this model may be

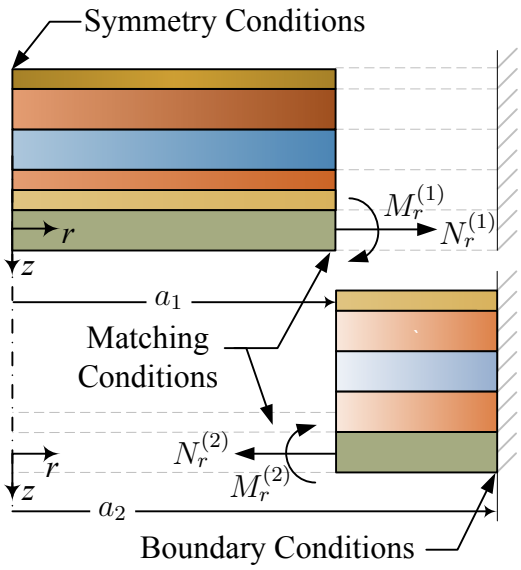

Figure 5-7. Boundary conditions applied to a radially non-uniform piezoelectric composite plate.

probed to determine the microphone frequency response function, $H_m(f)$. Simplification of the microphone frequency response function enables a direct estimate of the flat-band sensitivity, S. With minor alterations, the actuator sensitivity may also be calculated. These quantities are investigated in turn in the following sub-sections.

First, however, collecting impedances together facilitates the circuit analysis. Defining

$$Z_{ac} = j\omega M_{ac} + \frac{1}{j\omega C_{ac}}, \tag{5–29}$$

$$Z_{ad} = j\omega\left(M_{ad} + M_{ad,rad}\right) + R_{ad} + R_{ad,rad} + \frac{1}{j\omega C_{ad}}, \tag{5–30}$$

and

$$Z_{ep} = \frac{R_{ep}}{1 + j\omega R_{ep}\left(C_{eb} + C_{eo}\right)}, \tag{5–31}$$

condenses the math substantially. Here, Z_{ac} is simply the series combination of the cavity compliance and mass, Z_{ad} collects all of the diaphragm and radiation impedances in series, and Z_{ep} captures the parallel combination of C_{eb}, C_{ea}, and R_{ep}. Making use of these definitions, the condensed equivalent circuit for the microphone lumped element model in Figure 5-8 results.

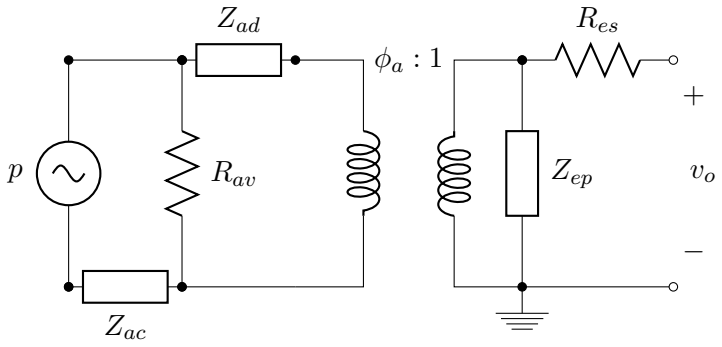

Figure 5-8. Lumped element model with collected impedances.

5.2.3.1 Sensor

Utilizing Figure 5-8, the open-circuit output voltage v_o is related to the input pressure p via circuit analysis as

$$H_{m,oc}(f) = \frac{v_o}{p} = \frac{1/\phi_a}{\left(1 + \frac{Z_{ac}}{R_{av}}\right)\left(1 + \frac{Z_{ad}}{Z_{ep}\phi_a^2}\right) + \frac{Z_{ac}}{Z_{ep}\phi_a^2}}, \tag{5–32}$$

which is the open-circuit frequency response function for the microphone. Figure 5-9 shows the typical magnitude associated with each of the impedance ratios appearing in Equation 5–32.[2] The cut-on behavior is dictated by the cavity/vent combination of the Z_{ac}/R_{av} term, which is only greater than or comparable to unity at low frequencies. Over the remaining frequency range, the Z_{ad}/Z_{ep} term dominates all others. The capacitive components of Equation 5–32 dominate in the flat band. Eliminating the inductive and resistive impedance components yields an estimation of the flat-band sensitivity,

$$S_{oc} = \frac{\phi_a}{\phi_a^2 + \frac{(C_{eb} + C_{eo})}{C_{ad}}\left(1 + \frac{C_{ad}}{C_{ac}}\right)}. \tag{5–33}$$

The cavity is ideally far more compliant than the diaphragm such that it does not have an appreciable effect on the microphone sensitivity, as in Figure 5-9. A key simplifying

[2] Refer to Table 5-1 for the example device geometry and Appendix D for material properties.

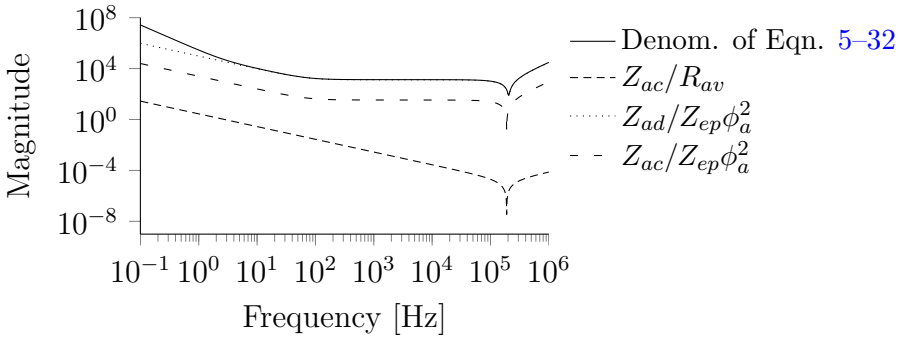

Figure 5-9. Impedance ratios appearing in the open circuit frequency response expression, Equation 5–32.

assumption is thus

$$\frac{C_{ad}}{C_{ac}} \ll 1. \tag{5–34}$$

Employing this approximation and making use of Equations 5–3 and 5–9, Equation 5–35 is further simplified to

$$S_{oc} \approx \frac{-d_a}{C_{ef} + C_{eo}}. \tag{5–35}$$

This extremely simple expression shows that the open circuit microphone sensitivity in the flatband is — to good approximation – only a function of the effective piezoelectric coefficient, the parallel plate capacitance of the piezoelectric film stack, and the small parasitic capacitance associated with electrode overhang beyond the diaphragm. Ideally, $C_{eo} \ll C_{ef}$ is satisfied and C_{eo} does not play a role, either. One perhaps surprising feature of Equation 5–35 is that the diaphragm compliance, C_{ad}, does not appear explicitly; however, the mechanical behavior of the diaphragm is still very much captured within the effective piezoelectric coefficient, d_a.

A comparison of the expressions for sensitivity, Equations 5–33 and 5–35, with the overall open-circuit frequency response function, Equation 5–32, is shown in Figure 5-10[3] . Agreement is excellent in the flatband, with Equation 5–35 slightly over-predicting the

[3] Refer to Table 5-1 for the example device geometry.

flatband sensitivity on the order of a few percent due to neglect of cavity compliance. As plotted, Equations 5–33 and 5–35 fall directly on top of each other.

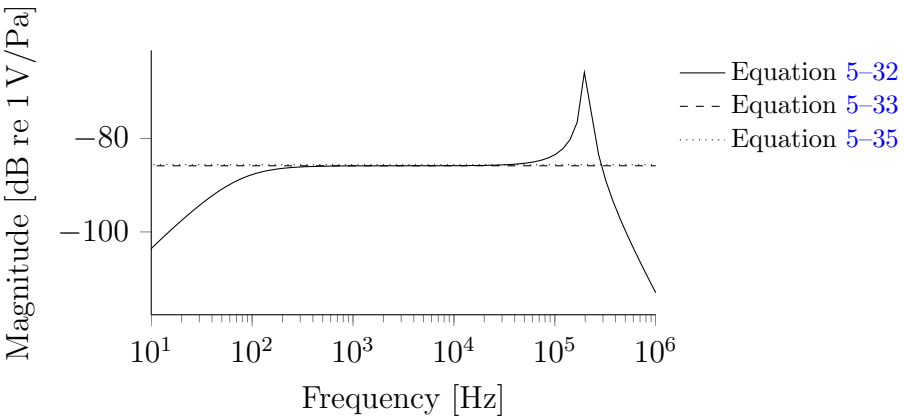

Figure 5-10. Comparison of open-circuit sensitivity expressions and the full open-circuit frequency response of the lumped-element model.

5.2.3.2 Actuator

Because it is far easier to apply a known voltage to the physical piezoelectric microphone than a known pressure, interrogating the microphone in its reciprocal resonator mode can provide useful information. It is instructive, then, to consider in the modeling stage how the actuator response compares to the sensor response. The equivalent piezoelectric actuator has been addressed previously [139], and the associated lumped element model, with voltage source added on the electrical side, is shown in Figure 5-11. Interrogating this model, the volume displacement $\forall$ $(=q/j\omega)$ through the diaphragm leg of the circuit per applied voltage v is

$$H_a(f) = \frac{\forall}{v} = \frac{\phi_a/j\omega}{Z_{ep}\phi_a^2 - \left(1 + \frac{R_{es}}{Z_{ep}}\right)\left(Z_{ep}\phi_a^2 + Z_{ad} + \frac{Z_{ac}Z_{av}}{Z_{ac}+Z_{av}}\right)}. \tag{5–36}$$

Although actuators are typically operated at resonance, probing the flatband actuator response is useful in the context of evaluating devices to serve as microphones. In the

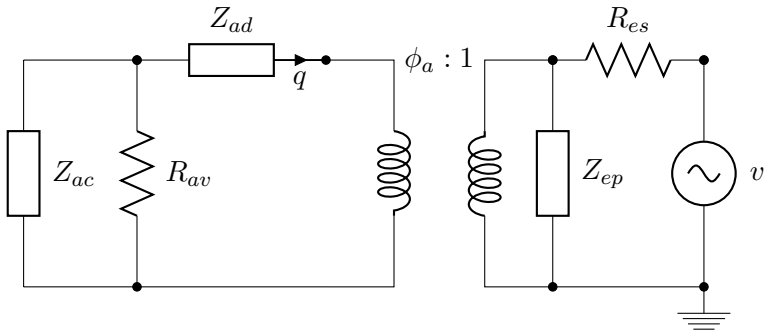

Figure 5-11. Lumped element model of the piezoelectric microphone as an actuator.

flatband, capacitive elements continue to dominate, giving

$$S_a = \frac{\forall}{v} = \frac{-\phi_a C_{ad}}{1 + \dfrac{C_{ad}}{C_{ac}}}. \tag{5–37}$$

Again under the assumption of Equation 5–34 and employing Equation 5–9, the end result is simply

$$S_a \approx d_a. \tag{5–38}$$

Comparing this expression to that for the open circuit sensitivity, Equation 5–32, one sees that they are both proportional to d_a. This implies that the actuator response provides some measure of the expected sensor response. This idea is revisited in Chapter 8 in the context of microphone selection.

5.2.4 Electrical impedance

The microphone's electrical impedance can impact circuit design choices and thus having a prediction is important. Interrogating the circuit in Figure 5-11, the equivalent electrical impedance seen by the voltage source is

$$Z_{eq} = (Z_{acv} + Z_{ad}) \parallel Z_{ep} + R_{es}, \tag{5–39}$$

or collecting terms [140],

$$Z_{eq} = R_{es} + Z_{ep}\frac{1}{1+\Gamma}, \tag{5–40}$$

where

$$\Gamma = \frac{Z_{ep}\phi_a^2}{Z_{acv} + Z_{ad}}. \tag{5–41}$$

Assuming the cavity is very compliant (Equation 5–34), Z_{eq} in the flatband reduces to

$$Z_{eq} = R_{es} + \frac{R_{ep}}{1 + j\omega R_{ep}\left(C_{ef} + C_{eo}\right)}. \tag{5–42}$$

5.2.5 Validation

The models presented in this chapter — both the diaphragm model alone and the complete lumped element model — were validated using the finite element method, a computational technique used to solve boundary values problems. Finite element models can generally capture more of the underlying physics of a problem than analytical models, which often require significant simplifying assumptions to be made tractable. The improved fidelity of finite element modeling comes with the cost of increased computation time associated with solving large systems of equations.

The finite element model was created and simulated in ABAQUS v6.8-2 using the basic geometry of Figure 5-5 and the associated geometric dimensions of Table 5-1, shown to scale in Figure 5-12. Material properties are found in Appendix D except the full AlN stiffness and piezoelectric matrices, which were drawn from Tsubouchi et al. (1985) [141]. Boundary conditions are pictured in Figure 5-12B and include a roller condition on the diaphragm edge at $r = a_3$ (to allow free expansion of the film in the thickness-direction) and fully clamped conditions along the bottom diaphragm edge, $a_2 \leq r \leq a_3$. A second model in Appendix A.8 compares the use of this boundary condition with one including the silicon substrate. The electrical boundary condition for the bottom piezoelectric surface was zero electric potential, and an equation constraint produced an equipotential top surface to simulate the top electrode. Remaining (free) surfaces were subject to default natural boundary conditions of zero traction [142] and zero normal component of electric flux density [97], respectively. No damping was applied in the model. The geometry was meshed with 52k bilinear axisymmetric continuum elements approximately

0.125 μm on a side of types CAX4E[4] for the piezoelectric layer and CAX4[5] otherwise. A close-up view of the mesh is shown in Figure 5-12C.

Table 5-1. Geometric dimensions of an example device.†

	Dimension	Symbol	Value [μm]
Thicknesses	Passivation	h_{pass}	0.14
	Top Mo Electrode	$h_{e,top}$	0.15
	Piezoelectric Layer (AlN)	h_p	1
	Bottom Mo Electrode	$h_{e,bot}$	0.6
	Structural Layer	h_{struct}	2
Radii	Inner	a_1	306
	Outer	a_2	345
	Outer with overhang	a_3	348

† Design D (see Chapter 6)

In each model run, the structure was first allowed to equilibrate from the residual stress, applied via the *INITIAL CONDITIONS command, in a static general step with geometric nonlinearity included (NLGEOM on). Afterward, various steps were performed depending on the nature of the validation exercise. Each of these is discussed in the following subsections.

5.2.5.1 Diaphragm model validation

The diaphragm model is required to provide accurate predictions of $w(r)$ from which elements such as C_{ad}, M_{ad}, and d_a are calculated for input to the lumped element model. Simulations were completed for ranges of both pressure and voltage loading to assess the accuracy of the model.

From the nonlinearly deflected base state, a range of pressure and voltage inputs were swept in a geometrically nonlinear static general step. Pressure was simply applied as a uniform load over the top of the diaphragm, with values ranging from 100 dB to beyond

[4] CAX4E: 4-node bilinear axisymmetric continuum element with electric potential degree of freedom

[5] CAX4: 4-node bilinear axisymmetric continuum element

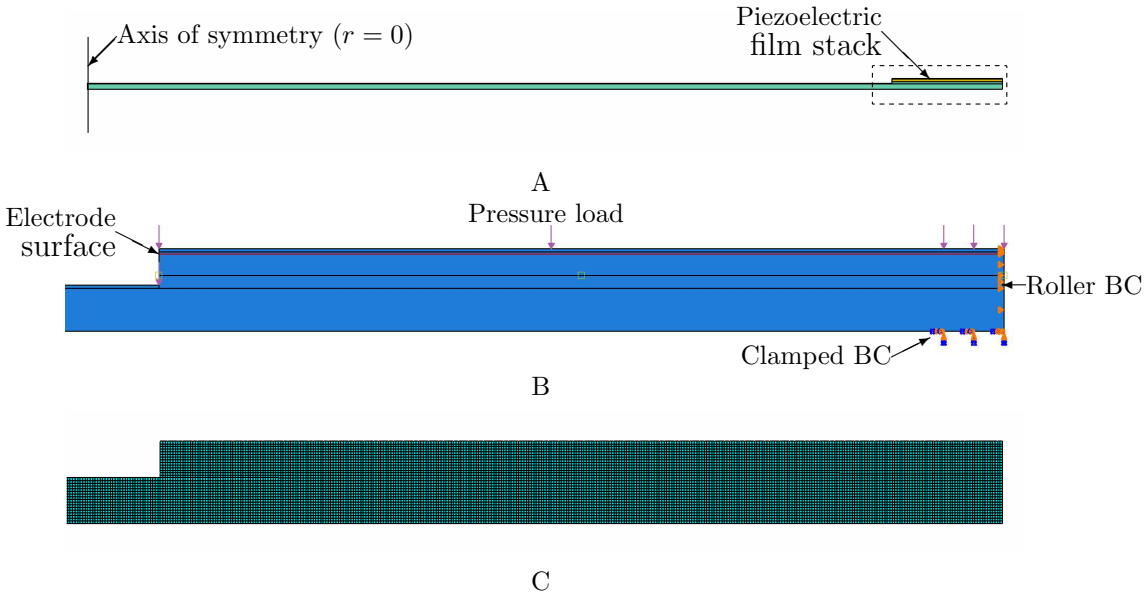

Figure 5-12. Finite element model for validation exercise. A) Geometry to scale. B) Zoomed-in view of annular piezoelectric film stack and boundary conditions. B) Zoomed-in view of meshed annular piezoelectric film stack.

180 dB. The results of the simulation are compared to the linear and nonlinear diaphragm models in Figure 5-13 in terms of incremental center deflection ($w_{inc}(0)$). Agreement with the nonlinear model is excellent over the entire range of inputs, while there is some deviation from the linear model, as expected, at very high sound pressure levels. The relative error between the two models and the finite element model is also shown in Figure 5-14, with error very nearly zero out to pressure levels approaching 170 dB for the linear model.

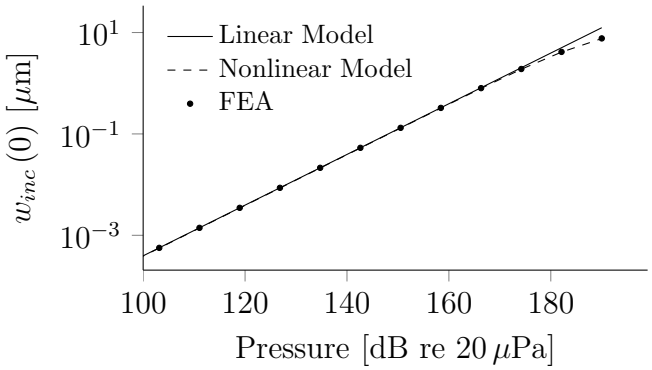

Figure 5-13. Analytical and FEA predictions of $w_{inc}(0)$ (pressure loading case).

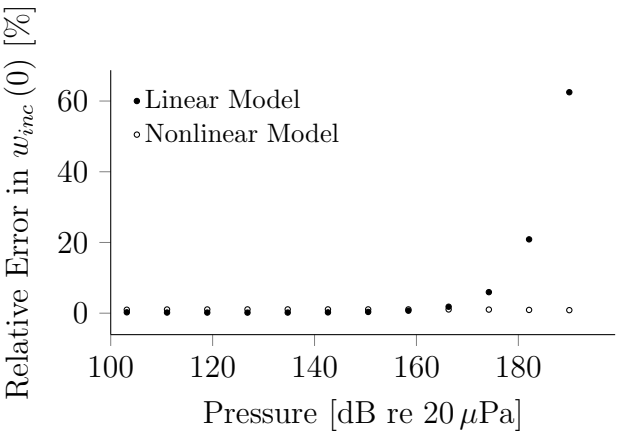

Figure 5-14. Relative error between analytical and FEA predictions of $w_{inc}(0)$ (pressure loading case).

In a second model run, various values of applied voltage were also swept in a static general step. An electric potential was applied to a reference node and the equation constraint enforced an equipotential top piezoelectric surface. The results from the finite element and analytical models are compared in Figure 5-15, which shows that all three models agree closely (from 3 % to 7 % relative error).

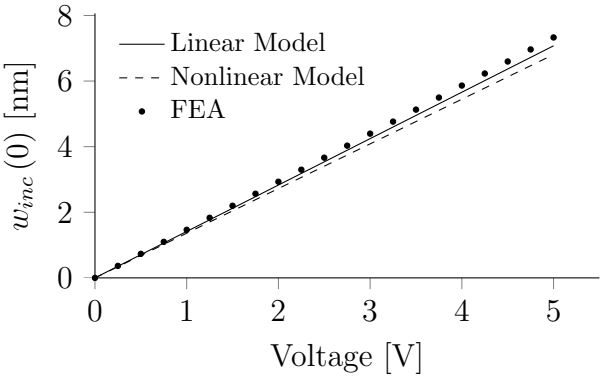

Figure 5-15. Analytical and FEA predictions of $w_{inc}(0)$ (voltage loading case).

5.2.5.2 Lumped element model validation

With the diaphragm model independently verified, the frequency response function of the microphone — sans some physics — was found via finite element modeling and compared to the lumped element model prediction. Properly capturing the acoustics would require a full three-dimensional model (for the vent geometry) and simulation

of free space on the diaphragm exterior. With the validity of the acoustic elements (particularly the cavity and radiation impedances) well-established [28, 35, 36], the finite element model validation was performed purely to prove the quality of predictions for the electromechanical elements. Essentially, then, this exercise further validated the piezocomposite plate model and also the lumped element modeling approach for predicting microphone diaphragm dynamics.

A steady-state dynamics (direct) step was used to find the steady-state harmonic response of the diaphragm to pressure loading. This step was a linear perturbation procedure that calculated the diaphragm response directly from the mass, damping, and stiffness matrices of the system [143]. The response was evaluated at 150 logarithmically spaced frequency points from 0.01 Hz to 350 kHz. The results are shown in Figure 5-16. With the acoustics not included in the finite element model, the cut-on was not predicted, but the flat band responses agreed to within 0.05 dB (0.6 %) and the resonant frequencies were also well-matched. Solution of this step took on the order of 10 minutes to solve using the finite element model compared to seconds using the lumped element model.

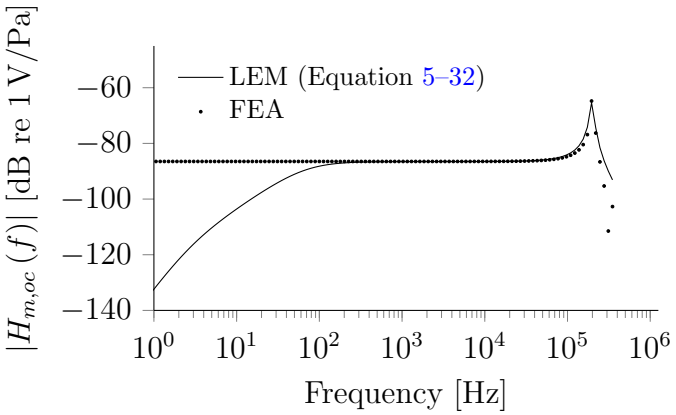

Figure 5-16. Lumped element model and FEA predictions of frequency response function.

5.3 Interface Circuitry

In Section 5.2, an equivalent circuit model of the entire piezoelectric microphone was used to predict its open circuit sensitivity. Unfortunately, the act of measuring the

output voltage of the microphone circuit necessarily loads it, and the change in output voltage can be substantial if the load impedance is not significantly higher than the source impedance [144]. A low-capacitance (single pF) piezoelectric microphone can easily have electrical impedance comparable to the typical input impedance of a data acquisition system (DAQ) (1 MΩ-10 GΩ) in the audio frequency range. As a result, the microphone by itself cannot be connected directly to a DAQ without experiencing an apparent change in sensitivity. A variety of circuit architectures exist for transforming the apparent source impedance of the microphone. Two such architectures — a voltage amplifier and charge amplifier — are addressed in Sections 5.3.1 and 5.3.2.

Unfortunately, connecting an ideal operational amplifier configuration to the microphone does not complete the story. Wirebonds and traces running from the physical microphone to the amplifier introduce parasitic capacitance. Internal transistors at the amplifier input also contribute a finite input capacitance [145]. For stability purposes, the amplifier requires a ground path for dc current flow. The impact of these additional impedances are addressed for both the voltage and charge amplifier cases.

5.3.1 Voltage Amplifier

One way to alleviate the problem of source loading is to use a voltage amplifier, which produces an output voltage proportional to input voltage [146] while also providing a low output impedance for the entire microphone/amplifier system. A voltage amplifier with unity gain is known as a *buffer* or *voltage-follower*. The model of the operational amplifier accounting for parasitic capacitance C_{ep}, amplifier input capacitance C_{ea}, and amplifier bias resistance R_{ea} is shown in Figure 5-17. From this model, the new impedance,

$$Z_{ea} = \frac{R_{ea}}{1 + j\omega R_{ea}\left(C_{ea} + C_{ep}\right)}, \tag{5–43}$$

is defined. However, early tests of prototype piezoelectric microphones indicated they could be operated in a stable manner with the dielectric loss of the piezoelectric serving as the dc ground path in place of a bias resistor. As a result, R_{ea} is not utilized in this study

(making Z_{ea} purely capacitive), though it is carried through for completeness. The voltage amplifier circuit is shown connected to the microphone circuit in Figure 5-18.

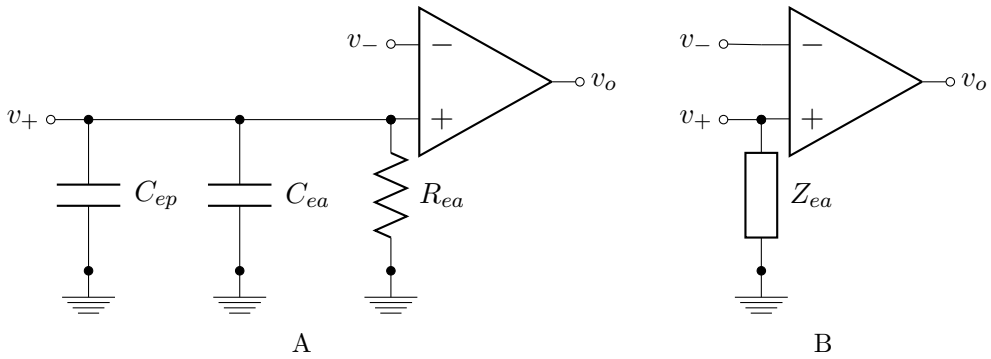

Figure 5-17. Non-ideal operational amplifier model. A) Operational amplifier with parasitic capacitances and bias resistor. B) Operational amplifier representation with equivalent impedance.

Before even beginning a circuit analysis, one can immediately intuit that the parallel combination of Z_{ep} and Z_{ea} (assuming here that R_{es} is negligible in comparison) alters the low frequency RC cutoff originally associated with only Z_{ep}. The presence of a bias resistor tends to raise the break frequency, while the added capacitance tends to lower it.

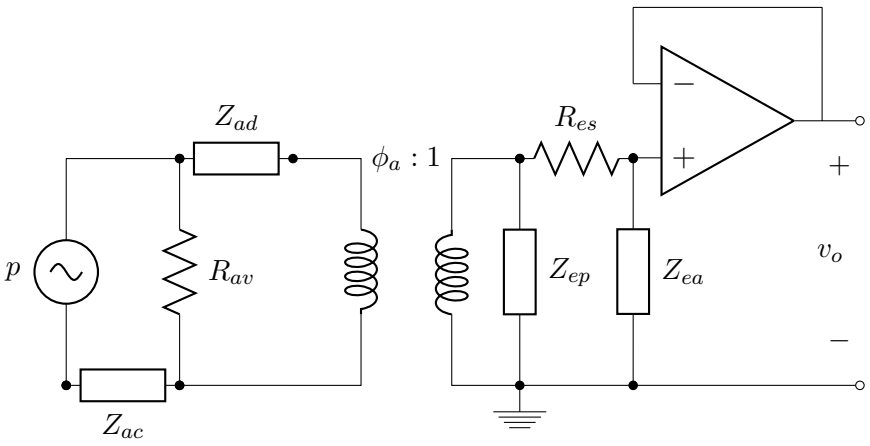

Figure 5-18. Lumped element model with voltage amplifier.

Analyzing the circuit of Figure 5-18, the frequency response function of the complete system is found to be

$$H_{m,va}(f) = \frac{v_o}{p} = \frac{1/\phi_a}{\left(1+\frac{Z_{ac}}{R_{av}}\right)\left(1+\frac{Z_{ad}}{Z_{ep}\phi_a^2}\right)+\frac{Z_{ac}}{Z_{ep}\phi_a^2}+\frac{1}{Z_{ea}\phi_a^2}} \cdot \left\{\left(1+\frac{Z_{ac}}{R_{av}}\right)\left[Z_{ad}+R_{es}\phi_a^2\left(1+\frac{Z_{ad}}{Z_{ep}\phi_a^2}\right)\right]+Z_{ac}\left(1+\frac{R_{es}}{Z_{ep}}\right)\right\}. \tag{5–44}$$

Equation 5–44 is a complicated expression that does not provide ready insight, but again simplifications are easily made. Taking capacitive elements as dominant in the flatband, the frequency response of the microphone/voltage amplifier configuration is

$$S_{va} = \frac{\phi_a}{\phi_a^2+\left(\frac{1}{C_{ad}}+\frac{1}{C_{ac}}\right)\left(C_{eb}+C_{eo}+C_{ep}+C_{ea}\right)}. \tag{5–45}$$

Again, employing the approximation $C_{ac} \gg C_{ad}$ and making use of Equations 5–3 and 5–9,

$$S_{va} \approx \frac{-d_a}{C_{ef}+C_{eo}+C_{ep}+C_{ea}}, \tag{5–46}$$

which in terms of the open-circuit sensitivity becomes

$$S_{va} = S_{oc}\left(\frac{C_{ef}+C_{eo}}{C_{et}}\right), \tag{5–47}$$

where

$$C_{et} = C_{ef}+C_{eo}+C_{ep}+C_{ea} \tag{5–48}$$

is the total capacitance. The repercussions of using the voltage amplifier are now clear. From Equation 5–47, one can see that the open circuit sensitivity is attenuated by the factor $\left(C_{ef}+C_{eo}\right)/C_{et}$, which is *always* less than unity. The problem is compounded for sensors with low capacitance, for which the parasitic capacitances are more likely to be of similar order to C_{ef}; attenuation of the sensitivity in this case can be significant.

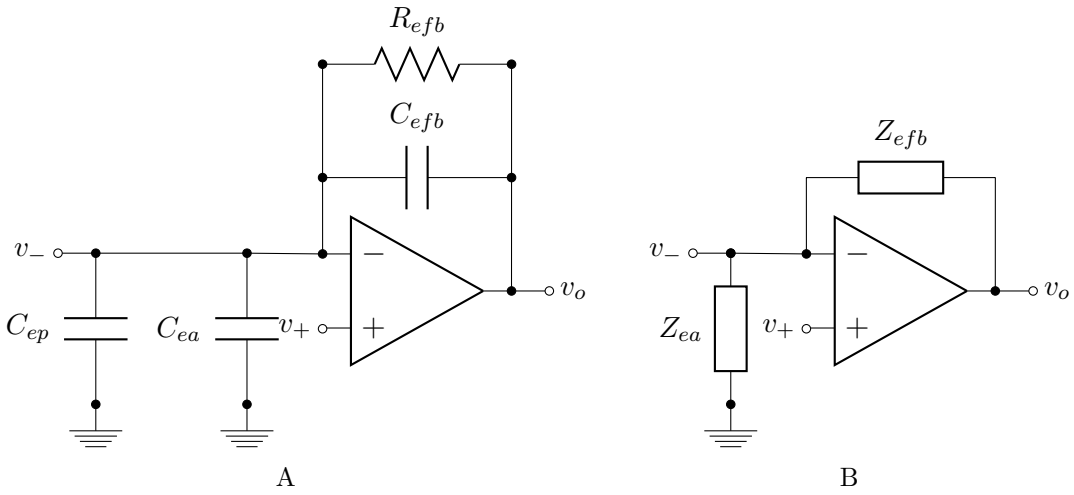

Figure 5-19. Non-ideal charge amplifier model. A) Operational amplifier with parasitic capacitances. B) Operational amplifier representation with equivalent impedance.

5.3.2 Charge Amplifier

Charge amplifiers are so-named because they produce an output voltage proportional to the input charge [146]. They are popular amplifiers for comparable technologies to the piezoelectric microphone, e.g. piezoelectric accelerometers [146, 147]. A model of the operational amplifier and the non-idealities that accompany it is shown in Figure 5-19.

The charge amplifier circuit topology is shown in Figure 5-20, where the feedback impedance Z_{efb} connected to the inverting terminal is a parallel combination of a feedback resistor and capacitor, R_{efb} and C_{efb}, respectively. This impedance introduces a new low-frequency RC cutoff that must be tuned to avoid cutting into the bandwidth of the sensor. However, with the non-inverting terminal serving as a dc path to ground, the impedance Z_{ea} is only capacitive (i.e. $C_{ep} + C_{ea}$). Performing circuit analysis on Figure 5-20, the microphone frequency response function is found to be

$$H_{m,ca}(f) = \frac{-Z_{efb}\phi_a}{Z_{ad}Z_{ac}R_{es}\left[\left(\frac{1}{Z_{acv}}+\frac{1}{Z_{ad}}\right)\left(\frac{\phi_a^2}{Z_{ad}}+\frac{1}{R_{es}}+\frac{1}{Z_{ep}}\right)-\phi_a^2\right]}, \tag{5–49}$$

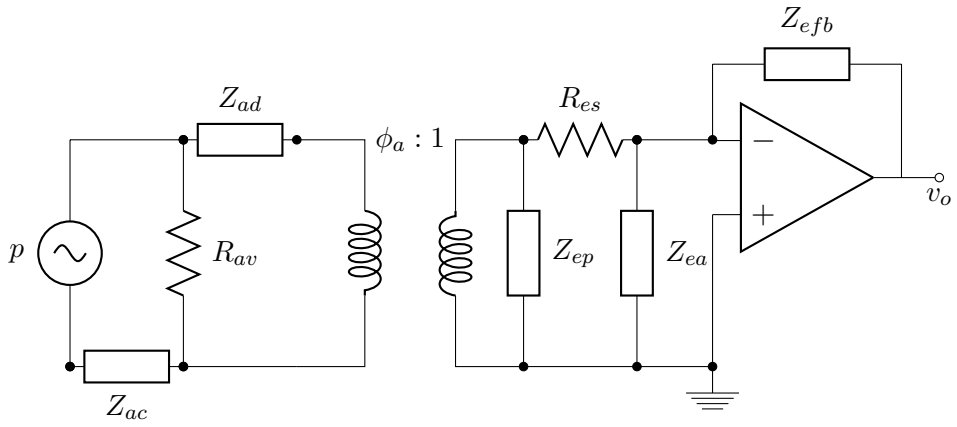

Figure 5-20. Lumped element model with charge amplifier.

where

$$\frac{1}{Z_{acv}} = \frac{1}{Z_{ac}} + \frac{1}{R_{av}}. \tag{5–50}$$

In the flatband, Equation 5–49 simply becomes

$$S_{ca} = \frac{\phi_a^2 / C_{efb}}{\dfrac{1}{C_{ad}} + \dfrac{1}{C_{ac}}}. \tag{5–51}$$

Assuming again that $C_{ac} \gg C_{ad}$,

$$S_{ca} \approx \frac{d_a}{C_{efb}}, \tag{5–52}$$

which can be rewritten in terms of open circuit sensitivity as

$$S_{ca} = -S_{oc} \frac{C_{ef} + C_{eo}}{C_{efb}}. \tag{5–53}$$

Equation 5–53 reveals that the charge amplifier gain factor is the ratio of the electrical free capacitance to the feedback capacitance and that the phase is shifted 180°. The choice of C_{efb} — sometimes called a "range capacitor" [148] — grants a designer the latitude to tune the sensitivity of the entire microphone/amplifier system. In addition, parasitic capacitances play no role because they are virtually grounded [147].

5.3.3 Noise Models

In this section, noise models are developed for both the voltage and charge amplifier circuit topologies. Ultimately, the goal of the noise models is to predict the output noise PSD associated with the microphone/circuitry combination. The minimum detectable pressure (MDP) is calculable from the result via Equation 2–11 or 2–12.

Noise has been previously discussed in Section 2.3.2. In the electrical domain, thermal noise is proportional to the resistance and temperature. In terms of power spectral density, the noise from an electrical resistor R_e is given as [43]

$$S^v_{R_e} = 4k_BTR_e \tag{5–54}$$

or

$$S^i_{R_e} = \frac{4k_BT}{R_e} \tag{5–55}$$

in units of [V^2/Hz] and [A^2/Hz], respectively. The superscripts v and i denote whether S_{R_e} defines a source of voltage or current noise. Similarly, in the acoustic domain, the noise contribution of a dissipative element in terms of power spectral density is

$$S^p_{R_a} = 4k_BTR_a \tag{5–56}$$

or

$$S^q_{R_a} = \frac{4k_BT}{R_a} \tag{5–57}$$

in units of [Pa^2/Hz] and [m^3/s/Hz], respectively. The superscripts p and q indicate whether S_{R_a} defines a source of noise in terms of pressure or volume velocity, respectively.

To find the output noise of the circuit, all sources are first removed and noise sources, defined by Equations 5–54 or 5–55 in the electrical domain and Equations 5–56 or 5–57 in the acoustic domain, are added at the site of each resistor/dissipator. Effort sources (superscript v and p) are added in series with the resistors/dissipators, while flow sources (i and q) are added in parallel [40, 42]. Under the assumption that the noise sources are uncorrelated, the method of superposition of sources is used to find the total power spectral density at the output due to all noise sources [40, 43]. The voltage and charge amplifier circuit architectures are treated in turn in the following subsections.

5.3.3.1 Noise model with voltage amplifier

The noise model for the microphone/voltage amplifier combination is found in Figure 5-21. The subscript of each source indicates the resistor with which it is associated. The choice of using an effort source in series or a flow source in parallel with each resistance is purely one of convenience. Additional noise sources are added for the amplifier at its input [39] that represent the input-referred noise associated with internal transistors and resistors [149]. These characteristics are known apriori based on the choice of amplifier.

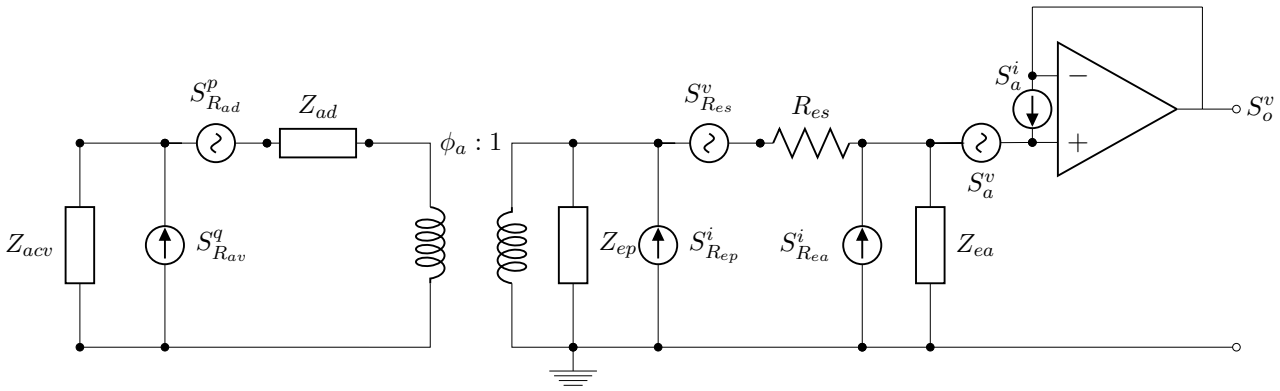

Figure 5-21. Noise model for the microphone with voltage amplifier circuitry.

Based on Figure 5-21, the output PSD [V^2/Hz] is

$$S^v_o = S^v_{o,R_{av}} + S^v_{o,R_{ad}} + S^v_{o,R_{ep}} + S^v_{o,R_{es}} + S^v_{o,R_{ea}} + S^v_{o,a}, \tag{5–58}$$

i.e. the summation of the output-referred noise of each individual source. From circuit analysis, the individual output noise contributions are

$$S^v_{o,R_{av}} = \left| \frac{Z_{acv}\phi_A}{(Z_{acv}+Z_{ad})\left(\frac{1}{Z_{ep}}+\frac{1}{Z_{ea}}+\frac{R_{es}}{Z_{ep}Z_{ea}}\right)+\phi_A^2\left(1+\frac{R_{es}}{Z_{ea}}\right)} \right|^2 \frac{4k_BT}{R_{av}}, \tag{5–59}$$

$$S^v_{o,R_{ad}+R_{a,rad}} = \left| \frac{\phi_A}{(Z_{acv}+Z_{ad})\left(\frac{1}{Z_{ep}}+\frac{1}{Z_{ea}}+\frac{R_{es}}{Z_{ep}Z_{ea}}\right)+\phi_A^2\left(1+\frac{R_{es}}{Z_{ea}}\right)} \right|^2 4k_BT\left(R_{ad}+R_{ad,rad}\right), \tag{5–60}$$

$$S^v_{o,R_{ep}} = \left| \frac{\left(Z_{eq}-R_{es}\right)Z_{ea}}{Z_{eq}+Z_{ea}} \right|^2 \frac{4k_BT}{R_{ep}}, \tag{5–61}$$

$$S^v_{o,R_{es}} = \left| \frac{Z_{ea}}{Z_{eq}+Z_{ea}} \right|^2 4k_BTR_{es}, \tag{5–62}$$

$$S^v_{o,R_{ea}} = \left| \frac{Z_{eq}Z_{ea}}{Z_{eq}+Z_{ea}} \right|^2 \frac{4k_BT}{R_{ea}}, \tag{5–63}$$

and

$$S^v_{o,amp} = \left| \frac{Z_{eq}Z_{ea}}{Z_{eq}+Z_{ea}} \right|^2 S^i_a + S^v_a. \tag{5–64}$$

Note in Equation 5–64 that the current noise S^i_a is multiplied by the parallel combination of the microphone output impedance Z_{eq} and Z_{ea}; low amplifier current noise is therefore very important for high impedance devices. The piezoelectric MEMS microphone, by virtue of its small expected capacitance, is just such a device.

Figure 5-22 shows a plot of output-referred noise contributions from each noise source, with R_{ea} neglected as established in Section 5.3.1. The same example geometry used for validation in Section 5.2.5 is used here. Amplifier noise characteristics were taken from the Linear Technologies LTC6240 amplifier, a low-noise amplifier with a 3 pF input capacitance and input-referred voltage and current noise floors of $7\,\mathrm{nV}/\sqrt{\mathrm{Hz}}$ and $0.56\,\mathrm{fA}/\sqrt{\mathrm{Hz}}$, respectively [44]. The noise associated with R_{ep} dominates at low frequencies until it gives way to amplifier current noise near 10 kHz. The voltage noise contribution, in this case, is well below the current noise contribution. Meanwhile, the combined acoustic noise contribution is completely insignificant compared to the electrical noise.

The noise associated with R_{ep} and the amplifier current noise are clearly dominant in the example of Figure 5-22. However, noise characteristics of different amplifiers are sufficiently variable that S^v_a also warrants continued inclusion in the noise model. Taking

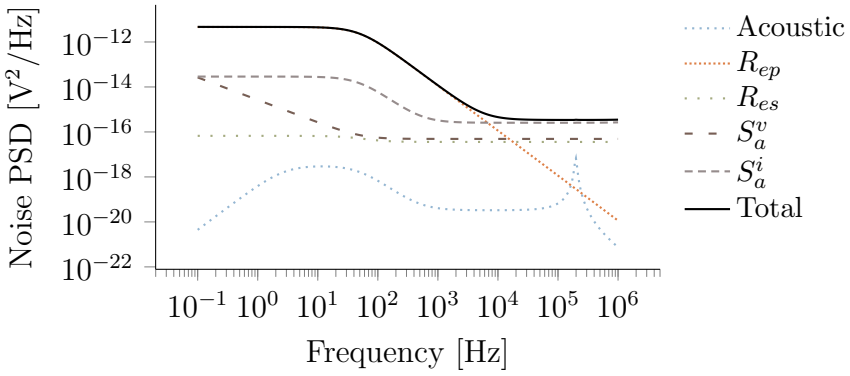

Figure 5-22. Output-referred noise floor for the microphone with a voltage amplifier.

just the noise associated with R_{ep} and the amplifier noise of the amplifier as dominant, the noise floor of the microphone with the voltage amplifier architecture can be approximated in the flatband as

$$S_o^v \approx \left(\frac{1}{\omega C_{et}}\right)^2 \left(S_a^i + \frac{4k_BT}{R_{ep}}\right) + S_a^v. \tag{5–65}$$

Note that per Figure 5-22, there is some error associated with Equation 5–65 in the current/voltage-noise dominant region, where the sum contribution of other noise sources becomes significant. Making use of Equations 2–11 and 5–46, the minimum detectable pressure is then

$$p_{min} \approx \sqrt{\int_{f_1}^{f_2} \frac{\left(\frac{1}{j\omega C_{et}}\right)^2 \left(S_a^i + \frac{4k_BT}{R_{ep}}\right) + S_a^v}{\left(\frac{C_{ef}+C_{eo}}{C_{et}} S_{oc}\right)^2} df}, \tag{5–66}$$

which after making use of Equation 5–35, becomes

$$p_{min} \approx \sqrt{\int_{f_1}^{f_2} \left[\frac{S_a^i + \frac{4k_BT}{R_{ep}}}{(\omega d_a)^2} + \frac{S_a^v C_{et}^2}{d_a^2}\right] df}. \tag{5–67}$$

Several important conclusions emerge from Equation 5–67. First, increasing d_a decreases p_{min}. This follows naturally from knowledge of the fact that increasing sensitivity decreases p_{min}, with $S_{oc} = -d_a/(C_{ef} + C_{eo})$ from Equation 5–35. Following this logic, the inverse relationship between S_{oc} and C_{ef} would also seem to suggest that a low capacitance device would yield a lower p_{min}. However, Equation 5–67 shows that this is

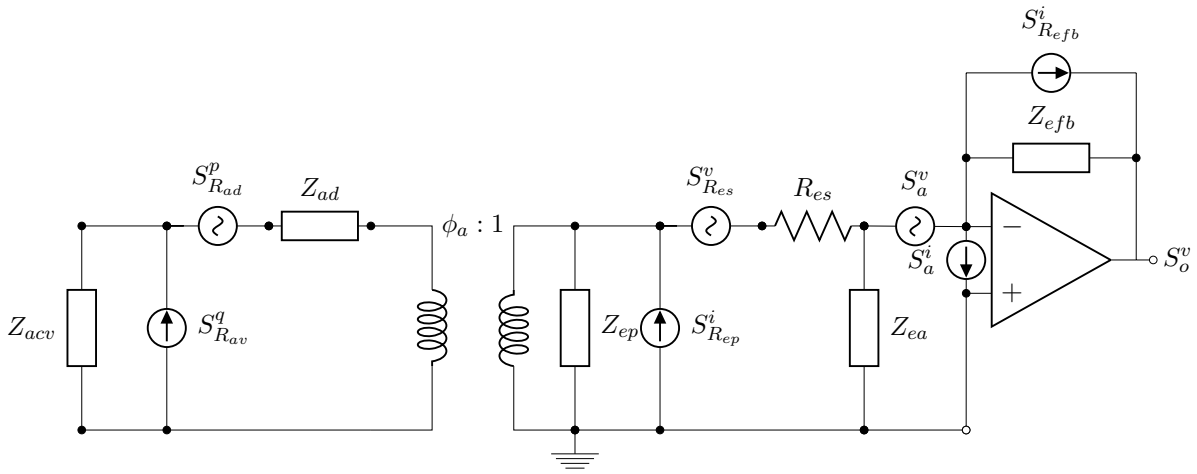

Figure 5-23. Noise model for the microphone with charge amplifier circuitry.

not always true; C_{ef} plays no role in the noise floor when the dominant contributors are R_{ep} and S^i_a. When the dominant contributor is S^v_a, a low total capacitance C_{et} is desirable. Finally, note that the first term rolls off as $1/\omega^2$; this results in attenuation of noise due to R_{ep} at high frequencies, but current noise PSD in amplifiers often increases as ω^2.

5.3.3.2 Noise model with charge amplifier

The noise model associated with the charge amplifier architecture is shown in Figure 5-23. From this model, the total output noise PSD is thus

$$S^v_o = S^v_{o,R_{av}} + S^v_{o,R_{ad}+R_{ad,rad}} + S^v_{o,R_{es}} + S^v_{o,R_{ep}} + S^v_{o,R_{efb}} + S^v_{o,amp}, \tag{5–68}$$

where the individual noise contributions are

$$S^v_{o,R_{av}} = \left| \frac{\phi_a Z_{acv} Z_{efb}}{(Z_{ad}+Z_{acv})\left(1+\frac{R_{es}}{Z_{ep}}\right)+\phi_a^2 R_{es}} \right|^2 \frac{4k_BT}{R_{av}}, \tag{5–69}$$

$$S^v_{o,R_{ad}} = \left| \frac{Z_{efb}\phi_a}{(Z_{ad}+Z_{acv})\left(1+\frac{R_{es}}{Z_{ep}}\right)+\phi_a^2 R_{es}} \right|^2 4k_BT(R_{ad}+R_{ad,rad}), \tag{5–70}$$

$$S^v_{o,R_{ep}} = \left| \frac{Z_{efb}\left(Z_{eq}-R_{es}\right)}{Z_{eq}} \right|^2 \frac{4k_BT}{R_{ep}}, \tag{5–71}$$

$$S^v_{o,R_{es}} = \left| \frac{Z_{efb}}{Z_{eq}} \right|^2 4k_BTR_{es}, \tag{5–72}$$

$$S^v_{o,R_{efb}} = |Z_{efb}|^2 \frac{4k_B T}{R_{efb}}, \tag{5–73}$$

and

$$S^v_{o,amp} = \left|1 + \frac{Z_{efb}}{Z_{eq} \parallel Z_{ea}}\right|^2 S^v_{amp} + |Z_{efb}|^2 S^i_{amp}, \tag{5–74}$$

where recall Z_{eq} is the electrical impedance of the microphone, introduced in Section 5.2.4. Clearly, one important conclusion from the noise model is that Z_{efb} figures prominently in each of Equations 5–68 to 5–74. In addition, only the voltage noise is impacted by the presence of parasitics.

Individual noise sources associated with the microphone and charge amplifier architecture are shown in Figure 5-24. The example amplifier was taken as the Texas Instruments OPA129, with an assumed input capacitance of 3 pF and manufacturer-supplied input-referred voltage and current noise floors of $15\,\text{nV}/\sqrt{\text{Hz}}$ and $0.1\,\text{fA}/\sqrt{\text{Hz}}$, respectively. The feedback impedances were chosen as $C_{efb} = C_{ef} + C_{eo} \approx 8\,\text{pF}$ (unity gain) and $R_{fb} = 2\,\text{G}\Omega$ (cut-off at 10 Hz). With this configuration, the dominant noise source is again seen to be R_{ep} at low frequencies, while amplifier voltage noise dominates beyond the corner frequency at approximately 10 kHz. The feedback resistance R_{efb} also shows potential of contributing if chosen as a lower value. Again, the acoustic noise is inconsequential.

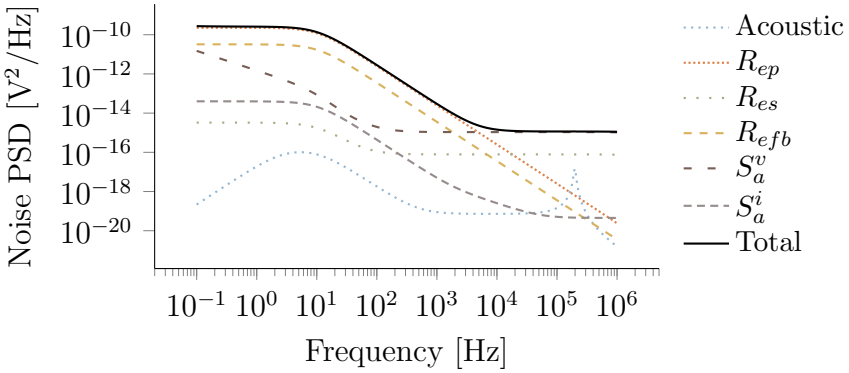

Figure 5-24. Output-referred noise floor for the microphone with charge amplifier.

Much latitude exists in the selection of R_{efb}, and the amplifier, so noise associated with each of them, together with the ever-dominant noise source R_{ep}, are included in

simplifications to the overall noise floor. In the flatband, S_o^v simplifies to

$$S_o^v \approx \left(1 + \frac{C_{et}}{C_{efb}}\right)^2 S_a^v + \left(\frac{1}{\omega C_{efb}}\right)^2 \left[S_a^i + 4k_B T \left(\frac{1}{R_{ep}} + \frac{1}{R_{efb}}\right)\right]. \tag{5–75}$$

Note from this equation that the resistor noise can be viewed as originating from an equivalent resistor, $R_{ep} \parallel R_{efb}$. The minimum detectable pressure then follows, after some simplification, as

$$p_{min} \approx \sqrt{\int_{f_1}^{f_2} \left[\frac{S_a^i + 4k_B T \left(\frac{1}{R_{ep}} + \frac{1}{R_{efb}}\right)}{(\omega d_a)^2} + \frac{(C_{efb} + C_{et})^2 S_a^v}{d_a^2}\right] df}. \tag{5–76}$$

Again, increasing d_a decreases p_{min}. Although parasitics do not impact the sensitivity in the charge amplifier case, Equation 5–76 shows that they still tend to increase p_{min} when S_a^v is important. The term containing S_a^i and $R_{ep} \parallel R_{efb}$ rolls-off as $1/\omega^2$, but again, S_a^i tends to increase as ω^2.

5.3.4 Selection

Table 5-2 contains a summary of the two main performance characteristics of the microphone and interface circuitry addressed in Sections 5.3.1 to 5.3.3: sensitivity and minimum detectable pressure. In the voltage amplifier case, the theoretical open-circuit sensitivity is always attenuated by parasitic capacitances, while in the charge amplifier case the sensitivity is not affected by parasitics. In the charge amplifier case, a designer has latitude to attenuate or gain the sensitivity via the choice of feedback capacitor as well.

Table 5-2. Comparison of voltage and charge amplifier topologies for use with a piezoelectric microphone.

	Sensitivity (S)	Minimum detectable pressure (p_{min})
Voltage Amplifier	$\frac{C_{ef}}{C_{et}} S_{oc}$	$\sqrt{\int_{f_1}^{f_2} \left[\frac{S_a^i + \frac{4k_B T}{R_{ep}}}{(\omega d_a)^2} + \frac{S_a^v C_{et}^2}{d_a^2}\right] df}$
Charge Amplifier	$-\frac{C_{ef}}{C_{efb}} S_{oc}$	$\sqrt{\int_{f_1}^{f_2} \left[\frac{S_a^i + 4k_B T \left(\frac{1}{R_{ep}} + \frac{1}{R_{efb}}\right)}{(\omega d_a)^2} + \frac{\left(C_{efb} + C_{et}\right)^2 S_a^v}{d_a^2}\right] df}$

Comparing the minimum detectable pressures for the two amplifier configurations term-by-term, the amplifier current noise contribution is seen to be the same for both, assuming both amplifiers have equivalent current noise characteristics. At best, the additional noise from the bias resistor in the charge amp case can be mitigated by choosing $R_{efb} \gg R_{ep}$. The final voltage noise term is where the two are truly differentiated; assuming equivalent amplifier voltage noise in both configurations, the total contribution to the minimum detectable pressure from the charge amp circuit will always be higher due to the appearance of C_{efb} in the numerator.

For a microphone with very high gain ($C_{efb} \ll C_{ef}$), the added voltage noise of the charge amp can be minimized, but C_{efb} cannot be decreased without bound. The feedback impedance introduces an additional cut-on frequency, $f_c = 1/2\pi R_{efb} C_{efb}$. As C_{efb} decreases, f_c increases and the bandwidth of the microphone can be reduced. Compensating with a larger R_{efb} is not always straightforward [149]. There is thus a delicate balance between gain, cut-off, and noise in the charge amplifier architecture.

The primary advantage of charge amplifiers is that the microphone sensitivity is not dependent on parasitic capacitance. Parasitic capacitance is introduced, for example, by wire bonds, traces, or cables between the sensor and the interface electronics. Charge amplifiers, then, are popular because they can be located remotely from the actual sensor; changes in cable or trace lengths (and the associated change in parasitic capacitance) do not affect the sensitivity or require subsequent recalibration [146]. Meanwhile, a voltage amplifier must be located close to the sensor to minimize the attenuation in sensitivity.

Deploying thousands of microphones on the exterior of an aircraft demands the utmost in simplicity. Collocating the microphone and signal conditioning circuitry in a single package yields a compact and complete sensor system that can be connected directly to a DAQ without regard for additional circuitry. Even in the laboratory setting, the amplifier may be located in close proximity to the microphone. The voltage amplifier

is the appropriate choice for such a case. In addition, the relative simplicity of the voltage amplifier configuration, with its low part count and fewer trade-offs to assess, is attractive.

As a result, the voltage amplifier was chosen as the interface circuit for this study. The majority of measurements presented in Chapter 8 are specific to the voltage amplifier case. Measurements for one microphone instrumented with a charge amplifier — for comparison of sensitivity and to estimate parasitic capacitances — are presented in Section 8.2.4.3.

5.4 Summary

In this chapter, models for the performance of a piezoelectric microphone have been developed, including a lumped element model, a diaphragm mechanical model, and noise models. In the next chapter, the developed models are used in a structural optimization formulation to determine the geometry that delivers optimal microphone performance.

CHAPTER 6
OPTIMIZATION

This chapter is concerned with choosing microphone dimensions within constraints such that the "best" performance is obtained; this process is known as optimization [150]. The lumped element model developed in Chapter 5 provides predictions of microphone performance and aids intuitive understanding of design tradeoffs. The intuitive selection of a "best" design in the presence of many design variables and constraints, however, is difficult. The low computational cost associated with the lumped element model makes it ideally suited for integration with an optimization algorithm that systematically identifies the "best" design. In this chapter, an overview of the design optimization problem is first given, including discussion of geometric dimensions available for selection and performance characteristics to be extremized. Next, the optimization problem is formally defined and the approach for solving it is outlined. Finally, the results of the optimization process are discussed.

6.1 Design Overview

6.1.1 Design Variables

The use of a commercial foundry process to fabricate devices leverages significant engineering investment but also places constraints on available geometries. With a compatible geometry established, an important early step in the design process is thus identification of design variables. Figure 6-1 shows a cross-sectional view of the piezoelectric microphone — as dictated by the film bulk acoustic resonator (FBAR) variant process discussed at length in Section 4.2 — with important dimensions labeled.

Free dimensions may serve as design variables for the structural optimization problem, while fixed dimensions, denoted in Figure 6-1 with a ⧋ symbol, may not. The cavity depth d_c is set by the wafer thickness. The diaphragm overlap Δa_0 and undercut Δa_c are standard features of the FBAR-variant fabrication process, as is the passivation

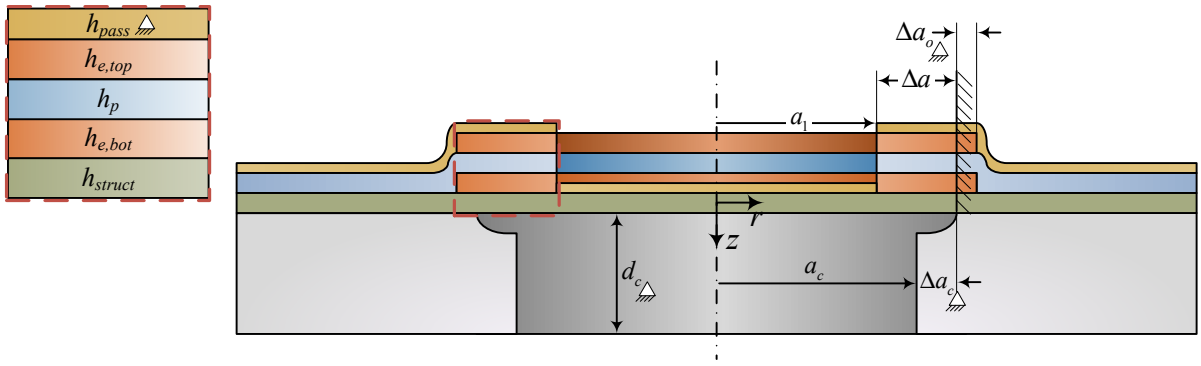

Figure 6-1. Cross-section of the piezoelectric microphone with notable dimensions to be considered; those denoted with ⧋ are fixed by the fabrication process.

layer thickness h_{pass}. The values associated with these fixed dimensions and others not shown in Figure 6-1 are collected in Table 6-1.

Table 6-1. Microphone dimensions fixed by the fabrication process.

Dimension	Value μm	Description
Δa_o	3	Width of diaphragm overhang
Δa_c	35	Width of diaphragm undercut
h_{pass}	0.14	Thickness of passivation layer
d_c	500	Cavity depth
L_v	50	Vent length
h_v	2	Vent height
b_v	25	Vent width

Meanwhile, several "free" dimensions remain whose values may be selected within bounds established by the fabrication process, including the film thicknesses and diaphragm radii. There are thus 7 design variables in total: the inner radius, a_1; the width of the annular piezoelectric film stack, Δa; and the film thicknesses associated with the top electrode, piezoelectric, bottom electrode, and structure layers, $h_{e,top}$, h_p, $h_{e,bot}$, and h_{struct}, respectively. The dimension Δa is used in place of a_2 to specify the outer radius of the diaphragm (i.e. $a_2 = a_1 + \Delta a$) because it makes selection of the two dimensions independent; using a_2 as a design variable requires enforcement of the condition $a_2 \geq a_1$. Note also that the cavity radius a_c is set by selection of the diaphragm

radii, as from Figure 6-1,

$$a_c = a_1 + \Delta a - \Delta a_c. \tag{6–1}$$

6.1.2 Objective

The extremization of a performance measure subject to certain constraints is the purpose of optimization. Determining an optimal design first requires the appropriate measure(s) of what constitutes "best" performance — called the objective function(s) — to be identified. The concept of the operational "space" in the frequency and pressure domains was introduced in Chapter 2 in terms of the microphone bandwidth and dynamic range. Maximizing this "space" subject to the needs of the particular application is one way of approaching microphone design. At minimum, a MEMS piezoelectric microphone design must be identified that precisely meets all sponsor performance specifications (Section 1.2). The first question to be answered in the optimization process is thus whether or not the specified performance is achievable within the design space established by the fabrication process, base geometry, material choices, etc. Beyond that, the questions to be answered are whether performance can be improved beyond the given specifications and what additional performance gains are most beneficial.

Microphone bandwidth exceeding the audio range (20 Hz–20 kHz) is not beneficial in any full-scale aeroacoustic measurement application, including the fuselage array application. Although additional bandwidth could enable the microphone to be leveraged to model-scale applications, examining the design trade-offs for full-scale and model-scale measurements was not a focus of this study. Exceeding the specified dynamic range, meanwhile, has an obvious benefit in the target fuselage array application: lowering MDP improves measurement resolution.[1] In addition to improving performance in the target application, exceeding specifications on MDP could enable the microphone to be leveraged

[1] Lowering MDP improves measurement resolution up to the limits of the associated data acquisition system.

directly to other full-scale applications, such as flyover arrays. Minimum detectable signal in general has been established as a key comparative figure of merit for sensors [151, 152].

Exceeding the specified maximum pressure level of 172 dB — the highest pressure level of practical interest in aeroacoustic measurements of aircraft — does not yield similar benefits. However, the design trade-off between the specified PMAX and obtainable MDP is of fundamental importance for the present design effort; in the event that specified performance for these two quantities is not achievable, knowledge of the trade-offs drives specification revisions or design space modifications. To study the trade-offs, extremization of both MDP and PMAX were taken as optimization objectives. The resulting optimization formulation is known as a *multicriteria* or *multiobjective* optimization [150, 153].

Due to competition among objective functions, multiobjective optimization problems are characterized by the non-existence of a unique solution. For example, any number of minimum values for MDP may be achievable given sacrifices in the maximum attainable value of PMAX. Without a decision-maker to express preference, a set of mathematically equivalent solutions known as the Pareto-optimal set emerges [153]. A solution is said to be *Pareto optimal* if the selection of any other set of design variable values results in all objective functions remaining unchanged or at least one getting "worse" [150]. An example of a set of Pareto-optimal solutions — often called a *Pareto front* — is shown in Figure 6-2, where maximization of PMAX and minimization of MDP are taken as the two objectives. In this figure, designs A, B, and C are Pareto-optimal but D is not. Similarly, Papila et al. (2006) [152] found Pareto-optimal solutions associated with simultaneous maximization of sensitivity and minimization of electronic noise for a piezoresistive microphone.

Algorithms exist for finding the set of Pareto-optimal solutions directly [153, 154]. However, more commonly-available single-objective optimization software tools may be used to find the Pareto front via solution of a sequence of constrained single-objective

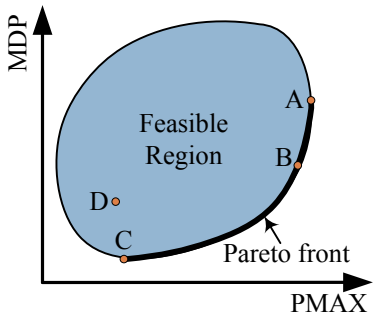

Figure 6-2. Pareto front example.

problems. Using this approach, one objective is extremized while the other is treated as a constraint [150]. The constraint is varied over a range of values until the Pareto front is resolved. This is known as the ε-constraint method [153] and is used in the optimization approach for the piezoelectric microphone, discussed further in Section 6.3.

6.2 Formulation

In this section, the optimization problem is formalized. The objective function, design variables, bounds, and constraints are all defined and discussed.

The objective of the optimization is

$$\min_{\boldsymbol{X}} f_{obj}\left(\boldsymbol{X}\right) = \text{MDP}, \tag{6–2}$$

where the narrow-band definition of MDP is selected for this study, i.e. MDP evaluated for a 1 Hz bin width centered at 1 kHz. The associated design variables are

$$\boldsymbol{X} = \{a_1, \Delta a, h_{etop}, h_p, h_{ebot}, h_{struct}\} \tag{6–3}$$

subject to bounds (or side constraints)

$$\boldsymbol{LB} \leq \boldsymbol{X} \leq \boldsymbol{UB}. \tag{6–4}$$

Specific values of $\boldsymbol{LB}$ and $\boldsymbol{UB}$ set by the FBAR-variant process are found in Table 6-2.

Geometrical, fabrication, modeling, and performance constraints are all present in the optimization problem. Many fabrication constraints are reflected in the bounds placed on

Table 6-2. Design variable bounds.

$\boldsymbol{X}$	$\boldsymbol{LB}$ [μm]	$\boldsymbol{UB}$ [μm]
a_1	5	600
Δa	5	600
$h_{e,top}$	0.1	0.2
h_p	0.3	1
$h_{e,bot}$	0.2	0.6
h_{struct}	1	2

each design variable, while other constraints are dependent on multiple design variables. These are classified as linear or nonlinear constraints depending on their functional dependence on the design variables. There are 3 linear constraints and 1 nonlinear constraint. The constraints are:

1. The microphone diaphragm must be sufficiently thin such that the Kirchhoff plate theory used in the diaphragm mechanical model remains applicable. The thinness of the diaphragm was quantified via the aspect ratio, AR (a/h), for both the inner $(0 \leq r \leq a_1)$ and outer $(a_1 \leq r \leq a_1 + \Delta a)$ regions of the diaphragm. The constraints are
$$a_1 \geq AR\,(h_{pass} + h_{struct}) \tag{6–5}$$
and
$$\Delta a \geq AR\,(h_{pass} + h_{e,top} + h_p + h_{e,bot} + h_{struct})\,. \tag{6–6}$$
AR was chosen to be 10 [121].[2]

2. A fabrication constraint on the maximum radius was more restrictive than the sensing element size requirement of Section 1.2:
$$a_1 + \Delta a \leq 600\,\mu\text{m}. \tag{6–7}$$

3. A fabrication constraint was also placed on the minimum radius:
$$a_1 + \Delta a \geq 250\,\mu\text{m}. \tag{6–8}$$

4. The sole nonlinear constraint was on the maximum pressure; the pressure at which total harmonic distortion (THD) reached 3% was required to meet or exceed 172 dB

[2] A plate is generally defined as "a structural element with planform dimensions that are large compared to its thickness" [121]. The specific minimum relationship between these dimensions is not precisely prescribed, though aspect ratios of 10–20 are commonly cited [37, 121].

per the design objectives in Section 1.2. With a computationally efficient prediction method for total harmonic distortion of the microphone unavailable, a constraint on static nonlinearity of the diaphragm was used instead. For the maximum pressure p_{max}, the total center deflection of the diaphragm predicted using the linear and nonlinear models (see Appendix A) was restricted to be $\leq 3\,\%$, i.e.

$$\left| \frac{w_{0,l} - w_{0,nl}}{w_{0,nl}} \right|_{p=p_{\max}} \leq 0.03, \tag{6–9}$$

where subscript $\square_l$ indicates the linear model and subscript $\square_{nl}$ indicates the nonlinear model. Although the quality of this measure of nonlinearity as a prediction for THD was unknown, intuition suggested that THD would trend similarly. Uncertainty in the constraint was partially addressed in the optimization approach, discussed in Section 6.3.

Note that no constraints on bandwidth were defined in order to meet the $f_{\pm 2\,\mathrm{dB}}$ targets set out in Chapter 1. Microphones designed for high p_{max} are necessarily stiff with high resonant frequencies, so it was not anticipated that satisfying $f_{+2\,\mathrm{dB}} \geq 20\,\mathrm{kHz}$ would be an issue. No constraint was placed on $f_{-2\,\mathrm{dB}}$ (i.e. $f_{-2\,\mathrm{dB}} \leq 20\,\mathrm{Hz}$) out of concern that unreliable predictions for this quantity, dominated by either the $R_{ep}C_{eb}$ or $R_{av}C_{ac}$ break frequencies, would drive the optimization. At the time of the optimization, predictions of R_{ep} were based on impedance measurements of early prototype devices, but there was little confidence in the measurement quality. Meanwhile, the R_{av} prediction was reliant on assumptions almost certain to not be satisfied, for example fully-developed flow in the vent channel. With the vent geometry set, enforcing $f_{-2\,\mathrm{dB}} \geq 20\,\mathrm{Hz}$ would lead the optimization algorithm to increase the $R_{av}C_{ac}$ product via enlarging the cavity radius, which by Equation 6–1 would lead to bigger diaphragms with lower stiffness and lower achievable p_{max}. Despite the lack of bandwidth constraints, the bandwidth of the optimal sensor was assessed for adherence to the design requirements following the optimization.

6.3 Approach

The optimization problem defined in Section 6.2 is a single-objective problem with both linear and nonlinear constraints. It was solved using the `fmincon` function in MATLAB, which is applicable to nonlinear constrained optimization problems. This

function uses a sequential quadratic programming (SQP) method [138] and thus is a local optimizer [155]. In implementing the optimization using `fmincon`, the constraints were written as $\leq$ inequalities and normalized to be of $O(1)$. Similarly, the design variables were scaled via their bounds to vary over $[0, 1]$.

The optimization approach using the ε-constraint method is shown in Figure 6-3. First, a starting value of PMAX was established and the optimization was run. With a feasible solution found, results were saved. PMAX was then incremented and the process repeated until a feasible solution was no longer available. Using a starting PMAX value of 160 dB with incrementation of 0.5 dB, the Pareto front was obtained for values of PMAX leading up to and beyond the target value of 172 dB. A major advantage to this approach was the ability to assess the sensitivity of MDP to uncertainty in PMAX, given aforementioned uncertainty in the closeness of the relationship between the 3% static nonlinearity constraint and the actual 3% distortion limit.

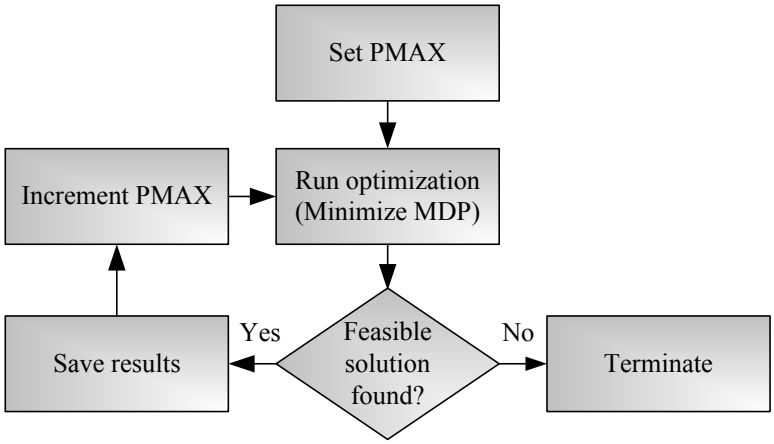

Figure 6-3. Optimization approach.

The values of constants used in the optimization are found in Table 6-3, target residual stresses supplied by Avago Technologies for each of the thin films are found in Table 6-4, and thin-film material properties are located in Appendix D. In Table 6-3, the damping ratio ζ was estimated from a similar piezoelectric device developed by Horowitz [119]. The value of the piezoelectric resistivity ρ_p and series resistance R_{es} came from

mean impedance measurements of several prototype microphones. The bias resistor R_{ea} was disregarded because early experiments showed that it was unnecessary for stable operation of the piezoelectric microphone with voltage amplifier. The amplifier input capacitance C_{ea} and noise characteristics S_a^v and S_a^i were all obtained from the datasheet for the chosen amplifier, the LTC6240 [44]. The residual stress characteristics of the thin-film stack found in Table 6-4 emerged from significant process development efforts at Avago Technologies, and the information was leveraged in the optimization to enhance model predictions.

Table 6-3. Constant values used in the optimization.

Parameter	Value
ζ [119]	0.03
R_{es}	$4.14\,\mathrm{k\Omega}$
ρ_p	$22.8\,\mathrm{M\Omega\,m}$
R_{ea}	∞
C_{ea} [44]	$3\,\mathrm{pF}$
S_a^v [44]	$\left(\frac{7950\,\mathrm{Hz}}{f} + 49\right)\mathrm{nV^2/Hz}^\dagger$
S_a^i [44]	$\left(\frac{1.27\times10^{-6}}{\mathrm{Hz^2}} f^2 - \frac{4.85\times10^{-5}}{\mathrm{Hz}} f + 0.354\right)\mathrm{fA^2/Hz}^\dagger$

† Curve fit to data in [44]

Table 6-4. Target thin-film residual stresses.

Layer	Residual Stress [MPa]
Passivation	−50
Top Electrode	−150
Piezoelectric	0
Bottom Electrode	−100
Structural	55

6.4 Results and Discussion

The optimization using the ε-constraint method yielded the Pareto front shown in Figure 6-4. In order to increase the effective piezoelectric coefficient, the general trend of the optimization algorithm is to increase the diaphragm outer radius $(a_1 + \Delta a)$ as much

as possible (while making minor changes to the percentage piezoelectric coverage, $\Delta a/a_1$) until the nonlinearity constraint becomes active. For PMAX $\leq$ 165 dB, the maximum radius constraint is activated and the optimization algorithm loses its primary method of reducing MDP. As a result, the attainable minimum values of MDP are seen to be less sensitive to the specified value of PMAX in this regime. Meanwhile, the relationship between PMAX and MDP is seemingly linear for PMAX $\geq$ 165 dB, indicating a power law relationship between p_{max} and p_{min}. Note that no feasible solutions were found for PMAX>174 dB, beyond which the minimum diaphragm radius constraint activates.

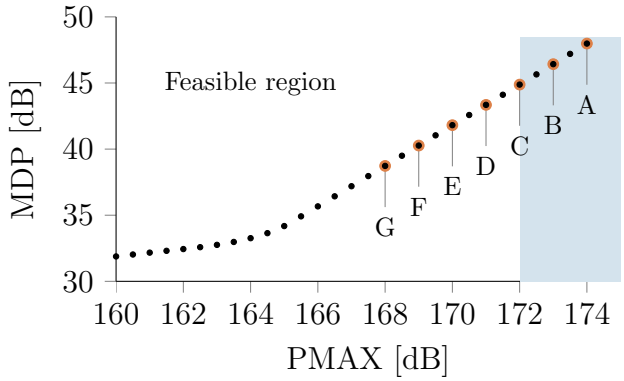

Figure 6-4. Pareto front associated with minimization of MDP and maximization of PMAX. The shaded region indicates the target design space.

Designs selected for fabrication are indicated with labels A–G in Figure 6-4. Designs A–C satisfied the design criteria — with PMAX$\geq$172 dB and MDP$\leq$48.5 dB — and were thus obvious choices. With the possibility that the static nonlinearity constraint was a conservative prediction for total harmonic distortion, designs D–G, which did not reach the PMAX=172 dB target, were also selected in order to provide the possibility of meeting the PMAX target with superior MDP compared to designs A–C. All of the selected designs featured the same optimal film thicknesses and thus were able to be fabricated together on a single wafer, eliminating the need for secondary optimization to constrain the designs to a single set of film thicknesses. When this additional step is required, performance is inevitably sacrificed for a subset of designs.

Figure 6-5 shows values for the optimal design variable values, X_i^* (* signifying "optimal"), normalized to [0,1] via their individual bounds and plotted versus PMAX. Both electrode thicknesses and the thickness of the piezoelectric layer were constant for all designs, and the structural layer thickness was nearly so. In the low PMAX regime in which the maximum radius constraint was active, the optimizer turns to reduction of h_{struct} to reduce diaphragm stiffness and increase d_a. In general, the optimization algorithm pushes the film thicknesses to their upper and lower bounds to tune the residual stress state such that the PMAX constraint is satisfiable. Both a_1 and Δa were held relatively constant for PMAX$\leq$165 dB since they could not be made bigger; for PMAX$>$165 dB, the maximum radius constraint deactivates and the optimization algorithm continuously reduces the diaphragm radius a_1 to stiffen the diaphragm.

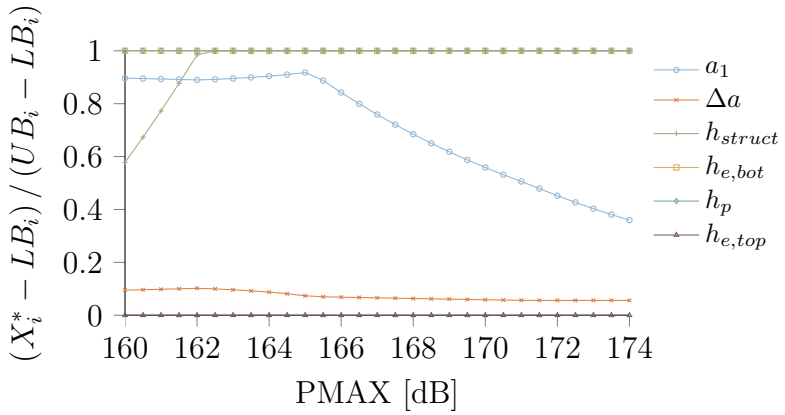

Figure 6-5. Normalized design variable values for each optimization performed, plotted against PMAX.

The common film thicknesses shared by the chosen designs are collected in Table 6-5 and the radial dimensions (rounded to the nearest μm) and performance characteristics of designs A–G are collected in Table 6-6. Designs A–C corresponding to PMAX of 174–172 dB were subject to the thinness constraint in the outer region, which dictated that Δa equal AR times the total thickness. Performing the optimizations after disabling this constraint yielded no better than 0.1 dB improvement in MDP, so it was not a significant performance-limiting factor.

Table 6-5. Optimal layer thicknesses.

Symbol	Value [μm]
h_{pass}	0.14[†]
$h_{e,top}$	0.1[‡]
h_p	1[§]
$h_{e,bot}$	0.6[§]
h_{struct}	2[§]

[†] Fixed [‡] At lower bound [§] At upper bound

Table 6-6. Optimization results.

	Design						
	A	B	C	D	E	F	G
PMAX [dB]	174	173	172	171	170	169	168
a_1[μm][†]	219	245	274	306	338	373	412
Δa [μm][†]	38[‡]	38[‡]	38[‡]	39	40	41	43
MDP [dB]	48.1	46.5	45.0	43.3	41.8	40.3	38.7
$f_{-2\,\mathrm{dB}}$ [Hz]	64	66	68	71	73	75	78
$f_{+2\,\mathrm{dB}}$ [kHz]	129	113	100	89	80	72	65
S_{oc} [dB re 1 V/Pa]	−88.8	−87.7	−86.6	−85.5	−84.5	−83.5	−82.5
S_{va} [dB re 1 V/Pa]	−92.4	−91.0	−89.6	−88.2	−87.0	−85.8	−84.5

[†] Rounded to the nearest μm [‡] AR constraint active

With no constraint placed on $f_{-2\,\mathrm{dB}}$, this metric did exceed 20 Hz for all of the selected designs. Further investigation revealed that it was dominated by R_{ep} rather than R_{av}. Only about 0.25 % of the total desired bandwidth did not meet specifications; given aforementioned uncertainty in R_{ep}, it was decided to go ahead with fabrication. Meanwhile, $f_{+2\,\mathrm{dB}}$ was well above 20 kHz as expected, and designs A–D were predicted to possess sufficient bandwidth for potential leveraging of the microphones to model-scale applications.

Analyzing the sensitivity of MDP and PMAX to perturbations in design variables or other inputs yields additional insight into the results. Figure 6-6 shows how perturbing

optimal dimensions associated with design C by ±10 % affected MDP.[3] The most important design variables were a_1 and Δa, for which a 10 % variation yielded approximately 1–1.5 dB change in MDP.

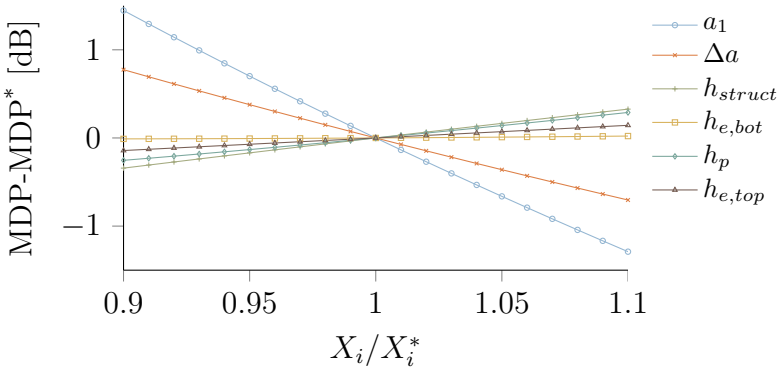

Figure 6-6. Sensitivity of MDP to ±10 % perturbations in the design variables for Design C. The x and y axes are referenced to the values of the design variables and MDP, respectively, at the optimal solution.

Similarly, Figure 6-7 shows the sensitivity of PMAX to perturbations in the optimal dimensions for design C.[3] PMAX is seen to be more sensitive to the design variables, most notably h_{struct}, a_1, and Δa in that order. PMAX is particularly sensitive to h_{struct} because the thick structural layer, with its tensile stress, plays a major role in setting the overall state of in-plane stress. Comparing Figures 6-6 and 6-7, it is seen that increasing h_{struct} 10 % beyond its optimal value yields nearly a 1 dB improvement in PMAX with only a 0.3 dB penalty in MDP. The calculus of modifying any of the other design variables is not as attractive, indicating that the 2 μm upper bound on h_{struct} is a significant performance-inhibitor.

Microphone performance metrics are also sensitive to uncertainty in model inputs, most notably those for in-plane stress. To study this sensitivity, a Monte Carlo simulation was performed in which the stresses were perturbed about their target values using

[3] Given the linear nature of Figure 6-6 and Figure 6-7, the sensitivities also could have been characterized directly via logarithmic derivatives [150, 152].

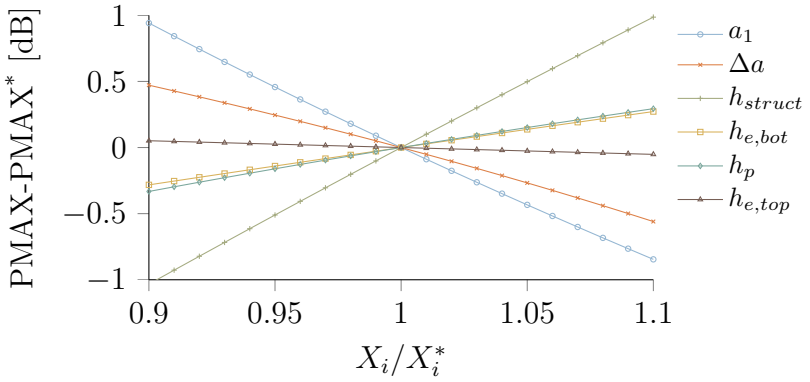

Figure 6-7. Sensitivity of PMAX to ±10 % perturbations in the design variables for Design C. The x and y axes are referenced to the values of the design variables and PMAX, respectively, at the optimal solution.

statistics supplied by Avago Technologies. The analysis was completed for the MDP of design C and results are shown in Figure 6-8. The simulation mean agreed with the predicted value of 45 dB, and the 95% confidence interval was calculated to be 45.2 dB to 46.7 dB. A similar analysis could not be completed for PMAX because of failures in the iterative nonlinear solver for a large percentage of stress values encountered during the Monte Carlo iterations.

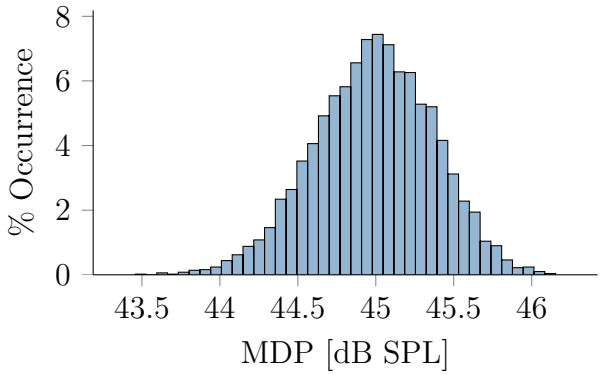

Figure 6-8. Sensitivity of MDP to in-plane stress variations for Design C, obtained via Monte Carlo simulation.

6.5 Summary

In this chapter, the problem of optimizing the performance of the piezoelectric microphone in terms of dynamic range (MDP and PMAX) was defined and executed.

Seven designs (A–G) were selected for fabrication, with 3 (A–C) meeting or exceeding requirements on MDP and PMAX. Optimization trends and the sensitivity of both MDP and PMAX to perturbations in the design variables were also discussed. The next chapter addresses the realization of these microphone designs and packaging of the microphones for experimental characterization.

CHAPTER 7
REALIZATION AND PACKAGING

This chapter focuses on the realization of individually packaged piezoelectric microphones, bridging the gap between the theoretical designs of Chapter 6 and experimental characterization in Chapter 8. First, the results of the fabrication process performed at Avago Technologies are discussed. Next, the method developed to separate the microphone die is explained. Finally, the laboratory test package developed specifically for the piezoelectric microphones is described.

7.1 Realization

This section focuses on realization of the piezoelectric microphones. The as-fabricated microphone geometries are explicitly given and fabrication results are discussed.

7.1.1 Geometry

Optimal piezoelectric microphone geometries were found in Chapter 6. From those results, seven different geometries covering a swath of design space were submitted for fabrication. With expected uncertainties in model predictions and film stress targeting, fabrication of multiple microphone geometries was judged to provide the most probable, cost-sensitive, and schedule-effective path to meeting performance specifications. The diaphragm dimensions for designs labeled A-G (in order of increasing diameter) are found in Table 7-1 and their common film thickness and stress targets are in Table 7-2. After the fabrication lot was started, Avago suggested based on recent experience that the top electrode thickness $h_{e,top}$ be changed from 0.1 μm to 0.15 μm. The models confirmed that sensitivity of MDP and PMAX to this design variable was low (recall Figures 6-6 and 6-7). It was thus decided to accept the change in $h_{e,top}$, which is reflected in Table 7-2.

7.1.2 Fabrication Results

Fabrication was performed at Avago Technologies using a variant of their film bulk acoustic resonator (FBAR) process [82, 83, 105]. The fabrication process was addressed

Table 7-1. Design dimensions.

Design	a_1 [μm]	Δa [μm]	a_2 [μm]
A	219	38	257
B	245	38	283
C	274	38	312
D	306	39	345
E	338	40	378
F	373	41	414
G	412	43	455

Table 7-2. Film properties.

Layer	Thickness [μm]	Stress Target [MPa]
Structural Layer	2	55
Bottom Mo	0.6	0
AlN	1	0
Top Mo	0.15	-150
Passivation	0.14	-50

in Section 4.2. A photograph of a completed wafer is found in Figure 7-1. In all, Avago Technologies delivered eight 6" wafers with microphone die 2 mm on a side.

Avago Technologies provided the wafers with film stress information. After each film deposition, wafer curvature was measured with a Tencor Flexus FLX 5400 and the film stress was estimated from these measurements using Stoney's Formula [107, 108, 156],

$$\sigma = \frac{E_s t_s^2}{6 t_f (1-\nu)} \left(\frac{1}{R} - \frac{1}{R_0} \right), \tag{7–1}$$

where σ is the film stress, E_s, ν, and t_s are the Young's Modulus, Poisson's Ratio, and thickness of the substrate, respectively, t_f is the film thickness, and R_0 and R are the radii of curvature before and after film deposition, respectively. Stoney's Formula is a wafer-level stress estimation that relies on a number of assumptions that may be only approximately valid, such as transverse isotropy of the substrate, uniform film thickness, and homogeneous stress, among others [107]. Despite the caveats, these estimates represented the best-available film stress information.

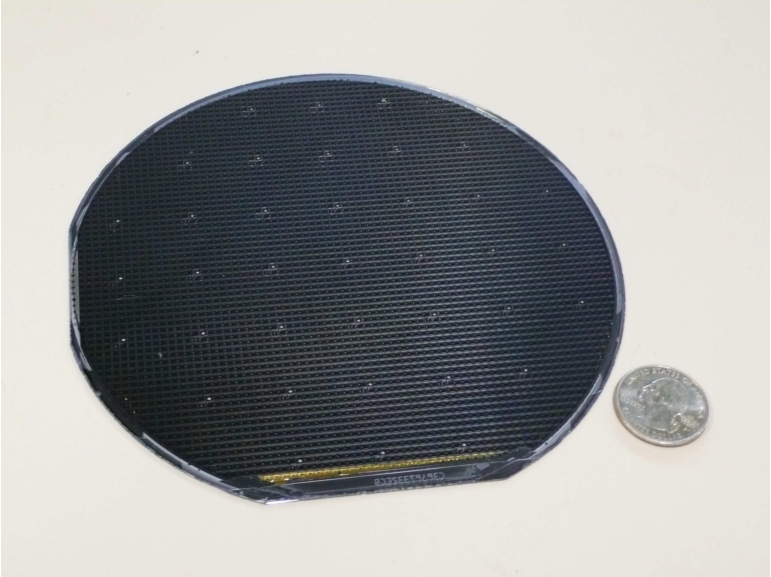

Figure 7-1. Wafer of piezoelectric microphones fabricated at Avago Technologies.

Experimental results in Chapter 8 are presented for devices from two wafers, identified as numbers 116 and 138. Stress data provided was utilized to predict microphone performance for comparison to characterized devices in Chapter 8. Devices from wafer 116 were visibly buckled. None of the wafers displayed any obvious visual signs of large cross-wafer stress variations.

7.2 Dicing

Processes for dicing fragile MEMS vary and are highly dependent on whether or not they require direct contact with the environment. MEMS accelerometers or oscillators, for example, can be encapsulated at the wafer level such that they are protected during dicing. Unfortunately, MEMS microphones must be exposed to the medium of acoustic propagation and thus do not share this luxury. In a traditional dicing saw operation, the fragile thin-film diaphragms can be damaged by vibration, debris, or water penetration. Methods exist to shepherd exposed MEMS structures through the dicing process, including the use of patterned or releasable tapes [43], temporary bonding to a handle wafer, delaying the release etch until after dicing [107], or choosing "clean" dicing methods

such as scribe/break [157] or laser cutting [158]. In this section, an in-house process for dicing the microphone die using protective tape is described.

7.2.1 Dicing Process

The most advanced dicing option available at UF's Nanoscale Research Facility is an ADT 7100 Dicing Saw, which uses a physical blade and associated jet of deionized water for cooling and debris removal. Figure 7-2 shows the blade dicing a wafer sample, with the water jet impinging on the sample opposite the cutting direction. Protection of the mic diaphragms is thus a necessity, but any substance used to protect the devices must be easily removable post-dice without damaging the diaphragms. Protective tapes, such as UV tape or thermal release tape are sound options. In the process described herein, Nitto Denko REVALPHA thermal release tape (No. 3198M) was used for diaphragm protection. This tape is double-sided, with a regular adhesive on one side and a temperature sensitive adhesive on the other. At 120 °C, the temperature sensitive adhesive releases completely.

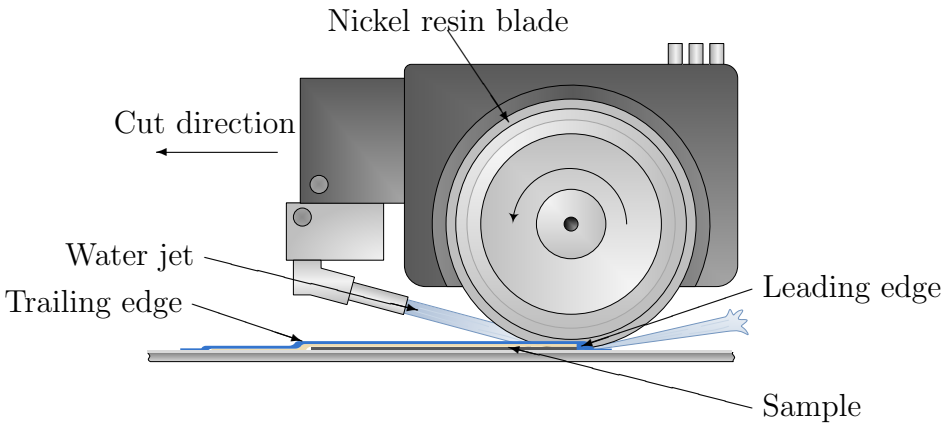

Figure 7-2. Dicing blade and sample orientation.

Early experiments on prototype 3 mm die using solely thermal release tape to protect the diaphragms proved extremely successful, with nearly 100% yield. However, the smaller 2 mm die did not provide sufficient area for reliable tape adhesion, resulting in peeling during dicing and significant die loss. As a result, an additional protective polyethylene tape (commonly used for surface protection in the construction industry) was used in a

more elaborate process. The entire process was performed on an ADT 7100 Dicing Saw equipped with nickel resin blades.

The method for using the protective tapes during the dicing process is depicted in Figure 7-3. To reduce the time and risk of each dice run, wafer sections (or samples) were individually diced. They were obtained via diamond scribing and breaking, with typical pieces containing 3-6 reticles. The backside of the sample was first affixed to medium tack dice tape, used for mounting the sample in the dicing machine. Next, the thermal release tape was applied to the front side (diaphragm side) of the sample, with only the protective backing associated with the thermal release adhesive removed. The thermal release tape was applied even with the sample edges on the cut entry edges, but extending off the sample up to 15 mm on the trailing edges (as shown in Figure 7-3A) to provide additional adhesion and protection from the dicing machine's water jet. Next, without removing the remaining plastic backing on the backside of the thermal release tape, the polyethylene tape was applied over the complete sample to provide additional protection, as shown in Figure 7-3A. The sample was then diced in the first direction, with cuts extending slightly off the leading and trailing edges of the sample. The complete tape layup for this step is shown in Figure 7-3B, and the tape thicknesses, which are important for setting the cut depth, are collected in Table 7-3. Important dicing machine settings are collected in Table 7-4.

Table 7-3. Tape and substrate thicknesses.

Material	Thickness [μm]
Substrate	500
Dice tape	130
Thermal release tape (without laminates)	160
Thermal release tape laminate	75
Polyethylene tape	70

With cuts completed in a single direction, the sample was then removed from the dicing machine and the polyethylene tape was smoothly peeled away from the thermal

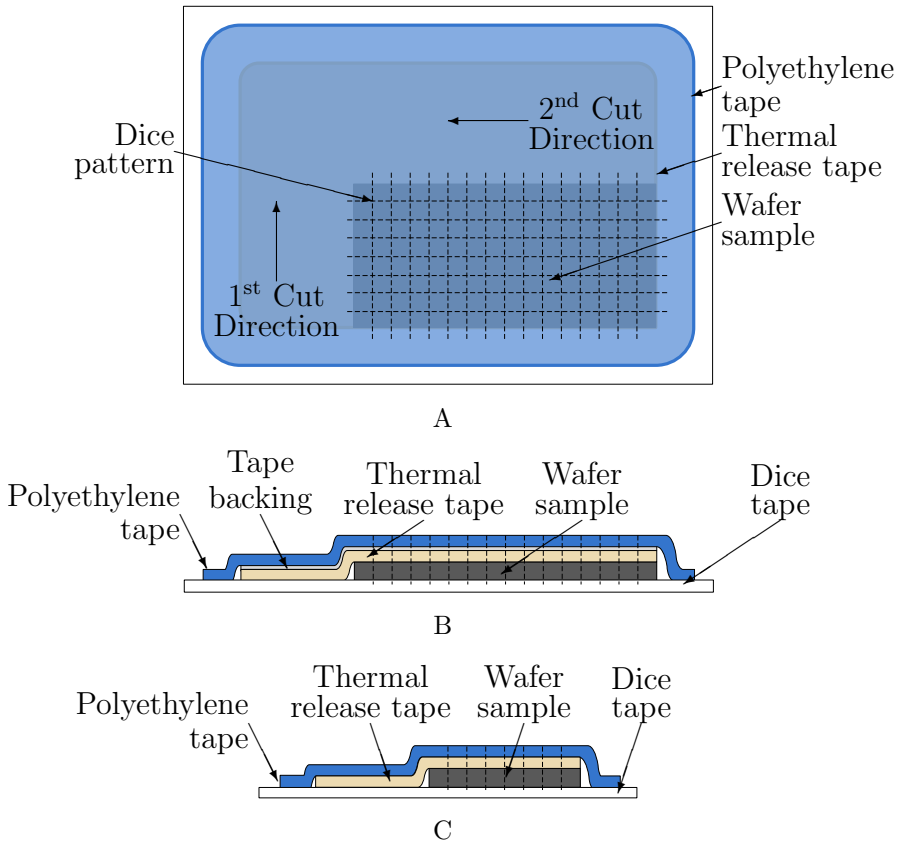

Figure 7-3. Dicing process for MEMS piezoelectric microphone die. A) Aerial view of dice process taping technique. B) Cross-sectional view of taping technique for first direction dice cuts. C) Cross-sectional view of taping technique for second direction dice cuts.

Table 7-4. Dicer settings.

Parameter	Setting
Spindle speed	30 krpm
Entry speed	0.5 mm/s
Cutting speed	2 mm/s
Illumination (Coaxial/Oblique)	11/53

release tape via the plastic backing layer. A new layer of polyethylene tape was then applied as in Figure 7-3A to yield the tape layup of Figure 7-3C. The sample was then diced in the second direction. The result, at this stage, was that the sample had been singulated into individual die with squares of thermal release tape still affixed on the diaphragm side, while strips of the polyethylene tape remained on top. Without removing

the sample from the dice tape, the polyethylene tape strips were then carefully peeled from the thermal release tape. Die were individually removed from the dice tape and placed on a hot plate at 120 °C. As the adhesive released, the tape became opaque and often "popped off" of the individual die. Otherwise, the released tape was easily removed with tweezers.

Individual die were stored in gridded Gel Sticky Carrier Boxes from MTI Corporation. The naming convention used to refer to a particular die was based on its wafer of origin, carrier box number, grid location within the carrier box, and design letter. For example, 138-1-E4-D refers to a microphone die originating from wafer 138, stored carrier box 1 at grid location E4, and of design D.

7.2.2 Dicing Results

A 66 mm × 34 mm section of wafer 116 and 20 mm × 60 mm section of wafer 138 were diced. Wafer 116 was diced with just thermal release tape for protection and a significant number of die were broken at the trailing edges due to the tape losing adhesion during the dicing operation. Only 58% yield was obtained for this segment of wafer 116, with yield calculated here as the ratio of unbroken die to the total number of die with released diaphragms. Wafer 138 was diced using the process described in Section 7.2.1, with significantly better results (83% yield). Microphone die that most frequently did not survive this approach were those with the largest diaphragms and thus the lowest non-diaphragm adhesion area, designs E-G.

Micrographs of individual microphone die of each design are pictured from smallest (A) to largest (G) in Figure 7-4. These die were from wafer 138 and thus obtained with the described dicing process. The undoctored micrographs show little edge damage or particulate.

7.3 Packaging

Packaging of the MEMS piezoelectric microphone for its intended operation in aeroacoustic applications such as fuselage arrays or engine tests requires a small, thin and

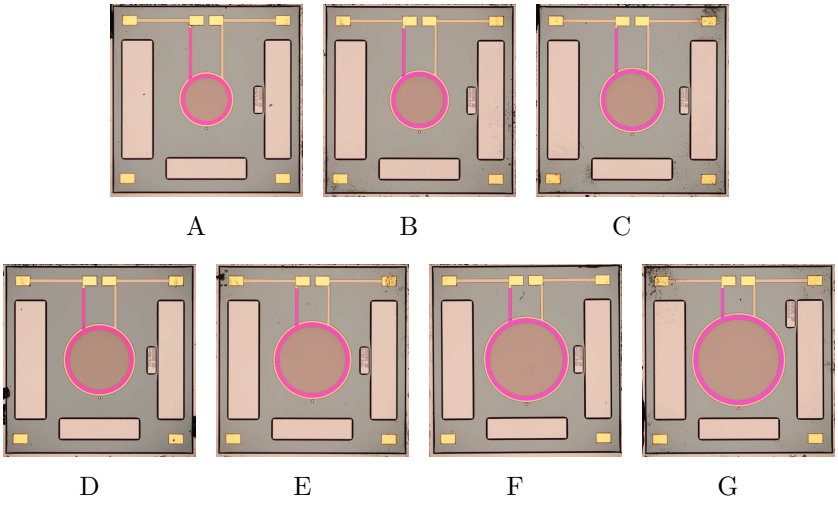

Figure 7-4. Micrographs of microphone die (designs A-G).

inexpensive solution. A package that meets all of the requirements for deployment in the field demands significant development and is beyond the scope of this study. However, laboratory test packaging that enables seamless transition of the MEMS microphone into multiple test setups among the research laboratory and project sponsor is also an important development in itself. This section describes the creation of a laboratory test package compatible with common test fixtures for 1/4" microphones at both the Interdisciplinary Microsystems Group and Boeing Corporation. An in-depth look at the Boeing flush-mount adapter designs can be found in [14].

The entire package was composed of structural and connectivity components as shown in the exploded view of Figure 7-5. The microphone die was epoxied into a circular printed circuit board — to be called the "endcap" — which was in turn connected to the end of a brass tube. Alignment was accomplished via mating alignment pins and holes on the brass tube and endcap. A circuit board with buffer amplifier was housed inside the brass tube and it was connected to the backside of the endcap via soldered wires. A nylon sleeve was fixed on the assembled brass tube and endcap via set screws in the thickest part of its base and served to electrically isolate the brass tube from test fixtures while also ensuring mounting flushness. Finally, heat shrink tubing (not shown) was used to

stress-relieve the wires protruding from the brass tube. Brass tubes and nylon sleeves were provided by Boeing Corporation.

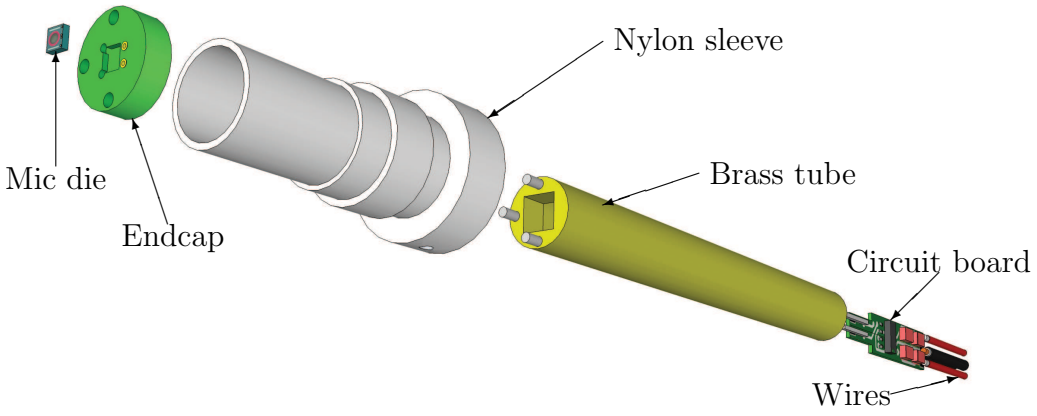

Figure 7-5. Exploded view of the laboratory test package.

A closeup rendering of the microphone die in the endcap is shown in Figure 7-6A. The 0.3485" diameter endcap, a two-layer printed-circuit board laid out in National Instruments' Ultiboard software and fabricated at Sierra Protoexpress (Sunnyvale, Ca), was 0.093" thick to accommodate post-milling of a 500 μm deep microphone die recess. The die recess, epoxy wells, pin holes, and board cut-out were all milled as post-processing steps at University of Florida using a Sherline Model 2000 CNC mill. Vias on the frontside were connected to solder pads on the backside for hookup to interface electronics. An additional via in one epoxy well provided substrate grounding as a precaution against hard-to-diagnose issues associated with a floating substrate potential. The frontside of the endcap was plated with soft bondable gold for ease of wire bonding. Figure 7-6B shows the printed circuit board layout.

The microphone die was epoxied into the endcap in a two stage process using an EFD Ultimus 2400 Precision Epoxy Dispenser. First, Ablebond 84-1LMI [159] (electrically conductive silver epoxy) was dispensed in the epoxy well that contained the via and then the die was placed in the recess. The epoxy was cured in a temperature controlled oven at 150 °C for 1 h. Next, Cyberbond DualBond 707 [160] was dispensed in both epoxy wells

and cured under a UV lamp for 24 h. During cure, the DualBond 707 became sufficiently fluid to seep underneath the microphone die and effectively seal the microphone back cavity. Wire bonds were made with a Kulicke & Soffa 4124 Series Manual Ball Bonding System and encapsulated with Dow Corning 3145 RTV MIL-A-46146 [161]. Important settings for epoxy dispensation and wire bonding are found in Table 7-5 and Table 7-6, respectively. A completed microphone in the endcap package is shown in Figure 7-7.

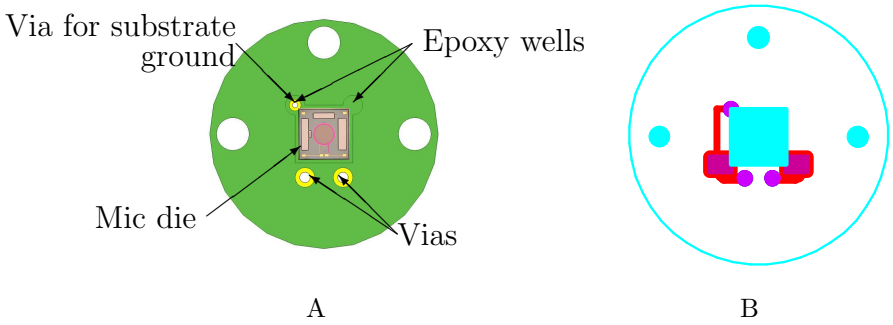

Figure 7-6. Microphone endcap. A) Drawing showing die in place. B) Circuit board layout [162].

Table 7-5. Epoxy dispenser settings.

	Ablebond 84-1LMI [159]	Dualbond 707 [160]	RTV [161]
Pressure [psi]	50	19	60
Back Pressure [mmHg]	16.4	0	7.4
Dispensing Time [s]	1	0.3	Variable
Tip [gauge]	25	25	20
Cure	150 °C for 1 h	24 h under UV lamp	Room temp. for 2 d

Table 7-6. Wire bond settings.

	Ball Bond	Wedge Bond
Force	7	7
Time	5	5
Power	3	4

The circuitry associated with the microphone package — a buffer amplifier with power supply filter capacitors (0.1 μF ceramic and 10 μF tantalum) — is shown schematically

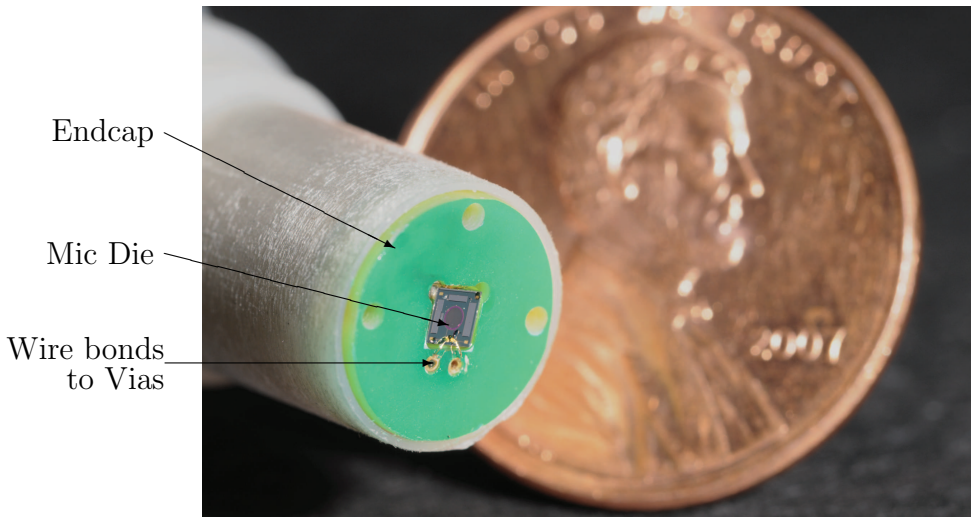

Figure 7-7. Closeup photograph of a packaged MEMS piezoelectric microphone.

in Figure 7-8. The amplifier used was the Linear Technologies LTC6240CS8, which was chosen for a variety of positive characteristics including low operating current and voltage, low noise (voltage noise $<10\,\mathrm{nV}/\sqrt{\mathrm{Hz}}$), and high input resistance ($1\,\mathrm{T\Omega}$) [44]. In order to reduce parasitic capacitance and the associated detrimental effects on device sensitivity (refer to Section 5.3.1), the amplifier was situated as physically close to the microphone die as possible. Figure 7-9 shows the circuit board layout. The boards were milled in-house on thin 0.028" FR4 and components were hand-soldered. Wiring terminated in banana connectors for v_+, v_-, and ground, in addition to a BNC connector for the output signal. The BNC ground was tied to the power supply ground on the board.

One device, 116-1-J7-A, was packaged for different measurements with both a voltage and charge amplifier. The circuit diagram for the charge amplifier is found in Figure 7-10. The selected operational amplifier was a Texas Instruments OPA129. The feedback loop was composed of a $1\,\mathrm{G\Omega}$ feedback resistor and two $4\,\mathrm{pF}$ feedback capacitors in parallel for a total capacitance of $C_{fb} = 8\,\mathrm{pF}$. These values were chosen to yield close to unity gain and to maintain a low cut-on frequency. The board layout is not shown but was similar to that for the voltage amplifier, except with additional length for the inclusion of the feedback resistor and capacitors.

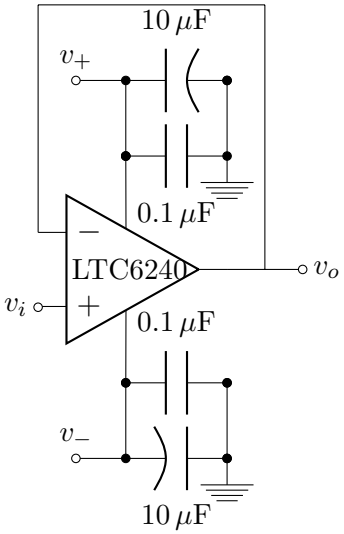

Figure 7-8. Voltage amplifier circuitry included in the microphone package.

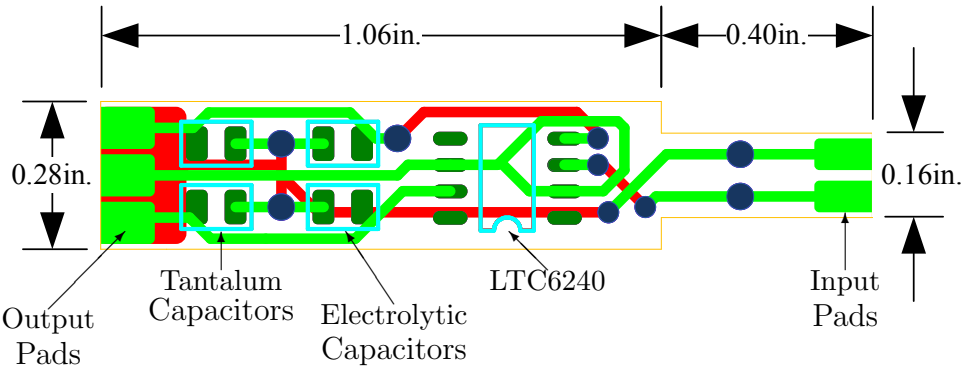

Figure 7-9. Voltage amplifier circuit board layout [162].

Electromagnetic interference (EMI) is a major problem for high-impedance devices [46] such as the piezoelectric microphone, and steps were taken to mitigate its impact. The brass tubing was connected to ground to provide a shield for the amplifier circuitry [46]. In addition, the amplifier board featured a guard ring to help limit leakage currents into the positive amplifier terminal [44]. Shielded coaxial cable was used for the microphone output signal.

The completed piezoelectric microphone laboratory test package is shown in Figure 7-11. The package fits a 3/8" hole with 1/2" depth. Flushness was not characterized but was estimated to be less than 500 μm.

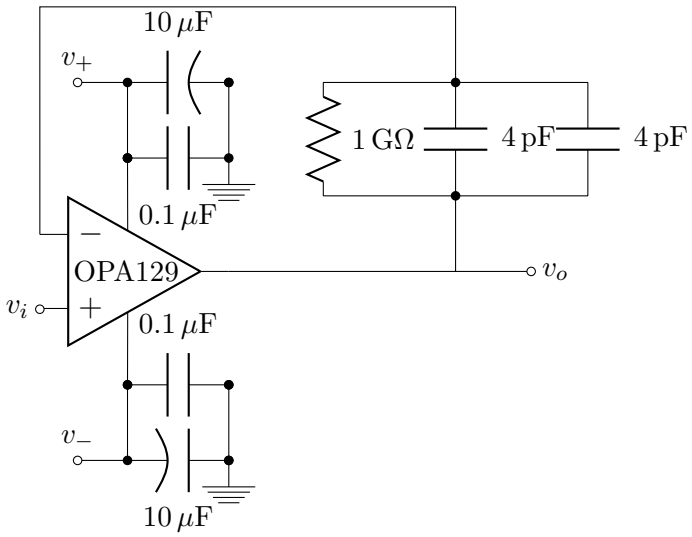

Figure 7-10. Charge amplifier circuit diagram.

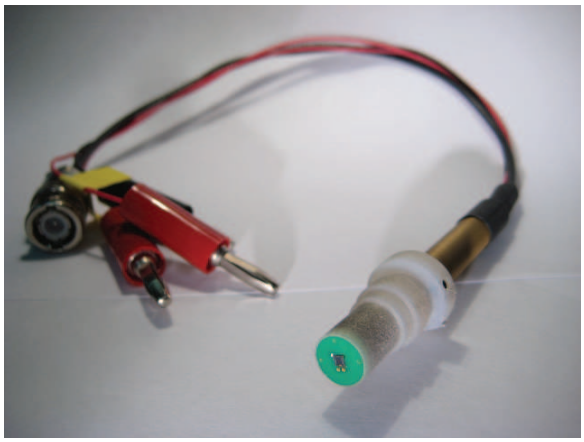

Figure 7-11. Complete packaged MEMS piezoelectric microphone.

7.4 Summary

This chapter discussed microphone realization and packaging. The laboratory test packaged was developed to enable device characterization in measurement setups at both the Interdisciplinary Microsystems Group and Boeing Corporation. The subject of the next chapter is experimental characterization of the packaged microphones.

CHAPTER 8
EXPERIMENTAL CHARACTERIZATION

This chapter describes the thorough experimental characterization of several MEMS piezoelectric microphones. First, experimental methods are introduced, starting with die selection and diaphragm topography measurements, then proceeding to acoustic and electrical characterization. A novel set of parameter extraction experiments are also described. Experimental setups and data processing techniques are covered. The experimental results presented thereafter quantify microphone performance in terms of common metrics, then give way to the results of parameter extraction experiments. Comparisons to the lumped element model presented in Chapter 5 are also made.

8.1 Experimental Setup

This section provides an overview of the experimental setups used in microphone selection, characterization, and parameter extraction. The microphone characterization is divided into acoustic characterization (direct measurements of the microphone response in a pressure field) and electrical characterization (determination of microphone electrical traits).

8.1.1 Die Selection Setup

Avago Technologies supplied eight 6" wafers with thousands of die per wafer. The dicing process discussed in Section 7.2 was carried out on small portions of two wafers, with a yield of 439 unbroken microphone die. With this many die available for characterization, an efficient die selection method was needed prior to investing significant time in the packaging of individual die (as described in Section 7.3).

Electrical measurements are a desirable means of die interrogation because they can often be done easily at the die level via probing. Electrical impedance is an obvious quantity to use for discriminating between die. However, the expectation of mechanical property variations (i.e. stress) being the primary factor separating good die from bad suggested the need for a more mechanical-oriented selection method.

For example, it is shown in Chapter 5 that high values of the effective piezoelectric coefficient d_a are associated with both high sensitivity and low noise. By the piezoelectric constitutive relations (Equation 5–2), d_a is equivalent to volume displacement per volt ($\forall/V$), calculable from an optical scan of the microphone diaphragm under electrical excitation. Unfortunately, optical scanning of the diaphragm is a time-consuming and equipment-intensive procedure that is not suited to be performed on a large number of die. However, $d_a = \forall/V$ may be rewritten as $d_a = A_{eff}w/V$, where w is the displacement at an arbitrary diaphragm location and A_{eff} is an effective area. This suggested that a quick single point interrogation could still provide useful comparative information.

Another useful metric easily obtainable via optical interrogation of the diaphragm under electrical excitation is the open-circuit resonant frequency, f_r. Tracking shifts in resonant frequency before and after the packaging process can provide information about changes in diaphragm stiffness due to unintended packaging stress. In addition, resonant frequency provides a second comparative measure, and is particularly useful when selection of like devices is necessary.

The experimental setup is pictured in Figure 8-1. A gridded gel pack with microphone die in situ was placed directly on the microscope stage of the Polytec scanning laser vibrometer (LV) system. Each die was interrogated only at a single point, chosen as the center of the diaphragm for measurement repeatability and to maximize the LV signal. Probes delivered a periodic chirp signal from the LV function generator (50 Ω output impedance) to the individual die over a wide frequency range, and the resonant frequency was selected from the displacement per voltage frequency response function, $H_{vw}(f)$. Next, a single tone excitation at 1 kHz was used to find the approximate flat band value of H_{vw}, denoted $S_{a,0}$. At each stage, the signal power was fine-tuned to obtain greater than 0.98 coherence between excitation signal and LV output. The important measurement settings are found in Table 8-1.

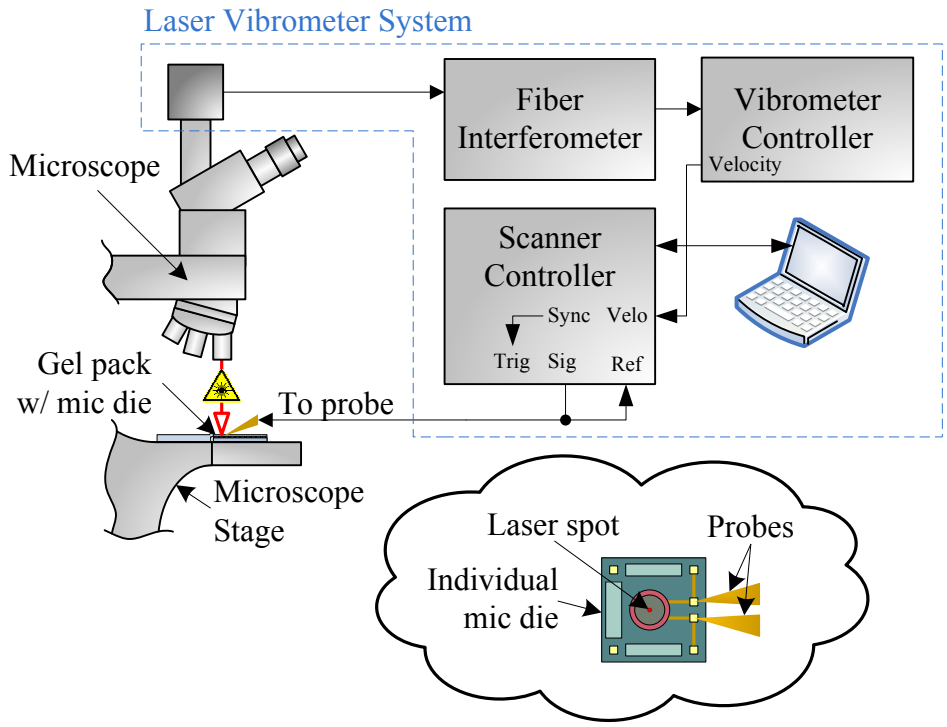

Figure 8-1. Experimental setup for die selection.

Table 8-1. Die selection laser vibrometer settings.

	Settings	
Parameter	Measurement of f_r	Measurement of $S_{a,0}$
Bandwidth	0 kHz to 200 kHz	0 kHz to 20 kHz
FFT lines	6400	6400
Frequency Resolution	31.25 Hz	3.125 Hz
Averages	100 (Complex)	
Excitation	Periodic Chirp	1 kHz Sine
Window	Rectangular	

Early in the process, measurements were repeated for several die that were removed from the gel pack and placed directly on the microscope stage in order to characterize the impact of the soft acoustic boundary condition presented by the gel. No difference between measurements was observed, and data in Section 8.2.1 are only given for microphones tested directly on gel packs.

Outlier rejection was employed before determining the means and standard deviations associated with $S_{a,0}$ and f_r for each microphone design. With values of both f_r and

$S_{a,0}$ known for each die, the data were bivariate [163]. As a result, straightforward univariate outlier detection, such as the Modified Thompson-Tau Technique [164], was not appropriate. Instead, multivariate outlier detection, which presumes multivariate outliers are univariate outliers in a particular 1-D projection, was needed [165]. The adjusted outlyingness (AO) algorithm [166], part of the LIBRA MATLAB toolbox [167, 168] developed by the Robust Statistics Research Group at the Katholieke Universiteit Leuven, was used. In the algorithm, a test statistic known as the AO is generated for each observation over many random 1-D projections, with the maximum AO estimate for each observation retained. An adjusted boxplot [169] is generated for the AO estimates and observations whose AO estimates exceed the boxplot upper whisker are regarded as outliers. The primary assumption of the AO algorithm is unimodality of the data [165]. Griffin et al. provide an accessible introduction to the AO algorithm [165].

After die selection, the same LV measurements used for die selection were repeated for the endcap-packaged microphone die (recall Section 7.3). For this measurement, the endcap was simply placed on the microscope stage and probed in a similar manner to the individual die. The same measurement was also performed prior to packaging of devices for parameter extraction (details in Section 8.1.5).

8.1.2 Diaphragm Topography Measurement Setup

Microphone die were packaged in multiple rounds, with the first round subjected to both pre- and post-packaging topographical measurements. The level of static deflection of the microphone diaphragm, a by-product of film stress, is informative of the diaphragm stress state. A ZYGO NewView 7200 scanning white light interferometer (SWLI) was used to perform the measurements. A SWLI works by illuminating a sample with white light, which reflects off the surface of the sample and recombines with a reference beam, creating interference fringes . A charge-coupled device (CCD) camera captures the fringes as the SWLI objective is scanned vertically; the surface topography is deduced from the captured images via a software algorithm [170]. The NewView 7200 featured a vertical resolution <

0.1 nm. Measurements were made with a 5X Michelson objective and 1X field zoom lens, yielding a measurement area of 1.41 mm×1.05 mm. The standard 640 px × 480 px high speed camera provided a lateral resolution of approximately 2.2 μm. Three averages were used in all measurements, which were referenced to the surrounding wafer surface. Other notable software settings are found in Table 8-2.

Table 8-2. Scanning white light interferometer software settings.

Control	Parameter	Setting
Measurement	FDA Res	High
	ACG	On
	Phase Res	Super
Surface Map	Remove	Plane
	Remove Spikes	Off
	Datafill	Off
	Filter	Off
	Trim	0

8.1.3 Acoustic Characterization Setup

Acoustic characterization refers to experimental quantification of the microphone response to acoustic pressure excitation. The goal of the acoustic characterization was to quantify the piezoelectric microphone performance in terms of frequency response (sensitivity, bandwidth) and linearity.

8.1.3.1 Frequency response measurement setup

The frequency response of the piezoelectric microphones, $H_m(f)$ [V/Pa], was determined over the audio range via a secondary calibration, and the procedures used hailed from the family of comparison methods [171]. Specifically, the performance of the DUT was determined via comparison with a measurement-grade reference microphone.

The acoustic characterization was performed in an approximately 1 m-long, 2.2 cm-thick, aluminum plane wave tube (PWT) with a 1 in × 1 in duct. A PWT is a rigid waveguide designed such that only planar waves propagate below a certain frequency, called the cut-off frequency of the tube, f^c. Below this frequency, higher-order acoustic

modes introduced to the PWT are evanescent, meaning they decay exponentially along its length. Two microphones mounted at the same lengthwise location are therefore simultaneously exposed to the same pressure for drive frequencies less than f^c. For a square waveguide with cross-sectional dimension a, the cut-off frequency is [28]

$$f^c = \frac{c_0}{2a}. \tag{8–1}$$

Equation 8–1 reveals the cut-off frequency may be tuned by the PWT cross-sectional dimension a or choice of gas. For the purposes of determining the frequency response of an audio microphone, $f^c \geq$20 kHz is desirable but f^c in air for $a = 1$ in is approximately 6.7 kHz. Helium's faster isentropic speed of sound makes it possible to increase f^c to approximately 19.8 kHz, allowing for a more comprehensive view of the audio band response of a microphone.

As a result, complementary frequency response measurements were performed using both air and helium in the PWT. The measurement in air was intended to yield accurate sensitivity information under normal operating conditions. The expanded frequency range of the helium measurement enabled assessment of the flatness of the frequency response over nearly the full audio range. The use of helium instead of air has a slight effect on the performances of both the DUT and reference microphones; for example, a helium-filled cavity is less compliant than an air-filled one, since $C_{ac} \propto 1/\rho_0 c_0^2$ and the $\rho_0 c_0^2$ product is higher in helium. Lumped element model predictions for the microphone frequency response in air and in helium are shown in Figure 8-2 for design D. Depending on the microphone design, the reduction in sensitivity in helium compared to air was predicted to be 0.04 dB to 0.4 dB.

The experimental setup for the frequency response measurement is shown in Figure 8-3, with both the reference microphone and DUT mounted at the end of the PWT. The reference microphone used was a Brüel and Kjær 4138 1/8" pressure field microphone [50] mounted on a Brüel and Kjær UA0160 adapter and connected to a

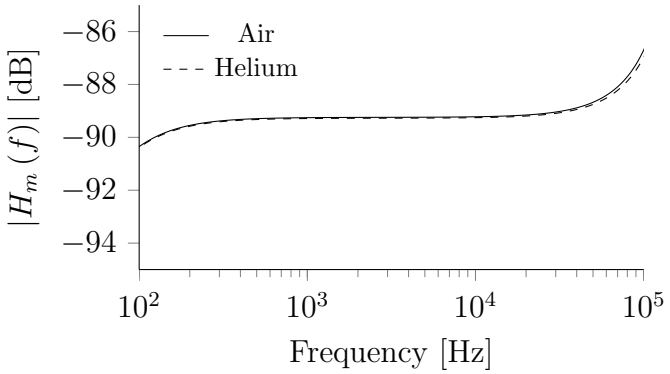

Figure 8-2. Predicted frequency response magnitude in air and helium for design D.

Brüel and Kjær 2670 preamplifier. A Brüel and Kjær Type 3560D Multichannel Portable PULSE system with a Type 3032A 6/1 Ch. Input/Output Module and Type 3109 4/2 Ch. Input/Output Module was used to generate the test signal and acquire data. The two microphones were connected to separate input/output modules to minimize cross-talk. A Techron 7540 Power Amplifier amplified the pseudorandom test signal before it reached a BMS 4590 compression driver. The poor response of the BMS 4590 compression driver below 300 Hz required all measurements to be conducted starting at that frequency. Measurement settings are collected in Table 8-3. Finally, for the helium measurement, the PWT was flooded with helium via a pressurized canister regulated at 10 psi. The helium exited the PWT into a cup of water.

In air, the frequency response of the DUT, $H_m(f)$, was determined simply as the frequency response function relating the output of the DUT [V] and the output of the calibrated reference microphone [Pa], a calculation performed natively in the PULSE software. The Brüel and Kjær 4138 frequency response magnitude was regarded as flat in this calculation and only relative phase was determined. In helium, concerns about stratification of the gas medium and resulting wavefront distortion led to the use of the substitution method [19, 172, 173] to improve measurement quality in helium.

The substitution method required two measurements with the microphones in original and swapped positions as indicated in Figure 8-4. Let H_{12}^o and H_{12}^s represent the measured

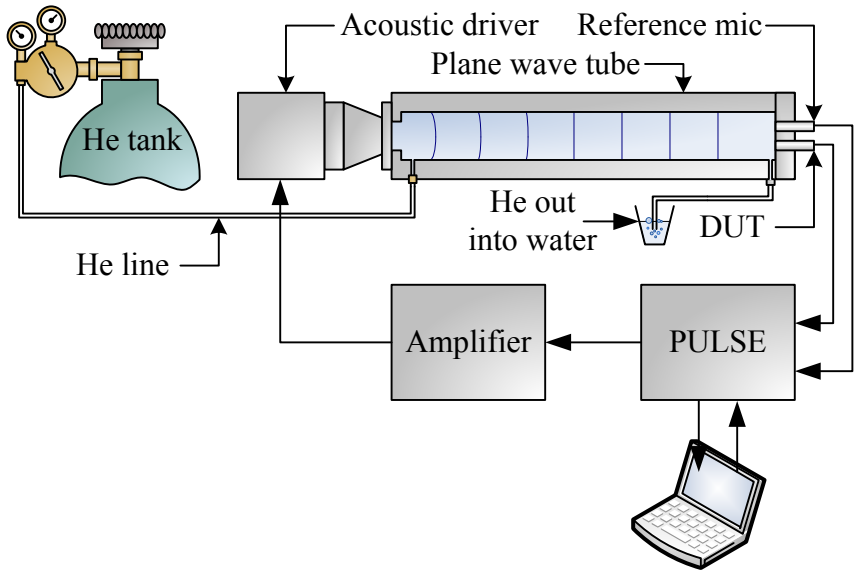

Figure 8-3. Plane wave tube setup for acoustic characterization.

Table 8-3. Settings for microphone frequency response measurements in PULSE.

Grouping	Parameter	Setting in Air	Setting in Helium
Acquisition	FFT Type	Zoom	Baseband
	Center Frequency [kHz]	3.5	N/A
	Bandwidth [kHz]	6.4	25.6
	Frequency Range	300 Hz–6.7 kHz	0 Hz–25.6 kHz
	# of FFT Lines	6400	
	Frequency Resolution [Hz]	1	4
	Window	Rectangular	
	Overlap	0 %	
	# of Averages	100	
Generator	Signal	Pseudo random noise	
	Frequency Range	300 Hz–6.7 kHz	300 Hz–25.9 kHz
	Spectral Lines	6400	

frequency response functions in the original and swapped positions, respectively, relating the output of microphone 2 (the DUT) to that of microphone 1 (the reference) in units of V/V. Also let the frequency response functions of the two microphones be denoted H_1 and H_2 [V/Pa]. In the original and swapped positions depicted in Figure 8-4,

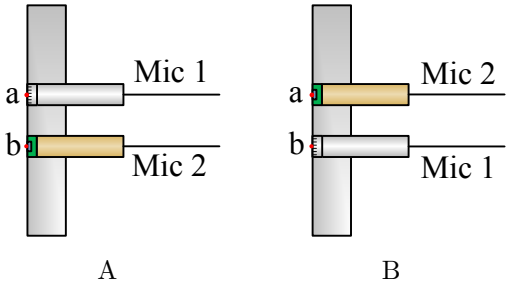

Figure 8-4. Microphone switching procedure. A) Original positions. B) Swapped positions.

$$H_{12}^{o} = \frac{G_{12}^{o}}{G_{11}^{o}} = H_{ab}\left(\frac{H_1^* H_2}{H_1^* H_1}\right) \tag{8–2}$$

and

$$H_{12}^{s} = \frac{G_{12}^{s}}{G_{11}^{s}} = H_{ba}\left(\frac{H_1^* H_2}{H_1^* H_1}\right), \tag{8–3}$$

where * denotes complex conjugate, G_{12} cross-spectral density, G_{11} is autospectral density, and H_{ab} and H_{ba} [Pa/Pa] are frequency response functions relating the actual pressures at the two measurement locations. A key assumption of Equations 8–2 and 8–3 is that there is no change in the pressure field between measurements, i.e. the pressures at location a and location b remain unchanged. To help adhere to this assumption, no alterations to the state of the measurement setup, particularly the acoustic source, were made between measurements save for swapping of the microphones, which was accomplished via removing and rotating the PWT endplate. Multiplying Equations 8–2 and 8–3 together, noting that $H_{ab}H_{ba} = 1$, taking the square root, and rearranging,

$$H_2 = H_1\sqrt{H_{12}^{o}H_{12}^{s}}. \tag{8–4}$$

Therefore, with the frequency response function of the reference microphone, H_1, well-known, the frequency response function of the DUT, $H_m\,(f) = H_2\,(f)$, can be

deduced from the geometric mean of measurements for H_{12}^{o} and H_{12}^{s} even when the two microphones are not exposed to precisely the same pressure. Over the range of measurement frequencies, it is sufficient to regard H_1 as having constant magnitude [50] and non-constant phase. The phase roll-off is approximately 7.5° by 20 kHz [174].

Due to the low-frequency limitations of the BMS 4590 compression driver used in the PWT setup, additional measurements to characterize the low-frequency roll-off of the piezoelectric microphone were performed at Boeing Corporation. Two piezoelectric microphones, 138-1-I2-D and 138-1-J3-F, were transferred to Boeing for this measurement and others. The measurement setup is pictured in Figure 8-5 and consisted of the DUT and Brüel and Kjær 4136 reference microphone mounted in a small acoustic cavity (though Figure 8-5B shows 2 Brüel and Kjær 4136 microphones mounted there) that was driven by a speaker and terminated into an "infinite" (100 ft) copper tube. The infinite tube termination was actually designed to suppress the formation of standing waves and enable high frequency measurements, but this existing setup was still attractive for the low frequency measurement.

An HP 35670 spectrum analyzer provided a broadband white noise signal and acquired the DUT and reference microphone signals. Measurement settings are found in Table 8-4. Using the spectrum analyzer, the frequency response function relating the DUT output to the calibrated reference microphone output [V/Pa] was calculated. The frequency response function was then post-processed to correct for the low-frequency roll-off in the reference microphone. The low-frequency calibration of the reference microphone was obtained at 1/3 octave bands down to 10 Hz using a Brüel and Kjær UA0033 electrostatic actuator with a G.R.A.S. actuator supply Type 14AA. The typical −3 dB lower limiting frequency for a Brüel and Kjær 4136 is 0.3 Hz to 3 Hz.

8.1.3.2 Linearity measurement setup

Characterization of microphone linearity refers to the quantification of how the voltage output of the DUT changes with sound pressure level. Measurements were

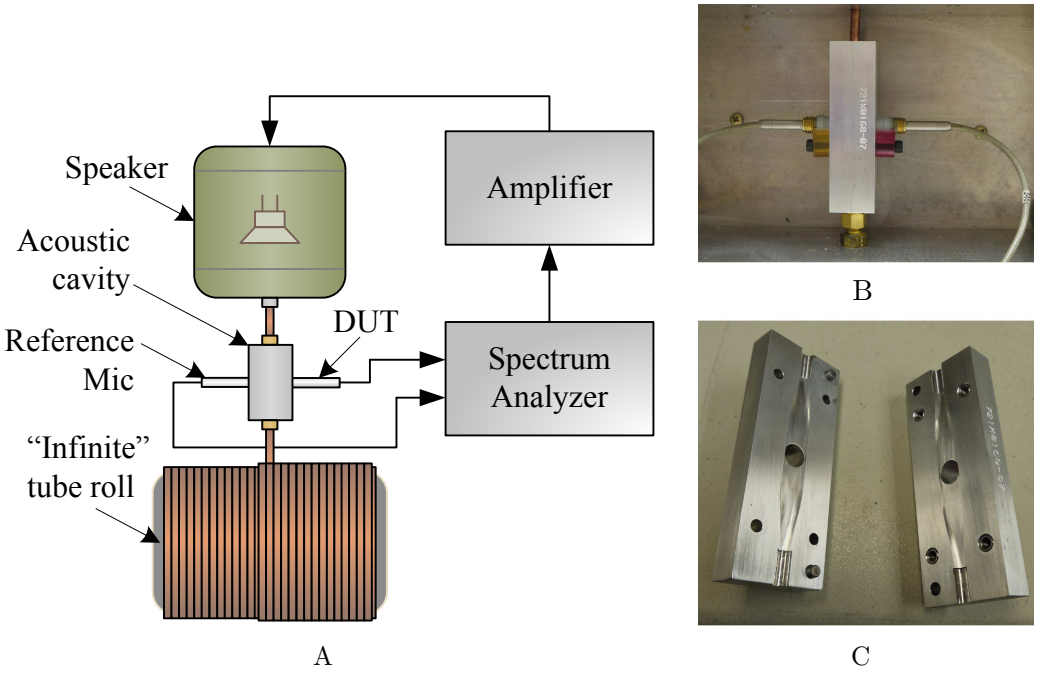

Figure 8-5. Infinite tube measurement setup. A) Measurement schematic. B) Two Brüel and Kjær 4136 microphones mounted in the acoustic cavity. C) Inside the acoustic cavity.

Table 8-4. Frequency response measurement settings used at Boeing.

Parameter	Setting
Bandwidth	1.6 kHz
FFT Lines	1600
Frequency Resolution	1 Hz
Test Signal	Broadband white noise

performed at both University of Florida and at Boeing Corporation. From the collected data, total harmonic distortion was calculated, rewritten here from Equation 2–13 in terms of power spectral density as [47]

$$\mathrm{THD} = \sqrt{\frac{\sum_{n=2}^{\infty} G_{xx}\left(f_n\right)}{G_{xx}\left(f_1\right)}} \times 100\%, \tag{8–5}$$

where f_1 is known as the fundamental frequency, excitation frequency, or first harmonic, and f_n is the nth harmonic. Assuming uniform microphone sensitivity at each f_n, G_{xx} can be regarded in units of $\mathrm{Pa}^2/\mathrm{Hz}$ or V^2/Hz.

At University of Florida, the same setup used to find the frequency response (in air), pictured in Figure 8-3, was used to obtain data for the total harmonic distortion calculation. A single tone signal at 1 kHz drove the BMS 4590 compression driver, which could reach a SPL of approximately 160 dB without exceeding its power rating. A PCB Piezotronics Model 377A51 precision condenser microphone, with a maximum SPL of 192 dB (3 % distortion), was connected to a Brüel and Kjær 2670 preamplifier and served as the reference. The DUT and reference microphone output signals were collected using the same settings found in Table 8-3 at multiple pressure levels. Starting from the lowest SPL with a detectable 2nd harmonic, the SPL was increased in steps of 3–4 dB SPL up to 160 dB. The 6.4 kHz bandwidth enabled the first six harmonics to be captured. An important consideration in getting a reliable pressure reference using the PWT for this measurement was that harmonics higher than the 6th propagate as higher-order modes and thus do not contribute equally to the response of the DUT and reference microphone. Therefore, power distributed to frequencies f_n for $n > 6$ must be negligible in order for the calculation to be valid.

Experimental results to be discussed in Section 8.2.3.2 show that the setup of Figure 8-3, apart from the microphones, suffers from significant harmonic contamination. Speaker distortion is one contributor, together with harmonic generation during nonlinear acoustic propagation at high sound pressure levels [28]; the latter source of distortion worsens with propagation distance.

A measurement setup at Boeing Corporation was designed specifically to minimize harmonic contamination at high sound pressure levels. Photographs of the setup are found in Figure 8-6. The measurement apparatus, an acoustical coupler [35], was better known as "the wedge," inside of which was a low-volume cavity driven by four manifolded speakers. A reference microphone (in this case the Brüel and Kjær 4938 1/4" pressure field microphone with Brüel and Kjær 2670-W-001 preamplifier) and the DUT were mounted facing each other, as shown in Figure 8-6B, at close proximity (0.231"). A single

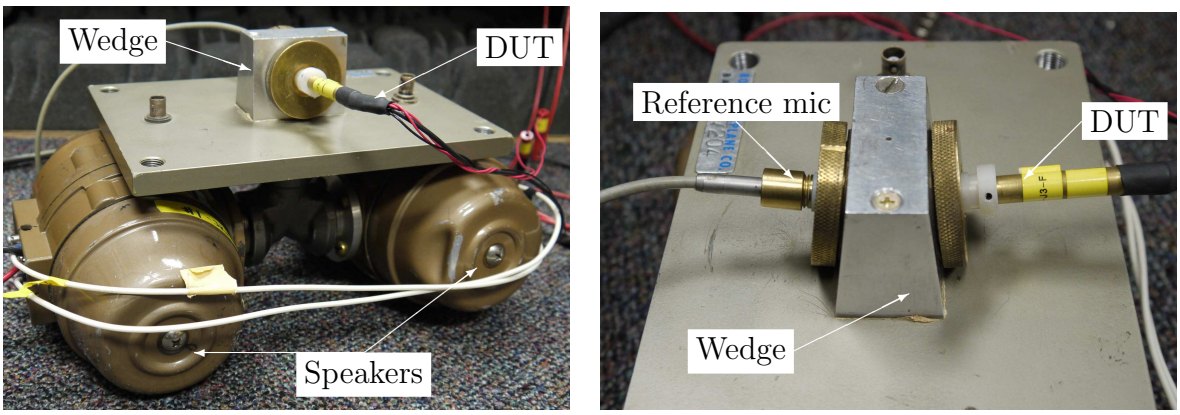

A B

Figure 8-6. Linearity measurement setup at Boeing Corporation. A) View of the entire wedge fixture, with speakers. B) Reference microphone and DUT mounted in the wedge. Photographs courtesy of Boeing Corporation.

tone signal at 2.5 kHz was chosen based on the speaker's frequency response characteristics to provide the highest sound pressure levels. The maximum SPL achievable in the wedge was approximately 172 dB and was limited by the speakers' power rating. Measurement settings for an HP35670A spectrum analyzer, used to collect the data and perform the THD calculation with ten harmonics included, are found in Table 8-5.

Table 8-5. Total harmonic distortion measurement settings used at Boeing.

Parameter	Setting
Bandwidth	25.6 kHz
FFT Lines	400
Frequency Resolution	64 Hz
Window	Flattop
Fundamental Frequency	2.5 kHz
# of Harmonics	10

8.1.4 Electrical Characterization Setup

There were two major goals in the electrical characterization of the piezoelectric microphones. First, the microphone's noise floor was measured to enable calculation of the important minimum detectable pressure metric. In addition, electrical elements found in the lumped element model of Chapter 5, including C_{eb} (or C_{ef}), C_{eo}, R_{ep}, and R_{es},

were extracted from impedance measurements. Finally, the total parasitic capacitances that served to attenuate the microphone sensitivities from open circuit values, $C_{ep} + C_{ea}$, were estimated for a single device via data from a combination of electrical and acoustic measurements.

8.1.4.1 Noise floor measurement setup

This section details the measurement strategy for the microphone's intrinsic noise floor. Section 2.3.2 addressed the presence of both intrinsic and extrinsic noise in sensors. The intrinsic noise floor is of primary importance because it indicates the best-achievable noise characteristics of the MEMS microphones when effectively shielded from extrinsic noise sources. Referring the intrinsic electrical output noise to the microphone input yields the minimum detectable pressure of the microphone.

The measurement setup [38] is pictured in Figure 8-7. The DUT is placed inside a triple Faraday cage, which serves to attenuate electromagnetic interference from the lab environment. Two sets of AA batteries powered the DUT buffer amplifier at $\pm 3\,\mathrm{V}$. The DUT output signal was fed through the innermost Faraday cage to the middle Faraday cage, where it was connected to a Stanford Research Systems (SRS) Model SR560 Low-Noise Preamplifier (itself battery-powered) and amplified by a factor of 1000. The amplifier output was then fed through the outer two Faraday cages to a SRS Model SR785 2 Channel Dynamic Signal Analyzer. A custom-programmed Labview VI performed the data collection via computer control of the SR785 and saved the measured output power spectral density [V^2/Hz].

Measurement settings are found in Table 8-6. The noise power spectral density of the DUT was collected over a total bandwidth from 0 Hz to the maximum frequency of 102.4 kHz using multiple separate measurements, each with the instrument maximum 800 FFT lines. Employing multiple frequency spans enabled measurements with better frequency resolution at low frequencies and more blocks at high frequencies, where measurement time was dramatically reduced. The start and end frequencies, frequency

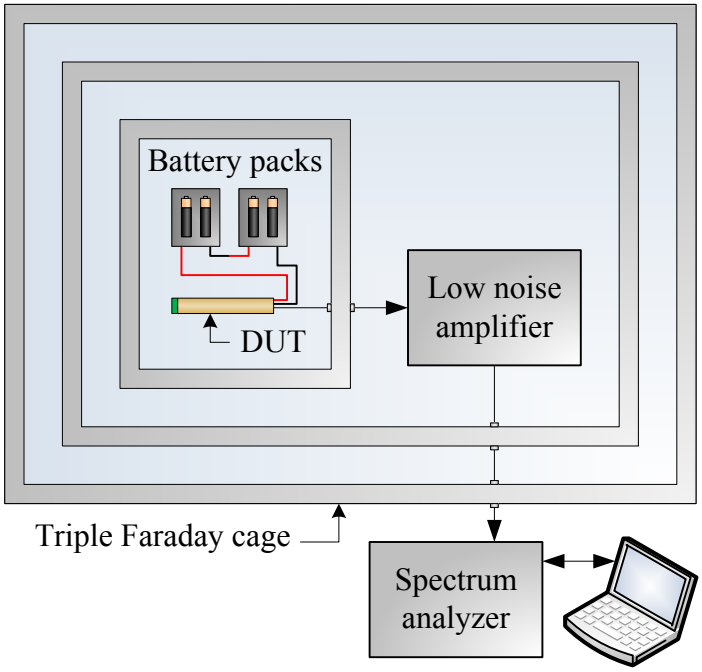

Figure 8-7. Triple Faraday cage setup for noise floor characterization.

resolution, and number of blocks for each span are shown graphically in Figure 8-8. The SR560 noise floor was also measured independently via shorting of the input and was subtracted, in terms of PSD, from the DUT output in all results presented in Section 8.2.4.1 before the noise was input-referred.

Table 8-6. Noise floor measurement settings.

Instrument	Parameter	Setting
Spectrum Analyzer	FFT lines per span	800
	Frequency Resolution # Blocks	See Figure 8-8
	Window	Hanning
	Overlap	75 %
Amplifier	Gain	1000
	Filter	Bandpass 0.03 Hz–300 kHz
	Mode	Low Noise
	Coupling	AC

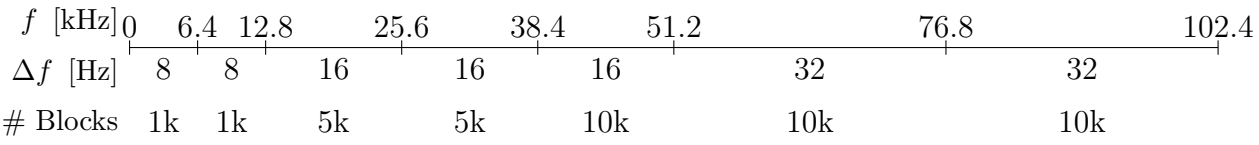

Figure 8-8. Noise floor measurements spans, frequency resolution, and averages.

8.1.4.2 Impedance measurement setup

The goal of the electrical impedance measurement was to obtain impedance data from which electrical parameters could be extracted. In Section 5.2.4, an expression was derived for the electrical impedance of a piezoelectric microphone,

$$Z_{eq} = R_{es} + \frac{R_{ep}}{1 + j\omega R_{ep}\left(C_{ef} + C_{eo}\right)}, \tag{8–6}$$

Using this equation, the elements R_{es}, R_{ep}, and $C_{ef} + C_{eo}$ were extracted from impedance measurements performed on 2 of each design from wafer 116 section 3 (14 measured die in total). An HP 4294A impedance analyzer [175] together with a Cascade Microtech M150 probe station were used to perform the measurement. The HP 4294A utilizes the accurate low-frequency auto-balancing-bridge method [176, 177] and a four terminal configuration that reduces the effects of lead impedances on the measurement [176]. The measurement setup is shown in Figure 8-9. The two terminals of each pair (Lc/Lp and Hc/Hp) come together at the very tip of the probe needle and all four terminal grounds were connected at the probe input. Calibration was performed using a GGB Industries CS-8 impedance standard substrate of the ground-short (GS) configuration. A custom-written program in HP Instrument BASIC collected and stored 31 complete impedance measurement sweeps for each device (no on-board averaging), enabling post-processing to establish confidence bounds. Measurement settings are found in Table 8-7.

For a capacitance-dominated device approximately in the range of 1–10 pF, the maximum bias error was not guaranteed in the operation manual [175] to be below 10% until the measurement frequency exceeded between 0.4 and 4 kHz. The provided bias error prediction equations were in fact invalid for impedances exceeding

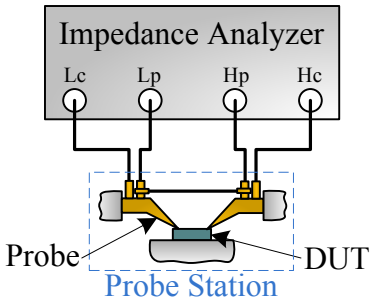

Figure 8-9. Impedance measurement setup using a probe station.

Table 8-7. Impedance measurement settings.

Parameter	Setting
Sweep Type	Logarithmic
Sweep Range	1 kHz to 200 kHz
Number of Points	801
Point Delay Time	0 s
Sweep Delay Time	0 s
Oscillator Level	500 mV
DC Bias	Off
Bandwidth	3
Sweep Averaging	Off
Point Averaging	Off

approximately 100 MΩ, where maximum bias error predictions easily surpassed 100% [178]. As a result, the measurement was conducted starting from 1 kHz, at which a 4 pF capacitance measurement was guaranteed to have $< 10\,\%$ bias error (or $< 3\,\%$ for a 16 pF measurement). The instrument-minimum frequency was 40 Hz.

Although impedance was the measurand, admittance is often a more convenient representation for piezoelectrics. Impedance data post-processed into admittance form ($Y_{eq} = 1/Z_{eq}$) was used for the model fit,

$$Y_{eq} = \frac{j\omega R_{ep}\left(C_{ef} + C_{eo}\right) + 1}{\left(j\omega R_{ep}\left(C_{ef} + C_{eo}\right) + 1\right) R_{es} + R_{ep}}, \tag{8–7}$$

The benefit of the admittance form is that when R_{es} is small, the admittance reduces to the very simple expression $Y_{eq} \approx 1/R_p + j\omega\left(C_{ef} + C_{eo}\right)$. The fit to Equation 8–7 was performed using the MATLAB function `invfreqs`, which like most curve-fitting tools

attempts to minimize the weighted sum of the squared residuals between the data and fit at each measurement point. The particular benefit of invfreqs is that it is specifically formulated to fit transfer functions to complex frequency response data. The form of Equation 8–7 that MATLAB uses for fitting is

$$Y_{eq} = \frac{B_1 s + B_2}{A_1 s + A_2}, \tag{8–8}$$

where $A_1 = 1$ always by convention. Comparing to Equation 8–7, the electrical parameters were extracted as

$$C_{ef} + C_{eo} = \frac{B_1}{A_2 - B_2/B_1}, \tag{8–9}$$

$$R_{ep} = \frac{A_2}{B_2} - \frac{1}{B_1}, \tag{8–10}$$

and

$$R_{es} = \frac{1}{B_1}. \tag{8–11}$$

A statistical distribution for these parameters was obtained via repeated fitting to perturbed mean measurements in Monte Carlo simulations. From these distributions, the mean and 95% confidence interval were calculated. Further details on the Monte Carlo simulations and accompanying uncertainty analysis are found in Section C.4.

8.1.4.3 Parasitic capacitance extraction setup

The expressions for the frequency response of a microphone packaged with a charge or voltage amplifier were developed in Section 5.2.3, including approximate expressions for flatband sensitivity. From those expressions, it is possible to estimate parasitic capacitance and open-circuit sensitivity with appropriate measurements. Equations 5–47 and 5–53 predict the flatband sensitivity for a microphone packaged with a voltage amplifier and charge amplifier, respectively. Equating the open circuit sensitivity, S_{oc}, that appears in Equations 5–47 and 5–53 and rearranging yields an estimate for parasitic capacitance,

$$C_{ep} + C_{ea} = \frac{S_{ca}}{S_{va}} C_{fb} - \left(C_{ef} + C_{eo}\right). \tag{8–12}$$

To make use of this expression, frequency response measurements replace the single-valued sensitivities in Equation 8–12 to yield

$$C_{ep} + C_{ea} = \frac{H_{m,ca}(f)}{H_{m,va}(f)} C_{fb} - (C_{ef} + C_{eo}), \tag{8–13}$$

where $H_{m,ca}$ and $H_{m,va}$ represent the frequency response functions [V/Pa] associated with a single microphone packaged consecutively with a charge and voltage amplifier. Microphone 116-1-J7-A was packaged solely for this purpose. Packaged with the voltage amplifier architecture, microphone 116-1-J7-A shared common electronics architecture, including consistent trace lengths, amplifier, etc. with the other piezoelectric microphones; this suggested consistent parasitic capacitance could be expected. With the parasitic capacitance known for 116-1-J7-A and assuming that it remained essentially unchanged from device-to-device, the open circuit sensitivity of all microphones was estimated from the rearranged Equation 5–47,

$$S_{oc} = S_{va} \frac{C_{ef} + C_{eo} + C_{ep} + C_{ea}}{C_{ef} + C_{eo}}. \tag{8–14}$$

Estimating the open-circuit sensitivities of the microphones in this way also enabled avoidance of the substantial risk of damage associated with packaging and re-packaging all of the microphones with both voltage and charge amplifier architectures.

Measurements of $H_{m,ca}$ and $H_{m,va}$ for microphone 116-1-J7-A were performed in air using the same PWT setup described in Section 8.1.3.1. Values for $C_{ef} + C_{eo}$ values were obtained from impedance measurements presented in Section 8.2.4.2 under the assumption that electrical properties were consistent device-to-device.

8.1.5 Electroacoustic Parameter Extraction

Extraction of electroacoustic parameters enables validation of individual lumped element predictions. Relatively simple elements representing, for example, the acoustic back cavity are well-known [28]. However, elements whose values are predicted from the diaphragm model, including the diaphragm compliance C_{ad} and mass M_{ad}, in addition to

the effective piezoelectric coefficient d_a, require validation. In this section, experiments for their extraction are described, with the approach driven by the more demanding needs for extraction of compliance and mass. A measurement procedure for microphone sensitivity compatible with the requirements of the parameter extraction experiment is also addressed.

8.1.5.1 Compliance and mass measurement setup

The diaphragm compliance and mass, as defined in Section 5.2.1.2, are calculated from the diaphragm displacement due to pressure loading. In nomenclature appropriate for the measurement setting, they may be redefined as

$$C_{ad} = \int_0^{2\pi} \int_0^{a_2} H_{pw}|_{V=0}\,(r,\theta) r dr d\theta \tag{8–15}$$

and

$$M_{ad} = \frac{\int_0^{2\pi} \int_0^{a_2} \rho_a \, H_{pw}|^2_{V=0}\,(r,\theta) r dr d\theta}{\left[\int_0^{2\pi} \int_0^{a_2} H_{pw}|_{V=0}\,(r,\theta) r dr d\theta\right]^2}, \tag{8–16}$$

where $H_{pw}|_{V=0}$ [m/Pa] is the frequency response function obtained under short-circuit conditions relating the location-dependent displacement $w\,(r,\theta)$ to pressure acting on the diaphragm, a_2 is the outer diaphragm diameter, and ρ_a is the aerial density, defined in Equation 5–13. Note that because ρ_a changes abruptly at $r = a_1$, the integral over r in the numerator of Equation 8–16 must be evaluated piece-wise.

From Equations 8–18 to 8–16, extraction of C_{ad} and M_{ad} requires the ability to apply a known pressure to the diaphragm while optically scanning its displacement. Although a measurement setup could be devised that would allow simultaneous excitation and optical measurement of the packaged microphones, the design of measurement fixtures providing optical access for a laser vibrometer system within its depth-of-field would be a significant challenge and expense. Instead, a simpler measurement setup was used in which specially-packaged microphones were excited with a known pressure via their back cavities and the accompanying diaphragm displacement was measured from the front side.

The packaging requirements for this measurement were dictated largely by the desire to use an existing pressure coupler [149]. Together with the need for compatibility with the pressure coupler, the need to enable measurements of microphone frequency response functions via inclusion of integrated interface electronics led to the choice of a circuit board to house the microphone die. A 0.059 in thick board milled in-house from FR-4, with the microphone die epoxied into a recess at one end, was used. An exploded view of the pressure coupler assembly and packaging solution are shown in Figure 8-10. The circuit board was clamped into position over the open topside of the pressure coupler's acoustic cavity with a Lucite end plate. A 0.03 in (762 μm) diameter hole centered within the die recess in the circuit board coupled the microphone back cavity with the pressure coupler cavity, while an optical window on the front side enabled laser access to the diaphragm, as shown in Figure 8-11.

The pressure coupler provided two access points for acoustic pressure measurements within the cavity. A reference microphone was mounted at normal incidence in a plug that inserted into the end of the cavity, as labeled in Figure 8-10. Meanwhile, the DUT was mounted at grazing incidence approximately 9 mm up the cavity. For low frequency sound with wavelength much greater than this dimension, the pressures were approximately equal. The pressures at the reference microphone and DUT locations were 90° out of phase at quarter wavelength separation (9.5 kHz driving frequency in air).

In Chapter 5, C_{ad} and M_{ad} were extracted from the theoretical prediction of static diaphragm deflection. They are equivalently calculable from dynamic measurements at sufficiently low frequencies (i.e. frequencies much lower than the resonant frequency of the diaphragm). With resonant frequencies upwards of 100 kHz for all devices measured, excitation at 1 kHz was sufficiently low to be considered quasi-static. The wavelength at 1 kHz (34 cm) was also 38 times the test and reference microphone separation and thus more than sufficient to regard the pressures at the two locations as nearly equal. This was confirmed experimentally.

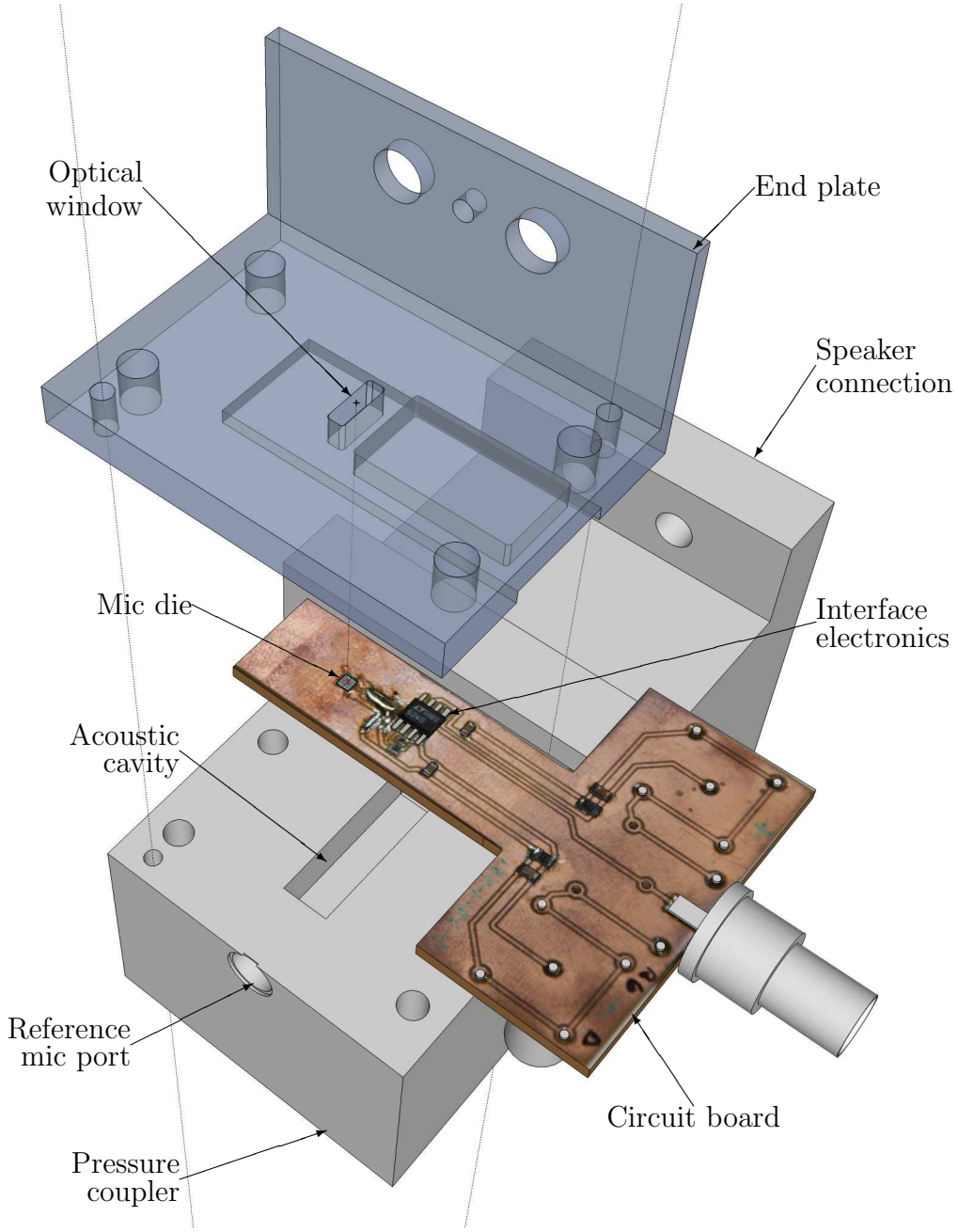

Figure 8-10. Pressure coupler assembly (fasteners not shown).

The measurement setup for extraction of acoustic mass and compliance is shown in Figure 8-12. A 1 kHz sinusoid generated by an Agilent 33120A function generator[1] and

[1] Although the laser vibrometer system possesses its own function generator as part of the scanner controller, intermittent problems with prolonged usage of sinusoids led to the use of the external function generator.

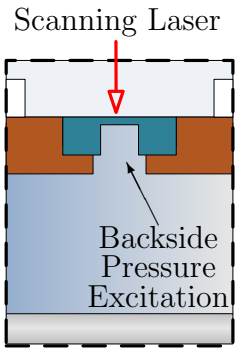

Figure 8-11. Closeup depiction of a microphone die in the pressure coupler setup.

amplified via a Stewart Electronics PA-1008 200 Watt Power Amplifier drove the BMS 4590P compression driver. The reference microphone was amplified using a SRS Model SR560 Low-Noise Preamplifier and the amplified signal served as the reference in the laser vibrometer system's native data acquisition system. The reference microphone calibration was entered directly into the laser vibrometer software to avoid the need to adjust data in a post-processing step. The velocity signal from the laser vibrometer itself was the other input for the two-channel system. Specific measurement settings are collected in Table 8-8.

Table 8-8. Pressure coupler measurement settings.

Parameter	Setting
Span	5 kHz
FFT Lines	400
Resolution	12.5 Hz
# of averages	100 (Complex)
Window	Rectangular
Signal	1 kHz Sine
LV sensitivity	DC 1 mm/s/V
Typical pressure level	95 dB to 105 dB
SR560 gain	100

Diaphragm scans were taken over polar grids of 20 azimuthal points and 13-15 radial points, depending on diaphragm size; Figure 8-13 shows one such grid. Prior to integration, the actual measured data — which was returned from the laser vibrometer system as a scattered dataset — was interpolated to form a surface via MATLAB's

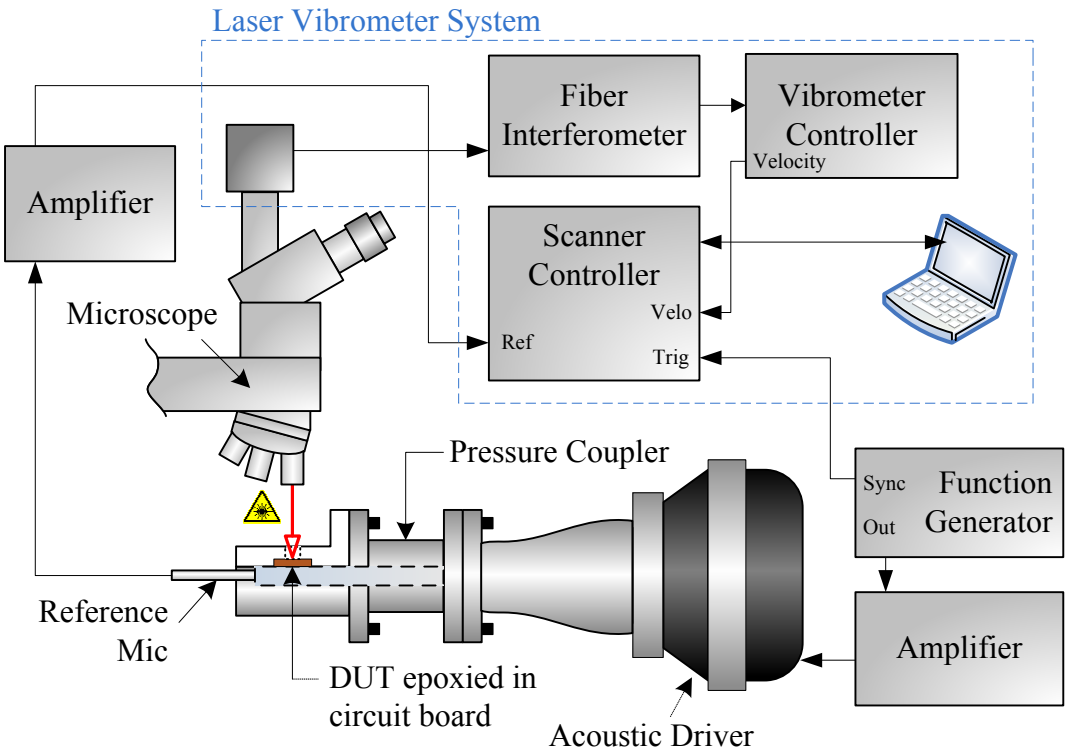

Figure 8-12. Experimental setup for extraction of acoustic mass and compliance.

`TriScatteredInterp` [138]. Independent surfaces were created for the real and imaginary part of the frequency response function and then recombined for integration in MATLAB's numerical routine `dblquad` [138], which employs Gauss quadrature over a rectangular domain in two dimensions. The integration was performed in r-θ space using surfaces originally interpolated in Cartesian space.

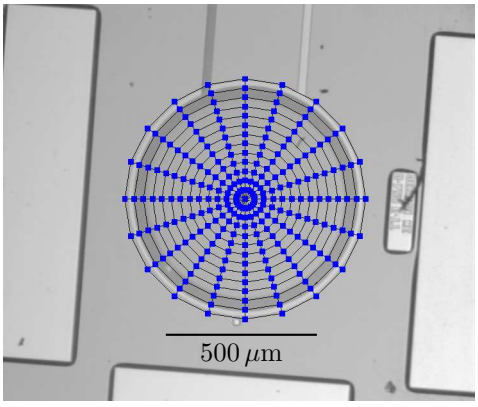

Figure 8-13. Laser vibrometer scan grid overlayed on design E micrograph (diaphragm outer diameter of 756 μm).

In order to predict the quality of the interpolation and integration routine apriori, a test numerical integration was performed using an analytical expression for the typical static deflection shape of a clamped plate subjected to a uniform pressure load [121],

$$w(r) = w_0 \left[1 - \left(\frac{r}{a}\right)^2\right]^2, \tag{8–17}$$

interpolated at the actual measurement scan points. Error was found to be approximately 1 % relative to the associated analytical volume displacement, $\Delta\forall = w_0 a^2 \pi/3$. The integration procedure was also compared to trapezoidal integration of the same test problem and it was confirmed that the Gauss quadrature routine was more accurate by several tenths of a percent.

8.1.5.2 Frequency response measurement setup

The requirement of short circuit conditions, in addition to input channel limitations of the laser vibrometer system, did not enable simultaneous acquisition of microphone electrical output during the actual parameter extraction experiment. Instead, the electrical acquisition was done in a separate measurement, also in the pressure coupler, to determine the microphone sensitivities.

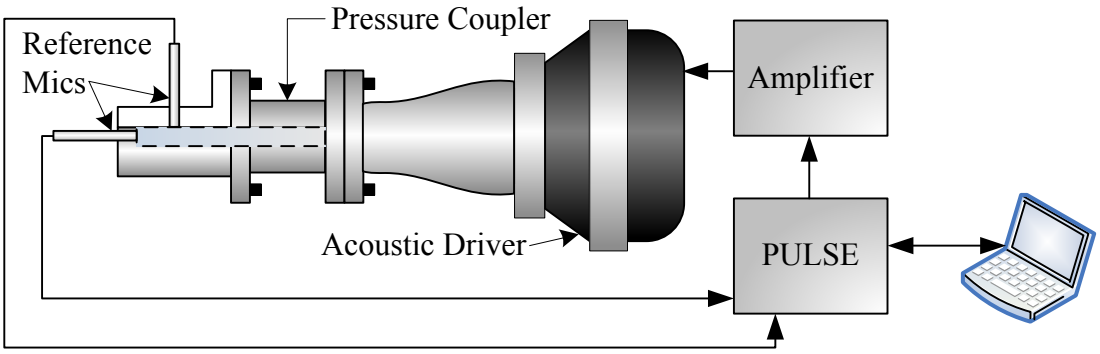

Figure 8-14. Experimental setup for pressure coupler calibration.

First, the relationship between the pressures at the two measurement locations was confirmed via the experimental setup pictured in Figure 8-14, in which two Brüel and Kjær 4138 microphones were mounted at the reference and DUT positions. The frequency

response function between the two microphones [Pa/Pa] was then computed using the Brüel and Kjær PULSE system and software.

For the actual sensitivity measurement, the experimental setup of Figure 8-15 was used, with the DUT and reference microphone installed as shown. Again utilizing the PULSE system, the frequency response function between the DUT and reference microphone was computed. Measurement settings for both sets of measurements are found in Table 8-9.

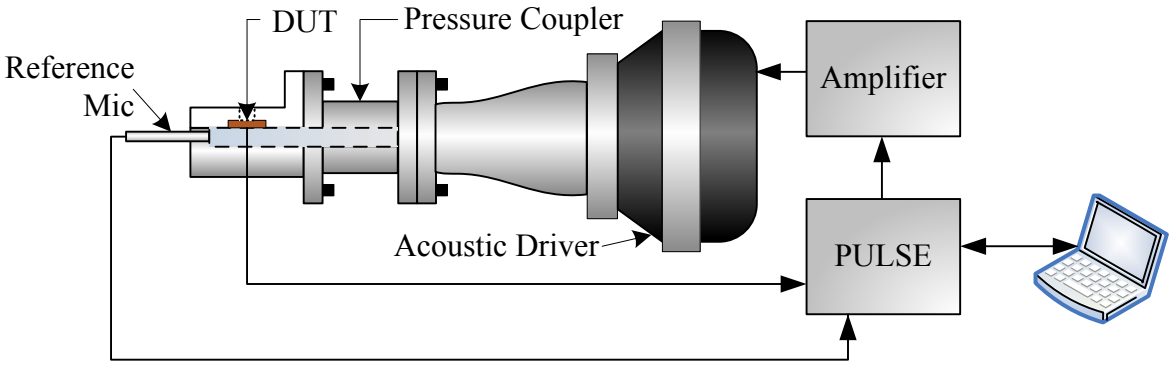

Figure 8-15. Experimental setup for microphone calibration in the pressure coupler.

Table 8-9. Settings for sensitivity measurement of pressure coupler microphones.

Grouping	Parameter	Setting
Acquisition	FFT Type	Zoom
	Center Frequency	1.9 kHz
	Bandwidth	3.2 kHz
	Frequency Range	300 Hz–3.5 kHz
	# of FFT Lines	3200
	Frequency Resolution	1 Hz
	Window	Rectangular
	Overlap	0%
	# of Averages	100
Generator	Signal	Pseudo random noise
	Frequency Range	300 Hz–3.5 kHz
	Spectral Lines	3200

8.1.5.3 Effective piezoelectric coefficient measurement setup

The expression for the effective piezoelectric coefficient, Equation 5–8, may be written for the measurement setting as

$$d_a = \int_0^{2\pi} \int_0^{a_2} H_{vw}|_{p=0}(r,\theta) r dr d\theta, \tag{8–18}$$

where H_{vw} is the frequency response function relating the displacement $w(r,\theta)$ to an excitation voltage. The subscript $_{p=0}$ follows from the theoretical definition of d_a and denotes an acoustic short circuit condition. Such a condition is only achievable for excitation well below the vent/cavity break frequency, which based on other sensitivity measurements must be in the vicinity of 50 Hz. Because the measurand of the laser vibrometer, velocity, is $\propto f$ for a harmonic input [34], the signal-to-noise ratio of the measurement degrades considerably at low frequencies. Instead, $H_{vw}|_{p=0}$ was obtained via excitation at 1 kHz. The diaphragm displacement due to voltage excitation for the

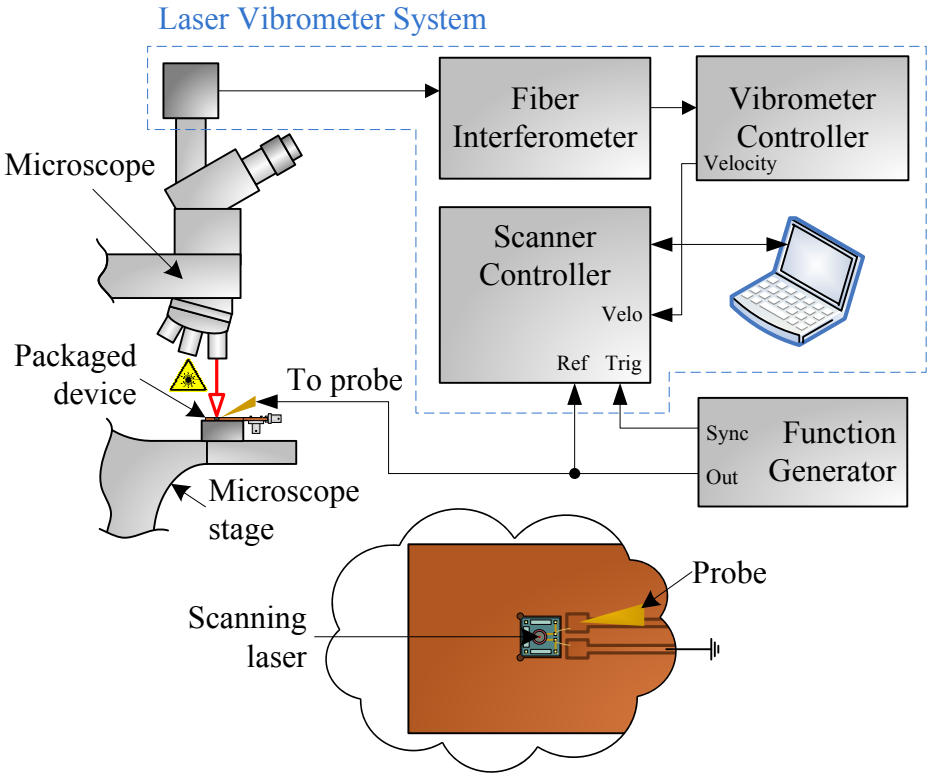

Figure 8-16. Experimental setup for extraction of effective piezoelectric coefficient.

devices packaged as described in Section 8.1.5.1 was measured via the experimental setup shown in Figure 8-16. In this setup, the circuit boards housing the microphones were affixed directly to the microscope stage under the laser vibrometer and electrically driven with a 1 kHz sinusoidal waveform delivered via probe needles. The interface electronics present on the board were disconnected from the microphone for this measurement. The measurement settings for the laser vibrometer scan were the same as those in Table 8-8 and the same integration strategy described in Section 8.1.5.1 was also used.

8.2 Experimental Results

Experimental results for each of the measurements discussed in Section 8.1 are found in this section. Calculation details for 95% confidence interval ($U_{95\%}$) estimates presented with many experimental results are found in Appendix C.

8.2.1 Die Selection

A series of wafer maps capturing the variation of f_r and $S_{a,0}$ over portions of wafers 116 and 138 are presented in Figures 8-17–8-22. Outliers were detected and removed from the datasets via the method discussed in Section 8.1.1 prior to mapping. In all, 14/249 die (5.6%) from wafer 116 and 7/190 die (3.7%) from wafer 138 were identified as outliers.

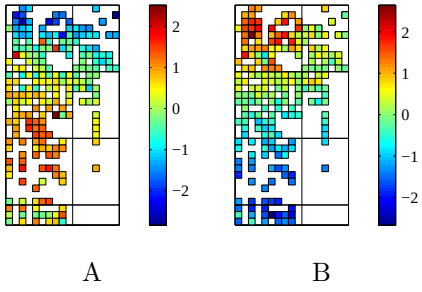

Figure 8-17. Maps of diced section of wafer 116 (all designs) with color corresponding to the number of standard deviations from individual mean of each design. A) f_r. B) $S_{a,0}$.

Figure 8-17 and 8-18 respectively show maps of the wafer 116 and 138 subregions in terms of the number of sample standard deviations each die was from the sample mean for its particular design. A trend clearly existed across both wafers, with f_r and $S_{a,0}$ trending

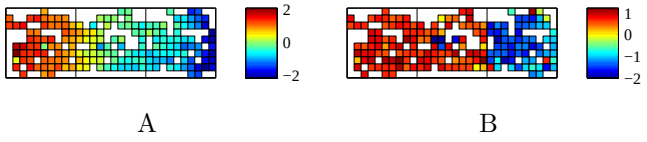

Figure 8-18. Maps of diced section of wafer 138 (all designs) with color corresponding to the number of standard deviations from individual mean of each design. A) f_r. B) $S_{a,0}$.

oppositely with respect to each other across wafer 116 but largely the same way with respect to each other across wafer 138.

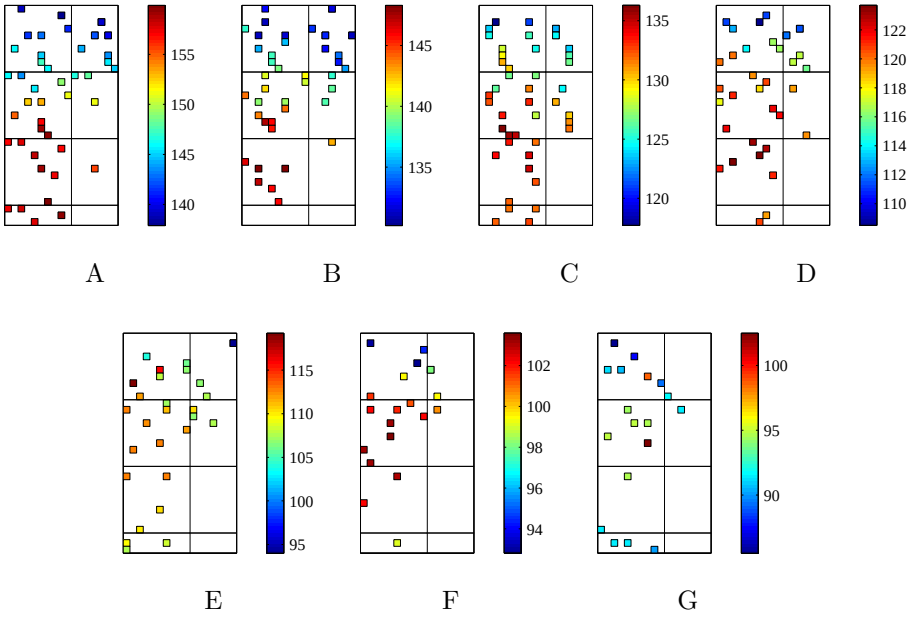

Figure 8-19. Resonant frequency maps for wafer 116 [kHz]. A) Design A. B) Design B. C) Design C. D) Design D. E) Design E. F) Design F. G) Design G.

Figure 8-19 and Figure 8-20 show f_r and $S_{a,0}$, respectively, for wafer 116 in individual maps for each design. Trends are clear for designs A–D, with resonant frequency increasing away from the wafer center and displacement sensitivity decreasing. In Figure 8-19(E–G), the lack of a corresponding cross-wafer trend in f_r for designs E–G, with larger diaphragms that are more susceptible to buckling, may indicate the diaphragm response to stress is not stable die-to-die for these designs.

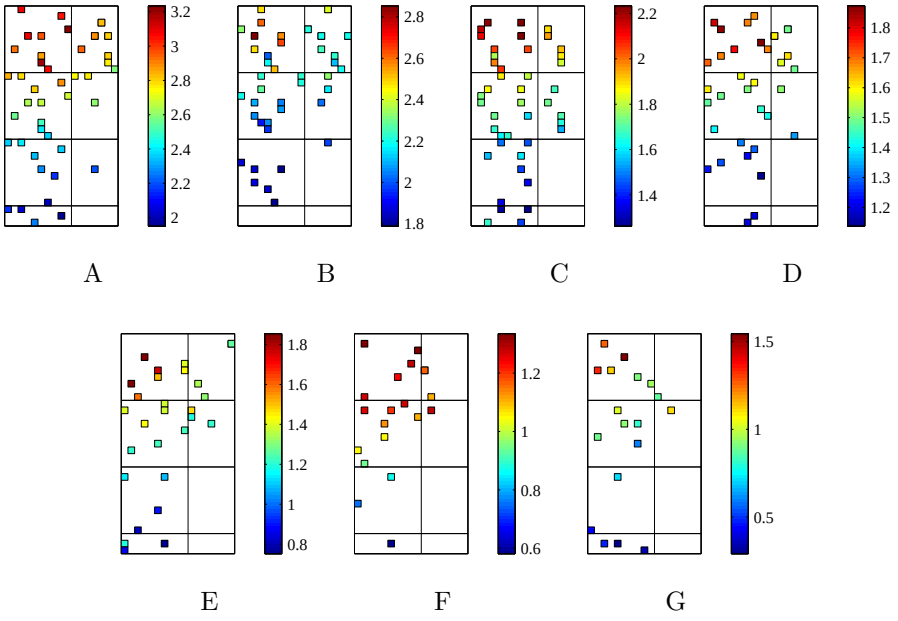

Figure 8-20. Center displacement sensitivity maps for wafer 116 [nm/V]. A) Design A. B) Design B. C) Design C. D) Design D. E) Design E. F) Design F. G) Design G.

Maps for f_r and $S_{a,0}$ on wafer 138, Figure 8-21 and 8-22, respectively, show an entirely different trend than wafer 116. On wafer 138, the resonant frequency and sensitivity both decrease together toward the outside of the wafer and the trend is consistent for all designs.

Table 8-10 collects the sample means (denoted with overbars) and sample standard deviations (s) of f_r and $S_{a,0}$ for each design. As expected, the resonant frequency decreases with design letter, reflecting the expected increase in compliance with diaphragm size. Perhaps unexpectedly, $\overline{S}_{a,0}$ actually decreases with diaphragm size for wafer 116, but again the buckled nature of those diaphragms makes drawing conclusions difficult. For wafer 138, $\overline{S}_{a,0}$ remains essentially constant for all designs, which is also unexpected. It is shown in Section 8.2.5 that the nearly constant $\overline{S}_{a,0}$ across all designs is only indicative of a consistent center deflection and that contrary to expectations, the piezoelectric coupling coefficient does not necessarily trend strongly with center deflection.

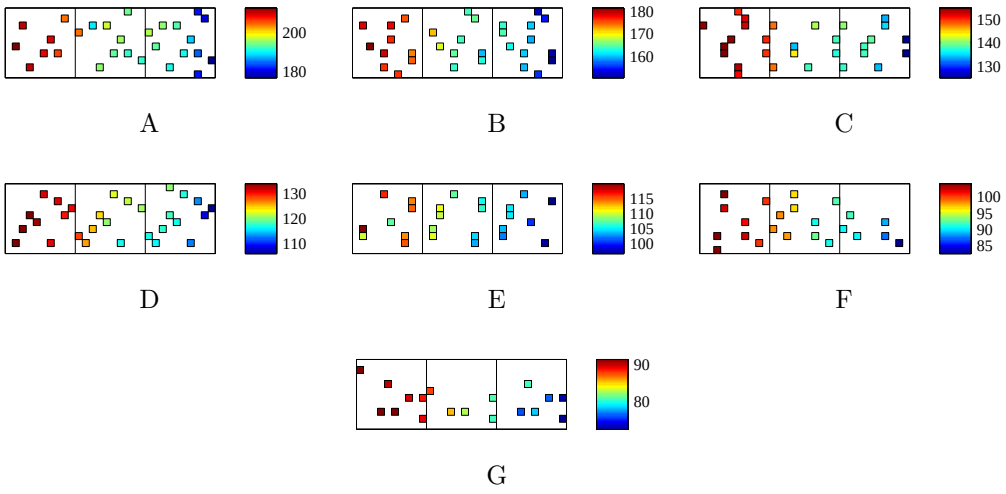

Figure 8-21. Resonant frequency maps for wafer 138 [kHz]. A) Design A. B) Design B. C) Design C. D) Design D. E) Design E. F) Design F. G) Design G.

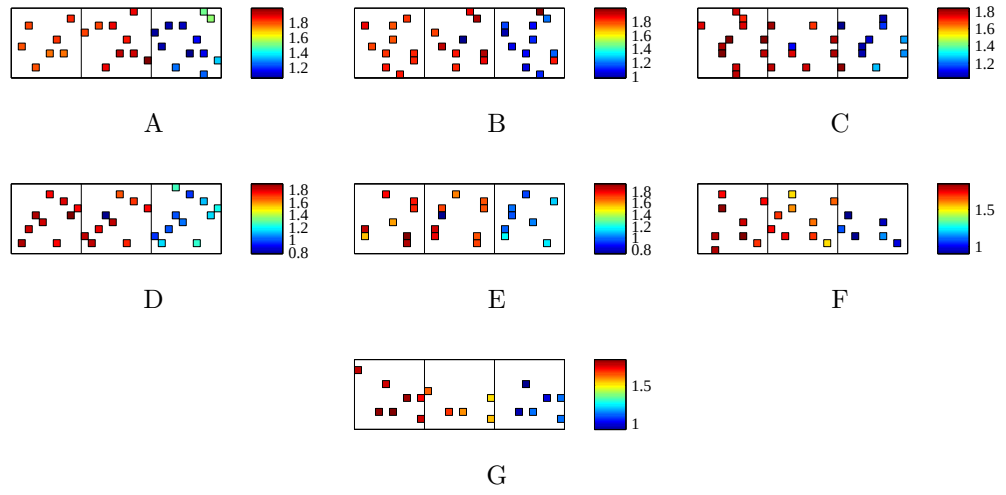

Figure 8-22. Center displacement sensitivity maps for wafer 138 [nm/V]. A) Design A. B) Design B. C) Design C. D) Design D. E) Design E. F) Design F. G) Design G.

One or more microphones of several designs were selected to be packaged for rigorous characterization and parameter extraction. For each design, the die with the highest values of $S_{a,0}$ were generally selected for packaging as microphones with the expectation that the piezoelectric coupling coefficient d_a, and thus sensitivity, would trend similarly. Section 8.2.5 addresses the validity of this assumption. As the only other comparative measure available, f_r was used as a second metric for choosing like microphones of the

Table 8-10. Wafer statistics.

	Wafer 116				Wafer 138			
	f_r [kHz]		$S_{a,0}$ [nm/V]		f_r [kHz]		$S_{a,0}$ [nm/V]	
Design	$\overline{f_r}$	s_{f_r}	$\overline{S_{a,0}}$	$s_{S_{a,0}}$	$\overline{f_r}$	s_{f_r}	$\overline{S_{a,0}}$	$s_{S_{a,0}}$
A	149.4	7.2	2.7	0.3	195.0	10.0	1.6	0.3
B	138.5	5.7	2.2	0.2	166.0	8.8	1.6	0.4
C	129.3	4.4	1.8	0.3	142.9	8.9	1.6	0.3
D	118.1	4.4	1.5	0.2	122.4	7.9	1.5	0.4
E	109.0	5.3	1.3	0.3	107.5	5.8	1.5	0.4
F	100.1	3.4	1.1	0.2	95.8	6.1	1.5	0.3
G	92.6	3.9	0.9	0.3	83.6	6.6	1.5	0.3

Table 8-11. Pre- and post-packaging LV measurements.

	Pre-Packaging		Post-Packaging	
DUT	f_r [kHz]	$S_{a,0}$ [nm/V]	f_r [kHz]	$S_{a,0}$ [nm/V]
116-1-I6-A	147.3	3.18	127.0	3.79
116-1-C4-B	133.0	2.51	127.5	2.17
116-3-F7-B	144.0	2.08	160.3	1.88
116-1-E2-C	124.9	2.11	123.5	2.10
138-1-E4-D	132.6	1.80	126.9	1.89
138-1-I2-D	133.5	1.91	116.5	1.68
138-1-I8-E	114.4	1.85	106.4	1.63
138-1-H3-F	103.9	1.82	99.9	1.45
138-1-J3-F	103.9	1.87	129.5	1.46

same design. In all, 10 die were successfully shepherded through the packaging process described in Section 7.3, with one used exclusively for the parasitic capacitance extraction.

Pre- and post-packaging laser vibrometer measurements of the nine packaged microphones are collected in Table 8-11 . Changes in resonant frequency were likely due to inadvertent introduction of packaging stress to the microphone diaphragm during the die epoxy step, which modifies the effective compliance of the diaphragm. A corresponding change in $S_{a,0}$ due to packaging stress was also observed. Figure 8-23 shows that the shifts in f_r and $S_{a,0}$ following the packaging process were not at all consistent, particularly the direction of the shifts. This suggests the epoxy is not entirely consistent; some notable

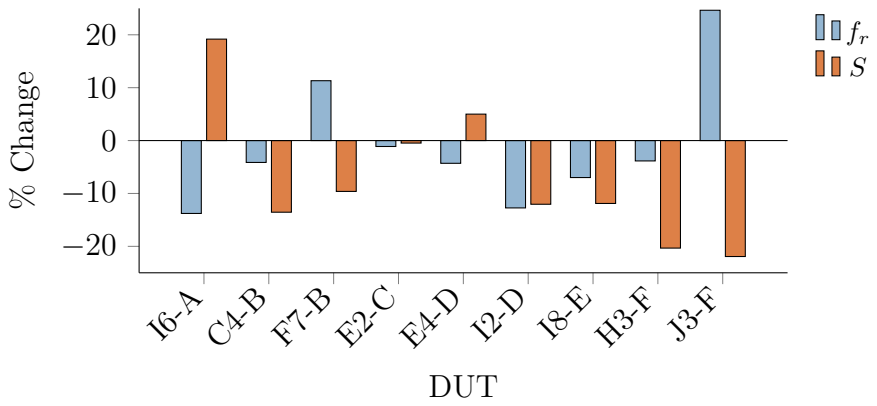

Figure 8-23. Changes in resonant frequency and displacement sensitivity due to packaging.

possibilities that were not investigated further are uneven sealing of the microphone die to the board or epoxy penetrating slightly into the back cavity.

8.2.2 Diaphragm Topography

The diaphragm static deflection profiles for pre- and post-packaged microphones are shown in Figures 8-24A–8-24B, respectively. Six devices representing one batch of packaged sensors are included, and just the inner regions of the diaphragms are shown for clarity. Displacements are referenced to the surrounding substrates and were taken along a line bisecting the diaphragm through the vent hole.

Microphone C4-B, the only device included in Figure 8-24 that hailed from wafer 116, is shown to be significantly buckled. This was expected given the visible buckling of all devices on wafer 116. The total deflection over the inner portion of the diaphragm before packaging was approximately 2.7 μm compared to a total thickness in that region of 2.14 μm. The static deflection profiles of the unpackaged microphones hailing from wafer 138 were consistent and much lower than microphone C4-B, typically about 300 nm from edge to center.

After packaging, the buckled amplitude of C4-B was reduced to approximately 2.3 μm and the static deflection profiles of the wafer 138 devices were no longer as tightly grouped. Figure 8-25 shows the differences in static deflection after the packaging process,

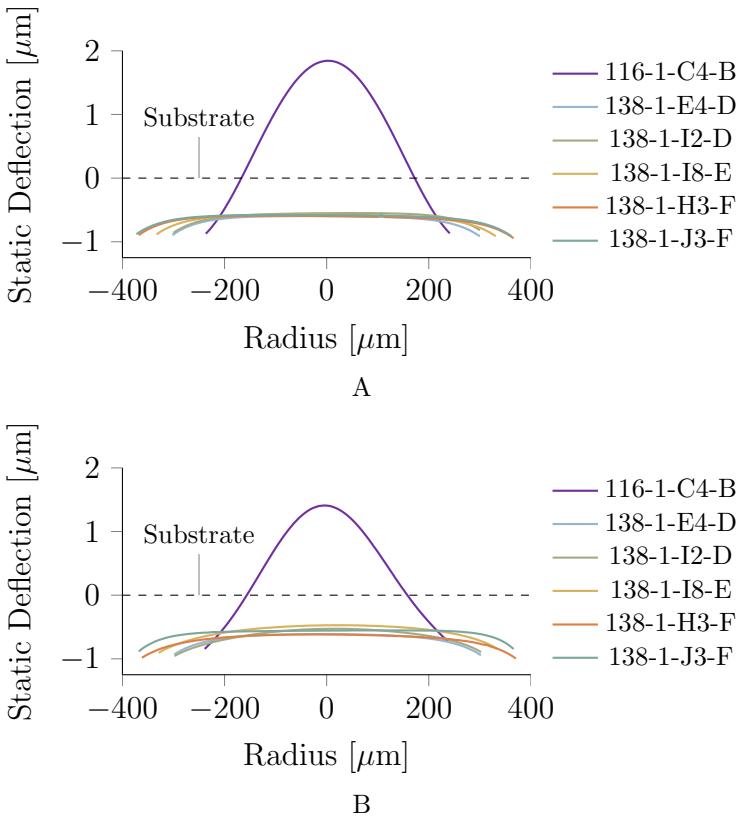

Figure 8-24. Static deflection profiles of several microphone diaphragms (inner portions). A) Before packaging. B) After packaging.

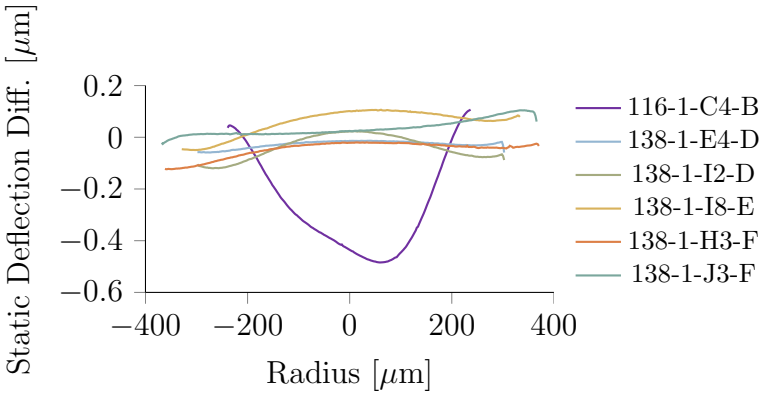

Figure 8-25. Static deflection differences for pre- and post-packaged microphones.

which were typically around 10 nm in total for wafer 138 microphones and clearly not of an axially symmetric nature.

8.2.3 Acoustic Characterization

8.2.3.1 Frequency response

The frequency response function measurements made in helium are collected in Figure 8-26, shown in terms of magnitude and relative phase to the reference microphone. The frequency response magnitude is flat to well within the stated goal of ±2 dB over the portion of the audio band measured (300 Hz–20 kHz). Deviations in the magnitude and phase close to 20 kHz are the result of higher-order acoustic modes beginning to propagate. Note that the phase is relative to the Brüel and Kjær 4138. The microphones were phase-matched to <2° out to 15 kHz.

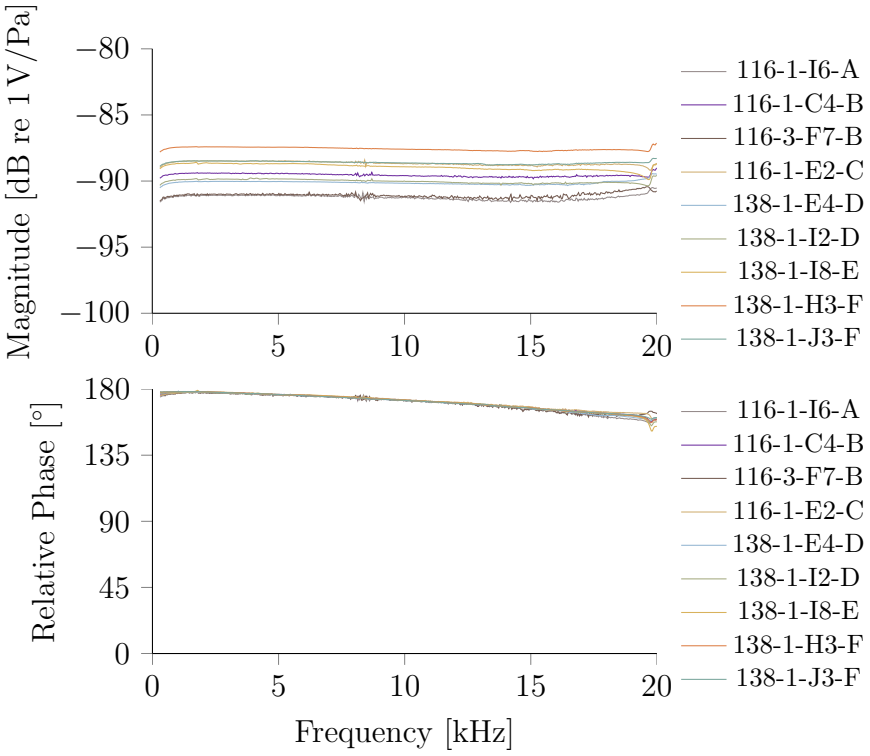

Figure 8-26. Microphone frequency responses in helium.

The sensitivities of the MEMS microphones are collected in Table 8-12 in both dB and μV/Pa for measurements performed in air. The sensitivities in helium were all lower than in air as expected, by up to 0.2 dB (2.3 %). The phase roll-off in helium was less than in air by approximately 5° at 6 kHz.

Table 8-12. Microphone frequency response characteristics† at 1 kHz in air.

DUT	Magnitude		Relative Phase [°]
	dB re 1 V/Pa	μV/Pa	
116-1-I6-A	-90.68 ± 0.06	29.2 ± 0.2	176.8 ± 0.1
116-1-C4-B	-89.24 ± 0.06	34.5 ± 0.2	177.6 ± 0.1
116-3-F7-B	-90.87 ± 0.06	28.6 ± 0.2	177.0 ± 0.1
116-1-E2-C	-88.52 ± 0.06	37.5 ± 0.2	177.6 ± 0.1
138-1-E4-D	-89.86 ± 0.06	32.1 ± 0.2	177.3 ± 0.1
138-1-I2-D	-89.77 ± 0.06	32.5 ± 0.2	177.9 ± 0.1
138-1-I8-E	-88.71 ± 0.06	36.7 ± 0.2	178.1 ± 0.1
138-1-H3-F	-87.19 ± 0.06	43.7 ± 0.3	178.3 ± 0.2
138-1-J3-F	-88.25 ± 0.06	38.7 ± 0.3	178.0 ± 0.2

† Uncertainties are for 95% confidence interval (see Section C.2).

The normalized frequency response measurements for microphones 138-1-I2-D and 138-1-J3-F obtained at low frequencies in Boeing Corporation's "infinite" tube setup are captured in Figure 8-27. The −2 dB frequencies for 138-1-I2-D and 138-1-J3-F were 85 Hz and 69 Hz, respectively, which compared well with theoretical predictions of 70 Hz and 75 Hz.

8.2.3.2 Linearity

Figure 8-28 shows plots of DUT voltage versus the reference microphone pressure level (both taken at the fundamental frequency of 1 kHz) in both linear units and decibels for 7 of the 9 microphones. Some variation from linearity can be detected for several devices in Figure 8-28A, most notably 116-1-I6-A and 116-1-C4-B. The response of the remaining two devices, 116-3-F7-B and 116-1-E2-C, are shown in Figure 8-29, with abrupt deviations from linearity happening near 1000 Pa and 1500 Pa, respectively. This behavior can likely be attributed to sudden snap-through of the buckled diaphragms, a nonlinear dynamic event. Further investigation of this unwanted phenomenon is beyond the scope of this study, but the interested reader is referred to various texts on nonlinear dynamics of structures [179, 180].

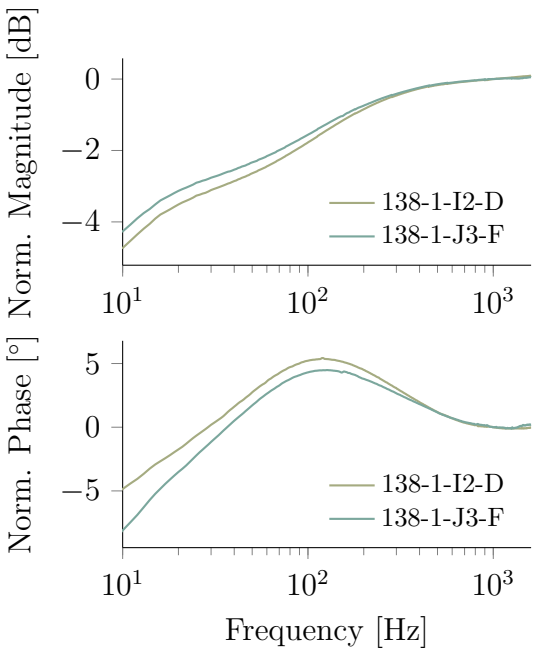

Figure 8-27. Piezoelectric microphone frequency response functions at low frequencies normalized to values at 1 kHz

The THD calculations for all 9 microphones are shown in Figure 8-30. The large levels of distortion (30–40%) for the reference microphone, which by specification should not exceed 3% until 190 dB, indicate the measurement environment is harmonic-rich. Nonlinearities in the amplifier, speaker, and acoustic propagation path are all possible contributors. As a result, the calculated THD of Figure 8-30 are not valid in an absolute sense, though comparison to the reference microphone "THD" provides valuable qualitative information. For DUT THD that aligns closely enough to that of the reference (as is the case with all wafer 138 microphones), one can be reasonably confident that the distortion limit is well above 160 dB. The same cannot be said definitively for the wafer 116 microphones, which exhibit varying levels of deviation from the reference microphone "THD."

The results of the Boeing linearity measurements are collected in Table 8-13. The calculated total harmonic distortion in both the DUT and reference microphone are given for each test, and SPLs are reported as the pressure measured at 2.5 kHz (the fundamental

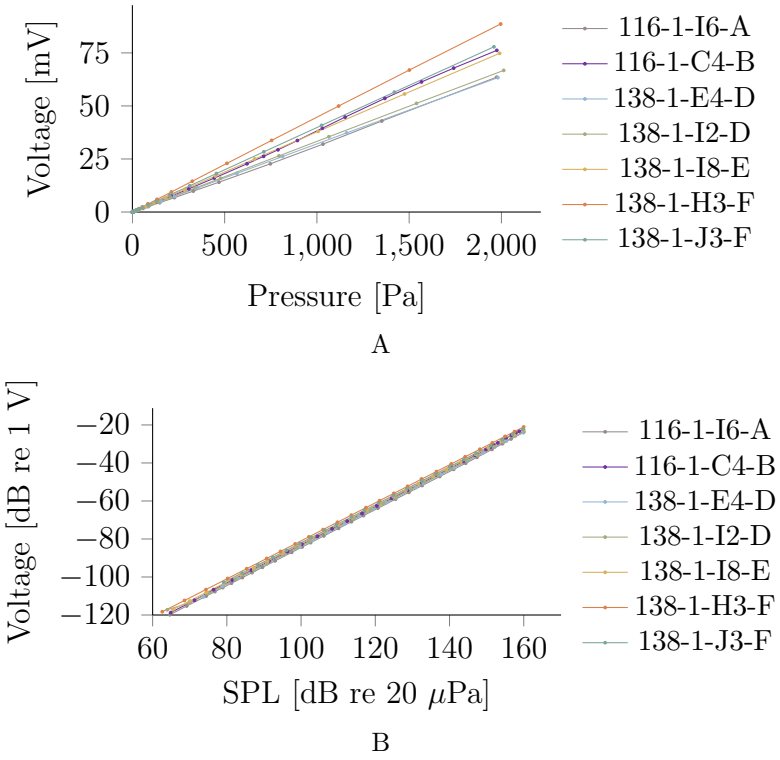

Figure 8-28. Linearity measurements. A) Linear scale. B) In dB.

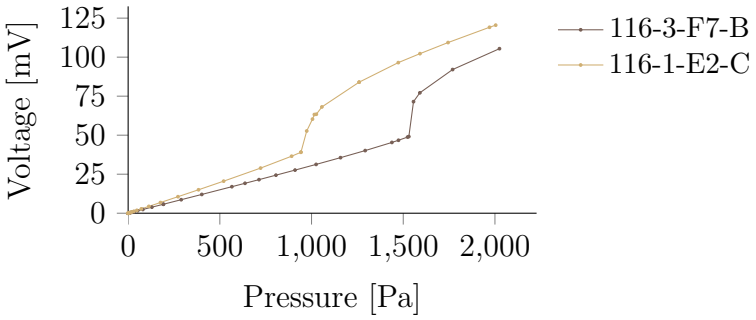

Figure 8-29. Linearity measurements showing unusual nonlinear behavior.

frequency) using each microphone. Because both the Brüel and Kjær 4938 and DUT distort while also serving as sources of the SPL measurement, the reported SPLs must be regarded as lower bounds on the distortion limits. That is, reported distortion occurs at a SPL greater than that given here. Therefore, the device 138-1-J3-F almost certainly meets the 172 dB specification for PMAX given in Section 1.2.

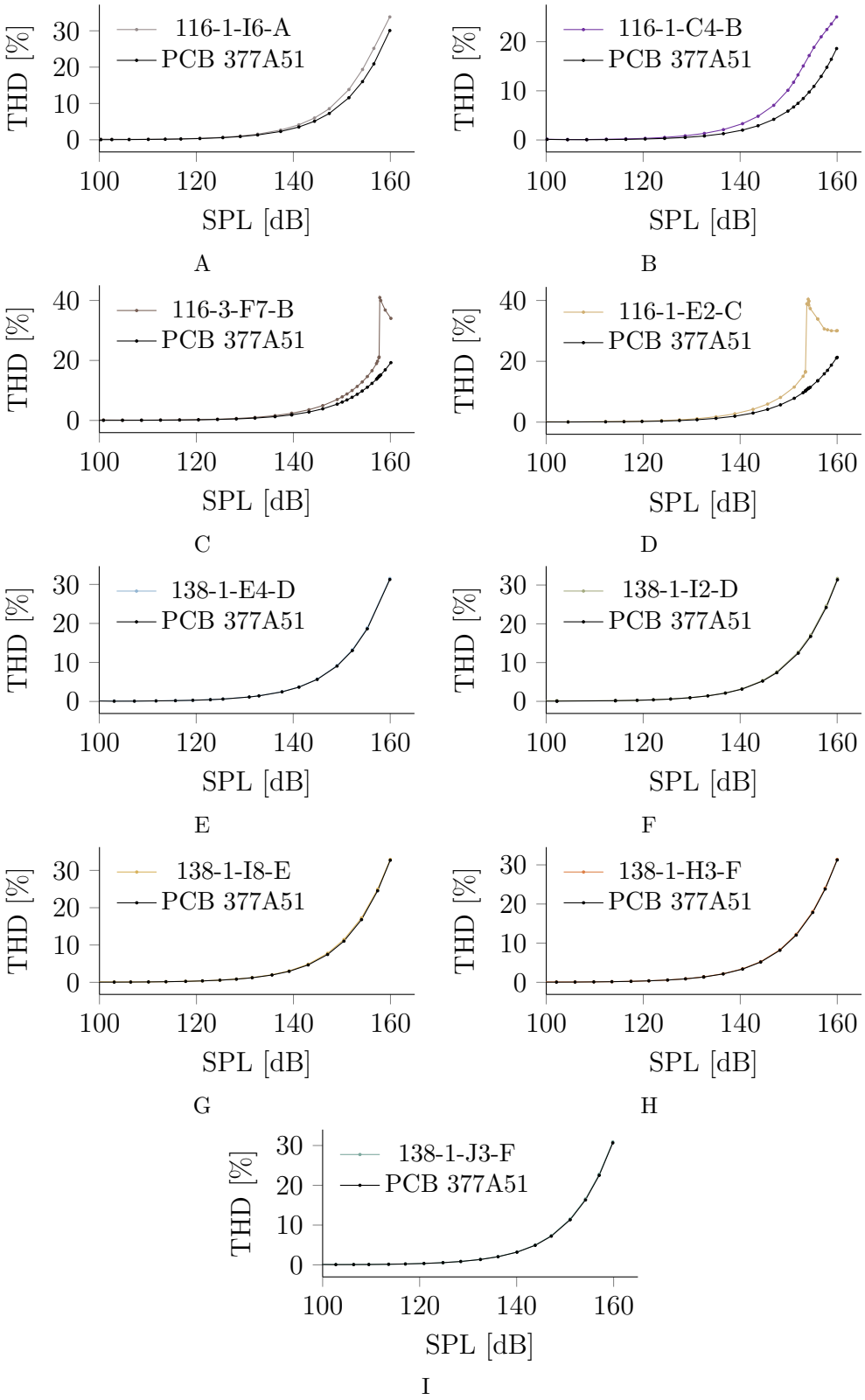

Figure 8-30. THD measurements. A) 116-1-I6-A. B) 116-1-C4-B. C) 116-1-F7-B. D) 116-1-E2-C. E) 138-1-E4-D. F) 138-1-I2-D. G) 138-1-I8-E. H) 138-1-H3-F. I) 138-1-J3-F.

Table 8-13. THD measurements performed at Boeing Corporation.

Measurement	Microphone	SPL [dB]	THD [%]
1	138-1-I2-D	166.0	3.0
	Brüel and Kjær 4938	167.6	2.4
2	138-1-J3-F	171.6	2.9
	Brüel and Kjær 4938	171.3	11.5

8.2.4 Electrical Characterization

8.2.4.1 Noise floor

Figure 8-31 shows the measured output-referred noise floor. Eight of the nine microphones show very similar behavior, with one (138-1-I8-E) serving as the outlier. As predicted, the noise associated with R_{ep} dominates at low frequencies before approaching the thermal noise floor, where the dominant noise contributor transitions to the buffer amplifier. The amplifier's current noise clearly dominates over its voltage noise, as predicted, since the noise level at 100 kHz is well above the voltage noise level of $8\,\text{nV}/\sqrt{\text{Hz}}$ to $10\,\text{nV}/\sqrt{\text{Hz}}$ (-162 dB to -160 dB).

Although differences between the noise curves of Figure 8-31 are small, they are greater than the measurement uncertainty (refer to Section C.3.1), and the microphones do have successively lower noise floors as the diaphragm diameter increases (A→F). This behavior is consistent with predictions in Section 5.3.3.1, which showed that output noise PSD associated with R_{ep} in the roll-off region was $\propto 1/R_{ep}C_{et}^2$; this implies that as predicted, the increase in C_{et}^2 across designs was dominant compared to the corresponding decrease in R_{ep}. In addition, the lower amplifier current noise contribution beyond the corner frequency for designs with large diaphragm diameters was attributed to the reduced electrical impedance (higher capacitance) of the devices per Equation 5–65.

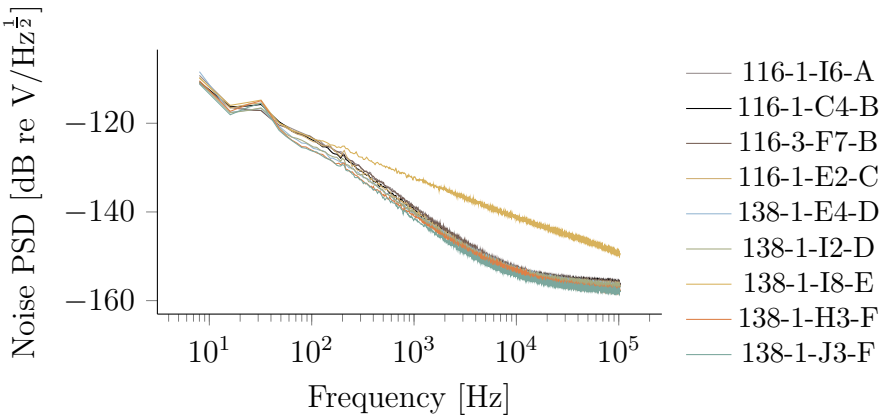

Figure 8-31. Output-referred noise floors.

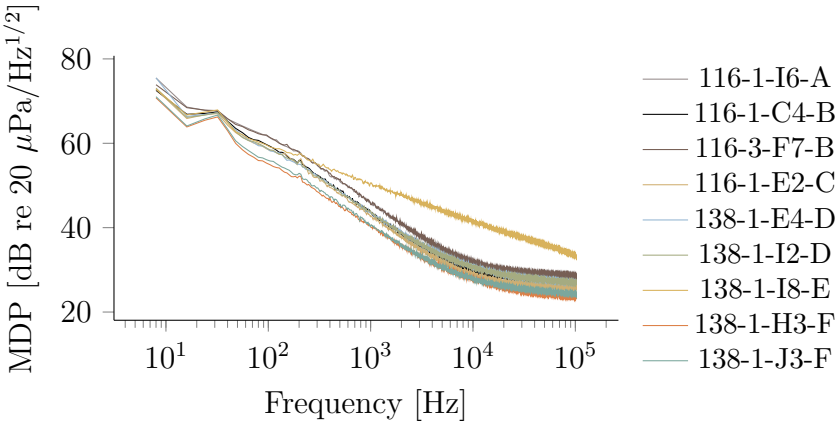

Figure 8-32. Minimum detectable pressure spectra.

Figure 8-32 shows the minimum detectable pressure spectra of the microphones, calculated from the measured output noise PSD S_o^v as

$$\mathrm{MDP} = 20\log_{10}\left(\frac{\sqrt{S_o^v/\left|S_{va}\right|^2}}{20\,\mu\mathrm{Pa/Hz^{1/2}}}\right), \tag{8–19}$$

with $|S_{va}|$ taken from Table 8-12. Because $|S_{va}|$ is a flatband sensitivity value, this calculation is not valid in the vicinity of and beyond $f_{\pm 2\,\mathrm{dB}}$.

Due to differences in sensitivity, the minimum detectable pressure curves are less tightly grouped compared to the output-referred equivalents. Figure 8-32 shows that the noise floor in the audio band is below 70 dB for all microphones, and below the target 1 kHz narrow bin MDP of 48.5 dB, save for the outlier, 138-1-I8-E. By 20 kHz, minimum

detectable pressure levels decline to 25–30 dB SPL. The uncertainties in the MDP spectra range from ±0.10 dB in the first two frequency spans (< 12.8 kHz) down to ±0.04 dB above 38.4 kHz; refer to Section C.3.1 for details.

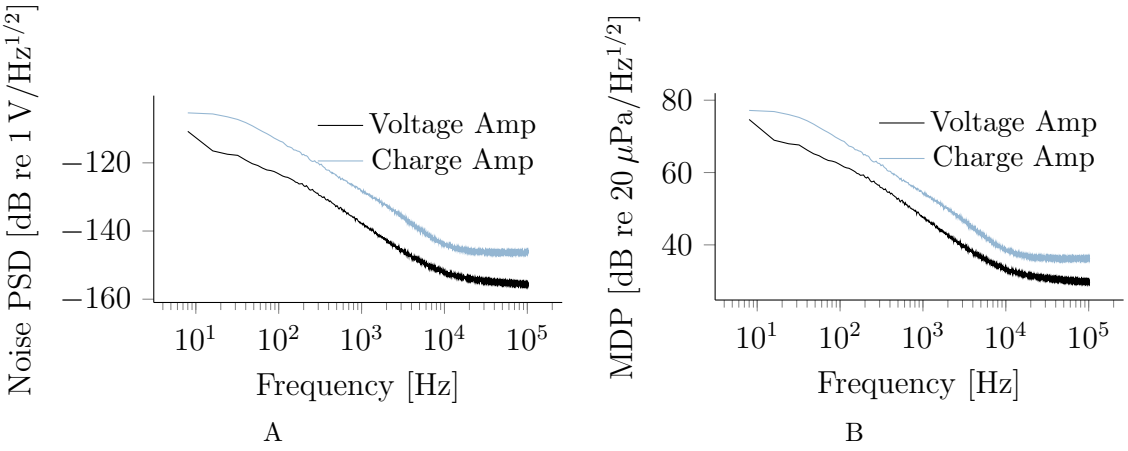

Figure 8-33. Noise floor spectra for 116-1-J7-A with a voltage amp and charge amp. A) Noise PSD. B) MDP.

The noise floor spectra for device 116-1-J7-A packaged with a voltage and charge amplifier are given in Figure 8-33. Figure 8-33A shows that the noise spectra of the system is nearly 10 dB higher when the device is packaged with a charge amplifier. For the charge amplifier case at low frequencies, the equivalent resistor $R_{ep} \parallel R_{efb}$ is a source of more noise than just R_{ep} in the voltage amplifier case. At higher frequencies, it is likely that the approximately 2× greater voltage noise of the OPA129 amplifier used in the charge amplifier circuit compared to the LTC6240 amplifier used in the voltage amplifier circuit dominates, especially given the extra gain factor for this noise source associated with the charge amplifier circuitry, $(1 + C_{et}/C_{efb})^2$ (per Equation 5–75). In terms of MDP, the charge amplifier configuration yields a minimum detectable pressure approximately 6.5 dB greater than that of the voltage amplifier configuration, even despite the higher sensitivity of the microphone for the former (discussed in Section 8.2.4.3).

From the data presented in Figure 8-32, several variants on minimum detectable pressure were computed and are presented in Table 8-14 with estimated 95% confidence

Table 8-14. Minimum detectable pressure metrics.

DUT	dB†	dB OASPL‡	dB(A) OASPL§
116-1-J7-A#	54.3	95.1	88.6
116-1-J7-A	47.6	88.1	82.0
116-1-I6-A	45.7	87.2	80.4
116-1-C4-B	43.7	85.6	78.1
116-3-F7-B	45.5	87.2	80.4
116-1-E2-C	42.8	85.0	77.3
138-1-E4-D	43.5	85.3	78.3
138-1-I2-D	43.9	85.3	78.2
138-1-I8-E	50.6	89.2	86.3
138-1-H3-F	40.2	82.7	75.0
138-1-J3-F	40.4	83.2	75.4

† Narrow bin ($f = 1\,\text{kHz}$, $\Delta f = 1\,\text{Hz}$); $|U_{95\%}| < 0.10\,\text{dB}$ ‡ $|U_{95\%}| < 0.01\,\text{dB}$ § $|U_{95\%}| < 0.007\,\text{dB(A)}$
# Packaged with charge amplifier

intervals (refer to Section C.3 for details). First, the already-discussed narrow bin MDP is given. The second and third columns of Table 8-14 contain integrated measures of MDP, the overall sound pressure level (OASPL) and A-weighted overall sound pressure level (AOASPL). In both cases, integration of the noise floor was completed over the individual 1/3 octave bands from 20 Hz–20 kHz, with A-weighting [33] also employed in the latter case before final summation. Every microphone had an MDP more than 3 dB below the specification of 93 dB OASPL except 116-1-J7-A packaged with the charge amplifier. The A-weighted MDP is lower in all cases because A-weighting de-emphasizes noise contributions at frequencies below 1 kHz, where the MDP spectrums are the highest.

8.2.4.2 Impedance

A typical impedance measurement, presented in terms of the real and imaginary components of admittance (conductance, G, and susceptance, B) are found in Figure 8-34. The standard and overall uncertainties associated with G and B are also included. The curve fit does an excellent job matching susceptance, which is capacitance-dominated; typical R-squared values for that fit were unity. The general character of the conductance is also captured, though clearly there is room for improvement in the model; typical

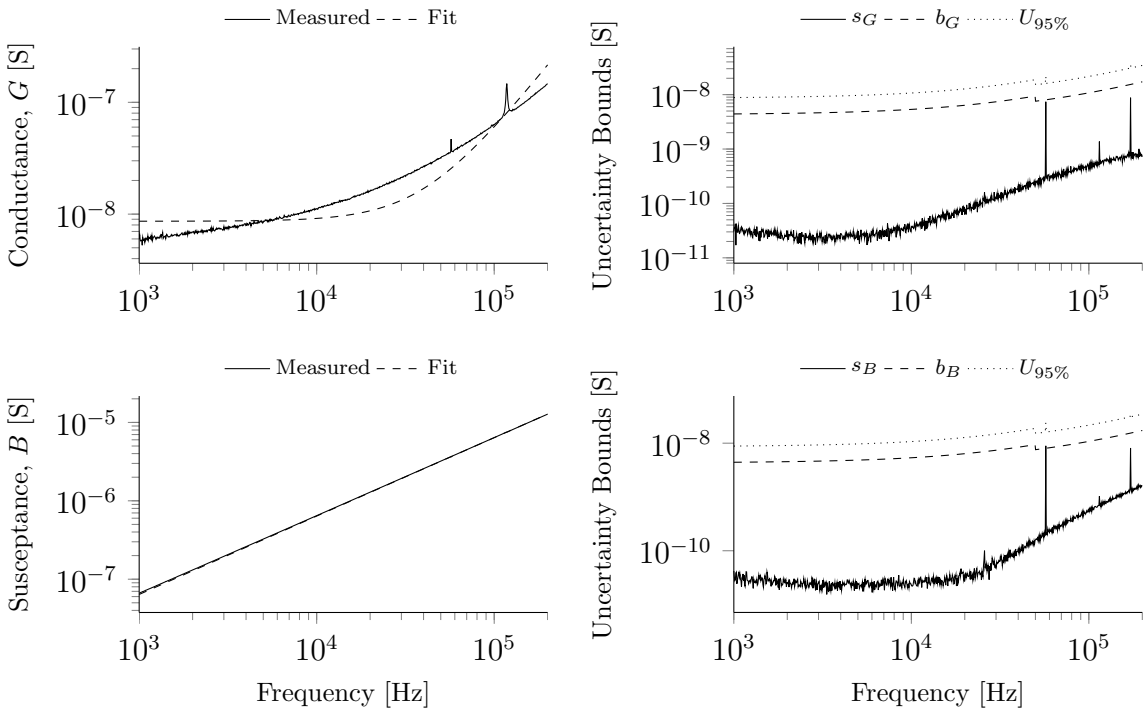

Figure 8-34. Admittance measurements and fits for microphone B5-E.

R-squared values for this fit were 0.84. Note that the resonance at approximately 118 kHz is not captured due to simplifications made in the equation for electrical impedance

Extracted parameters, together with their 95% confidence bounds, are collected and compared with the theory in Table 8-15, in which the final letter in the DUT label continues to stand for the design. Capacitance predictions are within 7 % to 15 % of extracted values, with the predictions improving with diaphragm size. The difference between measured and theoretical values is essentially constant at approximately 1 pF for all designs, suggesting the presence of additional parasitics and/or inherent bias in the parallel plate capacitance prediction. It is well-known that the parallel-plate approximation tends to underpredict capacitance, with the underprediction becoming more severe as lateral dimensions approach the electrode separation distance [181].

8.2.4.3 Parasitic capacitance extraction

Figure 8-35 shows the frequency response functions of microphone 116-1-J7-A packaged with a voltage and charge amplifier. The microphone's sensitivity when packaged

Table 8-15. Extracted electrical parameters.

	Measurement†						Theory‡	
DUT	$C_{ef}+C_{eo}$ [pF]		R_{ep} [MΩ]		R_{es} [kΩ]		$C_{ef}+C_{eo}$ [pF]	R_{ep} [MΩ]
116-3-B9-A	6.9	±0.03 %	96	±4 %	2.6	±2 %	5.9	401
116-3-C5-A	6.9	±0.03 %	98	±4 %	2.5	±2 %	5.9	401
116-3-B8-B	7.5	±0.03 %	131	±7 %	2.5	±2 %	6.5	362
116-3-C6-B	7.5	±0.03 %	127	±7 %	2.4	±2 %	6.5	362
116-3-B7-C	8.2	±0.03 %	122	±6 %	2.0	±2 %	7.2	326
116-3-C7-C	8.2	±0.02 %	120	±7 %	2.0	±2 %	7.2	326
116-3-C8-D	9.1	±0.02 %	116	±6 %	1.6	±2 %	8.2	286
116-3-E9-D	9.2	±0.02 %	115	±6 %	1.6	±2 %	8.2	286
116-3-B5-E	10.2	±0.02 %	116	±6 %	1.3	±2 %	9.2	253
116-3-C9-E	10.1	±0.02 %	113	±6 %	1.3	±2 %	9.2	253
116-3-B4-F	11.3	±0.02 %	115	±6 %	1.0	±2 %	10.4	225
116-3-C10-F	11.3	±0.02 %	116	±6 %	1.0	±2 %	10.4	225
116-3-B1-G	12.8	±0.02 %	112	±6 %	0.9	±2 %	12.0	195
116-3-D5-G	12.8	±0.02 %	112	±6 %	0.9	±2 %	12.0	195

† Uncertainties are 95% confidence intervals in the curve fit ‡ $R_{es} = 4.1\,\text{k}\Omega$

with the charge amplifier was approximately 3 dB (1.4×) higher, indicating the parasitic capacitance did indeed play a prominent role in limiting the sensitivity of the device. The phase component of Figure 8-35 shows the output of the microphone with charge amp was 180° out of phase with the voltage amplifier configuration, as predicted in Equations 5–53 and 5–53.

The extracted parasitic capacitance $C_{ep} + C_{ea}$ is plotted against frequency in Figure 8-36 together with its 95% confidence interval (see Section C.5). The parasitic capacitance was relatively constant over the measurement bandwidth, indicating the character of its impact was captured accurately by the models. Taking the mean of each of the curves, a single extracted value for C_{ep} is approximately 4 pF ± 1 pF. The uncertainty analysis, found in Section C.5, suggests that C_{fb} is a dominant error source. Also note that the measured capacitance approximating $C_{ef} + C_{eo}$ were selected from the B9-A and C5-A die.

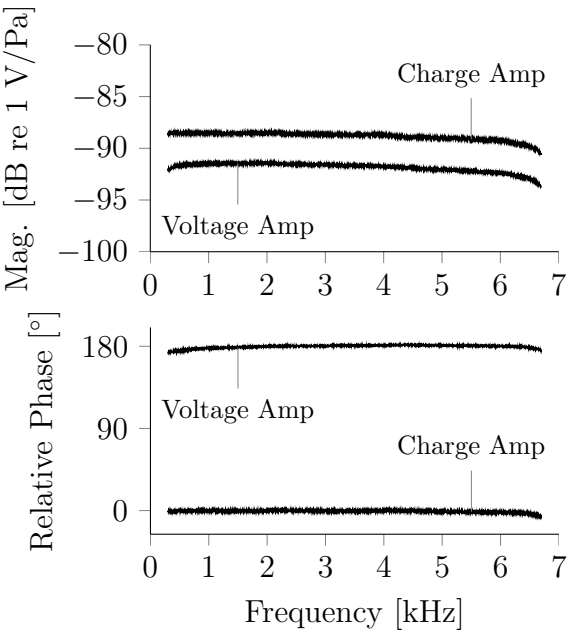

Figure 8-35. Frequency response function of microphone 116-1-J7-A tested with voltage and charge amplifier circuitry.

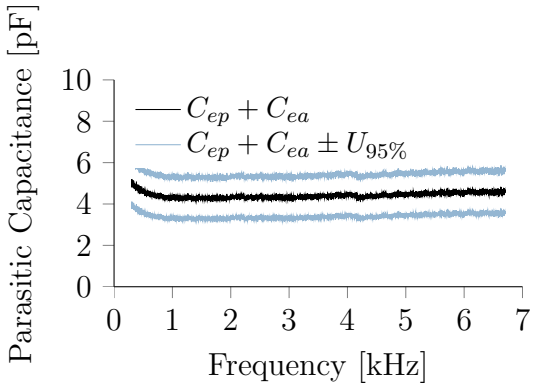

Figure 8-36. Parasitic capacitance extraction for microphone 116-1-J7-A.

The estimated open circuit sensitivities of all microphones, found using Equation 8–14 under the assumption of negligible change in C_p from device-to-device, are found in Table 8-16. Details of the uncertainty analysis are presented in Section C.5. In general, the extracted open circuit sensitivities of the microphones were 3–4 dB (40–60%) higher than the sensitivity measured with the voltage amplifier package (Section 8.1.3.1). Table 8-16 also compares the extracted open circuit sensitivites to those predicted using

Table 8-16. Open-circuit sensitivity estimates.

DUT	S_{oc}† [dB re 1 V/Pa] Measured‡	Predicted	$S_{oc} - S_{va}$‡ [dB re 1 V/Pa]
116-1-J7-A	-87.2 ± 0.8	-89.8	4.2 ± 0.8
116-1-I6-A	-86.4 ± 0.8	-89.8	4.3 ± 0.8
116-1-C4-B	-85.2 ± 0.8	-88.7	4.0 ± 0.8
116-3-F7-B	-86.8 ± 0.8	-88.7	4.0 ± 0.8
116-1-E2-C	-84.8 ± 0.7	-87.7	3.7 ± 0.7
138-1-E4-D	-86.4 ± 0.7	-86.6	3.4 ± 0.7
138-1-I2-D	-86.4 ± 0.7	-86.6	3.4 ± 0.7
138-1-I8-E	-85.6 ± 0.6	-85.6	3.1 ± 0.6
138-1-H3-F	-84.3 ± 0.6	-84.6	2.9 ± 0.6
138-1-J3-F	-85.4 ± 0.6	-84.6	2.9 ± 0.6

† Taken at 1 kHz ‡ With 95% confidence bounds (Section C.5)

the lumped element model. The agreement is excellent for wafer 138, but not so for the buckled devices of wafer 116.

8.2.5 Electroacoustic Parameter Extraction

Prior to performing measurements directly for electroacoustic parameter extraction, the pressure coupler assembly was characterized. Figure 8-37 shows the "gain" (really attenuation) between the DUT position and reference mic position. At 1 kHz the pressure was shown to be approximately 1.5 % less at the DUT location. Extracted parameters were therefore corrected for this difference in pressure.

Uncorrected frequency response measurements for each of the specially-packaged parameter extraction microphones are presented in Figure 8-38. The sensitivities trend lower than like designs measured in the PWT, suggesting increased parasitic capacitance was associated with the package for this experiment. This was not unexpected, as the FR4 boards in which microphones were packaged featured longer trace lengths, different routing of traces, extra solder connections, etc. Measurement uncertainty (95% confidence) was <1% and dominated by bias error in the reference microphone calibration (see Section C.2).

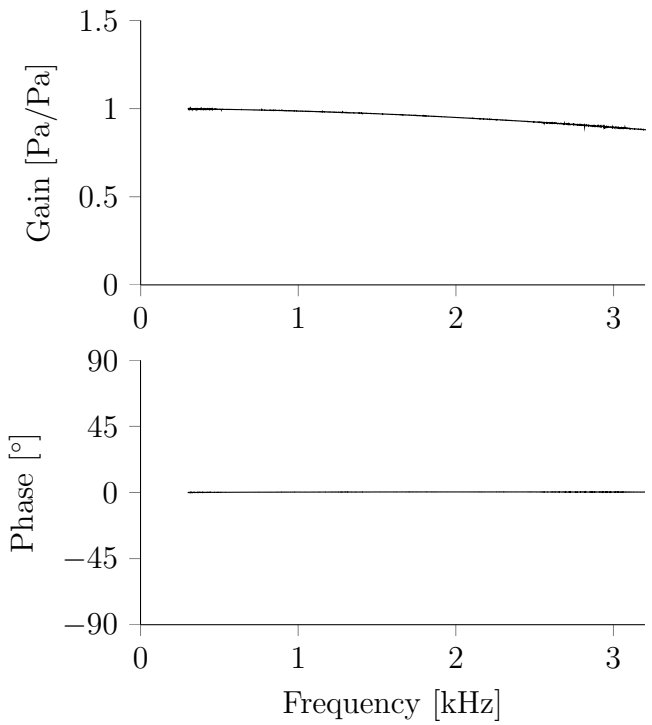

Figure 8-37. Comparison of pressure at test and reference locations in pressure coupler.

Mode shapes associated with the diaphragm displacement response under pressure loading, H_{pw}, are collected in Figure 8-39. In addition to surface maps, profiles taken through $x = 0$ and $y = 0$ are projected on the plot back planes to enable comparison. A clear trend of increasing center displacement and volume displacement from design D to design F is observed, providing an immediate visual indication that the measured compliance increases with diaphragm size. The corresponding mode shape predictions (incremental deflection) obtained from the static diaphragm model ranged from approximately 0.2 nm/Pa to 0.3 nm/Pa, lower than the observed 0.4 nm/Pa to 0.65 nm/Pa in Figure 8-39.

The acoustic compliance and mass extracted from the mode shapes of Figure 8-39 are presented in Table 8-17, with both compliance and mass trending as the models. The measured and predicted values of M_{ad} agreed to within 10%, though it is important to acknowledge that both values shared a common input — the aerial density ρ_a associated with the diaphragm materials (Equation 5–13). In general, the resolution

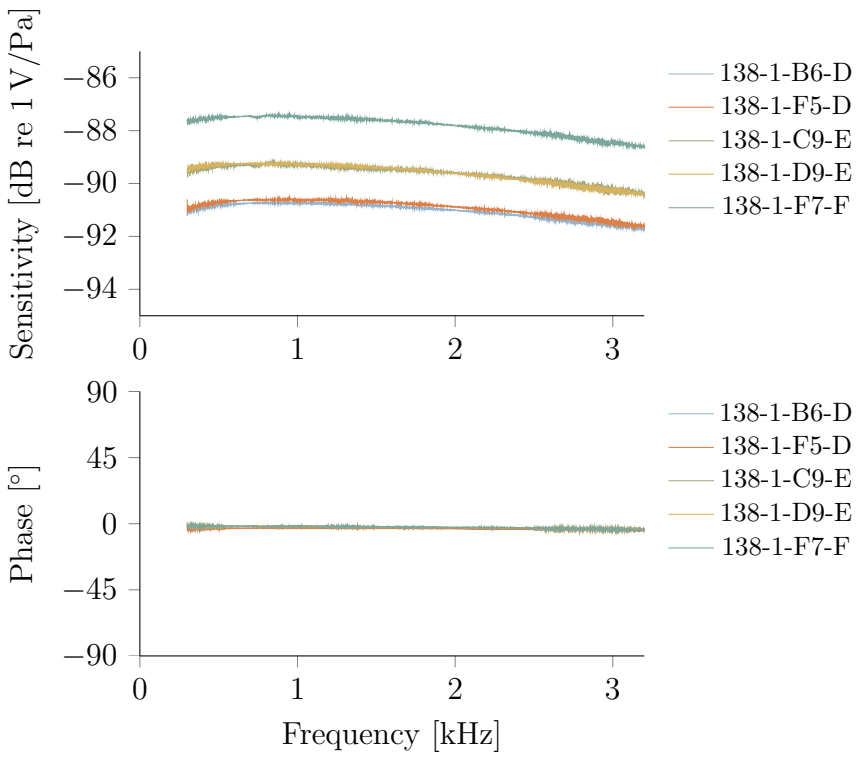

Figure 8-38. Frequency response of piezoelectric microphones in pressure coupler.

of a lumped element model is expected to be on the order of 10%. Measurement of C_{ad}, which possessed no such shared input, yielded nearly double the predicted value, though extracted values for like designs were consistent to within <7 %. Measurement uncertainty estimates were calculated via Monte Carloa simulation as addressed in Section C.6.

The under-prediction of C_{ad} via the diaphragm model could stem from one of several sources. Finite element analysis validation of an example microphone in Section 5.2.5 was in close agreement with the analytical predictions, but this analysis shared the same model inputs for residual stresses, material properties, etc. Error in residual stress inputs could have a significant impact on the model predictions. In addition, the geometry in both the analytical diaphragm model and finite element model was simplified from the true geometry, which does not truly possess the sharp step discontinuity at $r = a_1$. A final possibility is compliance in the boundary conditions of the diaphragm, which would

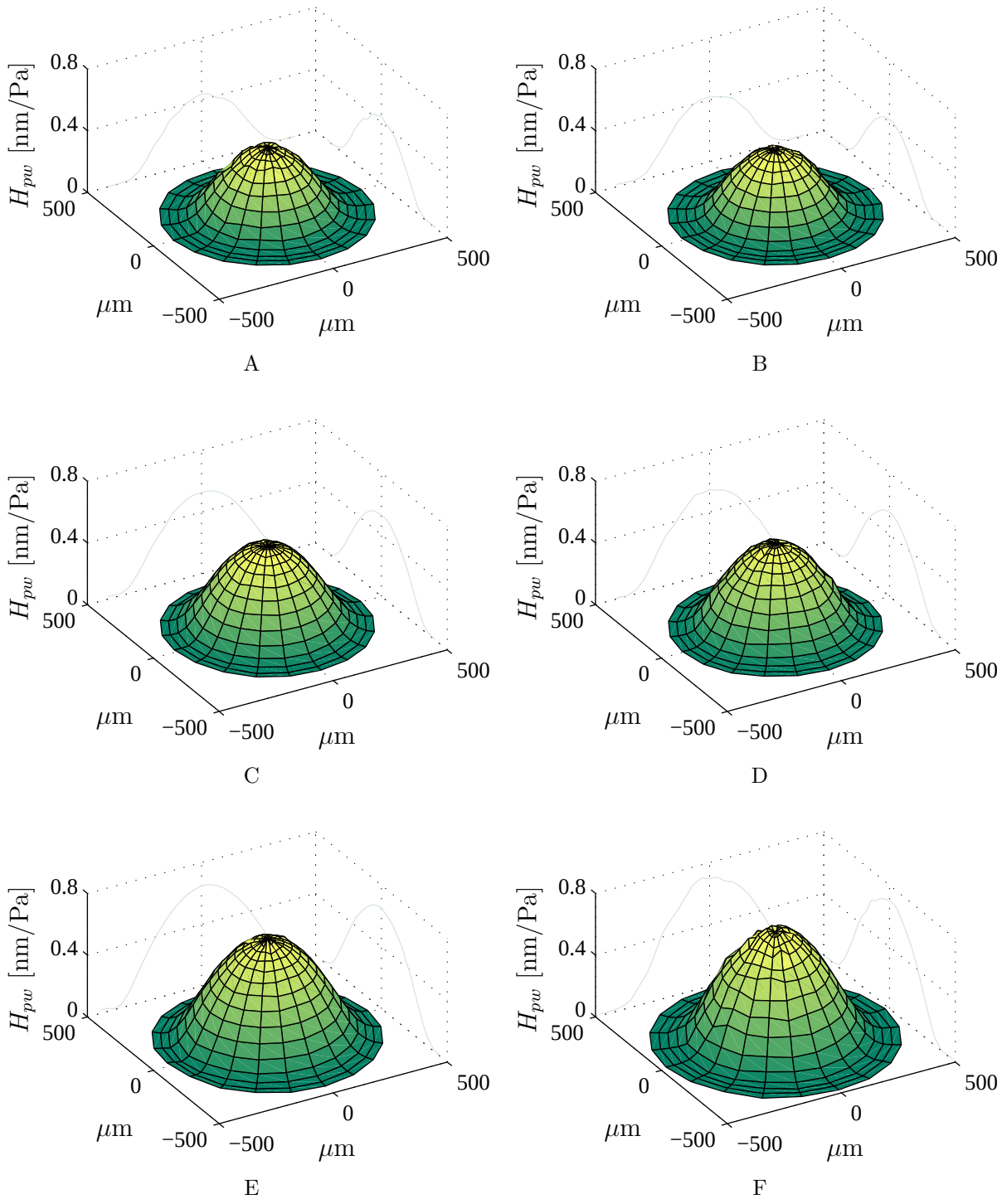

Figure 8-39. Displacement per pressure plots. A) 138-1-B6-D. B) 138-1-F5-D. C) 138-1-C9-E. D) 138-1-D9-E. E) 138-1-F7-F. F) 138-1-H7-F.

lead to larger deflection in reality than predicted by the model, which utilized an idealized clamped boundary condition.

Table 8-17. Extracted mechanoacoustic parameters.

	C_{ad} $[10^{-17}\,\mathrm{m^3/Pa}]^{\dagger}$		M_{ad} $[10^{4}\,\mathrm{kg/m^4}]^{\ddagger}$	
DUT	Measured	Predicted	Measured	Predicted
138-1-F5-D	5.3	2.7	2.4	2.2
138-1-B6-D	5.6	2.7	2.3	2.2
138-1-C9-E	8.7	4.2	1.8	1.8
138-1-D9-E	8.6	4.2	1.9	1.8
138-1-F7-F	12.7	6.3	1.5	1.5
138-1-H7-F	13.4	6.3	1.6	1.5

$^{\dagger}\,|U_{95\%}| < 1.4\%$ $^{\ddagger}\,|U_{95\%}| < 0.03\%$ (not accounting for density)

The mode shapes associated with diaphragm displacement response under voltage loading, H_{vw}, are shown in Figure 8-40. Unlike in the counterpart measurement for H_{pw}, there is very little change in center displacement from design to design in Figure 8-40. However, the increasing diaphragm area from design D to design F naturally leads to substantial increases in volume displacement given the stocky nature of the mode shapes. Thus, the center displacement per voltage $H_{vw}\,(r = 0)$ alone, as measured in the die selection methodology of Sections 8.1.1 and 8.2.1, does not provide a good measure of the relatively larger differences in d_a among different device designs. However, it probably remains a good screening metric among like designs. Alternatively, using the single point measurement to scale an experimental or analytical estimate of the diaphragm mode shape could prove to be a superior screening method among all designs.

Electroacoustic parameters are collected in Table 8-18, with measurement/theory agreement on the order of 20 % for d_a. The extracted value was consistent between like designs, with <3% variation. For an example of how d_a and $H_{vw}\,(r = 0)$ do not track consistently, consider the values associated with each quantity for microphones 138-1-H7-F and 138-1-B6-D in Figure 8-40 and Table 8-18. It is seen that d_a for 138-1-H7-F was approximately 65% greater than for 138-1-B6-D, but $H_{vw}\,(r = 0)$ was only 8% greater.

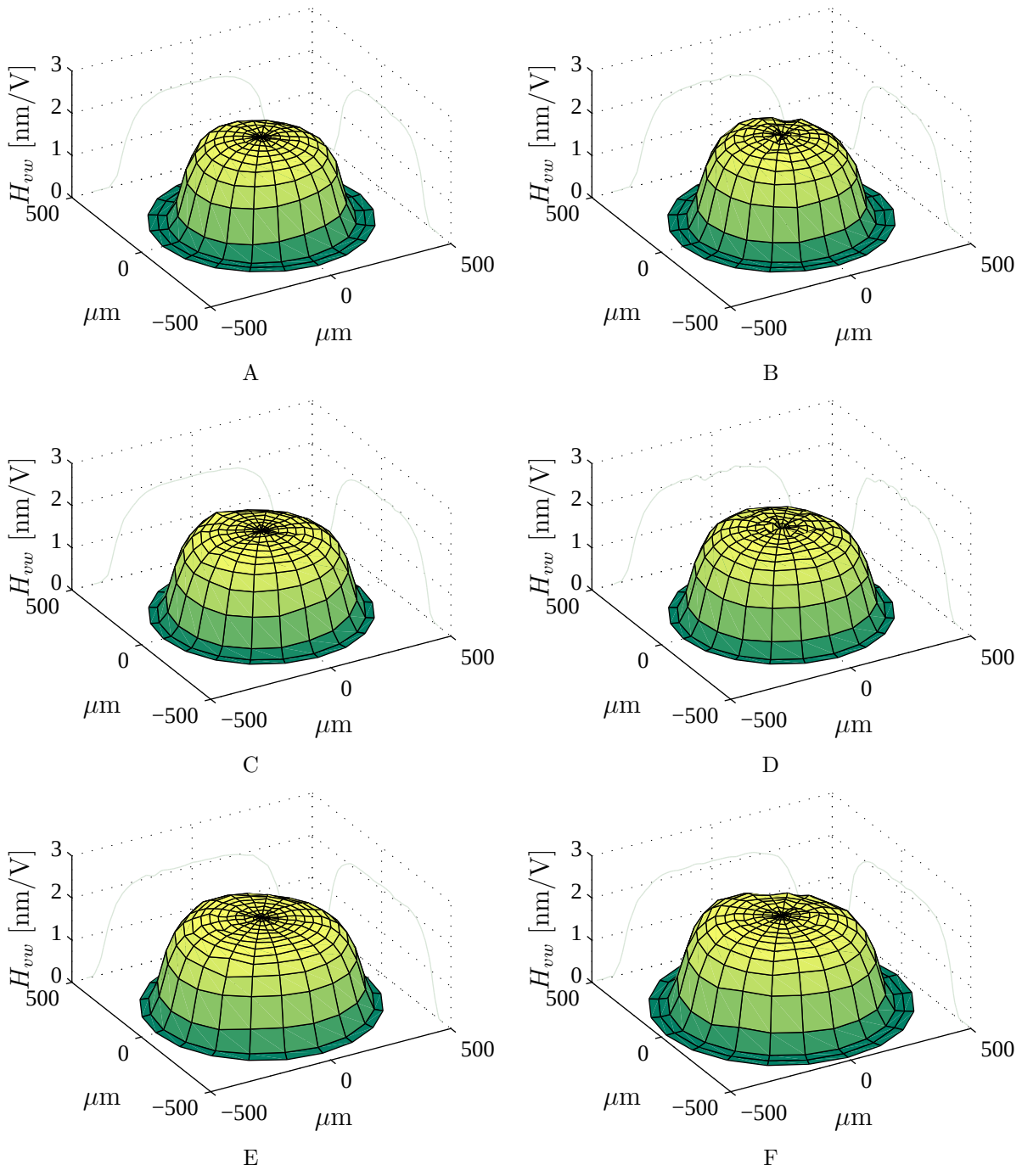

Figure 8-40. Displacement per voltage plots. A) 138-1-B6-D. B) 138-1-F5-D. C) 138-1-C9-E. D) 138-1-D9-E. E) 138-1-F7-F. F) 138-1-H7-F.

Measurement uncertainty estimates for d_a were calculated via Monte Carlo simulation and estimates as described in Section C.6.

Table 8-18. Extracted electroacoustic parameters.

	d_a [10^{-18} m^3/V]†		ϕ_a [Pa/V]‡		k^2 [10^{-3}] §	
DUT	Measured	Predicted	Measured	Predicted	Estimated*	Predicted
138-1-F5-D	489	396	-9.4	-14.5	0.49	0.76
138-1-B6-D	474	396	-8.7	-14.5	0.44	0.76
138-1-C9-E	585	502	-6.8	-12.1	0.38	0.71
138-1-D9-E	600	502	-7.1	-12.1	0.41	0.71
138-1-F7-F	772	634	-6.1	-10.1	0.41	0.67
138-1-H7-F	784	634	-6.0	-10.1	0.40	0.67

$^\dagger |U_{95\%}| < 1.1\%$ $^\ddagger |U_{95\%}| < 1.8\%$ $^\S |U_{95\%}| < 2.6\%$
* Estimated using nominal measured values, $C_{ef} \approx C_{ef} + C_{eo}$, for each design

The better agreement between measurement and theory for d_a as compared to C_{ad} — both of which have similar sensitivity to residual stress — suggested that uncertainty in stress values is not the dominant cause for the disagreement. Alternatively, uncertainties in other parameters used to calculate d_a (for example, in d_{31}) could have a compensatory effect that is not present for C_{ad}. Compliant boundary conditions would also have a similar impact on both d_a and C_{ad}.

Both the measured value of the transduction factor ϕ_a ($= -d_a/C_{ad}$) and the estimated value of electromechanical coupling factor k^2 ($= d_a^2/C_{ad}C_{ef}$) are also included in Table 8-18. Both are calculated from measurements of d_a as well as C_{ad} (refer to Section 5.2.1.1) and thus their agreement with the model is degraded due calculation with the latter. Note also that because C_{ef} could not be isolated in the impedance measurements, k^2 is estimated from measurements using $C_{ef} + C_{eo}$ in place of C_{ef}; the bias in the calculation is thus towards under-estimation of k^2 on the order of 10%.

Finally, Figure 8-41 collects the tabulated mechanoacoustic and electroacoustic data into individual plots, with each plot containing the six data points together with the theoretical trend. The trends are well-predicted, with visually consistent error in all

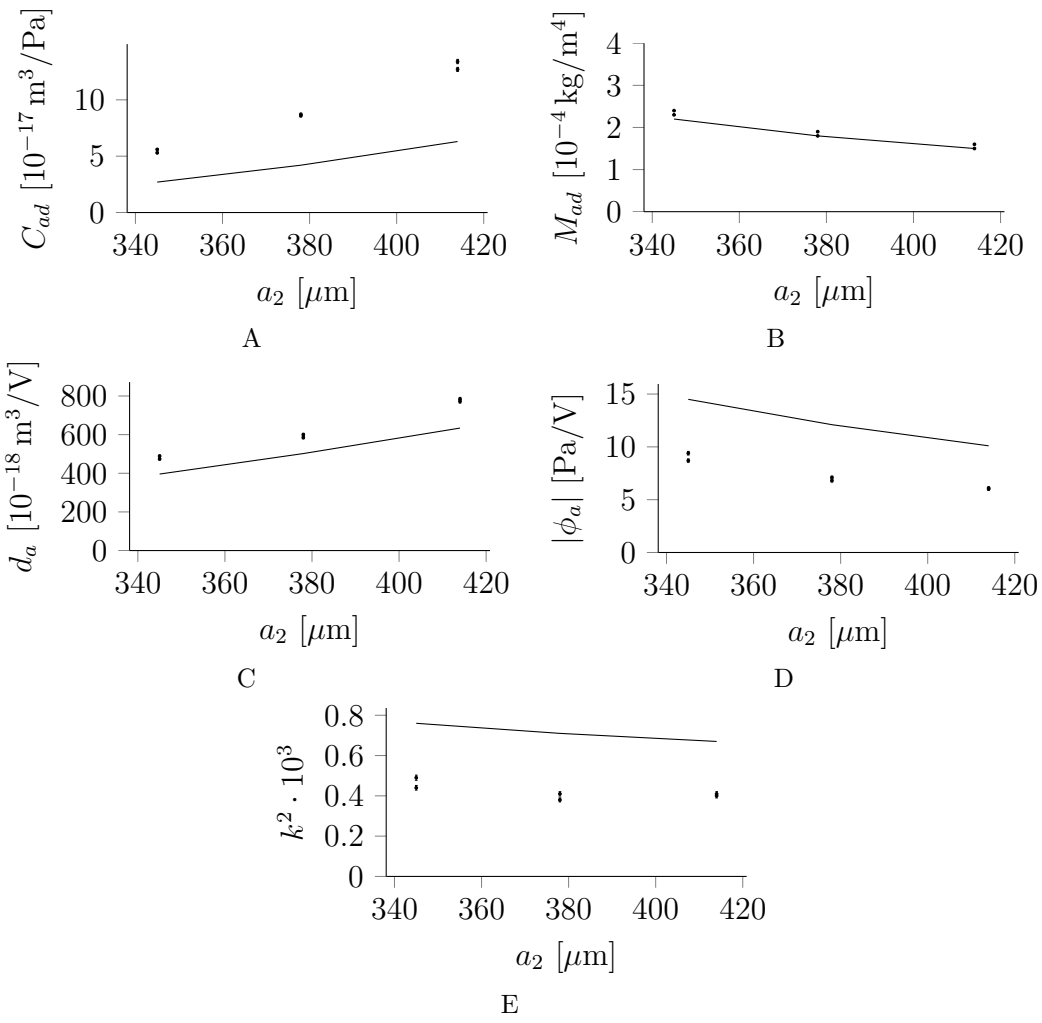

Figure 8-41. Comparison of measured and theoretical trends for extracted parameters versus diaphragm size. Measured values (dots) and theoretical predictions (lines) are shown. A)Diaphragm compliance, C_{ad}. B) Diaphragm mass, M_{ad}. C) Effective piezoelectric coefficient, d_a. D) Transduction factor, ϕ_a^2. E) Electromechanical coupling factor, k^2.

quantities except C_{ad}, for which disagreement between theory and measurement increases with diaphragm radius.

The extracted parameters C_{ad}, M_{ad}, d_a, in addition to the electrical impedance $C_{ef} + C_{eo}$, were substituted into the lumped element model, which was then used to predict the frequency response function of the microphones. Dependent parameters such as ϕ_a were also calculated from the extracted parameters. The predicted frequency response functions are plotted together with the measured frequency response of each

microphone, corrected here for the small pressure difference between reference and DUT locations (Figure 8-37), in Figure 8-42. Because measurements were performed with voltage amplifier architectures, parasitic capacitance was also accounted for in the analytical model and was estimated such that the theoretical and measured magnitude of the frequency response functions matched at 1 kHz. As a result, estimated parasitic capacitance values for each microphone are included in the legend of Figure 8-42. Extracted parasitic capacitance values ranged from 5.3 pF to 6.4 pF, somewhat higher than those extracted from the tubular-packaged microphones in Section 8.2.4.3 (4 ± 1 pF) as expected.

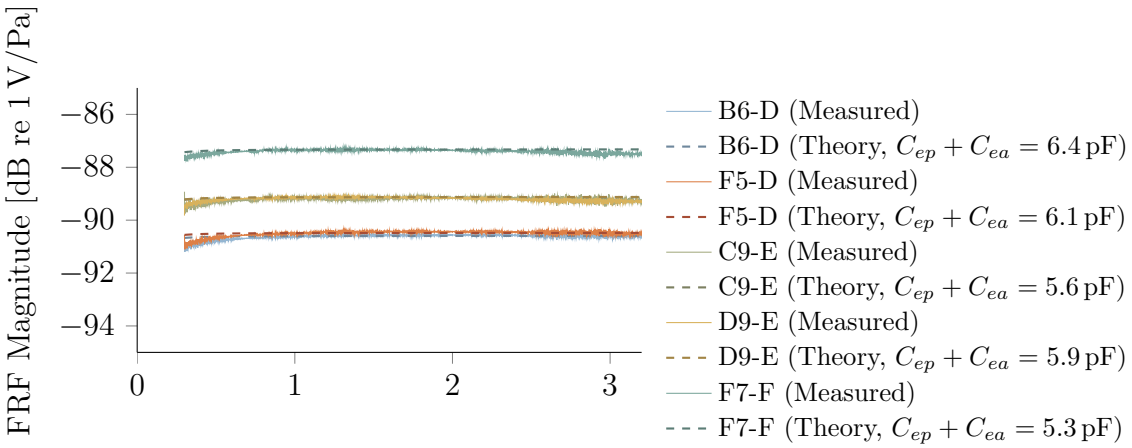

Figure 8-42. Corrected frequency response magnitude of microphones in pressure coupler together with theoretical predictions calculated using extracted parameters.

8.3 Summary

In this chapter, various characterization and parameter extraction experiments performed on the piezoelectric microphones were described. Nine microphones were characterized in terms of acoustic performance (bandwidth, sensitivity, linearity) and electrical properties (impedance, parasitic capacitance). One additional microphone was used to estimate parasitic capacitance. Electroacoustic parameters were extracted from 6 more microphones as an additional assessment of analytical model predictions. In the next section, final conclusions are drawn and the piezoelectric microphone developed in this study is compared to the prior art.

CHAPTER 9
CONCLUSION

This study focused on the development of microelectromechanical systems (MEMS) piezoelectric microphones (Figure 9-1) with the performance characteristics needed to enable superior technical measurements in full-scale flight tests. The audio-band microphone was required to be small ($\phi \leq 1.9\,\text{mm}$), thin ($< 1.3\,\text{mm}$), passive, and have a large maximum pressure ($\geq 172\,\text{dB}$) with moderate noise floor ($\leq 48.5\,\text{dB SPL}$). In previous chapters, the modeling, optimization, fabrication, packaging, and experimental characterization of just such a MEMS piezoelectric microphone was discussed. The ultimate goal was not just to develop a replacement for existing microphones, but to enable the types of measurements aircraft manufacturers envision for the future, potentially involving several arrays composed of hundreds of microphones blanketing an aircraft fuselage.

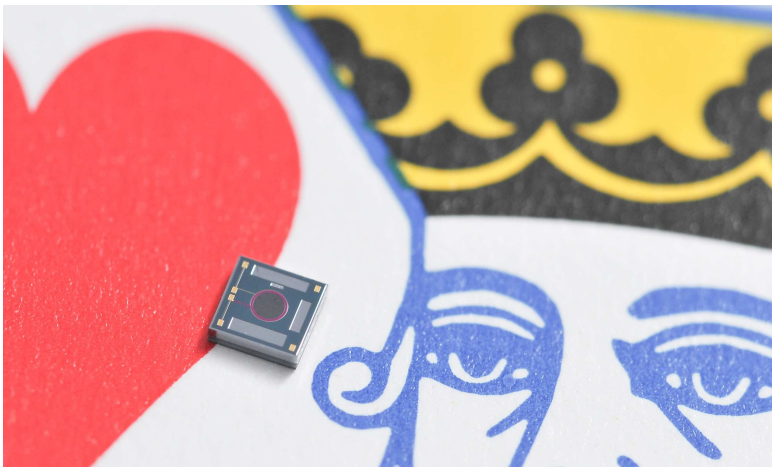

Figure 9-1. A MEMS piezoelectric microphone die on a playing card.

In Chapter 8, the MEMS microphones developed in this study were thoroughly characterized, and the results generally met or exceeded target specifications. The collected microphone performance characteristics, as compared both to target specifications and the Kulite microphone presently in-use for full-scale flight tests at Boeing Corporation, are found in Table 9-1. Most notably, the MEMS piezoelectric microphones were well

under the 48.5 dB SPL / 93 dB OASPL MDP specification (save for the outlier 138-1-I8-E) and had a lower noise floor with higher sensitivity (26–40 × greater) than the Kulite microphones. In addition, measurements showed that 5 of the tested microphones representing 3 different designs had PMAX>160 dB, and of the two microphones tested at even higher SPLs, one (138-1-J3-F) demonstrated PMAX≥171.6 dB SPL. Due to distortion in the reference microphone during this measurement (discussed in Section 8.2.3.2), the device performance almost certainly exceeded the target PMAX≥172 dB. On-board gain of slightly over 20 dB is sufficient to reach the sensitivity target of 500 μV/Pa. Although the measured $f_{-2\,\mathrm{dB}}$ point of 70 Hz slightly exceeded the 20 Hz minimum target, $f_{+2\,\mathrm{dB}} \geq 20$ kHz was met. Measured microphone resonant frequencies exceeding 100 kHz suggested a surplus of usable bandwidth that could expand the range of applications for the MEMS piezoelectric microphone to model-scale tests. Finally, even the diaphragm of the largest microphone tested, having a diameter of 828 μm (design F), was smaller than the Kulite diaphragm (864 μm on a side) and was less than half of the maximum diameter target specification (1.9 mm).

Table 9-1. Realized MEMS piezoelectric microphone performance compared to specifications and benchmark Kulite sensor.

Metric	Obtained	Target Specification	Kulite LQ-1-750-25SG
Sensing element size	ϕ 514–910 μm	$\phi \leq 1.9$ mm	864×864 μm^2
Sensitivity	29–44 μV/Pa	500 μV/Pa†	1.1 μV/Pa
MDP	40–51 dB‡	≤ 48.5 dB‡	48.5 dB‡
	83–89 dB OASPL	≤ 93 dB OASPL	93 dB OASPL
PMAX§	>171.6 dB SPL$^{\#}$	≥ 172 dB SPL	≈168 dB SPL
Bandwidth*	70 Hz$^{\#}$–20 kHz+	20 Hz–20 kHz	<20 Hz–20 kHz+

† With on-board gain ‡ 1 Hz bin centered at 1 kHz § 3% distortion * ±2 dB $^{\#}$ 138-1-J3-F

Microphone 138-1-J3-F developed in this study is compared in Table 9-2 to notable microphones from the academic literature with similar application area or technology utilization. Among the passive sensors included in Table 9-2, 138-1-J3-F featured the highest verified PMAX (≥ 171.6 dB), with the microphone of Horowitz et al. (2007) [20]

having the second highest (169 dB), though that result was limited by the test setup. The maximum pressure verified in [20] was limited by the measurement setup and may well have exceeded 172 dB. However, the MDP of microphone 138-1-J3-F (and others characterized in this study) was a significant improvement over [20] in terms of dB(A). The sensitivity obtained for 138-1-J3-F was also a 52× improvement over that in [20]. Microphone 138-1-J3-F and others developed in this study are thus the closest passive microphones in existence to meeting aircraft manufacturer needs for full-scale flight tests.

The primary contributions of this study are thus as follows:

1. Development of a MEMS piezoelectric microphone exhibiting the highest confirmed PMAX among passive MEMS microphones and performance characteristics more closely matching those needed for aircraft fuselage instrumentation than any prior passive sensor

2. Generalization of the radially non-uniform piezocomposite diaphragm mechanical model of Wang et al. (2002) [127] to include arbitrary layer composition and residual stresses on either side of the step-discontinuity, development of a geometrically nonlinear version of the model, and use of these models in the microphone design process

3. Solution of a formally-defined design optimization problem for a MEMS piezoelectric microphone utilizing lumped element modeling

4. Execution of a novel suite of parameter extraction experiments to assess the accuracy of individual lumped element predictions, most notably those obtained via the diaphragm mechanical model

The scope of this study was the design and characterization of MEMS piezoelectric microphones in the laboratory setting. Therefore, research remains to be done before the developed microphones can serve as true replacements for Kulite microphones in full-scale flight tests. In the next sections, recommendations are given for future design modifications and also for future work related to characterization.

9.1 Recommendations for Future Piezoelectric Microphones

Several improvements to the piezoelectric microphone design and design process can be made in future iterations. The most critical unmet need for deployment on an aircraft

Table 9-2. Performance characteristics of MEMS piezoelectric microphone 138-1-J3-F compared to notable microphones from the academic literature.

Author	Transduction Method	Sensing Element Dimensions	Sensitivity	Dynamic Range	Bandwidth (Predicted)
Franz 1988 [60]	Piezoelectric (AlN)	0.72 mm^2 × 1 μm$^{\#}$	25 μV/Pa$^{\#}$	68 dB(A)$^{\#}$–N/R	N/R–45 kHz$^{\#}$
Sheplak et al. 1998 [16, 17]	Piezoresistive	105 μm* × 0.15 μm	2.24 μV/Pa/V	92 dB‡–155 dB	200 Hz–6 kHz (100 Hz–300 kHz)
Arnold et al. 2001 [18]	Piezoresistive	500 μm* × 1 μm	0.6 μV/Pa/V	52 dB‡–160 dB	1 kHz–20 kHz (10 Hz–40 kHz)
Huang et al. 2002 [68]	Piezoresistive	710 μm† × 0.38 μm	1.1 mV/Pa/V	53 dB‡–174 dB	100 Hz–10 kHz
Scheeper et al. 2003 [79]	Capacitive	1.95 mm* × 0.5 μm	22.4 mV/Pa	23 dB(A)–141 dB	251 Hz–20 kHz
Hillenbrand et al. 2004 [81]	Piezoelectric (VHD40)	0.3 cm^2 × 55 μm	2.2 mV/Pa	37 dB(A)–164 dB	20 Hz–140 kHz
		0.3 cm^2 × 275 μm	10.5 mV/Pa	26 dB(A)–164 dB	20 Hz–28 kHz
Martin et al. 2007 [71, 72, 89]	Capacitive	230 μm* × 2.25 μm	390 mV/Pa	41 dB‡–164 dB	300 Hz–20 kHz
Martin et al. 2008 [73]	Capacitive	230 μm* × 2.25 μm	166 μV/Pa	22.7 dB‡–164 dB	300 Hz–20 kHz
Horowitz et al. 2007 [20]	Piezoelectric (PZT)	900 μm* × 3.0 μm	1.66 μV/Pa	35.7 dB‡/95.3 dB(A) – 169 dB	100 Hz–6.7 kHz (100 Hz–50 kHz)
Littrell 2010 [85]	Piezoelectric (AlN)	0.62 mm^2¶ 2.3 μm	1.82 mV/Pa	37 dB(A)–128 dB	50 Hz–8 kHz (18.4 kHz)
This study§	Piezoelectric (AlN)	414 μm* × 2.14 μm	39 μV/Pa	40.4 dB‡/75.4 dB(A)–171.6 dB+	69 Hz–20 kHz (>104 kHz)

$^{\#}$ References [62, 88] * Radius of circular diaphragm † Side length of square diaphragm
‡ 1 Hz bin at 1 kHz ¶ 2 cantilevers § Microphone 138-1-J3-F

fuselage is integration of through-silicon vias (TSVs) in place of front-side wire bonds. Wire bonds are a common contributor to failure in microsystems [182] and with the need for protective wire encapsulant, limit the achievable sensor surface roughness. Wafers with custom TSVs are available for purchase and only require qualification in a facility with AlN capabilities to be implemented in future designs.

The optimization of Chapter 6 showed that due to the stress states of the films, the moderately tensile structural layer thickness tended to its upper bound in order to mitigate the impact of high stresses — particularly compressive stresses — in the other films. Higher values of PMAX were shown to be achievable with a thicker structural layer in exchange for relatively small sacrifice in MDP (recall Section 6.4). To achieve a thicker structural layer, the fabrication process could be transitioned to silicon-on-insulator (SOI) wafers, with the approximately stress-free silicon device-layer serving as the structural layer. SOI wafers are available for purchase with a variety of silicon device-layer thicknesses and integrated TSVs. The piezoelectric/metal film deposition could remain virtually unchanged, with process development largely needed only for integration of a new vent structure.

The low frequency target of $f_{-2\,\mathrm{dB}} \leq 20\,\mathrm{Hz}$ was not quite met in this study. Modeling suggested that the dielectric loss in the piezoelectric film was the limiting agent in the low frequency reseponse. New values of R_{ep} were obtained via parameter extraction from impedance measurements, from which resistivity is calculable. Future design optimization processes should first focus on active reduction of $f_{-2\,\mathrm{dB}}$ using these extracted resistivities. Dielectric loss may also be reduced at the material level with improved AlN film quality [183]. Improved film quality and lower dielectric loss have been linked in some studies to thick AlN films [85] of up to $2\,\mu\mathrm{m}$ [184].

The diaphragm model presented in this study was a significant step forward from prior works [20, 113, 127, 128], but additional improvements could be made. A linear model was used to predict diaphragm performance both in terms of initial deflection (due to residual stress) and incremental deflection (due to voltage/pressure loading). Since the incremental deflection is the quantity that must be linear with respect to pressure, the model could be extended such that the initial deflection is solved as a nonlinear problem and then a linear problem is solved for incremental deflection with the initially-deflected diaphragm serving as the reference configuration. This approach would

increase computation time when implemented in an optimization algorithm, but it would also relax constraints on nonlinear transition behavior that were perhaps too conservative in this study.

Modeling of nonlinear transition behavior — characterized in this study via THD — also deserves renewed attention. Most notably, the static estimation of THD utilized in Chapter 6 has not been verified. A focused study utilizing finite element-based nonlinear dynamics simulations of the microphone diaphragm could reveal the relationship between static nonlinearity and THD for the microphone geometries in this study. However, a more general and computationally-efficient approach is needed. For example, the classical model for a Duffing spring might be used to estimate THD given inputs from static mechanical models. Such an approach would be highly valuable to microphone designers and integrate well with design optimization approaches.

This was the first study for which formal optimization was employed in the design of a piezoelectric MEMS microphone. A number of modifications could be made to the optimization formulation. First, using an overall measure of MDP rather than the narrow band definition might serve to lower the overall noise floor, since the optimization algorithm would then have additional incentive to simultaneously reduce noise due to R_{ep} and the amplifier rather than just the dominant source at 1 kHz. In addition, with confidence in low-frequency cut-off predictions experimentally established, future optimizations could include a constraint on $f_{-2\,\mathrm{dB}}$ to ensure sponsor specifications are met. Finally, the constraint on aspect ratio could be removed in favor of verifying prediction quality after optimization is completed rather than unnecessarily limiting the feasible design space.

The overall optimization approach could also be transitioned from deterministic to robust optimization, a design methodology in which the best design isn't defined simply by mean performance, but also by how sensitive mean performance is to variables like material properties, process variations, etc. [185]. In this study, the thin-film residual

stress model inputs were not well-known but had significant impact on microphone performance; microphones hailing from wafer 116, for example, had visibly-buckled diaphragms and had the worst performance of those characterized in Chapter 8. Material properties were also drawn from a variety of sources that may not have been truly representative of the material properties associated with the FBAR-variant process (e.g. d_{31} for AlN). Robust optimization formulations have been applied previously to the design of a MEMS gyroscope [186] and multistable mechanism [187], among others. There are two major hurdles to implementation of robust optimization in MEMS piezoelectric microphone design: robust optimization is often more computationally intensive than its deterministic counterpart and it ideally utilizes comprehensive statistical information for property and process variations that is rarely available. Methods have been developed for robust optimization when a dearth of statistical information is available, though at increased complexity and computational cost [188].

9.2 Recommendations for Future Work

Superior stability is one major characteristic that separates measurement microphones from those used in other applications. To be deployed on an aircraft fuselage, the MEMS piezoelectric microphone must demonstrate robustness to moisture and freezing, in addition to temperature stability from $-60\,^{\circ}\mathrm{F}$ to $150\,^{\circ}\mathrm{F}$. This kind of characterization was beyond the equipment capabilities at Interdisciplinary Microsystems Group and thus fell outside the scope of this study. A battery of environmental tests are needed to characterize stability and drift in the piezoelectric microphones. Such measurements could lead to design improvements or compensation schemes if necessary. Environmental testing of this kind is already in progress at Boeing Corporation.

The packaging scheme utilized in this study was designed for laboratory characterization. Moving to the aircraft fuselage application requires development of a low-cost, robust, thin package with adequate electromagnetic interference (EMI) shielding for the high-impedance sensors. The desire for low complexity and high levels of integration

when deploying thousands of sensors demands integration of interface electronics in the surface-mount package as well. All required circuitry must ideally operate off of a standard 4 mA constant current source commonly integrated with current-generation data acquisition systems. Package cost is also a significant concern moving forward, as packaging is known to often dominate the cost of MEMS sensors [43].

Modifications could also be made to the laboratory package to improve future characterization experiments. Although pre- and post-package measurements were taken to establish the impact of packaging on die performance, no effort was made to systematically identify causes for behavioral changes and remedy them. A study involving multiple substrate materials and die-attach methods is necessary for development of a package that does not impact microphone performance. A change in substrate material also has the potential to reduce parasitic capacitance. In addition, EMI issues were occasionally encountered in the laboratory testing of these microphones, both at Interdisciplinary Microsystems Group and Boeing Corporation. Focused effort should thus be made to reduce EMI in the laboratory package.

The parameter extraction experiments could also be improved. The pressure coupler hardware used in these experiments suffered from inconsistent sealing and a tendency to drift underneath the microscope objective. Clear design modifications that would reduce drift include better positioning of the pressure coupler, perhaps using micro-positioners, and a flexible connection with the speaker to help vibration-isolate the pressure coupler itself. Modification of the microphone package form-factor used in the parameter extraction (recall Section 8.1.5) to avoid cantilevering is also suggested. The most important modification to the pressure coupler experiment, however, is the use of charge amplifier rather than a voltage amplifier circuitry. Using the voltage amplifier, parasitic capacitance served as something of a confounding variable and limited the ability to verify parameter extractions via measured microphone frequency response functions. Utilizing a charge amplifier eliminates the impact of parasitic capacitance.

APPENDIX A
DIAPHRAGM MECHANICAL MODEL

In this appendix, a model of an axisymmetric, laminated, pre-stressed, and radially-discontinuous circular piezoelectric plate exposed to pressure and/or voltage loading is presented. Motivated in Section 5.2.1.2, this mechanical plate model provides crucial inputs to the overall piezoelectric microphone lumped element model in the form of displacement predictions for particular loading scenarios. The model is part of a natural evolution from prior work, including [113, 128, 189, 190], but most specifically Wang et al. (2002) [127]. Earlier forms of the model were utilized in [20, 139, 140, 140].

Figure A-1, repeated from Section 5.2.1.2, shows the geometry of the piezoelectric microphone, which features an annular piezoelectric ring and otherwise passive materials. The model derived here is generalized to include, but not be limited to, this specific geometry. In general, both the inner ($0 \leq r \leq a_1$) and outer ($a_1 \leq r \leq a_2$) regions (or "domains") may contain an arbitrary layup of piezoelectric and/or non-piezoelectric materials, with each piezoelectric layer individually addressable with an electric field. Uniform pressure loading and the effects of in-plane residual stress are also included.

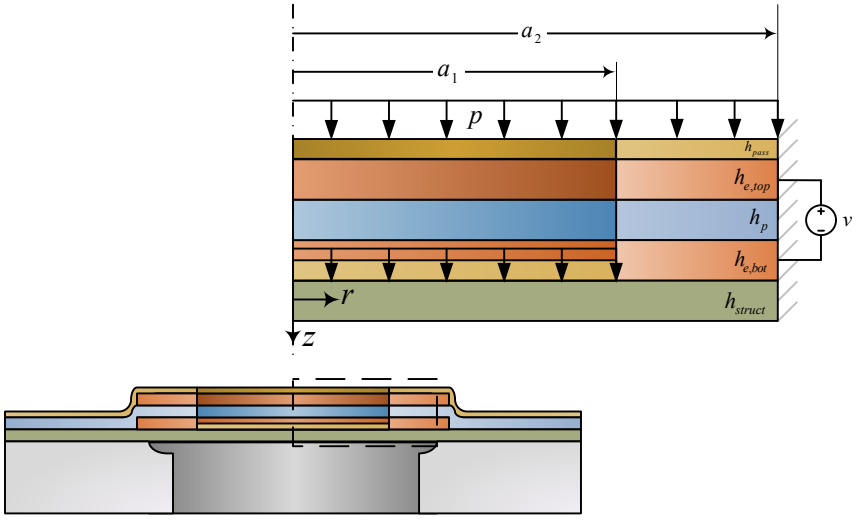

Figure A-1. Laminated composite plate representation of the thin-film diaphragm.

The derivation is broken into several parts. First, the strain displacement relations for small, finite deformations are derived from the Green strain tensor. Next, the equations of motion, and the associated generalized boundary conditions, are derived from Hamilton's principle. The electromechanical constitutive relations relating forces/moments, displacements, and electric field are then given and are combined with the equations of motion to yield the displacement-based governing equations for the piezoelectric composite plate. Both linear and nonlinear forms of the governing equations are presented.

With the governing equations derived, particular solutions for the single radial-discontinuity case depicted in Figure A-1 are presented. The linear governing equations are solved analytically up to the step of applying boundary conditions, at which time integration

coefficients are determined from the numerical solution of a system of linear algebraic equations. The nonlinear governing equations, meanwhile, are manipulated into a form solvable via a common boundary value problem solver, `bvp4c` in MATLAB.

The derivation contained herein strives for maximum generality while maintaining a delicate balance with readability. Simplifications specific to the problem of interest are employed only when they are necessary, usually at a time when continuing without simplification is no longer possible or would be too unwieldly. In this way, additional reference material is provided for future modeling efforts.

A.1 Strain-Displacement Relations

The starting point of this derivation lies with the nonlinear theory of elasticity and the Green strain tensor ε_{ij} , given as [98, 191]

$$\varepsilon_{ij} = \frac{1}{2}\left(\frac{\partial u_i}{\partial X_j} + \frac{\partial u_j}{\partial X_i} + \frac{\partial u_k}{\partial X_i}\frac{\partial u_k}{\partial X_j}\right) \qquad \bar{\varepsilon} = \frac{1}{2}\left[\vec{u}\nabla + \nabla\vec{u} + (\vec{u}\nabla)\cdot(\nabla\vec{u})\right] \tag{A–1}$$

where $u_i(X_j)$ is the displacement vector and X_j are the Cartesian coordinates of particles in the reference configuration and indicial notation [192–194] is used here to imply summation over repeated indices. The Gibbs notation [194] equivalent, which does not presuppose a coordinate system, is also given. The Green strain tensor is a Lagrangian measure of strain and is applicable for cases in which a body undergoes large, finite deformations [191]. Another form in which to write the Green strain tensor is

$$\varepsilon_{ij} = e_{ij} + \frac{1}{2}\left(e_{ik} + \omega_{ik}\right)\left(e_{kj} - \omega_{kj}\right) \qquad \bar{\varepsilon} = \bar{e} + \frac{1}{2}\left(\bar{e} + \bar{\omega}\right)\cdot\left(\bar{e} - \bar{\omega}\right), \tag{A–2}$$

where the infinitesimal strain tensor e_{ij} and rotation tensor ω_{ij} are defined as [193, 195]

$$e_{ij} = \frac{1}{2}\left(\frac{\partial u_i}{\partial X_j} + \frac{\partial u_j}{\partial X_i}\right) \qquad \bar{e} = \frac{1}{2}\left(\vec{u}\nabla + \nabla\vec{u}\right) \tag{A–3}$$

and

$$\omega_{ij} = \frac{1}{2}\left(\frac{\partial u_i}{\partial X_j} - \frac{\partial u_j}{\partial X_i}\right) \qquad \bar{\omega} = \frac{1}{2}\left(\vec{u}\nabla - \nabla\vec{u}\right). \tag{A–4}$$

It is important to note that e_{ij} is symmetric while ω_{ij} is anti-symmetric [193].

Thin, flexible structures such as beams, plates, and shells are characterized by large rotations of their cross sections but only minimal change in shape of individual elements [196]. The Green strain tensor may therefore be simplified under the assumption that [191, 195]

$$e_{ij} \ll \omega_{ij}, \tag{A–5}$$

that is, the strains are much less than the rotations. This is in contrast to the linear theory, in which both e_{ij} and ω_{ij} are much less than unity. Applying the assumption A–5 requires the removal of any terms containing products of e_{ij} from the Green strain tensor, Equation A–2. Performing this operation and making use of the anti-symmetry of ω_{ij}

(meaning $\omega_{ij} = -\omega_{ji}$), the Green strain tensor is simplified to [191, 195]

$$\varepsilon_{ij} \approx e_{ij} + \frac{1}{2}\omega_{ik}\omega_{jk} \qquad \bar{\varepsilon} \approx \bar{e} + \frac{1}{2}\bar{\omega}\cdot\bar{\omega}^T. \tag{A–6}$$

Equation A–6 is directly applicable to the analysis of a thin plate and is sometimes referred to as the case of *small, finite deformations* [191].

A plate with surface normal oriented along the x_3 axis in the undeformed state does not undergo large rotations about that axis compared to axes in the plane of the plate. In mathematical terms,

$$\omega_{12} \ll \omega_{31}, \omega_{32} \tag{A–7}$$

and ω_{12} may be neglected. In many texts [193, 197], a single subscript notation is used that clarifies the axis of rotation. In this notation, $\omega_{32} = \omega_1$, $\omega_{31} = \omega_2$, and $\omega_{12} = \omega_3$. These also correspond to components of a rotation vector. Under the assumption of Equation A–7, the six components of the reduced Green strain in cylindrical coordinates are

$$\varepsilon_{rr} = e_{rr} + \frac{1}{2}\omega_{rz}^2, \tag{A–8}$$

$$\varepsilon_{\theta\theta} = e_{\theta\theta} + \frac{1}{2}\omega_{\theta z}^2, \tag{A–9}$$

$$\varepsilon_{zz} = e_{zz} + \frac{1}{2}\left(\omega_{rz}^2 + \omega_{\theta z}^2\right), \tag{A–10}$$

$$\varepsilon_{r\theta} = e_{r\theta} + \frac{1}{2}\omega_{rz}\omega_{\theta z}, \tag{A–11}$$

$$\varepsilon_{\theta z} = e_{\theta z}, \tag{A–12}$$

and

$$\varepsilon_{rz} = e_{rz}. \tag{A–13}$$

The linear strains e_{ij} and rotations ω_{ij} are defined in cylindrical coordinates as [98]

$$e_{rr} = \frac{\partial u_r}{\partial r}, \tag{A–14}$$

$$e_{\theta\theta} = \frac{u_r}{r} + \frac{1}{r}\frac{\partial u_\theta}{\partial \theta}, \tag{A–15}$$

$$e_{zz} = \frac{\partial u_z}{\partial z}, \tag{A–16}$$

$$2e_{r\theta} = \frac{1}{r}\frac{\partial u_r}{\partial \theta} + \frac{\partial u_\theta}{\partial r} - \frac{u_\theta}{r}, \tag{A–17}$$

$$2e_{rz} = \frac{\partial u_r}{\partial z} + \frac{\partial u_z}{\partial r}, \tag{A–18}$$

$$2e_{\theta z} = \frac{\partial u_\theta}{\partial z} + \frac{1}{r}\frac{\partial u_z}{\partial \theta}, \tag{A–19}$$

$$2\omega_{r\theta} = \frac{1}{r}\frac{\partial u_r}{\partial \theta} - \frac{\partial u_\theta}{\partial r} - \frac{u_\theta}{r}, \tag{A–20}$$

$$2\omega_{rz} = \frac{\partial u_r}{\partial z} - \frac{\partial u_z}{\partial r}, \tag{A–21}$$

and

$$2\omega_{\theta z} = \frac{\partial u_\theta}{\partial z} - \frac{1}{r}\frac{\partial u_z}{\partial \theta}. \tag{A–22}$$

With the Green strain tensor simplified significantly, the next part of the derivation focuses on the individual displacement components.

A.2 Kirchhoff Hypothesis

In 1850, the German physicist Gustav Kirchhoff proposed a kinematic assumption for the deformation of thin plates. The so-called *Kirchhoff hypothesis* focuses on the deformation of cross sections within the plate. It states that during deformation, lines initially normal to the reference surface (1) remain straight (in-plane displacements are linear functions of z), (2) remain normal ($\varepsilon_{rz} = \varepsilon_{\theta z} = 0$), and (3) do not extend ($u_z = u_z(r, \theta)$). Plate equations derived under these assumptions are said to come from the classical theory of plates [121].

The assumed displacement forms

$$u_r(r, \theta, z; t) = u(r, \theta; t) - z\frac{\partial w}{\partial r}, \tag{A–23}$$

$$u_\theta(r, \theta, z; t) = v(r, \theta; t) - z\frac{1}{r}\frac{\partial w}{\partial \theta}, \tag{A–24}$$

and

$$u_z(r, \theta, z; t) = w(r, \theta; t) \tag{A–25}$$

are consistent with the Kirchhoff hypothesis. Here, u, v, and w represent the displacements of a particle on the surface $z = 0$ [121], called the "reference plane" or "reference surface" and chosen for convenience at an arbitrary location within the thickness of the plate. Substituting the displacements into Equations A–8, A–9, and A–11 yields

$$\begin{Bmatrix} \varepsilon_{rr} \\ \varepsilon_{\theta\theta} \\ 2\varepsilon_{r\theta} \end{Bmatrix} = \begin{Bmatrix} \varepsilon_r^0 \\ \varepsilon_\theta^0 \\ \varepsilon_{r\theta}^0 \end{Bmatrix} + z \begin{Bmatrix} \kappa_r \\ \kappa_\theta \\ \kappa_{r\theta} \end{Bmatrix}, \tag{A–26}$$

where the in-plane strains ε^0 and curvatures κ are defined as

$$\varepsilon_r^0 = \frac{\partial u}{\partial r} + \frac{1}{2}\left(\frac{\partial w}{\partial r}\right)^2, \tag{A–27}$$

$$\varepsilon_\theta^0 = \frac{u}{r} + \frac{1}{r}\frac{\partial v}{\partial \theta} + \frac{1}{2r^2}\left(\frac{\partial w}{\partial \theta}\right)^2, \tag{A–28}$$

$$\varepsilon_{r\theta}^0 = \frac{1}{r}\frac{\partial u}{\partial \theta} - \frac{v}{r} + \frac{\partial v}{\partial r} + \frac{1}{r}\frac{\partial w}{\partial r}\frac{\partial w}{\partial \theta}, \tag{A–29}$$

$$\kappa_r = -\frac{\partial^2 w}{\partial r^2}, \tag{A–30}$$

$$\kappa_\theta = -\frac{1}{r}\left(\frac{1}{r}\frac{\partial^2 w}{\partial \theta^2} + \frac{\partial w}{\partial r}\right), \tag{A–31}$$

and

$$\kappa_{r\theta} = -\frac{2}{r}\left(\frac{\partial^2 w}{\partial r \partial \theta} - \frac{1}{r}\frac{\partial w}{\partial \theta}\right). \tag{A–32}$$

Equation A–26 can be written compactly as

$$\boldsymbol{\varepsilon} = \boldsymbol{\varepsilon}^{\mathbf{0}} + z\boldsymbol{\kappa}, \tag{A–33}$$

with boldface indicating array quantities. The remaining shear strains ε_{rz} and $\varepsilon_{\theta z}$ and ε_{zz} vanish per Kirchhoff's hypothesis. Equations A–27 to A–32 are collectively known as the von Kármán strains, and the plate theory making use of them is sometimes called the von Kármán plate theory [121].

A.3 Equations of Motion

The derivation of the equations of motion for the piezoelectric composite plate makes use of variational methods, whose primary advantage is that consistent boundary conditions are also produced. The variational formulation makes immediate use of the von Kármán strains derived in Sections A.1–A.2. The derivation begins with Hamilton's principle for a conservative system [142, 195],

$$\int_{t_1}^{t_2} \delta L dt = 0, \tag{A–34}$$

where the integrand is the variation of the Lagrangian function [191] for an elastic body,

$$L = T - (U + V). \tag{A–35}$$

Here, T is the kinetic energy of the body, U is the strain energy stored in the body, and V is the potential energy associated with external forces applied to the body [142]. Hamilton's principle is the dynamic analog of the principle of virtual work, and may in fact be derived from it via the use of D'Alembert's principle [191, 195]. Dym and Shames [195] summarize as follows:

> "Hamilton's principle states that of all paths of admissible configurations that the body can take as it goes from configuration 1 at time t_1 to configuration 2 at time t_2, the path that satisfies Newton's law at each instant during the interval (and is thus the actual locus of configurations) is the path that extremizes the time integral of the Lagrangian during the interval."

Virtual displacements (infinitesimal variations from the true equilibrium configuration to an arbitrary admissible configuration [92]) must vanish at t_1 and t_2 and on any region of the body where displacement is prescribed [191].

The first variations of kinetic energy T and strain energy U are [122, 195]

$$\delta T = \int_{\forall} \rho \dot{u}_i \delta \dot{u}_i d\forall \qquad \delta T = \int_{\forall} \rho \vec{\dot{u}} \cdot \delta \vec{\dot{u}} d\forall \tag{A–36}$$

and

$$\delta U = \int_{\forall} \sigma_{ij} \delta \varepsilon_{ij} d\forall \qquad \delta U = \int_{\forall} \bar{\sigma} : \delta \bar{\varepsilon} d\forall, \tag{A–37}$$

where an overdot denotes partial differentiation with respect to time, $\partial/\partial t$, and the integrals are over the plate volume, $\forall$. Restricting the external loading to an arbitrary distributed load directed in the z direction, q_z, the first variation of the potential energy of this applied load is

$$\delta V = -\int_{\forall} q_z \delta u_z d\forall. \tag{A–38}$$

The key to deriving the equations of motion using variational methods is to manipulate the integrand of Equation A–34 via integration by parts until the governing equations and boundary conditions can be extracted. The virtual displacements for this problem are the reference plane displacements, u, v, and w. For convenience, the individual terms δU, δT, and δV are manipulated independently and then combined into Equation A–34 at the end of the derivation. The simplest expression, δV, requires only substitution of Equation A–25, yielding

$$\delta V = -\int_{\forall} q_z \delta w d\forall. \tag{A–39}$$

.

Next, Equation A–36 (δT), may be treated. Performing the vector dot product,

$$\delta T = \int_{\forall} \rho \left(\dot{u}_r \delta \dot{u}_r + \dot{u}_\theta \delta \dot{u}_\theta + \dot{u}_z \delta \dot{u}_z \right) d\forall. \tag{A–40}$$

Integrating by parts over time yields

$$\begin{aligned} \int_{t_1}^{t_2} \delta T dt \;\; = \;\; & -\int_{t_1}^{t_2} \int_{\forall} \rho \left(\ddot{u}_r \delta u_r + \ddot{u}_\theta \delta u_\theta + \ddot{u}_z \delta u_z \right) d\forall dt \\ & + \int_{\forall} \rho \left[\dot{u}_r \delta u_r + \dot{u}_\theta \delta u_\theta + \dot{u}_z \delta u_z \right]_{t_1}^{t_2} d\forall, \end{aligned} \tag{A–41}$$

where the second term on the right-hand side of Equation A–41 must vanish because admissible virtual displacements δu_r, δu_θ, and δu_z are required to be zero at $t = t_1$ and $t = t_2$. Thus,

$$\delta T = -\int_{\forall} \rho \left(\ddot{u}_r \delta u_r + \ddot{u}_\theta \delta u_\theta + \ddot{u}_z \delta u_z \right) d\forall. \tag{A–42}$$

Substituting Equations A–23 to A–25 into the above, noting $d\forall = rdrd\theta dz$, and integrating with respect to z yields

$$\begin{aligned}\delta T &= -\int \left[\left(I_0\ddot{u} - I_1\frac{\partial \ddot{w}}{\partial r}\right)\delta u + \left(I_0\ddot{v} - I_1\frac{1}{r}\frac{\partial \ddot{w}}{\partial \theta}\right)\delta v + I_0\ddot{w}\delta w \right. \\ &\quad \left. + \left(I_2\frac{\partial \ddot{w}}{\partial r} - I_1\ddot{u}\right)\frac{\partial \delta w}{\partial r} + \frac{1}{r}\left(I_2\frac{1}{r}\frac{\partial \ddot{w}}{\partial \theta} - I_1\ddot{v}\right)\frac{\partial \delta w}{\partial \theta}\right] rdrd\theta, \end{aligned} \tag{A–43}$$

where the moments of inertia I_0–I_2 are

$$\{I_0, I_1, I_2\} = \int_{z_b}^{z_t} \rho\left\{1, z, z^2\right\} dz \tag{A–44}$$

and the integration limits are from the bottom surface of the plate ($z = z_b$) to the top surface ($z = z_t$). Note that I_0 and I_2 may be referred to as the aerial density and rotary inertia, respectively. The term I_1 is only nonzero if the density of the plate is not symmetric about the reference plane ($z = 0$). Performing integration by parts on the final two terms in the integrand finally yields

$$\begin{aligned}\delta T &= -\int_A \left\{\left(I_0\ddot{u} - I_1\frac{\partial \ddot{w}}{\partial r}\right)\delta u + \left(I_0\ddot{v} - I_1\frac{1}{r}\frac{\partial \ddot{w}}{\partial \theta}\right)\delta v + I_0\ddot{w}\delta w \right. \\ &\quad \left. -\frac{1}{r}\left[\frac{\partial}{\partial r}\left(rI_2\frac{\partial \ddot{w}}{\partial r} - rI_1\ddot{u}\right) + \frac{\partial}{\partial \theta}\left(I_2\frac{1}{r}\frac{\partial \ddot{w}}{\partial \theta} - I_1\ddot{v}\right)\right]\delta w\right\} rdrd\theta \\ &\quad -\int_\theta \left[r\left(I_2\frac{\partial \ddot{w}}{\partial r} - I_1\ddot{u}\right)\delta w\right]_{r=r_1}^{r=r_2} d\theta - \int_r \left[\left(I_2\frac{1}{r}\frac{\partial \ddot{w}}{\partial \theta} - I_1\ddot{v}\right)\delta w\right]_{\theta=0}^{\theta=2\pi} dr, \end{aligned} \tag{A–45}$$

where the first integral will contribute to the equations of motion and the remaining integrals will contribute to the boundary conditions for the equations of motion. The integration is performed here over a general domain $[r_1, r_2]$ which could present $[0, a_1]$ or $[a_1, a_2]$, for example.

Attention is now turned to the expression for δU, Equation A–37. Given that $\epsilon_{rz} = \epsilon_{\theta z} = 0$ and the plate is in a state of plane stress ($\sigma_{zz} \approx 0$), Equation A–37 can be written simply as

$$\delta U = \int_\forall \left(\sigma_{rr}\delta\varepsilon_{rr} + \sigma_{\theta\theta}\delta\varepsilon_{\theta\theta} + 2\sigma_{r\theta}\delta\varepsilon_{r\theta}\right) d\forall. \tag{A–46}$$

Substituting Equation A–26 and integrating with respect to z gives

$$\delta U = \int_A \left(N_r\delta\varepsilon_r^0 + M_r\delta\kappa_r + N_\theta\delta\varepsilon_\theta^0 + M_\theta\delta\kappa_\theta + N_{r\theta}\delta\varepsilon_{r\theta}^0 + M_{r\theta}\delta\kappa_{r\theta}\right) rdrd\theta, \tag{A–47}$$

with the force and moment resultants [121] defined as

$$\{N_r, N_\theta, N_{r\theta}\} = \int_{z_b}^{z_t} \{\sigma_{rr}, \sigma_{\theta\theta}, \sigma_{r\theta}\} dz \tag{A–48}$$

and

$$\{M_r, M_\theta, M_{r\theta}\} = \int_{z_b}^{z_t} \{\sigma_{rr}, \sigma_{\theta\theta}, \sigma_{r\theta}\}\, z dz, \tag{A–49}$$

respectively. Next, substituting Equations A–23 to A–25 into Equation A–47,

$$\begin{aligned}
\delta U \;=\; & \int_A \left[\frac{N_\theta}{r}\delta u - \frac{N_{r\theta}}{r}\delta v + N_r \frac{\partial \delta u}{\partial r} + N_{r\theta}\frac{\partial \delta v}{\partial r} + \frac{N_{r\theta}}{r}\frac{\partial \delta u}{\partial \theta} + \frac{N_\theta}{r}\frac{\partial \delta v}{\partial \theta} \right. \\
& + \left(r N_r \frac{\partial w}{\partial r} + N_{r\theta}\frac{\partial w}{\partial \theta} - M_\theta \right) \frac{1}{r}\frac{\partial \delta w}{\partial r} + \left(r N_{r\theta}\frac{\partial w}{\partial r} + N_\theta \frac{\partial w}{\partial \theta} + 2M_{r\theta} \right) \frac{1}{r^2}\frac{\partial \delta w}{\partial \theta} \\
& \left. - \left(M_r \frac{\partial^2 \delta w}{\partial r^2} + M_\theta \frac{1}{r^2}\frac{\partial^2 \delta w}{\partial \theta^2} + M_{r\theta}\frac{1}{r}\frac{\partial^2 \delta w}{\partial r \partial \theta} + M_{r\theta}\frac{1}{r}\frac{\partial^2 \delta w}{\partial \theta \partial r} \right) \right] r dr d\theta.
\end{aligned} \tag{A–50}$$

Integrating by parts once (and paying special attention to the $M_{r\theta}$ terms per [142]),

$$\begin{aligned}
\delta U \;=\; & \int_A \left[\frac{N_\theta}{r}\delta u - \frac{N_{r\theta}}{r}\delta v + N_r \frac{\partial \delta u}{\partial r} + N_{r\theta}\frac{\partial \delta v}{\partial r} + \frac{N_{r\theta}}{r}\frac{\partial \delta u}{\partial \theta} + \frac{N_\theta}{r}\frac{\partial \delta v}{\partial \theta} \right. \\
& + \left(r N_r \frac{\partial w}{\partial r} + N_{r\theta}\frac{\partial w}{\partial \theta} + \frac{\partial}{\partial r}(r M_r) - M_\theta + \frac{\partial M_{r\theta}}{\partial \theta} \right) \frac{1}{r}\frac{\partial \delta w}{\partial r} \\
& \left. + \left(r N_{r\theta}\frac{\partial w}{\partial r} + N_\theta \frac{\partial w}{\partial \theta} + 2M_{r\theta} + r\frac{\partial M_{r\theta}}{\partial r} + \frac{\partial M_\theta}{\partial \theta} \right) \frac{1}{r^2}\frac{\partial \delta w}{\partial \theta} \right] r dr d\theta \\
& - \int_\theta \left(r M_r \frac{\partial \delta w}{\partial r} + M_{r\theta}\frac{\partial \delta w}{\partial \theta} \right)_{r=r_1}^{r=r_2} d\theta - \int_r \left(M_\theta \frac{1}{r}\frac{\partial \delta w}{\partial \theta} + M_{r\theta}\frac{\partial \delta w}{\partial r} \right)_{\theta=0}^{\theta=\theta_0} dr
\end{aligned} \tag{A–51}$$

Integrating by parts a second time completes the process:

$$\begin{aligned}
\delta U \;=\; & -\int \left\{ \left(\frac{\partial (r N_r)}{\partial r} + \frac{\partial N_{r\theta}}{\partial \theta} - N_\theta \right) \frac{1}{r}\delta u + \left(N_{r\theta} + \frac{\partial (r N_{r\theta})}{\partial r} + \frac{\partial N_\theta}{\partial \theta} \right) \frac{1}{r}\delta v \right. \\
& + \left[\frac{1}{r}\frac{\partial}{\partial r}\left(r N_r \frac{\partial w}{\partial r} + N_{r\theta}\frac{\partial w}{\partial \theta} + \frac{\partial (r M_r)}{\partial r} - M_\theta \right) \right. \\
& \left. \left. + \frac{1}{r^2}\frac{\partial}{\partial \theta}\left(r N_{r\theta}\frac{\partial w}{\partial r} + N_\theta \frac{\partial w}{\partial \theta} + 2\frac{\partial}{\partial r}(r M_{r\theta}) + \frac{\partial M_\theta}{\partial \theta} \right) \right] \delta w \right\} r dr d\theta \\
& + \int \left[N_r \delta u + N_{r\theta}\delta v + \left(N_r \frac{\partial w}{\partial r} + N_{r\theta}\frac{1}{r}\frac{\partial w}{\partial \theta} + \frac{1}{r}\frac{\partial (r M_r)}{\partial r} - \frac{1}{r}M_\theta + \frac{2}{r}\frac{\partial M_{r\theta}}{\partial \theta} \right) \delta w \right. \\
& \left. - M_r \frac{\partial \delta w}{\partial r} \right]_{r=r_1}^{r=r_2} r d\theta + \int \left[N_{r\theta}\delta u + N_\theta \delta v + \frac{1}{r}\left(r N_{r\theta}\frac{\partial w}{\partial r} + N_\theta \frac{\partial w}{\partial \theta} + 2\frac{\partial (r M_{r\theta})}{\partial r} \right. \right. \\
& \left. \left. + \frac{\partial M_\theta}{\partial \theta} \right) \delta w - M_\theta \frac{1}{r}\frac{\partial \delta w}{\partial \theta} \right]_{\theta=0}^{\theta=\theta_0} dr - 2M_{r\theta}\delta w \Big|_{(r,\theta)=(r_2,0),(r_1,\theta_0)}^{(r,\theta)=(r_1,0),(r_2,\theta_0)}.
\end{aligned} \tag{A–52}$$

The terms δT, δU, and δV in equations Equation A–45, Equation A–52, and Equation A–39, respectively, may now be combined into the single expression of Equation A–34; the complete expression is not given here for brevity. Because the virtual displacements are arbitrary, the "coefficients" for each must be zero to satisfy Hamilton's

principle. The extracted equations of motion are then, after moving inertial terms to the right-hand side,

$$\frac{\partial N_r}{\partial r} + \frac{1}{r}\frac{\partial N_{r\theta}}{\partial \theta} + \frac{N_r - N_\theta}{r} = I_0\ddot{u} - I_1\frac{\partial \ddot{w}}{\partial r} \tag{A–53}$$

$$\frac{\partial N_{r\theta}}{\partial r} + \frac{1}{r}\frac{\partial N_\theta}{\partial \theta} + \frac{2N_{r\theta}}{r} = I_0\ddot{v} - I_1\frac{1}{r}\frac{\partial \ddot{w}}{\partial \theta}, \tag{A–54}$$

and

$$\begin{aligned}\frac{\partial^2 M_r}{\partial r^2} + \frac{2}{r}\frac{\partial M_r}{\partial r} + \frac{1}{r^2}\frac{\partial^2 M_\theta}{\partial \theta^2} - \frac{1}{r}\frac{\partial M_\theta}{\partial r} + \frac{2}{r}\frac{\partial^2 M_{r\theta}}{\partial r \partial \theta} + \frac{2}{r^2}\frac{\partial M_{r\theta}}{\partial \theta} \\ + \frac{1}{r}\frac{\partial}{\partial r}\left(rN_r\frac{\partial w}{\partial r} + N_{r\theta}\frac{\partial w}{\partial \theta}\right) + \frac{1}{r^2}\frac{\partial}{\partial \theta}\left(rN_{r\theta}\frac{\partial w}{\partial r} + N_\theta\frac{\partial w}{\partial \theta}\right) \\ + q_z = I_0\ddot{w} + \frac{1}{r}\frac{\partial}{\partial r}\left(rI_1\ddot{u} - rI_2\frac{\partial \ddot{w}}{\partial r}\right) + \frac{1}{r}\frac{\partial}{\partial \theta}\left(I_1\ddot{v} - I_2\frac{1}{r}\frac{\partial \ddot{w}}{\partial \theta}\right).\end{aligned} \tag{A–55}$$

Although they have been carried through to this point for completeness, terms containing in-plane accelerations $\ddot{u}$ and $\ddot{v}$ are negligible because the motion of the plate is primarily in the z-direction. Rotary inertia terms containing I_2 can also be neglected, as they primarily contribute to higher-order vibration modes [121, 198]. The first vibration mode is the primary one of interest for this investigation. The equations of equilibrium then become

$$\frac{\partial N_r}{\partial r} + \frac{1}{r}\frac{\partial N_{r\theta}}{\partial \theta} + \frac{N_r - N_\theta}{r} = 0, \tag{A–56}$$

$$\frac{\partial N_{r\theta}}{\partial r} + \frac{1}{r}\frac{\partial N_\theta}{\partial \theta} + \frac{2N_{r\theta}}{r} = 0, \tag{A–57}$$

and

$$\begin{aligned}\frac{\partial^2 M_r}{\partial r^2} + \frac{2}{r}\frac{\partial M_r}{\partial r} + \frac{1}{r^2}\frac{\partial^2 M_\theta}{\partial \theta^2} - \frac{1}{r}\frac{\partial M_\theta}{\partial r} + \frac{2}{r}\frac{\partial^2 M_{r\theta}}{\partial r \partial \theta} + \frac{2}{r^2}\frac{\partial M_{r\theta}}{\partial \theta} \\ + \frac{1}{r}\frac{\partial}{\partial r}\left(rN_r\frac{\partial w}{\partial r} + N_{r\theta}\frac{\partial w}{\partial \theta}\right) + \frac{1}{r^2}\frac{\partial}{\partial \theta}\left(rN_{r\theta}\frac{\partial w}{\partial r} + N_\theta\frac{\partial w}{\partial \theta}\right) + q_z = I_0\ddot{w}.\end{aligned} \tag{A–58}$$

These equations are subject to boundary conditions that are also extracted from the combined equation for Hamilton's principle. On each boundary, there is an essential (or geometric) boundary condition and a natural boundary condition, from which one must be specified [121]. On $r = r_1$ and $r = r_2$, specify [122]:

$$u \quad \text{or} \quad N_r \tag{A–59}$$

$$v \quad \text{or} \quad N_{r\theta} \tag{A–60}$$

$$w \quad \text{or} \quad Q_r + N_r\frac{\partial w}{\partial r} + N_{r\theta}\frac{1}{r}\frac{\partial w}{\partial \theta} + \frac{1}{r}\frac{\partial M_{r\theta}}{\partial \theta} \tag{A–61}$$

$$\frac{\partial w}{\partial r} \quad \text{or} \quad M_r. \tag{A–62}$$

Similarly, on $\theta = 0, \theta_0$ specify [122]:

$$u \quad \text{or} \quad N_{r\theta} \tag{A–63}$$

$$v \quad \text{or} \quad N_{\theta} \tag{A–64}$$

$$w \quad \text{or} \quad Q_{\theta} + N_{r\theta}\frac{\partial w}{\partial r} + N_{\theta}\frac{1}{r}\frac{\partial w}{\partial \theta} + \frac{\partial M_{r\theta}}{\partial r} \tag{A–65}$$

$$\frac{\partial w}{\partial \theta} \quad \text{or} \quad M_{\theta}. \tag{A–66}$$

Finally, at $(r, \theta) = (r_1, 0), (r_2, \theta_0), (r_2, 0), (r_1, \theta_0)$, specify [122]:

$$w \quad \text{or} \quad M_{r\theta}. \tag{A–67}$$

The shear intensities [122] appearing in Equation A–61 and Equation A–65 are defined as

$$Q_r = \frac{1}{r}\left[\frac{\partial}{\partial r}\left(rM_r\right) + \frac{\partial M_{r\theta}}{\partial \theta} - M_{\theta}\right] \tag{A–68}$$

and

$$Q_{\theta} = \frac{1}{r}\left[\frac{\partial}{\partial r}\left(rM_{r\theta}\right) + M_{r\theta} + \frac{\partial M_{\theta}}{\partial \theta}\right]. \tag{A–69}$$

Note that Equations A–56 to A–58 are completely general within the confines of the von Kármán plate theory, i.e. they are valid for a circular plate with arbitrary composite layup and arbitrary distributed load q_z.

Restricting the problem to one exhibiting axial symmetry, all quantities are no longer regarded as functions of θ ($\partial/\partial\theta = 0$). In addition, the θ-directed displacement, v, is necessarily zero. For the axisymmetric case, the equations of motion simplify to

$$\frac{\partial N_r}{\partial r} + \frac{N_r - N_{\theta}}{r} = 0 \tag{A–70}$$

and

$$\frac{\partial^2 M_r}{\partial r^2} + \frac{2}{r}\frac{\partial M_r}{\partial r} - \frac{1}{r}\frac{\partial M_{\theta}}{\partial r} + \frac{1}{r}\frac{\partial}{\partial r}\left(rN_r\frac{\partial w}{\partial r}\right) + q_z = I_0\ddot{w}. \tag{A–71}$$

The boundary conditions are simplified as well. On $r = a$ and $r = b$, specify:

$$u \quad \text{or} \quad N_r \tag{A–72}$$

$$w \quad \text{or} \quad Q_r + N_r\frac{\delta w}{\delta r} \tag{A–73}$$

$$\frac{\partial w}{\partial r} \quad \text{or} \quad M_r. \tag{A–74}$$

The remaining derivation will focus on the axisymmetric case, as carrying the mathematics through for a non-axisymmetric, nonlinear circular composite plate with unsymmetric layup is an unnecessarily laborious task. The axisymmetric restriction also implies that the materials composing the composite laminate must be transversely isotropic and that both external loadings and boundary conditions must not vary in θ. Note also that with

the axisymmetric restriction in place, non-axisymmetric buckling or vibration modes — even those resulting from symmetric loadings — cannot be predicted in a buckling or dynamic analysis, respectively. The nonlinear treatment of a non-axisymmetric isotropic circular plate can be found in [122] and it is relatively straightforward to extend it to the symmetric laminate case starting from Equations A–56 to A–58.

A.4 Constitutive Equation

To solve for the reference plane displacements, the equations of motion must be written in terms of these quantities. Thus, the forces and moments must be related to the displacements; this is accomplished through incorporation of the constitutive behavior of the material(s) of which the plate is composed. In general, the plate considered here is an asymmetrically laminated composite with integrated piezoelectric layers. The general constitutive relationship for a piezoelectric material is

$$\boldsymbol{\varepsilon} = \boldsymbol{S}^{\boldsymbol{E_f}}\boldsymbol{\sigma} + \boldsymbol{d}^T\boldsymbol{E_f}, \tag{A–75}$$

where $\boldsymbol{S}^{\boldsymbol{E_f}}$ is the elastic compliance matrix (measured under constant electric field), $\boldsymbol{d}$ is the matrix of piezoelectric constants, and $\boldsymbol{E_f}$ is the electric field vector. For a piezoelectric material of the Tetragonal 4mm or Hexagonal 6mm crystal class (e.g. PZT and aluminum nitride, respectively), the specific form of the constitutive relation is

$$\begin{Bmatrix} \varepsilon_r \\ \varepsilon_\theta \\ \varepsilon_z \\ 2\varepsilon_{\theta z} \\ 2\varepsilon_{rz} \\ 2\varepsilon_{r\theta} \end{Bmatrix} = \begin{bmatrix} \frac{1}{E_p} & -\frac{\nu_p}{E_p} & -\frac{\nu_{zp}}{E_z} & 0 & 0 & 0 \\ -\frac{\nu_p}{E_p} & \frac{1}{E_p} & -\frac{\nu_{zp}}{E_z} & 0 & 0 & 0 \\ -\frac{\nu_{zp}}{E_z} & -\frac{\nu_{zp}}{E_z} & \frac{1}{E_z} & 0 & 0 & 0 \\ 0 & 0 & 0 & \frac{1}{G_{zp}} & 0 & 0 \\ 0 & 0 & 0 & 0 & \frac{1}{G_{zp}} & 0 \\ 0 & 0 & 0 & 0 & 0 & \frac{1}{G_p} \end{bmatrix} \begin{Bmatrix} \sigma_r \\ \sigma_\theta \\ \sigma_z \\ \sigma_{\theta z} \\ \sigma_{rz} \\ \sigma_{r\theta} \end{Bmatrix} + \begin{bmatrix} 0 & 0 & d_{31} \\ 0 & 0 & d_{31} \\ 0 & 0 & d_{33} \\ 0 & d_{15} & 0 \\ d_{15} & 0 & 0 \\ 0 & 0 & 0 \end{bmatrix} \begin{Bmatrix} E_{fr} \\ E_{f\theta} \\ E_{fz} \end{Bmatrix}, \tag{A–76}$$

where the subscript p refers to properties in the plane of the plate and $G_p = 2\left(1+\nu_p\right)/E_p$. Note also that based on the given definition for $\boldsymbol{S}^{\boldsymbol{E_f}}$, $\boldsymbol{\varepsilon}$ represent engineering — not tensoral — strains [98].

Recognizing that a thin plate exists in a state of plane stress and that electrode layers promote potential gradients only in the z-direction, the constitutive equation may be reduced to [198]

$$\begin{Bmatrix} \varepsilon_r \\ \varepsilon_\theta \\ 2\varepsilon_{r\theta} \end{Bmatrix} = \begin{bmatrix} 1/E & -\nu/E & 0 \\ -\nu/E & 1/E & 0 \\ 0 & 0 & 2\left(1+\nu\right)/E \end{bmatrix} \begin{Bmatrix} \sigma_r \\ \sigma_z \\ \sigma_{r\theta} \end{Bmatrix} + \begin{Bmatrix} d_{31} \\ d_{31} \\ 0 \end{Bmatrix} E_f. \tag{A–77}$$

Equation A–77 is consistent with a material exhibiting transverse isotropy, a necessity for this derivation given the assumption of axisymmetry. The p subscript has been dropped here for convenience, and it will be understood henceforth that the Young's modulus, E, and Poisson's ratio, ν, correspond to the properties in the plane of the plate. The subscript z has also been dropped from the electric field term, which is now understood to

be oriented in the z-direction. Next, letting

$$\boldsymbol{\varepsilon} = \left\{ \begin{array}{ccc} \varepsilon_r & \varepsilon_\theta & 2\varepsilon_{r\theta} \end{array} \right\}^T, \tag{A–78}$$

$$\boldsymbol{\sigma} = \left\{ \begin{array}{ccc} \sigma_r & \sigma_\theta & \sigma_{r\theta} \end{array} \right\}^T, \tag{A–79}$$

and

$$\boldsymbol{d} = \left\{ \begin{array}{ccc} d_{31} & d_{31} & 0 \end{array} \right\}^T, \tag{A–80}$$

Equation A–77 is solved for the stresses,

$$\boldsymbol{\sigma} = \boldsymbol{Q}\left(\boldsymbol{\varepsilon} - \boldsymbol{d}E_f\right), \tag{A–81}$$

where

$$\boldsymbol{Q} = \begin{bmatrix} Q_{11} & Q_{12} & 0 \\ Q_{12} & Q_{11} & 0 \\ 0 & 0 & Q_{66} \end{bmatrix} \tag{A–82}$$

$$= \frac{E}{1-\nu^2} \begin{bmatrix} 1 & \nu & 0 \\ \nu & 1 & 0 \\ 0 & 0 & (1-\nu)/2 \end{bmatrix} \tag{A–83}$$

are the plane stress-reduced stiffnesses.

In-plane residual stresses — analogous to thermal stresses — are introduced here via adding an extra term to the constitutive relation, Equation A–81. The result is then

$$\boldsymbol{\sigma} = \boldsymbol{\sigma_0} + \boldsymbol{Q}\left(\boldsymbol{\varepsilon} - E_f\boldsymbol{d}\right), \tag{A–84}$$

where

$$\boldsymbol{\sigma_0} = \left\{ \begin{array}{ccc} \sigma_0 & \sigma_0 & 0 \end{array} \right\}^T. \tag{A–85}$$

No assumptions are made at this time about the spatial distributin of the in-plane stresses. Next, substituting Equation A–26 into Equation A–84 gives the stresses in terms of the reference surface strains and curvatures as

$$\boldsymbol{\sigma} = \boldsymbol{\sigma_0} + \boldsymbol{Q}\left(\boldsymbol{\varepsilon^0} + z\boldsymbol{\kappa} - E_f\boldsymbol{d}\right) \tag{A–86}$$

Integrating Equation A–86 through the thickness (i.e. from $z = z_b$ to z_t) subject to the definitions of the in-plane forces and moments found in Equations A–48 to A–49 yields

$$\boldsymbol{N} = \boldsymbol{N_0} + \boldsymbol{A\varepsilon^0} + \boldsymbol{B\kappa} - \boldsymbol{N_p} \tag{A–87}$$

and

$$\boldsymbol{M} = \boldsymbol{M_0} + \boldsymbol{B\varepsilon^0} + \boldsymbol{D\kappa} - \boldsymbol{M_p}, \tag{A–88}$$

where

$$\boldsymbol{N} = \left\{ \begin{array}{ccc} N_r & N_\theta & N_{r\theta} \end{array} \right\}^T, \tag{A–89}$$

$$\boldsymbol{M} = \left\{ \begin{array}{ccc} M_r & M_\theta & M_{r\theta} \end{array} \right\}^T, \tag{A–90}$$

$$\boldsymbol{N_0} = \int_{z_b}^{z_t} \boldsymbol{\sigma_0} dz, \tag{A–91}$$

$$\boldsymbol{M_0} = \int_{z_b}^{z_t} \boldsymbol{\sigma_0} z dz, \tag{A–92}$$

$$\boldsymbol{N_p} = \int_{z_b}^{z_t} E_f \boldsymbol{Q d} dz, \tag{A–93}$$

and

$$\boldsymbol{M_p} = \int_{z_b}^{z_t} E_f \boldsymbol{Q d} z dz. \tag{A–94}$$

The extensional stiffnesses $\boldsymbol{A}$, bending-extensional coupling stiffnesses $\boldsymbol{B}$, and bending stiffnesses $\boldsymbol{D}$ are given as

$$\boldsymbol{A} = \int_{z_b}^{z_t} \boldsymbol{Q} dz, \tag{A–95}$$

$$\boldsymbol{B} = \int_{z_b}^{z_t} \boldsymbol{Q} z dz, \tag{A–96}$$

and

$$\boldsymbol{D} = \int_{z_b}^{z_t} \boldsymbol{Q} z^2 dz, \tag{A–97}$$

respectively. For a symmetric laminate, i.e. one in which the layers above the reference surface are exact mirror images of those below the reference surface (in terms of material properties, orientation, and thickness), $\boldsymbol{B} = \boldsymbol{0}$. In the typical case of constant properties within each individual layer of the composite, the integrals used in Equations A–91 to A–97 can be rewritten as summations in terms of individual layer coordinates (Figure A-2) as

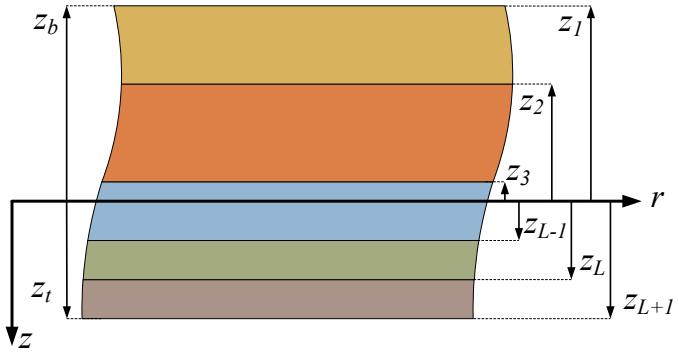

Figure A-2. Layer coordinates for an arbitrary composite layup.

$$\int_{z_b}^{z_t} (\,)\, dz = \sum_{i=1}^{L} (\,)_i \, (z_{i+1} - z_i) = \sum_{i=1}^{L} (\,)_i \, H_i, \tag{A–98}$$

$$\int_{z_b}^{z_t} (\,)\, z dz = \frac{1}{2} \sum_{i=1}^{L} (\,)_i \left(z_{i+1}^2 - z_i^2 \right) = \sum_{i=1}^{L} (\,)_i \, \overline{z}_i H_i, \tag{A–99}$$

and

$$\int_{z_b}^{z_t} (\,)\, z^2 dz = \frac{1}{3}\sum_{i=1}^{L} (\,)_i \left(z_{i+1}^3 - z_i^3\right) = \sum_{i=1}^{L} (\,)_i \left(\frac{H_i^3}{12} + H_i \overline{z}_i^2\right), \tag{A–100}$$

where $(\,)_i$ refers to the value of the integrand in the ith layer, H_i is the ith layer thickness, and $\overline{z}_i$ is the coordinate of the center of the ith layer. Equations A–87 to A–88 are often written in a more compact form as

$$\left\{ \begin{array}{c} \boldsymbol{N} \\ \boldsymbol{M} \end{array} \right\} = \left\{ \begin{array}{c} \boldsymbol{N_0} \\ \boldsymbol{M_0} \end{array} \right\} + \left[\begin{array}{cc} \boldsymbol{A} & \boldsymbol{B} \\ \boldsymbol{B} & \boldsymbol{D} \end{array} \right] \left\{ \begin{array}{c} \boldsymbol{\varepsilon^0} \\ \boldsymbol{\kappa} \end{array} \right\} - \left\{ \begin{array}{c} \boldsymbol{M_p} \\ \boldsymbol{N_p} \end{array} \right\}. \tag{A–101}$$

Also, for convenience, let

$$\left\{ \begin{array}{c} \tilde{\boldsymbol{N}} \\ \tilde{\boldsymbol{M}} \end{array} \right\} = \left[\begin{array}{cc} \boldsymbol{A} & \boldsymbol{B} \\ \boldsymbol{B} & \boldsymbol{D} \end{array} \right] \left\{ \begin{array}{c} \boldsymbol{\varepsilon^0} \\ \boldsymbol{\kappa} \end{array} \right\}. \tag{A–102}$$

such that the overall constitutive equation for the laminated composite becomes

$$\left\{ \begin{array}{c} \boldsymbol{N} \\ \boldsymbol{M} \end{array} \right\} = \left\{ \begin{array}{c} \boldsymbol{N_0} \\ \boldsymbol{M_0} \end{array} \right\} + \left\{ \begin{array}{c} \tilde{\boldsymbol{N}} \\ \tilde{\boldsymbol{M}} \end{array} \right\} - \left\{ \begin{array}{c} \boldsymbol{M_p} \\ \boldsymbol{N_p} \end{array} \right\}. \tag{A–103}$$

Observing the axisymmetric assumption, $N_{r\theta} = M_{r\theta} = 0$ and the third component can be dropped from $\boldsymbol{N}$ and $\boldsymbol{M}$ because $\varepsilon_{r\theta} = \kappa_{r\theta} = 0$. The various stiffness matrices then only need be regarded as 2×2.

A.5 Displacement Differential Equations of Motion

The axisymmetric form of the constitutive relations developed in Section A.4 may now be combined with the axisymmetric equations of motion, Equations A–70 to A–71, to yield governing differential equations for the reference plane displacements $u\,(r;t)$ and $w\,(r;t)$. First, Equation A–102 is expanded to explicitly define each of the force and moment terms,

$$\tilde{N}_r = A_{11}\left[\frac{du}{dr} + \frac{1}{2}\left(\frac{dw}{dr}\right)^2\right] + A_{12}\frac{u}{r} - B_{11}\frac{d^2w}{dr^2} - B_{12}\frac{1}{r}\frac{dw}{dr}, \tag{A–104}$$

$$\tilde{N}_\theta = A_{11}\frac{u}{r} + A_{12}\left[\frac{du}{dr} + \frac{1}{2}\left(\frac{dw}{dr}\right)^2\right] - B_{11}\frac{1}{r}\frac{dw}{dr} - B_{12}\frac{d^2w}{dr^2}, \tag{A–105}$$

$$\tilde{M}_r = B_{11}\left[\frac{du}{dr} + \frac{1}{2}\left(\frac{dw}{dr}\right)^2\right] + B_{12}\frac{u}{r} - D_{11}\frac{d^2w}{dr^2} - D_{12}\frac{1}{r}\frac{dw}{dr}, \tag{A–106}$$

and

$$\tilde{M}_\theta = B_{11}\frac{u}{r} + B_{12}\left[\frac{du}{dr} + \frac{1}{2}\left(\frac{dw}{dr}\right)^2\right] - D_{11}\frac{1}{r}\frac{dw}{dr} - D_{12}\frac{d^2w}{dr^2}. \tag{A–107}$$

Continuing, Equation A–70 is first solved for N_θ and then substituted into Equation A–71 to yield

$$\frac{\partial^2 M_r}{\partial r^2} + \frac{2}{r}\frac{\partial M_r}{\partial r} - \frac{1}{r}\frac{\partial M_\theta}{\partial r} + \frac{1}{r}\frac{\partial}{\partial r}\left(rN_r\frac{\partial w}{\partial r}\right) + q_z = I_0\ddot{w}. \tag{A–108}$$

Substituting Equations A–106 to A–107 into Equation A–108 yields

$$-D_{11}\nabla^4 w + B_{11}\left[\frac{\partial^3 u}{\partial r^3} + \frac{2}{r}\frac{\partial^2 u}{\partial r^2} - \frac{1}{r^2}\frac{\partial u}{\partial r} + \frac{1}{r^3}u + \left(\frac{\partial^2 w}{\partial r^2}\right)^2 + \frac{\partial w}{\partial r}\frac{\partial^3 w}{\partial r^3} + \frac{2}{r}\frac{\partial w}{\partial r}\frac{\partial^2 w}{\partial r^2}\right] - \frac{B_{12}}{r}\frac{\partial w}{\partial r}\frac{\partial^2 w}{\partial r^2} + \nabla^2\left(M_0 - M_p\right) + \frac{1}{r}\frac{\partial}{\partial r}\left(rN_r\frac{\partial w}{\partial r}\right) + q_z = I_0\ddot{w}, \quad \text{(A–109)}$$

where the familiar biharmonic and Laplacian operators are defined for the axisymmetric problem as

$$\begin{aligned}\nabla^4(\,) &= \frac{1}{r}\frac{d}{dr}\left(r\frac{d}{dr}\left(\frac{1}{r}\frac{d}{dr}\left(r\frac{d(\,)}{dr}\right)\right)\right) \\ &= \frac{d^4(\,)}{dr^4} + \frac{2}{r}\frac{d^3(\,)}{dr^3} - \frac{1}{r^2}\frac{d^2(\,)}{dr^2} + \frac{1}{r^3}\frac{d(\,)}{dr}\end{aligned} \quad \text{(A–110)}$$

and

$$\begin{aligned}\nabla^2(\,) &= \frac{1}{r}\frac{d}{dr}\left(r\frac{d(\,)}{dr}\right) \\ &= \frac{d^2(\,)}{dr^2} + \frac{1}{r}\frac{d(\,)}{dr},\end{aligned} \quad \text{(A–111)}$$

respectively. Similarly, taking $\frac{1}{r}\frac{\partial[r()]}{\partial r}$ of Equation A–70 and then substituting in for N_r and N_θ using Equations A–104 to A–105 yields

$$-B_{11}\nabla^4 w + A_{11}\left[\frac{\partial^3 u}{\partial r^3} + \frac{2}{r}\frac{\partial^2 u}{\partial r^2} - \frac{1}{r^2}\frac{\partial u}{\partial r} + \frac{1}{r^3}u + \left(\frac{\partial^2 w}{\partial r^2}\right)^2 + \frac{\partial w}{\partial r}\frac{\partial^3 w}{\partial r^3} + \frac{2}{r}\frac{\partial w}{\partial r}\frac{\partial^2 w}{\partial r^2}\right] - \frac{A_{12}}{r}\frac{\partial w}{\partial r}\frac{\partial^2 w}{\partial r^2} + \nabla^2\left(N_0 - N_p\right) = 0. \quad \text{(A–112)}$$

Clearly both Equations A–112 and A–109 have very similar forms. Multiplying Equation A–112 by B_{11}/A_{11} and subtracting Equation A–109 from the result gives the governing equation for w,

$$I_0\ddot{w} + D_{11}^*\nabla^4 w = q_z - B_{12}^*\frac{1}{r}\frac{\partial w}{\partial r}\frac{\partial^2 w}{\partial r^2} + \frac{1}{r}\frac{\partial}{\partial r}\left(rN_r\frac{\partial w}{\partial r}\right) + \nabla^2\left[\left(M_0 - M_p\right) - \frac{B_{11}}{A_{11}}\left(N_0 - N_p\right)\right]. \quad \text{(A–113)}$$

where

$$D_{11}^* = D_{11} - \frac{B_{11}^2}{A_{11}} \quad \text{(A–114)}$$

and

$$B_{12}^* = B_{12} - \frac{B_{11}A_{12}}{A_{11}}. \quad \text{(A–115)}$$

Equation A–113 contains two unknowns, w and N_r. A second equation for N_r is therefore required. To find this equation, Equation A–28 is solved for u and substituted

into Equation A–27 to yield

$$\frac{\partial \varepsilon_\theta^0}{\partial r} + \frac{\varepsilon_\theta^0 - \varepsilon_r^0}{r} + \frac{1}{2r}\left(\frac{\partial w}{\partial r}\right)^2 = 0. \tag{A–116}$$

This is known as a compatibility condition. Inverting Equation A–102 to find ε_r^0 and ε_θ^0 in terms of $\tilde{N}_r$, $\tilde{N}_\theta$, and w and then substituting the result into Equation A–116 and dividing by r^2 yields

$$\frac{\partial^2 \tilde{N}_r}{\partial r^2} + \frac{3}{r}\frac{\partial \tilde{N}_r}{\partial r} = -B_{12}^*\left(\frac{1}{r}\frac{\partial^3 w}{\partial r^3} + \frac{1}{r^2}\frac{\partial^2 w}{\partial r^2} - \frac{1}{r^3}\frac{\partial w}{\partial r}\right) - \frac{A_{11}^2 - A_{12}^2}{A_{11}}\frac{1}{2r^2}\left(\frac{\partial w}{\partial r}\right)^2. \tag{A–117}$$

Together, Equations A–113 and A–117 are the mixed-form differential equations for the motion of the piezoelectric composite plate. Alternatively, Equation A–112 may be rearranged into a differential equation for u in terms of w,

$$\begin{aligned}\frac{\partial^3 u}{\partial r^3} + \frac{2}{r}\frac{\partial^2 u}{\partial r^2} - \frac{1}{r^2}\frac{\partial u}{\partial r} + \frac{1}{r^3}u = \frac{B_{11}}{A_{11}}\nabla^4 w - \left(\frac{\partial^2 w}{\partial r^2}\right)^2 - \frac{\partial w}{\partial r}\frac{\partial^3 w}{\partial r^3} - \frac{2}{r}\frac{\partial w}{\partial r}\frac{\partial^2 w}{\partial r^2} \\ + \frac{A_{12}}{A_{11}}\frac{1}{r}\frac{\partial w}{\partial r}\frac{\partial^2 w}{\partial r^2} - \frac{1}{A_{11}}\nabla^2\left(N_0 - N_p\right)\end{aligned} \tag{A–118}$$

and N_r may be substituted into Equation A–113 to give a set of governing differential equations purely in terms of displacement.

A.6 Equations of Equilibrium

At this juncture, the focus shifts to particulars of the problem being pursued, and several new assumptions are made. First, the problem is restricted to the static case for which $\ddot{w} = 0$; the partial differential equations (PDEs) therefore become ordinary differential equations (ODEs). Next, σ_0 and E_f are restricted to be constant in any given layer of the composite plate, which results in N_0, M_0, N_p, and M_p not being functions of r. Finally, the loading is restricted to a uniform pressure acting in the z-direction, i.e. $q_z = p$. In the following two sections, these assumptions are applied to the nonlinear equations of motion, which are then linearized.

A.6.1 Nonlinear

Under the assumptions presented in the introduction, the governing equations become, with some manipulation,

$$D_{11}^*\nabla^4 w = p - B_{12}^*\frac{1}{2r}\frac{d}{dr}\left[\left(\frac{dw}{dr}\right)^2\right] + \frac{1}{r}\frac{d}{dr}\left(rN_r\frac{dw}{dr}\right), \tag{A–119}$$

with

$$\nabla^4(\,) = \frac{1}{r}\frac{d}{dr}\left(r\frac{d}{dr}\left(\frac{1}{r}\frac{d}{dr}\left(r\frac{d(\,)}{dr}\right)\right)\right). \tag{A–120}$$

Equation A–119 is multipled by r, integrated with respect to r, and then divided by $D_{11}^* r$ to yield

$$\frac{d^3w}{dr^3} + \frac{1}{r}\frac{d^2w}{dr^2} - \frac{1}{r^2}\frac{dw}{dr} = \frac{pr}{2D_{11}^*} + \frac{N_r}{D_{11}^*}\frac{dw}{dr} - \frac{B_{12}^*}{2r}\left(\frac{dw}{dr}\right)^2 \tag{A–121}$$

Writing this equation in terms of transverse rotation,

$$\phi = -\frac{dw}{dr}, \tag{A–122}$$

yields

$$\frac{d^2\phi}{dr^2} + \frac{1}{r}\frac{d\phi}{dr} - \frac{\phi}{r^2} = -\frac{pr}{2D_{11}^*} + \frac{N_r}{D_{11}^*}\phi + \frac{B_{12}^*}{2D_{11}^*}\frac{\phi^2}{r} \tag{A–123}$$

Either of Equations A–121 or A–123 may be taken as the governing equation for transverse reference surface displacements.

The governing equation for in-plane reference surface displacements is found from Equation A–118, which first may be equivalently rewritten as

$$\frac{1}{r}\frac{d}{dr}\left(r\frac{d}{dr}\left(\frac{1}{r}\frac{d\left(ru\right)}{dr}\right)\right) = \frac{B_{11}}{A_{11}}\nabla^4 w - \frac{1}{r}\frac{d}{dr}\left(r\frac{dw}{dr}\frac{d^2w}{dr^2}\right) + \left(\frac{A_{12}}{A_{11}} - 1\right)\frac{1}{2r}\frac{d}{dr}\left[\left(\frac{dw}{dr}\right)^2\right] \tag{A–124}$$

Substituting Equation A–122 into Equation A–124, multiplying Equation A–124 by r, integrating with respect to r, and dividing by r gives

$$\frac{d^2u}{dr^2} + \frac{1}{r}\frac{du}{dr} - \frac{u}{r^2} = -\frac{B_{11}}{A_{11}}\left(\frac{d^2\phi}{dr^2} + \frac{1}{r}\frac{d\phi}{dr} - \frac{\phi}{r^2}\right) - \left(\frac{1 - A_{12}}{A_{11}}\right)\frac{\phi^2}{2r} - \phi\frac{d\phi}{dr}. \tag{A–125}$$

Equations A–123 and A–125 are additionally linked by N_r. Substituting Equation A–122 into Equation A–117 and Equation A–102 into Equation A–123 gives

$$\frac{d^2\tilde{N}_r}{dr^2} + \frac{3}{r}\frac{d\tilde{N}_r}{dr} = B_{12}^*\left(\frac{1}{r}\frac{d^2\phi}{dr^2} + \frac{1}{r^2}\frac{d\phi}{dr} - \frac{\phi}{r^3}\right) - \frac{A_{11}^2 - A_{12}^2}{A_{11}}\frac{\phi^2}{2r^2}. \tag{A–126}$$

and

$$\frac{d^2\phi}{dr^2} + \frac{1}{r}\frac{d\phi}{dr} - \left(\frac{N_0 - N_p}{D_{11}^*} + \frac{1}{r^2}\right)\phi = -\frac{pr}{2D_{11}^*} + \frac{\phi\tilde{N}_r}{D_{11}^*} + \frac{\phi^2 B_{12}^*}{2rD_{11}^*}, \tag{A–127}$$

which together are the mixed-form differential equations of equilibrium. Alternatively, Equation A–125 and Equation A–127, with $\tilde{N}_r$ substituted in from Equation A–102, together compose the displacement-based differential equations of equilibrium.

For convenience in future steps, let the in-plane stress parameter be defined as

$$k^{*2} = \left|N_0 - N_p\right|\frac{a^2}{D_{11}^*}, \tag{A–128}$$

where a is a characteristic dimension of the plate (such as outer radius). Substituting into Equation A–127,

$$\frac{d^2\phi}{dr^2} + \frac{1}{r}\frac{d\phi}{dr} - \left(x\frac{k^{*2}}{a^2} + \frac{1}{r^2}\right)\phi = -\frac{pr}{2D_{11}^*} + \frac{\phi\tilde{N}_r}{D_{11}^*} + \frac{\phi^2 B_{12}^*}{2rD_{11}^*}, \tag{A–129}$$

where x is a flag denoting the net sense of the in-plane force terms, i.e.

$$x = \operatorname{sgn}\left(N_0 - N_r^P\right). \tag{A–130}$$

A.6.2 Linear

In order to linearize Equations A–125 to A–127, second order products of displacements are neglected, including the product $\phi\tilde{N}_r$ since $\tilde{N}_r$ is a function of the displacements. In addition, since N_p is proportional to voltage, there always exists a sufficiently small voltage input for which $N_p \ll N_0$, and therefore it may be neglected from the governing differential equation. Alternatively, for the case of small N_0, both may be negligible compared to the remaining terms in the linearized governing differential equation. Thus, neglecting second order products of displacements and the N_p term from the governing differential equations yields

$$\frac{d^2u}{dr^2} + \frac{1}{r}\frac{du}{dr} - \frac{u}{r^2} = -\frac{B_{11}}{A_{11}}\left(\frac{d^2\phi}{dr^2} + \frac{1}{r}\frac{d\phi}{dr} - \frac{\phi}{r^2}\right). \tag{A–131}$$

$$\frac{d^2\tilde{N}_r}{dr^2} + \frac{3}{r}\frac{d\tilde{N}_r}{dr} = \frac{B_{12}^*}{r}\left(\frac{d^2\phi}{dr^2} + \frac{1}{r}\frac{d\phi}{dr} - \frac{\phi}{r^2}\right), \tag{A–132}$$

and

$$\frac{d^2\phi}{dr^2} + \frac{1}{r}\frac{d\phi}{dr} - \left(x\frac{k^{*2}}{a^2} + \frac{1}{r^2}\right)\phi = -\frac{pr}{2D_{11}^*}, \tag{A–133}$$

where k^{*2} is now redefined as

$$k^{*2} = |N_0|\frac{a^2}{D_{11}^*}, \tag{A–134}$$

The solution of Equation A–133 takes on three forms that are dependent on its classification. It is a first-order, non-homogeneous modified Bessel equation for $x > 0$, a first-order, non-homogeneous Bessel equation for $x < 0$, and a non-homogeneous Cauchy-Euler equation when $x = 0$ [199]. Equation A–133 is next substituted into Equations A–131 to A–132, giving the simplified forms

$$\frac{d^2u}{dr^2} + \frac{1}{r}\frac{du}{dr} - \frac{u}{r^2} = -\frac{B_{11}}{A_{11}}\left(-\frac{pr}{2D_{11}^*} + x\frac{k^{*2}}{a^2}\phi\right). \tag{A–135}$$

and

$$\frac{d^2\tilde{N}_r}{dr^2} + \frac{3}{r}\frac{d\tilde{N}_r}{dr} = \frac{B_{12}^*}{r}\left(-\frac{pr}{2D_{11}^*} + x\frac{k^{*2}}{a^2}\phi\right). \tag{A–136}$$

Equation A–133 and Equations A–135 to A–136 are now sequentially coupled, in that the solution for ϕ must first be obtained before the solution to $\tilde{N}_r$ or u may be. In addition,

it is also now clear that both Equation A–135 and Equation A–136 are forms of the non-homogeneous Cauchy-Euler equation [199].

A.7 Problem Solutions

In this section, solutions are presented for the linear and nonlinear forms of the equilibrium equations of the piezoelectric composite plate. The linear solution is fully analytical, though the equations become sufficiently cumbersome that a matrix inversion is suggested for use in determining integration coefficients. Meanwhile, the nonlinear equations are written in a convenient form for numerical solution via readily-available multi-point boundary value problem solvers.

The solution domain is divided into an inner and outer region and the solutions, material properties, geometric properties, etc. within a particular domain will be denoted by a superscript $^{(1)}$ for the inner region and $^{(2)}$ for the outer region. Let the arbitrary length scale a found in the governing equations correspond to the outer radius of the region of interest.

The boundary conditions follow from the choices given in Equations A–72 to A–74. Using the two-domain notation, the boundary conditions for the problem include symmetry conditions at the plate center ($r = 0$),

$$\phi^{(1)}(0) = 0, \tag{A–137}$$
$$u^{(1)}(0) = 0, \tag{A–138}$$

matching conditions at the interface between the inner and outer region ($r = a^{(1)}$),

$$\phi^{(1)}\left(a^{(1)}\right) = \phi^{(2)}\left(a^{(1)}\right), \tag{A–139}$$
$$u^{(1)}\left(a^{(1)}\right) = u^{(2)}\left(a^{(1)}\right), \tag{A–140}$$
$$w^{(1)}\left(a^{(1)}\right) = w^{(2)}\left(a^{(1)}\right), \tag{A–141}$$
$$M_r^{(1)}\left(a^{(1)}\right) = M_r^{(2)}\left(a^{(1)}\right), \tag{A–142}$$
$$N_r^{(1)}\left(a^{(1)}\right) = N_r^{(2)}\left(a^{(1)}\right), \tag{A–143}$$

and boundary conditions on the outer radius ($r = a^{(2)}$)

$$M_r^{(1)}\left(a^{(2)}\right) = -k_\phi \phi^{(2)}\left(a^{(2)}\right) \tag{A–144}$$
$$u^{(2)}\left(a^{(2)}\right) = 0 \tag{A–145}$$
$$w^{(2)}\left(a^{(2)}\right) = 0 \tag{A–146}$$

The compliant boundary condition of Equation A–144 effectively means both the simply-supported ($k_\phi = 0$) and clamped ($k_\phi = \infty$) cases are available from the final solution.

The solutions in the coming sections make use of the Bessel functions of the first and second kind, J_n and Y_n, respectively and the modified-Bessel functions of the first and second kind, I_n and K_n, respectively [200].

A.7.1 Linear

A.7.1.1 General solutions

The general solutions to the governing linear equations of equilibrium, Equations A–133, A–135, and A–136, are

$$\phi(r) = \begin{cases} c_1 I_1\left(k^* \frac{r}{a}\right) + c_2 K_1\left(k^* \frac{r}{a}\right) + \frac{1}{2}\frac{pa^2 r}{D_{11}^* k^{*2}}, & x > 0 \\ c_1 r + \frac{c_2}{r} - \frac{1}{16}\frac{pr^3}{D_{11}^*}, & x = 0 \\ c_1 J_1\left(k^* \frac{r}{a}\right) + c_2 Y_1\left(k^* \frac{r}{a}\right) - \frac{1}{2}\frac{pa^2 r}{D_{11}^* k^{*2}}, & x < 0, \end{cases} \tag{A–147}$$

$$u(r) = \begin{cases} c_3 r + \frac{c_4}{r} - \frac{B_{11}}{A_{11}}\left[c_1 I_1\left(k^* \frac{r}{a}\right) + c_2 K_1\left(k^* \frac{r}{a}\right)\right], & x > 0 \\ c_3 r + \frac{c_4}{r} + \frac{1}{16}\frac{B_{11}}{A_{11}}\frac{pr^3}{D_{11}^*}, & x = 0 \\ c_3 r + \frac{c_4}{r} - \frac{B_{11}}{A_{11}}\left[c_1 J_1\left(k^* \frac{r}{a}\right) + c_2 Y_1\left(k^* \frac{r}{a}\right)\right], & x < 0, \end{cases} \tag{A–148}$$

and

$$w(r) = \begin{cases} -c_1 \frac{a}{k^*} I_0\left(k^* \frac{r}{a}\right) + c_2 \frac{a}{k^*} K_0\left(k^* \frac{r}{a}\right) - \frac{1}{4}\frac{pa^2 r^2}{D_{11}^* k^{*2}} + c_5, & x > 0 \\ -c_1 \frac{1}{2} r^2 - c_2 \ln(r) + \frac{1}{64}\frac{pr^4}{D_{11}^*} + c_5, & x = 0 \\ c_1 \frac{a}{k^*} J_0\left(k^* \frac{r}{a}\right) + c_2 \frac{a}{k^*} Y_0\left(k^* \frac{r}{a}\right) + \frac{1}{4}\frac{pa^2 r^2}{D_{11}^* k^{*2}} + c_5, & x < 0. \end{cases} \tag{A–149}$$

Following from these solutions are the force and moment resultants, Equation A–102, which with nonlinear terms neglected are

$$N_r(r) = \begin{cases} N_0 - N_p + B_{12}^* I_1\left(k^* \frac{r}{a}\right)\frac{1}{r} c_1 + B_{12}^* K_1\left(k^* \frac{r}{a}\right)\frac{1}{r} c_2 \\ + (A_{11} + A_{12}) c_3 - (A_{11} - A_{12})\frac{1}{r^2} c_4 + \frac{1}{2}(B_{11} + B_{12})\frac{pa^2}{D_{11}^* k^{*2}}, & x > 0 \\ -N_p + (B_{11} + B_{12}) c_1 - (B_{11} - B_{12})\frac{1}{r^2} c_2 + (A_{11} + A_{12}) c_3 \\ - (A_{11} - A_{12})\frac{1}{r^2} c_4 - B_{12}^* \frac{1}{16}\frac{pr^2}{D_{11}^*}, & x = 0 \\ N_0 - N_p + B_{12}^* J_1\left(k^* \frac{r}{a}\right)\frac{1}{r} c_1 + B_{12}^* Y_1\left(k^* \frac{r}{a}\right)\frac{1}{r} c_2 + (A_{11} + A_{12}) c_3 \\ - (A_{11} - A_{12})\frac{1}{r^2} c_4 - \frac{1}{2}(B_{11} + B_{12})\frac{pa^2}{D_{11}^* k^{*2}}, & x < 0, \end{cases} \tag{A–150}$$

and

$$M_r(r) = \begin{cases} M_0 - M_p + \left[\dfrac{D_{11}^* k^*}{a} I_0\left(k^* \dfrac{r}{a}\right) - \left(D_{11}^* - D_{12}^*\right) I_1\left(k^* \dfrac{r}{a}\right) \dfrac{1}{r}\right] c_1 \\ - \left[\dfrac{D_{11}^* k^*}{a} K_0\left(k^* \dfrac{r}{a}\right) + \left(D_{11}^* - D_{12}^*\right) K_1\left(k^* \dfrac{r}{a}\right) \dfrac{1}{r}\right] c_2 & x > 0 \\ + \left(B_{11} + B_{12}\right) c_3 - \left(B_{11} - B_{12}\right) \dfrac{1}{r^2} c_4 + \dfrac{1}{2}\left(D_{11} + D_{12}\right) \dfrac{p a^2}{D_{11}^* k^{*2}}, \\ \\ M_0 - M_p + \left(D_{11} + D_{12}\right) c_1 - \left(D_{11} - D_{12}\right) \dfrac{1}{r^2} c_2 + \left(B_{11} + B_{12}\right) c_3 \\ - \left(B_{11} - B_{12}\right) \dfrac{1}{r^2} c_4 - \left(3 D_{11}^* + D_{12}^*\right) \dfrac{1}{16} \dfrac{p r^2}{D_{11}^*}, & x = 0 \\ \\ M_0 - M_p + \left[\dfrac{D_{11}^* k^*}{a} J_0\left(k^* \dfrac{r}{a}\right) - \left(D_{11}^* - D_{12}^*\right) J_1\left(k^* \dfrac{r}{a}\right) \dfrac{1}{r}\right] c_1 \\ + \left[\dfrac{D_{11}^* k^*}{a} Y_0\left(k^* \dfrac{r}{a}\right) - \left(D_{11}^* - D_{12}^*\right) Y_1\left(k^* \dfrac{r}{a}\right) \dfrac{1}{r}\right] c_2 & x < 0. \\ + \left(B_{11} + B_{12}\right) c_3 - \left(B_{11} - B_{12}\right) \dfrac{1}{r^2} c_4 - \dfrac{1}{2}\left(D_{11} + D_{12}\right) \dfrac{p a^2}{D_{11}^* k^{*2}}, \end{cases} \tag{A–151}$$

A.7.1.2 Particular solutions

In total, there are 5 unknown integration constants introduced via Equations A–147 to A–149: c_1, c_2, c_3, c_4, and c_5. As the solution to each of these equations is sought in either domain, there are actually a total of 10 unknown integration constants in the two-domain problem: $c_i^{(1)}$ and $c_i^{(2)}$ with $i = 1 \ldots 5$. With the ten boundary conditions of Equations A–137 to A–146, the problem is thus well-posed.

Given the length of the equations introduced in Section A.7.1.1, solving for the integration constants explicitly is a burdensome task. Instead, they are found via writing the boundary conditions as a system of linear equations solved via matrix inversion. Before that process, though, the symmetry conditions of Equations A–137 to A–138 immediately reveal that $c_2^{(1)} = c_4^{(1)} = 0$ because each of the terms they are associated with in Equations A–147 to A–148 are unbounded at $r = 0$. This reduces the unknown integration constants to 8 in total. After substituting the appropriate general solutions of Section A.7.1.1 into any of the remaining boundary conditions, the result may always be written in the form

$$\boldsymbol{C_i^{(1)}}^T \boldsymbol{c^{(1)}} + f_i^{(1)} = \boldsymbol{C_i^{(2)}}^T \boldsymbol{c^{(2)}} + f_i^{(2)}, \tag{A–152}$$

where each $\boldsymbol{C_i^{(j)}}$ is an array which contains the coefficients of the integration constants, $\boldsymbol{c^{(j)}}$ contains the integration constants themselves, and $f_i^{(j)}$ represents the collected free terms for the ith boundary condition ($i = 1, 2 \ldots 8$) in the jth domain ($j = 1, 2$). Collecting the eight equations represented by Equation A–152 into a single matrix equation gives

$$\underset{8x3}{\left[-\boldsymbol{C^{(1)}} \right.} \quad \underset{8x5}{\left. \boldsymbol{C^{(2)}} \right]} \left\{ \begin{matrix} 3x1 \\ \boldsymbol{c^{(1)}} \\ \boldsymbol{c^{(2)}} \\ 5x1 \end{matrix} \right\} = \underset{8x1}{\boldsymbol{f^{(1)}}} - \underset{8x1}{\boldsymbol{f^{(2)}}}. \tag{A–153}$$

The utility of Equation A–153 is that the integration constants are found in a modular manner that allows for the coupled solution of any inner region case ($x^{(1)} = -1, 0, 1$) and any outer region case ($x^{(2)} = -1, 0, 1$) simply via matrix inversion of the combined $[C]$ matrix.

Deflection of the diaphragm occurs due to any or all of 3 inputs: initial stress, pressure, or voltage. In the case of an initially stressed diaphragm, there is an existing static deflection before the application of voltage or pressure. Voltage or pressure loading leads to an additional incremental deflection which in the context of lumped element modeling is the quantity of interest. It is thus convenient to solve for the incremental deflection directly. This is made possible via dividing the array of forcing terms, $\boldsymbol{f}^{(j)}$, into its components parts,

$$\boldsymbol{f}^{(j)} = \boldsymbol{f}_{\boldsymbol{0}}^{(j)} + \boldsymbol{f}_{\boldsymbol{p}}^{(j)} + \boldsymbol{f}_{\boldsymbol{v}}^{(j)}, \tag{A–154}$$

where each of $\boldsymbol{f}_{\boldsymbol{0}}^{(j)}$, $\boldsymbol{f}_{\boldsymbol{p}}^{(j)}$, and $\boldsymbol{f}_{\boldsymbol{v}}^{(j)}$ include only those terms relating to in-plane stress, pressure, and voltage, respectively, with all others zero. To solve for the initial deflection alone, replace $\boldsymbol{f}^{(j)}$ with only the in-plane component, $\boldsymbol{f}_{\boldsymbol{0}}^{(j)}$ (equivalent to letting $v = p = 0$). To solve for the incremental deflection directly, replace the total $\boldsymbol{f}^{(j)}$ by $\boldsymbol{f}_{\boldsymbol{p}}^{(j)}$ or $\boldsymbol{f}_{\boldsymbol{v}}^{(j)}$ for incremental deflection due to pressure and voltage, respectively. In these latter cases, the in-plane stress still affects the stiffness via its inclusion in $\boldsymbol{C}$.

In each of the following subsections, the specific definitions of the $\boldsymbol{C}^{(j)}$ and each of the components of $\boldsymbol{f}^{(j)}$ are given for all cases. The solution of the problem is obtained by using these expressions to assemble Equation A–153, solving for the integration constants numerically via matrix inversion, and then plugging the numerical values into any of Equations A–147 to A–151 depending on the quantity of interest. The substitution part of the process is performed for each domain, so in the end there are two equations for each of the displacements and force components — corresponding to the inner and outer domain — with validity over $0 \leq r \leq a^{(1)}$ and $a^{(1)} \leq r \leq a^{(2)}$, respectively.

A.7.1.3 Inner region: tension ($x^{(1)} > 0$)

$$\boldsymbol{C^{(1)}} = \begin{bmatrix} I_1\left(k^{*(1)}\right) & 0 & 0 \\ -\frac{B_{11}^{(1)}}{A_{11}^{(1)}} I_1\left(k^{*(1)}\right) & a^{(1)} & 0 \\ -\frac{a^{(1)}}{k^{*(1)}} I_0\left(k^{*(1)}\right) & 0 & 1 \\ \left[D^{*(1)}k^{*(1)} I_0\left(k^{*(1)}\right) - \left(D^{*(1)} - D_{12}^{*(1)}\right) I_1\left(k^{*(1)}\right)\right] \frac{1}{a^{(1)}} & B_{11}^{(1)} + B_{12}^{(1)} & 0 \\ B_{12}^{*(1)} I_1\left(k^{*(1)}\right) \frac{1}{a^{(1)}} & A_{11}^{(1)} + A_{12}^{(1)} & 0 \\ 0 & 0 & 0 \\ 0 & 0 & 0 \\ 0 & 0 & 0 \end{bmatrix} \tag{A–155}$$

$$\boldsymbol{f^{(1)}} = \begin{Bmatrix} 0 \\ 0 \\ 0 \\ M_0^{(1)} \\ N_0^{(1)} \\ 0 \\ 0 \\ 0 \end{Bmatrix} + \begin{Bmatrix} \frac{1}{2}\frac{pa^{(1)3}}{D^{*(1)}k^{*(1)2}} \\ 0 \\ -\frac{1}{4}\frac{pa^{(1)4}}{D^{*(1)}k^{*(1)2}} \\ \frac{1}{2}\left(D_{11}^{(1)} + D_{12}^{(1)}\right)\frac{pa^{(1)2}}{D^{*(1)}k^{*(1)2}} \\ \frac{1}{2}\left(B_{11}^{(1)} + B_{12}^{(1)}\right)\frac{pa^{(1)2}}{D^{*(1)}k^{*(1)2}} \\ 0 \\ 0 \\ 0 \end{Bmatrix} + \begin{Bmatrix} 0 \\ 0 \\ 0 \\ -M_p^{(1)} \\ -N_p^{(1)} \\ 0 \\ 0 \\ 0 \end{Bmatrix} \tag{A–156}$$

A.7.1.4 Inner region: $x^{(1)} = 0$

$$\boldsymbol{C^{(1)}} = \begin{bmatrix} a^{(1)} & 0 & 0 \\ 0 & a^{(1)} & 0 \\ -\frac{1}{2}{a^{(1)}}^2 & 0 & 1 \\ D_{11}^{(1)} + D_{12}^{(1)} & B_{11}^{(1)} + B_{12}^{(1)} & 0 \\ B_{11}^{(1)} + B_{12}^{(1)} & A_{11}^{(1)} + A_{12}^{(1)} & 0 \\ 0 & 0 & 0 \\ 0 & 0 & 0 \\ 0 & 0 & 0 \end{bmatrix} \tag{A–157}$$

$$\boldsymbol{f^{(1)}} = \begin{Bmatrix} 0 \\ 0 \\ 0 \\ M_0^{(1)} \\ 0 \\ 0 \\ 0 \\ 0 \end{Bmatrix} + \begin{Bmatrix} -\frac{1}{16}\frac{pa^{(1)^3}}{D^{*(1)}} \\ \frac{1}{16}\frac{B_{11}^{(1)}}{A_{11}^{(1)}}\frac{pa^{(1)3}}{D^{*(1)}} \\ \frac{1}{64}\frac{pa^{(1)4}}{D^{*(1)}} \\ -\left[3D^{*(1)} + D_{12}^{*(1)}\right]\frac{1}{16}\frac{pa^{(1)2}}{D^{*(1)}} \\ -B_{12}^{*(1)}\frac{1}{16}\frac{pa^{(1)2}}{D^{*(1)}} \\ 0 \\ 0 \\ 0 \end{Bmatrix} + \begin{Bmatrix} 0 \\ 0 \\ 0 \\ -M_p^{(1)} \\ -N_p^{(1)} \\ 0 \\ 0 \\ 0 \end{Bmatrix} \tag{A–158}$$

A.7.1.5 Inner region: compression ($x^{(1)} < 0$)

$$\boldsymbol{C^{(1)}} = \begin{bmatrix} J_1\left(k^{*(1)}\right) & 0 & 0 \\ -\frac{B_{11}^{(1)}}{A_{11}^{(1)}}J_1\left(k^{*(1)}\right) & a^{(1)} & 0 \\ \frac{a^{(1)}}{k^{*(1)}}J_0\left(k^{*(1)}\right) & 0 & 1 \\ \left[D^{*(1)}k^{*(1)}J_0\left(k^{*(1)}\right) - \left(D^{*(1)} - D_{12}^{*(1)}\right)J_1\left(k^{*(1)}\right)\right]\frac{1}{a^{(1)}} & B_{11}^{(1)} + B_{12}^{(1)} & 0 \\ B_{12}^{*(1)}J_1\left(k^{*(1)}\right)\frac{1}{a^{(1)}} & A_{11}^{(1)} + A_{12}^{(1)} & 0 \\ 0 & 0 & 0 \\ 0 & 0 & 0 \\ 0 & 0 & 0 \end{bmatrix} \tag{A–159}$$

$$\boldsymbol{f^{(1)}} = \begin{Bmatrix} 0 \\ 0 \\ 0 \\ M_0^{(1)} \\ N_0^{(1)} \\ 0 \\ 0 \\ 0 \end{Bmatrix} + \begin{Bmatrix} -\frac{1}{2}\frac{pa^{(1)3}}{D^{*(1)}k^{*(1)2}} \\ 0 \\ \frac{1}{4}\frac{pa^{(1)4}}{D^{*(1)}k^{*(1)2}} \\ -\frac{1}{2}\left(D_{11}^{(1)} + D_{12}^{(1)}\right)\frac{pa^{(1)2}}{D^{*(1)}k^{*(1)2}} \\ -\frac{1}{2}\left(B_{11}^{(1)} + B_{12}^{(1)}\right)\frac{pa^{(1)2}}{D^{*(1)}k^{*(1)2}} \\ 0 \\ 0 \\ 0 \end{Bmatrix} + \begin{Bmatrix} 0 \\ 0 \\ 0 \\ -M_p^{(1)} \\ -N_p^{(1)} \\ 0 \\ 0 \\ 0 \end{Bmatrix} \tag{A–160}$$

A.7.1.6 Outer region: tension ($x^{(2)} > 0$)

$$\boldsymbol{C^{(2)}} = \begin{bmatrix} I_1\left(k^{*(2)}\alpha\right) & K_1\left(k^{*(2)}\alpha\right) & 0 & 0 & 0 \\ -\frac{B_{11}^{(2)}}{A_{11}^{(2)}} I_1\left(k^{*(2)}\alpha\right) & -\frac{B_{11}^{(2)}}{A_{11}^{(2)}} K_1\left(k^{*(2)}\alpha\right) & a^{(1)} & 1/a^{(1)} & 0 \\ -\frac{a^{(2)}}{k^{*(2)}} I_0\left(k^{*(2)}\alpha\right) & \frac{a^{(2)}}{k^{*(2)}} K_0\left(k^{*(2)}\alpha\right) & 0 & 0 & 1 \\ \frac{D^{*(2)}k^{*(2)}}{a^{(2)}} I_0\left(k^{*(2)}\alpha\right) & -\frac{D^{*(2)}k^{*(2)}}{a^{(2)}} K_0\left(k^{*(2)}\alpha\right) & & & \\ -\left(D^{*(2)} - D_{12}^{*(2)}\right) I_1\left(k^{*(2)}\alpha\right) \frac{1}{a^{(1)}} & -\left(D^{*(2)} - D_{12}^{*(2)}\right) K_1\left(k^{*(2)}\alpha\right) \frac{1}{a^{(1)}} & B_{11}^{(2)} + B_{12}^{(2)} & -\left(B_{11}^{(2)} - B_{12}^{(2)}\right) \frac{1}{a^{(1)2}} & 0 \\ -B_{12}^{*(2)} I_1\left(k^{*(2)}\alpha\right) \frac{1}{a^{(1)}} & -B_{12}^{*(2)} K_1\left(k^{*(2)}\alpha\right) \frac{1}{a^{(1)}} & A_{11}^{(2)} + A_{12}^{(2)} & -\left(A_{11}^{(2)} - A_{12}^{(2)}\right) \frac{1}{a^{(1)2}} & 0 \\ \left[\begin{array}{l} D^{*(2)}k^{*(2)} I_0\left(k^{*(2)}\right) \\ -\left(D^{*(2)} - D_{12}^{*(2)} - k_\phi a^{(2)}\right) I_1\left(k^{*(2)}\right) \end{array}\right] \frac{1}{a^{(2)}} & -\left[\begin{array}{l} D^{*(2)}k^{*(2)} K_0\left(k^{*(2)}\right) \\ +\left(D^{*(2)} - D_{12}^{*(2)} - k_\phi a^{(2)}\right) K_1\left(k^{*(2)}\right) \end{array}\right] \frac{1}{a^{(2)}} & B_{11}^{(2)} + B_{12}^{(2)} & -\left(B_{11}^{(2)} - B_{12}^{(2)}\right) \frac{1}{a^{(2)2}} & 0 \\ -\frac{B_{11}^{(2)}}{A_{11}^{(2)}} I_1\left(k^{*(2)}\right) & -\frac{B_{11}^{(2)}}{A_{11}^{(2)}} K_1\left(k^{*(2)}\right) & a^{(2)} & 1/a^{(2)} & 0 \\ -\frac{a^{(2)}}{k^{*(2)}} I_0\left(k^{*(2)}\right) & \frac{a^{(2)}}{k^{*(2)}} K_0\left(k^{*(2)}\right) & 0 & 0 & 1 \end{bmatrix} \tag{A–161}$$

$$\boldsymbol{f^{(2)}} = \begin{Bmatrix} 0 \\ 0 \\ 0 \\ M_0^{(2)} \\ N_0^{(2)} \\ M_0^{(2)} \\ 0 \\ 0 \end{Bmatrix} + \begin{Bmatrix} \frac{1}{2}\frac{pa^{(2)2}a^{(1)}}{D^{*(2)}k^{*(2)2}} \\ 0 \\ -\frac{1}{4}\frac{pa^{(2)2}a^{(1)2}}{D^{*(2)}k^{*(2)2}} \\ \frac{1}{2}\left(D_{11}^{(2)} + D_{12}^{(2)}\right)\frac{pa^{(2)2}}{D^{*(2)}k^{*(2)2}} \\ \frac{1}{2}\left(B_{11}^{(2)} + B_{12}^{(2)}\right)\frac{pa^{(2)2}}{D^{*(2)}k^{*(2)2}} \\ \left(D_{11}^{(2)} + D_{12}^{(2)} + k_\phi a^{(2)}\right)\frac{1}{2}\frac{pa^{(2)2}}{D^{*(2)}k^{*(2)2}} \\ 0 \\ -\frac{1}{4}\frac{pa^{(2)4}}{D^{*(2)}k^{*(2)2}} \end{Bmatrix} + \begin{Bmatrix} 0 \\ 0 \\ 0 \\ -M_p^{(2)} \\ -N_p^{(2)} \\ -M_p^{(2)} \\ 0 \\ 0 \end{Bmatrix} \tag{A–162}$$

A.7.1.7 Outer region: $x^{(2)} = 0$

$$\boldsymbol{C^{(2)}} = \begin{bmatrix} a^{(1)} & 1/a^{(1)} & 0 & 0 & 0 \\ 0 & 0 & a^{(1)} & 1/a^{(1)} & 0 \\ -\frac{1}{2}a^{(1)2} & -\ln\left(a^{(1)}\right) & 0 & 0 & 1 \\ D_{11}^{(2)} + D_{12}^{(2)} & -\left(D_{11}^{(2)} - D_{12}^{(2)}\right)\frac{1}{a^{(1)2}} & B_{11}^{(2)} + B_{12}^{(2)} & -\left(B_{11}^{(2)} - B_{12}^{(2)}\right)\frac{1}{a^{(1)2}} & 0 \\ B_{11}^{(2)} + B_{12}^{(2)} & -\left(B_{11}^{(2)} - B_{12}^{(2)}\right)\frac{1}{a^{(1)2}} & A_{11}^{(2)} + A_{12}^{(2)} & -\left(A_{11}^{(2)} - A_{12}^{(2)}\right)\frac{1}{a^{(1)2}} & 0 \\ D_{11}^{(2)} + D_{12}^{(2)} + a^{(2)}k_\phi & -\left(D_{11}^{(2)} - D_{12}^{(2)} - a^{(2)}k_\phi\right)\frac{1}{a^{(2)2}} & B_{11}^{(2)} + B_{12}^{(2)} & -\left(B_{11}^{(2)} - B_{12}^{(2)}\right)\frac{1}{a^{(2)2}} & 0 \\ 0 & 0 & a^{(2)} & 1/a^{(2)} & 0 \\ -\frac{1}{2}a^{(2)2} & -\ln\left(a^{(2)}\right) & 0 & 0 & 1 \end{bmatrix} \tag{A–163}$$

$$\boldsymbol{f^{(2)}} = \begin{Bmatrix} 0 \\ 0 \\ 0 \\ M_0^{(2)} \\ N_0^{(2)} \\ M_0^{(2)} \\ 0 \\ 0 \end{Bmatrix} + \begin{Bmatrix} -\frac{1}{16}\frac{pa^{(1)3}}{D^{*(2)}} \\ \frac{1}{16}\frac{B_{11}^{(2)}}{A_{11}^{(2)}}\frac{pa^{(1)3}}{D^{*(2)}} \\ \frac{1}{64}\frac{pa^{(1)4}}{D^{*(2)}} \\ -\left(3D^{*(2)} + D_{12}^{*(2)}\right)\frac{1}{16}\frac{pa^{(1)2}}{D^{*(2)}} \\ -B_{12}^{*(2)}\frac{1}{16}\frac{pa^{(1)2}}{D^{*(2)}} \\ -\left(3D^{*(2)} + D_{12}^{*(2)} + k_\phi a^{(2)}\right)\frac{1}{16}\frac{pa^{(2)2}}{D^{*(2)}} \\ \frac{1}{16}\frac{B_{11}^{(2)}}{A_{11}^{(2)}}\frac{pa^{(2)3}}{D^{*(2)}} \\ \frac{1}{32}\frac{a^{(2)3}}{D^{*(2)}}\frac{1}{2}pa^{(2)} \end{Bmatrix} + \begin{Bmatrix} 0 \\ 0 \\ 0 \\ -M_p^{(2)} \\ -N_p^{(2)} \\ -M_p^{(2)} \\ 0 \\ 0 \end{Bmatrix} \tag{A–164}$$

A.7.1.8 Outer region: compression ($x^{(2)} = 0$)

$$\boldsymbol{C^{(2)}} = \begin{bmatrix} J_1\left(k^{*(2)}\alpha\right) & Y_1\left(k^{*(2)}\alpha\right) & 0 & 0 & 0 \\ -\frac{B_{11}^{(2)}}{A_{11}^{(2)}} J_1\left(k^{*(2)}\alpha\right) & -\frac{B_{11}^{(2)}}{A_{11}^{(2)}} Y_1\left(k^{*(2)}\alpha\right) & a^{(1)} & 1/a^{(1)} & 0 \\ \frac{a^{(2)}}{k^{*(2)}} J_0\left(k^{*(2)}\alpha\right) & \frac{a^{(2)}}{k^{*(2)}} Y_0\left(k^{*(2)}\alpha\right) & 0 & 0 & 1 \\ \frac{D^{*(2)}k^{*(2)}}{a^{(2)}} J_0\left(k^{*(2)}\alpha\right) & \frac{D^{*(2)}k^{*(2)}}{a^{(2)}} Y_0\left(k^{*(2)}\alpha\right) & & & \\ -\left(D^{*(2)} - D_{12}^{*(2)}\right) J_1\left(k^{*(2)}\alpha\right) \frac{1}{a^{(1)}} & -\left(D^{*(2)} - D_{12}^{*(2)}\right) Y_1\left(k^{*(2)}\alpha\right) \frac{1}{a^{(1)}} & B_{11}^{(2)} + B_{12}^{(2)} & -\left(B_{11}^{(2)} - B_{12}^{(2)}\right) \frac{1}{a^{(1)2}} & 0 \\ B_{12}^{*(2)} J_1\left(k^{*(2)}\alpha\right) \frac{1}{a^{(1)}} & B_{12}^{*(2)} Y_1\left(k^{*(2)}\alpha\right) \frac{1}{a^{(1)}} & A_{11}^{(2)} + A_{12}^{(2)} & -\left(A_{11}^{(2)} - A_{12}^{(2)}\right) \frac{1}{a^{(1)2}} & 0 \\ \left[\begin{array}{l} D^{*(2)}k^{*(2)} J_0\left(k^{*(2)}\right) \\ -\left(D^{*(2)} - D_{12}^{*(2)} - k_\phi a^{(2)}\right) J_1\left(k^{*(2)}\right) \end{array}\right] \frac{1}{a^{(2)}} & \left[\begin{array}{l} D^{*(2)}k^{*(2)} Y_0\left(k^{*(2)}\right) \\ -\left(D^{*(2)} - D_{12}^{*(2)} - k_\phi a^{(2)}\right) Y_1\left(k^{*(2)}\right) \end{array}\right] \frac{1}{a^{(2)}} & B_{11}^{(2)} + B_{12}^{(2)} & -\left(B_{11}^{(2)} - B_{12}^{(2)}\right) \frac{1}{a^{(2)2}} & 0 \\ -\frac{B_{11}^{(2)}}{A_{11}^{(2)}} J_1\left(k^{*(2)}\right) & -\frac{B_{11}^{(2)}}{A_{11}^{(2)}} Y_1\left(k^{*(2)}\right) & a^{(2)} & 1/a^{(2)} & 0 \\ \frac{a^{(2)}}{k^{*(2)}} J_0\left(k^{*(2)}\right) & \frac{a^{(2)}}{k^{*(2)}} Y_0\left(k^{*(2)}\right) & 0 & 0 & 1 \end{bmatrix} \tag{A–165}$$

$$\boldsymbol{f^{(2)}} = \begin{Bmatrix} 0 \\ 0 \\ 0 \\ M_0^{(2)} \\ N_0^{(2)} \\ M_0^{(2)} \\ 0 \\ 0 \end{Bmatrix} + \begin{Bmatrix} -\frac{1}{2}\frac{pa^{(2)2}a^{(1)}}{D^{*(2)}k^{*(2)2}} \\ 0 \\ \frac{1}{4}\frac{pa^{(2)2}a^{(1)2}}{D^{*(2)}k^{*(2)2}} \\ -\frac{1}{2}\left(D_{11}^{(2)} + D_{12}^{(2)}\right)\frac{pa^{(2)2}}{D^{*(2)}k^{*(2)2}} \\ -\frac{1}{2}\left(B_{11}^{(2)} + B_{12}^{(2)}\right)\frac{pa^{(2)2}}{D^{*(2)}k^{*(2)2}} \\ -\left(D_{11}^{(2)} + D_{12}^{(2)} + k_\phi a^{(2)}\right)\frac{1}{2}\frac{pa^{(2)2}}{D^{*(2)}k^{*(2)2}} \\ 0 \\ \frac{1}{4}\frac{pa^{(2)4}}{D^{*(2)}k^{*(2)2}} \end{Bmatrix} + \begin{Bmatrix} 0 \\ 0 \\ 0 \\ -M_p^{(2)} \\ -N_p^{(2)} \\ -M_p^{(2)} \\ 0 \\ 0 \end{Bmatrix} \tag{A–166}$$

A.7.2 Nonlinear

In this section, the solution methodology for the nonlinear displacement-based governing equations is addressed. The approach is to manipulate the governing equations into a form that is easily solved using existing boundary value problem solvers, for example `bvp4c` or `bvp5c` in MATLAB [138]. A prospective solver must be capable of simultaneously handling the classes of singular boundary value problems (due to the $1/r$ terms that appears in the governing equations) and multipoint boundary value problems (due to boundary conditions applied at the interface between the inner and outer regions). Both `bvp4c` and `bvp5c` meet this criteria. They specifically solve systems of first-order ODEs of the form [138]

$$\mathbf{y}' = \frac{1}{r}\mathbf{S}\mathbf{y} + \mathbf{f}\left(r, \mathbf{y}\right), \tag{A–167}$$

subject to the condition that

$$\mathbf{S}\mathbf{y}\left(\mathbf{0}\right) = \mathbf{0}, \tag{A–168}$$

where $\mathbf{S}$ is a matrix of constants. The goal of this section, then, is to manipulate the nonlinear governing equations into such a form.

First, the $1/r^2$ singularity is removed via changing the independent variables in Equations A–125 and A–129 from ϕ and u to ϕ/r and u/r, respectively. Performing the manipulation,

$$\frac{d^2}{dr^2}\left(\frac{\phi}{r}\right) + \frac{3}{r}\frac{d}{dr}\left(\frac{\phi}{r}\right) - \left(x\frac{k^{*2}}{a^2}\right)\frac{\phi}{r} = -\frac{p}{2D_{11}^*} + \frac{\tilde{N}_r}{D_{11}^*}\frac{\phi}{r} + \frac{B_{12}^*}{2D_{11}^*}\left(\frac{\phi}{r}\right)^2 \tag{A–169}$$

and

$$\begin{aligned}\frac{d^2}{dr^2}\left(\frac{u}{r}\right) + \frac{3}{r}\frac{d}{dr}\left(\frac{u}{r}\right) = -\frac{B_{11}}{A_{11}}\left[\left(x\frac{k^{*2}}{a^2} + \frac{\tilde{N}_r}{D_{11}^*}\right)\frac{\phi}{r} - \frac{p}{2D_{11}^*} + \frac{B_{12}^*}{2D_{11}^*}\left(\frac{\phi}{r}\right)^2\right] \\ - \left(1 - \frac{A_{12}}{A_{11}}\right)\frac{1}{2}\left(\frac{\phi}{r}\right)^2 - \left[r\frac{d}{dr}\left(\frac{\phi}{r}\right) + \frac{\phi}{r}\right]\frac{\phi}{r}.\end{aligned} \tag{A–170}$$

The governing equations are thus to be solved directly for ϕ/r and u/r, which are easily post-processed back to ϕ and u.

Next, Equations A–169 to A–170 are rewritten as a series of first-order ODEs via the following definitions:

$$y_1 = \frac{\phi}{r}, \tag{A–171}$$

$$y_3 = \frac{u}{r}, \tag{A–172}$$

and

$$y_5 = w. \tag{A–173}$$

The system of first-order ODEs is then

$$y_1' = y_2 = \frac{d}{dr}\left(\frac{\phi}{r}\right) \tag{A–174}$$

$$y_2{}' = -\frac{3}{r}y_2 + \left(x\frac{k^{*2}}{a^2} + \frac{\tilde{N}_r}{D_{11}^*}\right)y_1 - \frac{p}{2D_{11}^*} + \frac{B_{12}^*}{2D_{11}^*}{y_1}^2 \tag{A–175}$$

$$y_3{}' = y_4 = \frac{d}{dr}\left(\frac{u}{r}\right) \tag{A–176}$$

$$y_4{}' = -\frac{3}{r}y_4 - \frac{B_{11}}{A_{11}}\left[\left(x\frac{k^{*2}}{a^2} + \frac{\tilde{N}_r}{D_{11}^*}\right)y_1 - \frac{p}{2D_{11}^*} + \frac{B_{12}^*}{2D_{11}^*}{y_1}^2\right] - \left(1 - \frac{A_{12}}{A_{11}}\right)\frac{1}{2}{y_1}^2 - \left(ry_2 + y_1\right)y_1 \tag{A–177}$$

$$y_5' = \frac{dw}{dr} = -\phi = -ry_1 \tag{A–178}$$

Writing these equations explicitly in the form of Equation A–167 gives

$$\begin{Bmatrix} y_1' \\ y_2' \\ y_3' \\ y_4' \\ y_5' \end{Bmatrix} = \frac{1}{r}\begin{bmatrix} 0 & 0 & 0 & 0 & 0 \\ 0 & -3 & 0 & 0 & 0 \\ 0 & 0 & 0 & 0 & 0 \\ 0 & 0 & 0 & -3 & 0 \\ 0 & 0 & 0 & 0 & 0 \end{bmatrix}\begin{Bmatrix} y_1 \\ y_2 \\ y_3 \\ y_4 \\ y_5 \end{Bmatrix} + \begin{Bmatrix} y_2 \\ \left(x\frac{k^{*2}}{a^2} + \frac{\tilde{N}_r}{D_{11}^*}\right)y_1 - \frac{p}{2D_{11}^*} + \frac{B_{12}^*}{2D_{11}^*}{y_1}^2 \\ y_4 \\ -\frac{B_{11}}{A_{11}}\left[\left(x\frac{k^{*2}}{a^2} + \frac{\tilde{N}_r}{D_{11}^*}\right)y_1 - \frac{p}{2D_{11}^*} + \frac{B_{12}^*}{2D_{11}^*}{y_1}^2\right] - \left(1 - \frac{A_{12}}{A_{11}}\right)\frac{1}{2}{y_1}^2 - \left(ry_2 + y_1\right)y_1 \\ -ry_1 \end{Bmatrix}. \tag{A–179}$$

To satisfy Equation A–168, it must be true that

$$y_2\left(0\right) = \left.\frac{d}{dr}\left(\frac{\phi}{r}\right)\right|_0 = 0 \tag{A–180}$$

and

$$y_4\left(0\right) = \left.\frac{d}{dr}\left(\frac{u}{r}\right)\right|_0 = 0. \tag{A–181}$$

For proof, start by expanding y_2,

$$y_2 = \frac{1}{r}\frac{d\phi}{dr} - \frac{1}{r^2}\phi. \tag{A–182}$$

The second term is indeterminate at $r = 0$ by boundary condition A–137. Applying L'Hospital's rule to this term and combining the result with the first term gives

$$y_2(0) = \left[\frac{1}{2r}\frac{d\phi}{dr}\right]_{r=0} \tag{A–183}$$

Proof that Equation A–183 is true is found via application of L'Hospital's rule to Equation A–129, which yields Equation A–183 exactly. The same analysis holds for y_4 (using Equation A–125 for the final step), proving that condition A–168 is satisfied.

To complete the nonlinear solution strategy, the boundary conditions must also be considered. It is therefore first convenient to reformulate equations for N_r and M_r in terms of the new independent variables. First, they become

$$N_r = xk^{*2}\frac{D_{11}^*}{a^2} + A_{11}\left\{\left[r\frac{d}{dr}\left(\frac{u}{r}\right) + \frac{u}{r}\right] + \frac{1}{2}r^2\left(\frac{\phi}{r}\right)^2\right\} + A_{12}\frac{u}{r} + B_{11}\left[r\frac{d}{dr}\left(\frac{\phi}{r}\right) + \frac{\phi}{r}\right] + B_{12}\frac{\phi}{r} \tag{A–184}$$

and

$$M_r = M_0 - M_p + B_{11}\left\{\left[r\frac{d}{dr}\left(\frac{u}{r}\right) + \frac{u}{r}\right] + \frac{1}{2}r^2\left(\frac{\phi}{r}\right)^2\right\} + B_{12}\frac{u}{r} + D_{11}\left[r\frac{d}{dr}\left(\frac{\phi}{r}\right) + \frac{\phi}{r}\right] + D_{12}\frac{\phi}{r}, \tag{A–185}$$

which are equivalent to the solver-friendly forms

$$N_r = xk^{*2}\frac{D_{11}^*}{a^2} + A_{11}\left(ry_4 + y_3 + \frac{1}{2}(ry_1)^2\right) + A_{12}y_3 + B_{11}(ry_2 + y_1) + B_{12}y_1 \tag{A–186}$$

and

$$M_r = M_0 - M_r^P + B_{11}\left(ry_4 + y_3 + \frac{1}{2}(ry_1)^2\right) + B_{12}y_3 + D_{11}(ry_2 + y_1) + D_{12}y_1. \tag{A–187}$$

The boundary conditions, transformed from Equations A–137 to A–146 are then

$$y_2^{(1)}(0) = 0, \tag{A–188}$$
$$y_4^{(1)}(0) = 0, \tag{A–189}$$
$$y_1^{(1)}\left(a^{(1)}\right) = y_1^{(2)}\left(a^{(1)}\right), \tag{A–190}$$
$$y_3^{(1)}\left(a^{(1)}\right) = y_3^{(2)}\left(a^{(1)}\right), \tag{A–191}$$
$$y_5^{(1)}\left(a^{(1)}\right) = y_5^{(2)}\left(a^{(1)}\right), \tag{A–192}$$
$$M_r^{(1)}\left(a^{(1)}\right) = M_r^{(2)}\left(a^{(1)}\right), \tag{A–193}$$
$$N_r^{(1)}\left(a^{(1)}\right) = M_r^{(2)}\left(a^{(1)}\right), \tag{A–194}$$
$$M_r^{(2)}\left(a^{(2)}\right) = -k_\phi r y_1^{(2)}\left(a^{(2)}\right), \tag{A–195}$$
$$y_3^{(2)}\left(a^{(2)}\right) = 0, \text{ and} \tag{A–196}$$
$$y_5^{(2)}\left(a^{(2)}\right) = 0. \tag{A–197}$$

This completes the solution strategy for the nonlinear governing differential equations. Note that boundary value problem solvers are of course also capable of solving linear differential equations, and in fact a straightforward way of solving the linear problem is to program a variant of the solution presented in this section with nonlinear terms removed.

A.8 Closing

In this appendix, solution procedures for both the linear and nonlinear problem of a an axisymmetric, laminated, pre-stressed, and radially-discontinuous circular piezoelectric plate exposed to pressure and/or voltage loading were presented. These linear solution is utilized to provide inputs to the lumped element model in Chapter 5, while the nonlinear solution is used to form a constraint in the optimization of Chapter 6. The models are validated against finite element analysis in Section 5.2.5.

APPENDIX B
BOUNDARY CONDITION INVESTIGATION

This appendix briefly describes an investigation of the outer boundary condition (at $r = a_2$) used in the diaphragm model. The clamped boundary condition utilized in the model development of Appendix A and also in the validation exercise of Section 5.2.5.1 is an idealization that does not take into account the compliance of the substrate. A finite element model that includes the substrate is developed here to compare to the finite element simulation completed in Section 5.2.5.1, which utilized a clamped boundary condition.

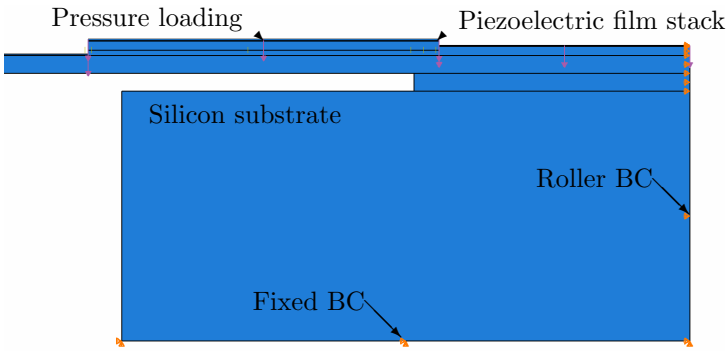

A

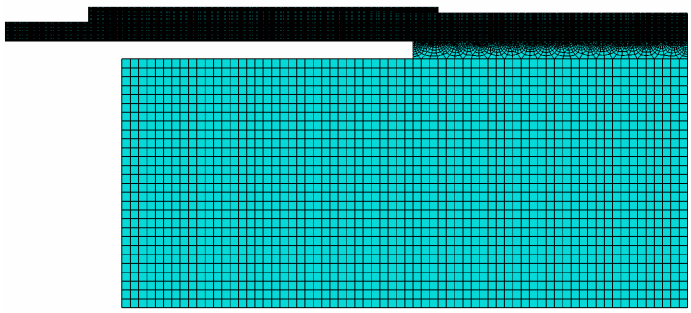

B

Figure B-1. Finite element model for investigation of boundary compliancy. A) Boundary geometry with boundary conditions. B) Mesh.

A finite element model that includes a section of the silicon substrate — with the substrate reduced here to 60 μm × 30 μm because stress is concentrated in the surface region — is pictured in Figure B-1. Boundary conditions, which include a fixed boundary condition on the bottom of the substrate and a roller boundary condition on the far right side, are shown in Figure B-1A. The displacement profiles were found for a pressure loading along the entire top surface of the model. All other conditions, including those involving the piezoelectric film stack and stress, are retained from Section 5.2.5.1.

The linear mode shapes predicted from the finite element models with both clamped and compliant boundaries are found in Figure B-2 for an applied pressure of 111 dB.

Agreement is very good; when integrated, the total difference in volume displacement $\Delta\forall$ is less than 1%. This indicates that at least for the geometry used in this model (design D), compliant boundary conditions aren't likely to be a large contributor to error in linear model predictions.

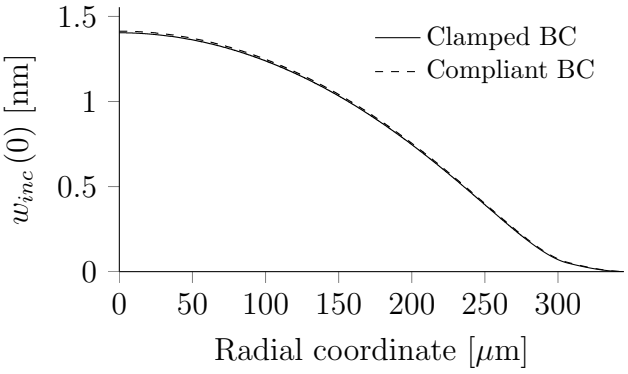

Figure B-2. Deflection profiles from FEA with clamped and compliant boundary conditions (P=111 dB).

Figure B-3A shows a comparison between the incremental deflection at $r = 0$ found from the finite element model with a clamped outer boundary condition (Section 5.2.5.1) and that found from the finite element model with substrate. The two agree extremely closely over much of the interval. A plot of the relative error between the two sets of simulation results is found in Figure B-3B, which shows that the compliance in the boundary conditions becomes more important at high pressure levels. The relative error is below 5.5% up to 172 dB, with a maximum of 11.4% at 190 dB.

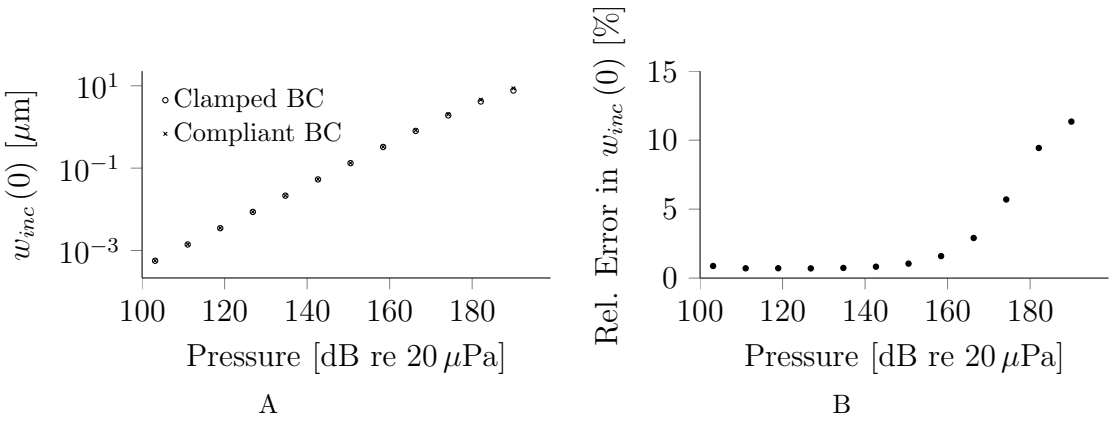

Figure B-3. FEA results for models with clamped and compliant boundary conditions (versus pressure). A) Incremental center deflection. B) Relative error.

APPENDIX C
UNCERTAINTY ANALYSIS

This appendix addresses the calculation of uncertainty estimates for measured quantities in Chapter 8.

C.1 Approach

The general approach to uncertainty estimation to be used here is consistent with the methodology presented in Coleman & Steele [201], which is drawn from the ISO standard [202]. In each case, the combined standard uncertainty for a random variable is first found via the root sum square method

$$u = \sqrt{s^2 + \sum_{k=1}^{M} b_k^2}, \tag{C–1}$$

where s is the standard deviation estimate for the random uncertainty and b_k is the standard deviation estimate for the kth systematic uncertainty (bias). Note that the use of Equation C–1 requires that error sources are uncorrelated. The confidence bounds are then determined using a coverage factor via

$$U_{\%} = t_{\%} u, \tag{C–2}$$

where $t_{\%}$ is the t-statistic with ν degrees of freedom associated with a selected confidence level in percent. The t-statistic may be drawn from standard tables [34, 163, 201] or from MATLAB as tinv(1-α/2,ν) for the $(1-\alpha) \times 100\%$ confidence bound. The degrees of freedom ν in the presence of bias errors can be estimated from the Welch-Satterthwaite formula [201]. The statistic $t_{95\%}$ is typically taken as 2 for $\nu > 30$, which is often the case when bias errors are well-defined and a large number of measurements ($N = \nu + 1 > 31$) were taken. This assumption will be made throughout the uncertainty analysis presented in the following sections. In the case of uncertainty in a result calculated from several variables, the Taylor Series Method (TSM) is employed [201]. The combined standard uncertainty for a function $r = r(x_1, x_2, \ldots, x_n)$ is given as [201]

$${u_r}^2 = \sum_{i=1}^{J} \left(\frac{\partial r}{\partial x_i} \right)^2 b_{x_i}^2 + \sum_{i=1}^{J} \left(\frac{\partial r}{\partial x_i} \right)^2 s_{x_i}^2, \tag{C–3}$$

where b_{x_i} and s_{x_i} are associated with the ith variable.

The uncertainty estimation approach discussed here requires some knowledge of the statistical properties of bias errors. In the absence of data, a distribution must be assumed. In the sections to follow, a bias error of $\pm a$ is typically drawn from a uniform distribution, yielding a standard deviation estimate of $a/\sqrt{3}$.

Error estimates for spectral quantities [34] used repeatedly include the normalized standard errors of autospectral density,

$$\frac{s_{G_{xx}}}{G_{xx}} = \frac{1}{\sqrt{n_{d_{eff}}}}, \tag{C–4}$$

frequency response function magnitude,

$$\frac{s_{|H_{xy}|}}{|H_{xy}(f)|} = \frac{\sqrt{1-\gamma_{xy}^2(f)}}{|\gamma_{xy}(f)|\sqrt{2n_{d_{eff}}}}, \tag{C–5}$$

and phase (in radians),

$$s_{\phi_{xy}} = \frac{\sqrt{1-\gamma_{xy}^2(f)}}{|\gamma_{xy}(f)|\sqrt{2n_{d_{eff}}}}, \tag{C–6}$$

where $n_{d_{eff}}$ is the effective number of averages and γ_{xy}^2 is the ordinary coherence function. For a rectangular window with 0 % overlap, $n_{d_{eff}} = n_d$, the actual number of averages. For an arbitrarily windowed measurement with overlap,

$$n_d = \lfloor 1 + (b_{\text{blocks}} - 1)/(1-r) \rfloor, \tag{C–7}$$

where b_{blocks} is the number of blocks and r is the fraction of overlap. The effective number of averages depends on both the window and the overlap as [203]

$$n_{d_{eff}} = \lambda n_d, \tag{C–8}$$

where for the Hanning window with 75 % overlap ($r = 0.75$), $\lambda = 0.52$. The concept of the effective number of averages — with different nomenclature — was addressed by Welch [204].

C.2 Frequency Response Function

This section addresses the uncertainty estimates for frequency response functions of the developed microphones, for instance as presented in Section 8.2.3.1.

The PULSE software only enables specification of the pistonphone pressure level (which is corrected for atmospheric pressure) up to the nearest 0.1 dB SPL; this implies a bias error of up to ±0.05 dB propagates into the DUT frequency response function. Drawing the bias error from a uniform distribution over ±0.05 dB, the standard bias error estimate is

$$\begin{aligned} b_{|H_{xy}|} &= \frac{10^{0.05/20} - 1}{\sqrt{3}} |H_{xy}(f)| \\ &\approx 0.0033 \, |H_{xy}(f)| \, . \end{aligned} \tag{C–9}$$

The standard deviation estimate for the random uncertainty is found from Equation C–5 and $U_{95\%}$ is calculated from Equations C–1 to C–2 with $t_{95\%} = 2$ since 100 averages were taken in all frequency microphone frequency response measurements.

C.3 Noise Floor

This section addresses uncertainty for noise floor measurements presented in Section 8.2.4.1. Uncertainty for minimum detectable pressure metrics calculated from noise floor measurements are also given.

C.3.1 Spectra

The random uncertainty of the noise floor measurement was estimated using Equation C–4 for power spectral density, taking into account the different numbers of blocks collected over each frequency span, the 75 % overlap, and Hanning window via the procedure addressed in the opening. The 95 % confidence interval is then

$$U_{95\%} = 2s_{S_o^v} \tag{C–10}$$

$$= 2\frac{S_o^v}{\sqrt{n_{d_{eff}}}}. \tag{C–11}$$

Letting $\tilde{U}_{95\%} = U_{95\%}/S_o^v$, the generally unsymmetric ± error bounds in dB can be determined as $10\log_{10}\left(1+\tilde{U}_{95\%}\right)$ and $-10\log_{10}\left(1-\tilde{U}_{95\%}\right)$, respectively. Subtracting the two bounds gives $10\log_{10}\left(1-\tilde{U}_{95\%}\right)$ and one sees that the asymmetry is not important when $\tilde{U}_{95\%}^2 \ll 1$. The uncertainty for each span is shown graphically in Figure C-1.

f [kHz]	0	6.4	12.8	25.6	38.4	51.2	76.8	102.4
$\pm U_{95\%}$ [dB]	0.19	0.19	0.08	0.08	0.06	0.06	0.06	

Figure C-1. Noise spectra 95% confidence intervals.

The standard combined uncertainty of the minimum detectable pressure spectra accounting for the uncertainty in both the noise floor and microphone sensitivities was estimated using the TSM as

$$u_{\text{MDP}}^2 = \left(\frac{\partial MDP}{\partial S_o^v}\right)^2 s_{S_o^v} + \left(\frac{\partial MDP}{\partial |S|}\right)^2 u_{|S|}^2, \tag{C–12}$$

which after performing the partial differentiations and normalizing gives

$$\frac{u_{\text{MDP}}^2}{\text{MDP}^2} = \left(\frac{1}{2}\frac{s_{S_o^v}}{S_o^v}\right)^2 + \left(\frac{u_{|S|}}{|S|}\right)^2. \tag{C–13}$$

Note the use of the combined standard error for $|S|$, which accounts for both random and bias error in the individual microphone sensitivities. The uncertainties are the same for all microphones and are shown for each frequency span in Figure C-2.

f [kHz]	0	6.4	12.8	25.6	38.4	51.2	76.8	102.4
$\pm U_{95\%}$ [dB]	0.10	0.10	0.05	0.05	0.04	0.04	0.04	

Figure C-2. MDP spectra 95% confidence intervals.

C.3.2 Narrow Band

The expression of the 95% confidence interval of the narrow band MDP is unchanged from Equation C–13. It is simply the uncertainty value for the MDP spectrum at 1 kHz, $U_{95\%} = \pm 0.19\,\text{dB}$.

C.3.3 Integrated

Uncertainty of the integrated MDP measures, in OASPL and AOASPL, required complex integration processes and were therefore obtained via Monte Carlo simulations. Random perturbations of the minimum detectable pressure spectra were taken from a normal distribution with a standard deviation equal to the combined standard uncertainty $u_{p_{min}}$ $(= 20\,\mu\text{Pa}10^{\frac{u_{MDP}}{20}})$ defined in Section C.3.1. The two integration processes were performed on 5000 randomly perturbed spectra, which yielded converged statistics. Calculation of $U_{95\%}$ from Monte Carlo results via $t_{95\%}u$ and also from an empirical cumulative distribution function agreed to at least the number of decimal places reported in Table 8-14 for all designs.

C.4 Impedance

Impedance measurement results were given in Section 8.2.4.2. The kth impedance measurement from the HP 4294A impedance analyzer post-processed into admittance form is written as

$$Y_k(f) = G_k(f) + jB_k(f). \tag{C–14}$$

From n total measurements, the mean values $\overline{G}$ and $\overline{B}$ were computed, together with their sample standard deviations, $s_{\overline{G}} = s_G/\sqrt{n}$ and $s_{\overline{B}} = s_B/\sqrt{n}$. Five thousand Monte Carlo simulations were used to fit the data to Equation 8–7, with perturbations to $\overline{G}$ and $\overline{B}$ and a curve fit performed at each iteration. The perturbations representing the random error were drawn from a normal distribution (mean zero and standard deviation $s_{\overline{G}}$ and $s_{\overline{B}}$, respectively), and those representing the bias error were drawn from a uniform distribution with bounds equal to the bias error, calculable from expressions in the equipment manual [175]. The extracted values $C_{ef} + C_{eo}$, R_{ep}, and R_{es} were saved at each iteration together with R-squared values for the goodness of fit to the experimental data, yielding statistical distributions for all of those quantities. From those, the 95% confidence bounds were extracted directly from an experimental cumulative distribution function.

C.5 Parasitic Capacitance Extraction

The TSM was applied to Equation 8–12 to yield the combined standard uncertainty expression,

$$u^2_{C_{ep}+C_{ea}} = (C_{et})^2 \left[\frac{u^2_{S_{ca}} + b^2_{S_{ca}}}{S^2_{ca}} + \frac{u^2_{S_{va}} + b^2_{S_{va}}}{S^2_{va}} + \frac{s^2_{C_{fb}}}{C^2_{fb}} \right] + u^2_{C_{ef}}, \tag{C–15}$$

which because $S_{ca} = S_{ca}(f)$ and $S_{va} = S_{va}(f)$, is evaluated at each frequency. The errors used in Equation C–15 are found in Table C-1. Similarly, the uncertainty in the open circuit sensitivity was estimated from

$$u^2_{S_{oc}} = \left(\frac{C_{et}}{C_{ef}}\right)^2 \left(s^2_{S_{va}} + b^2_{S_{va}}\right) + \left(\frac{C_{ep} + C_{ea}}{C^2_{ef}} S_{va}\right)^2 u^2_{C_{ef}} + \left(\frac{S_{va}}{C_{ef}}\right)^2 u^2_{C_{ep}+C_{ea}}. \tag{C–16}$$

In both cases, $U_{95\%} = 2u$.

Table C-1. Parasitic capacitance extraction uncertainties.

Uncertainty	Value
$s_{S_{ca}}$	Equation C–5
$b_{S_{ca}}$	$0.0033 S_{ca}$ (see Equation C–9)
$s_{S_{va}}$	Equation C–5
$b_{S_{va}}$	$0.0033 S_{va}$ (see Equation C–9)
$s_{C_{fb}}$	± 0.25 pF

C.6 Parameter Extraction

Uncertainty estimates for the primary parameter extraction quantities found in Section 8.2.5, C_{ad}, M_{ad}, and d_a, were obtained via Monte Carlo simulations. The spatial frequency response functions from which they were calculated, $H_{pw}(r, \theta; f)$ and $H_{vw}(r, \theta; f)$ contained random error (defined by Equation C–5) and bias error from the microphone calibration in the case of H_{pw} (defined via the general form of Equation C–9). The bias error associated with the actual laser vibrometer measurement was deemed negligible. The perturbations representing the random error were drawn from a normal distribution, with each individual scan point perturbed individually. Perturbations associated with the bias error were drawn from a uniform distribution and applied uniformly to each scan point. The integration routines associated with the calculation of C_{ad}, M_{ad} and d_a were performed for each perturbation to build statistical distributions and $U_{95\%}$ for each was calculated directly from the experimental cumulative probability distribution function.

Secondary parameters ϕ_a and k were calculated via the below equations using the standard uncertainties derived from the Monte Carlo simulations:

$$\left(\frac{u_{\phi_a}}{\phi_a}\right)^2 = \left(\frac{u_{d_a}}{d_a}\right)^2 + \left(\frac{u_{C_{ad}}}{C_{ad}}\right)^2 \tag{C–17}$$

and

$$\left(\frac{u_{k^2}}{k^2}\right)^2 = \left(2\frac{u_{d_a}}{d_a}\right)^2 + \left(\frac{u_{C_{ef}}}{C_{ef}}\right)^2 + \left(\frac{u_{C_{ad}}}{C_{ad}}\right)^2. \tag{C–18}$$

Uncertainty in C_{ef} in the above equation was drawn from Table 8.2.4.2.

APPENDIX D
MATERIAL PROPERTIES

This appendix collects the material properties used in simulations throughout this study into two tables: one for properties of materials used in the microphone diaphragm and one for properties of gases in which the microphone was tested.

Table D-1. Properties of microphone diaphragm materials.

	Passivation	Molybdenum (Mo)	Aluminum Nitride (AlN) [141]	Structural
E [GPa]	73	329	283	73
ν	0.17	0.31	0.27	0.17
ρ [kg/m^3]	2200	10289	3250	2200
d_{31} [m/V]	-	-	-2.65×10^{-12}	-
ε [F/m]	-	-	9.5×10^{-11}	-
ρ_e [MΩ m]	-	-	22.8	-

Table D-2. Properties of gases.

	Air	Helium
c_0 [m/s]	343	1007
ρ_0 [kg/m^3]	1.21	0.161
μ [m kg/s]	1.81×10^{-5}	1.9×10^{-5}

REFERENCES

[1] B. Burnett, "Ssshh, we're flying a plane around here," *Boeing Frontiers*, vol. 4, no. 8, Jan. 2006.

[2] P. A. Sheikh and C. Uhl, "Airplane noise: A pervasive disturbance in Pennsylvania parks, USA," *Journal of Sound and Vibration*, vol. 274, no. 1-2, pp. 411–420, Jul. 2004. [Online]. Available: http://dx.doi.org/10.1016/j.jsv.2003.09.014

[3] "Aeronautics and space, noise standards: Aircraft type and airworthiness certification," *Title 14 US Code of Federal Regulations, pt. 36*, 2004.

[4] V. G. Mengle, U. Ganz, E. J. Bultemeier, and F. T. Calkins, "Clocking effects of chevrons with azimuthally-varying immersions on shockcell/cabin noise," in *Proceedings of the 29th AIAA Aeroacoustics Conference*, Vancouver, Canada, May 5–7, 2008, AIAA paper 08-3000, pp. 1–14.

[5] *Occupational safety and health protections for cabin crew members*, International Civil Aviation Organization Working Paper, Rev. A36-WP/208, Sep. 2007.

[6] W. H. Herkes, R. F. Olsen, and S. Uellenberg, "The quiet technology demonstrator program : Flight validation of airplane noise-reduction concepts," in *Proceedings of the 12th AIAA/CEAS Aeroacoustics Conference (27th Aeroacoustics Conference)*, Cambridge, MA, May 8–10, 2006, AIAA paper 2006-2720, pp. 1–9.

[7] E. J. Bultemeier, U. Ganz, J. Premo, and E. Nesbitt, "Effect of uniform chevrons on cruise shockcell noise," in *Proceedings of the 12th AIAA/CEAS Aeroacoustics Conference (27th AIAA Aeroacoustics Conference)*, Cambridge, MA, May 8–10, 2006, AIAA paper 2006-2440, pp. 1–15.

[8] D. Reed, S. Uellenberg, and E. Davis, "An in-flight study of cabin buzz-saw noise," *The Journal of the Acoustical Society of America*, vol. 112, no. 5, pp. 2347–2347, 2002. [Online]. Available: http://link.aip.org/link/?JAS/112/2347/2

[9] W. Herkes, E. Nesbitt, B. Callender, B. Janardan, J. Moe, and J. Yu, "The quiet technology demonstrator program : Static test of airplane noise-reduction concepts," in *Proceedings of the 13th AIAA/CEAS Aeroacoustics Conference (28th AIAA Aeroacoustics Conference)*, Rome, Italy, May 21–23, 2007, AIAA paper 2007-3670, pp. 1–11.

[10] S. Bailey, G. Kunkel, M. Hultmark, M. Vallikivi, J. Hill, K. Meyer, C. Tsay, C. Arnold, and A. Smits, "Turbulence measurements using a nanoscale thermal anemometry probe," *Journal of Fluid Mechanics*, vol. 663, pp. 160–179, Nov. 2010. [Online]. Available: http://dx.doi.org/10.1017/S0022112010003447

[11] J. W. Naughton and M. Sheplak, "Modern developments in shear-stress measurement," *Progress in Aerospace Sciences*, vol. 38, no. 6–7, pp. 515–570, Aug.–Oct. 2002. [Online]. Available: http://dx.doi.org/10.1016/S0376-0421(02)00031-3

[12] H. Tennekes and J. Lumley, *A first course in turbulence*. Cambridge, MA: MIT Press, 1972.

[13] L. Löfdahl and M. Gad-el-Hak, "MEMS-based pressure and shear stress sensors for turbulent flows," *Measurement Science and Technology*, vol. 10, no. 8, p. 665, Aug. 1999. [Online]. Available: http://stacks.iop.org/0957-0233/10/i=8/a=302

[14] T. J. Mueller, Ed., *Aeroacoustic Measurements*. Berlin, Germany: Springer-Verlag, 2002, ch. 3, pp. 98–217.

[15] D. P. Arnold, T. Nishida, L. N. Cattafesta, and M. Sheplak, "A directional acoustic array using silicon micromachined piezoresistive microphones," *Journal of the Acoustical Society of America*, vol. 113, no. 1, pp. 289–298, Jan. 2003. [Online]. Available: http://dx.doi.org/10.1121/1.1527960

[16] M. Sheplak, K. S. Breuer, and M. A. Schmidt, "A wafer-bonded, silicon-nitride membrane microphone with dielectrically-isolated single crystal silicon piezoresistors," in *Proceedings of 1998 Solid-State Sensor and Actuator Workshop*, Hilton Head Island, SC, Jun. 8–11, 1998, pp. 23–26.

[17] M. Sheplak, M. Seiner, K. S. Breuer, and M. A. Schmidt, "A MEMS microphone for aeroacoustic measurements," in *Proceedings of 37th AIAA Aerospace Sciences Meeting*, Reno, NV, Jan. 11–14, 1999, AIAA paper 99-0606.

[18] D. P. Arnold, S. Gururaj, S. Bhardwaj, T. Nishida, and M. Sheplak, "A piezoresistive microphone for aeroacoustic measurements," in *Proceedings of ASME IMECE 2001 International Mechanical Engineering Congress and Exposition*, New York, NY, Nov. 11–16, 2001, paper MEMS-23841, pp. 281–288.

[19] P. J. King and J. R. Underbrink, "Characterization of a microelectromechanical systems (MEMS) microphone," in *Proceedings of the 14th AIAA/CEAS Aeroacoustics Conference*, Vancouver, Canada, May 5–7, 2008, AIAA paper 2008-2912.

[20] S. Horowitz, T. Nishida, L. Cattafesta, and M. Sheplak, "Development of a micromachined piezoelectric microphone for aeroacoustics applications," *Journal of the Acoustical Society of America*, vol. 122, no. 6, pp. 3428–3436, Dec. 2007. [Online]. Available: http://dx.doi.org/10.1121/1.2785040

[21] D. Martin, "Design, fabrication, and characterization of a MEMS dual-backplate capacitive microphone," Ph.D. dissertation, University of Florida, Gainesville, FL, Aug. 2007. [Online]. Available: http://purl.fcla.edu/fcla/etd/UFE0017526

[22] V. G. Mengle, U. Ganz, E. Nesbitt, E. J. Bultemeier, and R. Thomas, "Flight test results for uniquely tailored propulsion-airframe aeroacoustic chevrons: Shockcell noise," in *Proceedings of the 27th AIAA Aeroacoustics Conference*, Cambridge, MA, May 5–7, 2008, AIAA paper 08-3000.

[23] P. Sijtsma and R. Stoker, "Determination of absolute contributions of aircraft noise components using fly-over array measurements," in *Proceedings of the 10th AIAA/CEAS Aeroacoustics Conference*, Manchester, Great Britain, May 10–12, 2004, AIAA paper 2004-2958.

[24] H. Siller, M. Drescher, G. Saueressig, and R. Lange, "Fly-over source localisation on a Boeing 747-400," in *Proceedings of the 3rd Berlin Beamforming Conference*, Berlin, Germany, Feb. 24–25, 2010, pp. 1–11.

[25] K. Veggeberg, "High channel-count aircraft noise mapping applications," *Sound and Vibration Magazine*, pp. 14–16, May 2009.

[26] J. Lan, J. Premo, G. Zlavog, C. Breard, B. Callender, and M. Martinez, "Phased array measurements of full-scale engine inlet noise," in *Proceedings of the 13th AIAA/CEAS Aeroacoustics Conference (28th AIAA Aeroacoustics Conference)*, Rome, Italy, May 21–23, 2007, AIAA paper 2007-3434, pp. 1–14.

[27] L. Brusniak, J. R. Underbrink, E. Nesbitt, D. Lynch, and M. Martinez, "Phased array measurements of full-scale engine exhaust noise," in *Proceedings of the 13th AIAA/CEAS Aeroacoustics Conference (28th AIAA Aeroacoustics Conference)*, Rome, Italy, May 21–23, 2007, AIAA paper 2007-3612, pp. 1–18.

[28] D. T. Blackstock, *Fundamentals of Physical Acoustics*. New York, NY: John Wiley & Sons, Inc, 2000, ch. 1,4,14.

[29] J. E. F. Williams, "Hydrodynamic noise," *Annual Review of Fluid Mechanics*, vol. 1, no. 1, pp. 197–222, Jan. 1969. [Online]. Available: http://dx.doi.org/10.1146/annurev.fl.01.010169.001213

[30] M. Lighthill, "Sound generated aerodynamically," *Philosophical Transactions of the Royal Society A: Mathematical, Physical and Engineering Sciences*, vol. 267, no. 1329, pp. 147–182, Jun. 1961. [Online]. Available: http://www.jstor.org/stable/2414246

[31] *Microphone Handbook*, Brüel and Kjær, Nærum, Denmark, Jul. 1996. [Online]. Available: http://www.bksv.com/doc/be1447.pdf

[32] H. H. Hubbard, "Aeroacoustics of flight vehicles: theory and practice," National Aeronautics and Space Administration, Tech. Rep. 90-3052, 1991.

[33] C. M. Harris, *Handbook of Acoustical Measurements and Noise Control*, 3rd ed. Woodbury, NY: Acoustical Society of America, 1998, ch. 1.

[34] J. S. Bendat and A. G. Piersol, *Random Data Analysis and Measurement Procedures*, 3rd ed. New York, NY: John Wiley and Sons, 2000, ch. 2,6,9.

[35] M. Rossi, *Acoustics and Electroacoustics*. Norwood, MA: Artech House, Inc., 1988, ch. 4–6,8.

[36] L. L. Beranek, *Acoustics*. New York, NY: Acoustical Society of America, 1993, ch. 3,5,6.

[37] S. S. Rao, *Vibration of Continuous Systems*. Hoboken, N.J.: Wiley, 2007, ch. 14.

[38] R. Dieme, G. Bosman, M. Sheplak, and T. Nishida, "Source of excess noise in silicon piezoresistive microphones," *Journal of the Acoustical Society of America*, vol. 119, no. 5, pp. 2710–2720, May 2006. [Online]. Available: http://dx.doi.org/10.1121/1.2188367

[39] C. Motchenbacher and J. Connelly, *Low Noise Electronic System Design*. New York, NY: John Wiley & Sons, 1993, ch. 1,2.

[40] T. B. Gabrielson, "Mechanical-thermal noise in micromachined acoustic and vibration sensors," *IEEE Transactions on Electron Devices*, vol. 40, no. 5, pp. 903–909, May 1993. [Online]. Available: http://dx.doi.org/10.1109/16.210197

[41] H. B. Callen and T. A. Welton, "Irreversibility and generalized noise," *Physical Review*, vol. 83, no. 1, pp. 34–40, Jul. 1951. [Online]. Available: http://dx.doi.org/10.1103/PhysRev.83.34

[42] T. B. Gabrielson, "Fundamental noise limits for miniature acoustic and vibration sensors," *Journal of Vibration and Acoustics*, vol. 117, no. 4, pp. 405–410, Oct. 1995. [Online]. Available: http://dx.doi.org/10.1115/1.2874471

[43] S. D. Senturia, *Microsystem Design*. Norwell, MA: Kluwer Academic Publishers, 2001, ch. 1,2,5,13,16.

[44] *LTC6240/LTC6241/LTC6242 Single/Dual/Quad 18 MHz, Low Noise, Rail-to-Rail Output, CMOS Op Amps*, Linear Technology, 2011.

[45] G. Vasilescu, *Electronic Noise and Interfering Signals: Principles and Applications*. Berlin, Germany: Springer, 2005, ch. 1.

[46] P. Horowitz and W. Hill, *The Art of Electronics*, 2nd ed. Cambridge, UK: Cambridge University Press, 1989, ch. 7.

[47] B. Boulet, *Fundamentals of Signals and Systems*. Hingham, MA: Da Vinci Engineering Press, 2006, vol. 1, ch. 4.

[48] *Audio Distortion Measurements*, Brüel and Kjær, Nærum, Denmark, 1992. [Online]. Available: http://www.bksv.com/doc/BO0385.pdf

[49] *Measurement Microphones*, 2nd ed., Brüel and Kjær, Nærum, Denmark, Aug. 1994. [Online]. Available: http://www.bksv.com/doc/br0567.pdf

[50] *1/8 in Pressure-Field Microphone - Type 4138*, Brüel and Kjær, Sep. 2008.

[51] *1/4 in Pressure-Field Microphone - Type 4938*, Brüel and Kjær, May 2008.

[52] *Kulite High Intensity Microphones*, Kulite, Feb. 2011. [Online]. Available: http://www.kulite.com/pdfs/pdf_Data_Sheets/Mic.pdf

[53] P. R. Scheeper, A. G. H. van der Donk, W. Olthuis, and P. Bergveld, "A review of silicon microphones," *Sensors and Actuators A*, vol. 44, no. 1, pp. 1–11, Jul. 1994. [Online]. Available: http://dx.doi.org/10.1016/0924-4247(94)00790-X

[54] B. Homeijer, "Design, fabrication and characterization of a MEMS piezoresistive microphone for use in aeroacoustic measurements," Ph.D. dissertation, University of Florida, Gainesville, FL, Dec. 2008. [Online]. Available: http://purl.fcla.edu/fcla/etd/UFE0022840

[55] M. Royer, J. O. Holmen, M. A. Wurm, O. S. Aadland, and M. Glenn, "ZnO on Si integrated acoustic sensor," *Sensors and Actuators*, vol. 4, no. 3, pp. 357–362, 1983. [Online]. Available: http://dx.doi.org/10.1016/0250-6874(83)85044-6

[56] E. S. Kim and R. S. Muller, "IC-processed piezoelectric microphone," *IEEE Electron Device Letters*, vol. 8, no. 10, pp. 467–468, Oct. 1987. [Online]. Available: http://dx.doi.org/10.1109/EDL.1987.26696

[57] R. S. Muller and E. S. Kim, "IC processed piezoelectric microphone," U.S. Patent 4 783 821, Nov. 8, 1988.

[58] E. S. Kim, R. S. Muller, and P. R. Gray, "Integrated microphone with CMOS circuits on a single chip," in *Proceedings of 1989 International Electron Devices Meeting*, Washington, DC, Dec. 3–6, 1989, pp. 880–883. [Online]. Available: http://dx.doi.org/10.1109/IEDM.1989.74193

[59] E. S. Kim, J. R. Kim, and R. S. Muller, "Improved IC-compatible piezoelectric microphone and CMOS process," in *Proceedings of 1991 International Conference on Solid-State Sensors and Actuators*, San Francisco, CA, Jun. 24–27, 1991, pp. 270–273. [Online]. Available: http://dx.doi.org/10.1109/SENSOR.1991.148858

[60] J. Franz, "Piezoelektrische sensoren auf siliziumbasis für akustische anwendungen," Ph.D. dissertation, Darmstadt University of Technology, Darmstadt, Germany, 1988.

[61] R. Schellin, G. Hess, W. Kuehnel, G. M. Sessler, and E. Fukada, "Silicon subminiature microphones with organic piezoelectric layers: Fabrication and acoustical behaviour," in *Proceedings of 7th International Symposium on Electrets*, Berlin, Germany, Sep. 25–27, 1992, pp. 929–934. [Online]. Available: http://dx.doi.org/10.1109/ISE.1991.167338

[62] R. Schellin, G. Hess, R. Kressmann, and P. Wassmuth, "Micromachined silicon subminiature microphones with piezoelectric P(VDF/TRFE)-layers and silicon-nitride-membranes," in *Proceedings of 8th International Symposium on Electrets*, Paris, France, Sep. 7–9, 1994, pp. 1004–1009. [Online]. Available: http://dx.doi.org/10.1109/ISE.1994.515262

[63] R. P. Ried, E. S. Kim, D. M. Hong, and R. S. Muller, "Piezoelectric microphone with on-chip CMOS circuits," *Journal of Microelectromechanical Systems*, vol. 2, no. 3, pp. 111–120, Sep. 1993. [Online]. Available: http://dx.doi.org/10.1109/84.260255

[64] S. S. Lee, R. P. Reid, and R. M. White, "Piezoelectric cantilever microphone and microspeaker," *Journal of Microelectromechanical Systems*, vol. 5, no. 4, pp. 238–242, Dec. 1996. [Online]. Available: http://dx.doi.org/10.1109/84.546403

[65] S. S. Lee and R. M. White, "Piezoelectric cantilever acoustic transducer," *Journal of Micromechanics and Microengineering*, vol. 8, no. 3, pp. 230–238, 1998. [Online]. Available: http://dx.doi.org/10.1088/0960-1317/8/3/009

[66] A. Naguib, E. Soupos, H. Nagib, C. Huang, and K. Najafi, "Characterization of a MEMS acoustic/pressure sensor," in *Proceedings of 37th AIAA Aerospace Sciences Meeting*, Reno, NV, Jan. 11–14, 1999, AIAA paper 99-0520, pp. 1–7.

[67] ——, "A piezoresistive MEMS sensor for acoustic noise measurements," in *Proceedings of 5th AIAA/CEAS Aeroacoustics Conference & Exhibit*, Bellevue, WA, May 10–12, 1999, AIAA paper 99-1992, pp. 1–8.

[68] C. Huang, A. Naguib, E. Soupos, and K. Najafi, "A silicon micromachined microphone for fluid mechanics research," *Journal of Micromechanics and Microengineering*, vol. 12, no. 6, pp. 767–774, Nov. 2002. [Online]. Available: http://dx.doi.org/10.1088/0960-1317/12/6/307

[69] D. P. Arnold, "A MEMS-based directional acoustic array for aeroacoustic measurements," Master's thesis, University of Florida, Gainesville, FL, Dec. 2001.

[70] K. Kadirvel, R. Taylor, S. Horowitz, M. Sheplak, and T. Nishida, "Design and characterization of MEMS optical microphone for aeroacoustic measurement," in *Proceedings of 42nd Aerospace Sciences Meeting and Exhibit*, Reno, NV, Jan. 5–8, 2004, AIAA paper 2004-1030.

[71] D. T. Martin, L. Jian, K. Kadirvel, R. M. Fox, M. Sheplak, and T. Nishida, "A micromachined dual-backplate capacitive microphone for aeroacoustic measurements," *Journal of Microelectromechanical Systems*, vol. 16, no. 6, pp. 1289–1302, Dec. 2007. [Online]. Available: http://dx.doi.org/10.1109/JMEMS.2007.909234

[72] D. T. Martin, K. Kadirvel, J. Liu, R. M. Fox, M. Sheplak, and T. Nishida, "Surface and bulk micromachined dual back-plate condenser microphone," in *Proceedings of 18th IEEE International Conference on Micro Electro Mechanical Systems (MEMS 2005)*, Miami, FL, Jan. 30–Feb. 3, 2005, pp. 319–322. [Online]. Available: http://dx.doi.org/10.1109/MEMSYS.2005.1453842

[73] D. T. Martin, K. Kadirvel, T. Nishida, and M. Sheplak, "A surface micromachined capacitive microphone for aeroacoustic applications," in *Solid-state sensor, actuator, and microsystems workshop*, Hilton Head, SC, Jun. 1–5, 2008, pp. 1–4.

[74] L.-T. Zhang, T.-L. Ren, J.-S. Liu, L.-T. Liu, and Z.-J. Li, "Fabrication of a cantilever structure for piezoelectric microphone," *Japanese Journal of Applied Physics*, vol. 41, no. 11B, pp. 7158–7159, Nov. 2002. [Online]. Available: http://dx.doi.org/10.1143/JJAP.41.7158

[75] H. J. Zhao, T. L. Ren, J. S. Liu, L. T. Liu, and Z. J. Li, "Fabrication of high-quality PZT-based piezoelectric microphone," in *Proceedings of 12th International Conference on Solid State Sensors, Actuators, and Microsystems*, vol. 1, Boston, MA, Jun. 8-12, 2003, pp. 234–237. [Online]. Available: http://dx.doi.org/10.1109/SENSOR.2003.1215296

[76] H. Zhao, T. Ren, J. Liu, L. Liu, and Z. Li, "A novel structure for PZT-based piezoelectric microphone," in *2003 Nanotechnology Conference and Trade Show*, vol. 1, San Fransisco, CA, Feb. 23–27, 2003, pp. 356–359.

[77] S. C. Ko, Y. C. Kim, S. S. Lee, S. H. Choi, and S. R. Kim, "Micromachined piezoelectric membrane acoustic device," *Sensors and Actuator A*, vol. 103, no. 1–2, pp. 130–134, Jan. 2003. [Online]. Available: http://dx.doi.org/10.1016/S0924-4247(02)00310-2

[78] M. Niu and E. S. Kim, "Piezoelectric bimorph microphone built on micromachined parylene diaphragm," *Journal of Microelectromechanical Systems*, vol. 12, no. 6, pp. 892–898, Dec. 2003. [Online]. Available: http://dx.doi.org/10.1109/JMEMS.2003.820288

[79] P. R. Scheeper, B. Nordstrand, B. L. J. O. Gullov, T. Clausen, L. Midjord, and T. Storgaard-Larsen, "A new measurement microphone based on MEMS technology," *Journal of Microelectromechanical Systems*, vol. 12, no. 6, pp. 880–891, Dec. 2003. [Online]. Available: http://dx.doi.org/10.1109/JMEMS.2003.820260

[80] R. Polcawich, "A piezoelectric MEMS microphone based on lead zirconate titanate (PZT) thin films," Army Research Laboratory, Adelphi, MD, Tech. Rep. ARL-TR-3387, Nov. 2004. [Online]. Available: http://handle.dtic.mil/100.2/ADA429041

[81] J. Hillenbrand and G. M. Sessler, "High-sensitivity piezoelectric microphones based on stacked cellular polymer films," *Journal of the Acoustical Society of America*, vol. 116, no. 6, pp. 3267–3270, Dec. 2004. [Online]. Available: http://dx.doi.org/10.1121/1.1810272

[82] R. S. Fazzio, T. Lamers, O. Buccafusca, A. Goel, and W. Dauksher, "Design and performance of aluminum nitride piezoelectric microphones," in *14th International Conference on Micro-Sensors, Actuators and Microsystems*, Lyon, France, Jun. 10–14, 2007, pp. 1255–1258. [Online]. Available: http://dx.doi.org/10.1109/SENSOR.2007.4300365

[83] T. L. Lamers and R. S. Fazzio, "Accelerating development of a mems piezoelectric microphone," in *Proceedings of the ASME 2007 International Design Engineering*

Technical Conferences & Computers Information in Engineering Conference, Las Vegas, NV, Sep. 4–7, 2007, paper DETC2007-34958, pp. 593–601. [Online]. Available: http://dx.doi.org/10.1115/DETC2007-34958

[84] R. S. Fazzio, W. Dauksher, A. Goel, and T. Lamers, "Analysis of micromachined piezoelectric transducers operating in a flexural mode," in *Proceedings of IMECE 2007, ASME International Mechanical Engineering Congress and Exposition*, Nov. 11–15, 2007, paper IMECE2007-41460, pp. 1–9.

[85] R. J. Littrell, "High performance piezoelectric MEMS microphones," Ph.D. dissertation, University of Michigan, Ann Arbor, MI, 2010.

[86] M. Pedersen, W. Olthius, and P. Bergveld, "Harmonic distortion in silicon condenser microphones," *Journal of the Acoustical Society of America*, vol. 102, no. 3, pp. 1582–1587, Sep. 1997. [Online]. Available: http://dx.doi.org/10.1121/1.420070

[87] T. Hoevenaars, K. LeDoux, and M. Colosino, "Interpreting IEEE STD 519 and meeting its harmonic limits in VFD applications," in *IEEE Industry Applications Society 50th Annual Petroleum and Chemical Industry Conference*, Houston, TX, Sep. 15–17, 2003, pp. 145–150. [Online]. Available: http://dx.doi.org/10.1109/PCICON.2003.1242609

[88] G. M. Sessler, "Acoustic sensors," *Sensors and Actuators A: Physical*, vol. 26, no. 1–3, pp. 323–330, Mar. 1991. [Online]. Available: http://dx.doi.org/10.1016/0924-4247(91)87011-Q

[89] D. T. Martin, J. Liu, K. Kadirvel, R. M. Fox, M. Sheplak, and T. Nishida, "Development of a MEMS dual backplate capacitive microphone for aeroacoustic measurements," in *Proceedings of 44th AIAA Aerospace Sciences Meeting and Exhibit*, Reno, NV, Jan. 9–12, 2006, AIAA paper 2006-1246.

[90] W. S. Lee and S. S. Lee, "Piezoelectric microphone built on circular diaphragm," *Sensors and Actuators A: Physical*, vol. 144, no. 2, pp. 367–373, Jun. 2008. [Online]. Available: http://dx.doi.org/10.1016/j.sna.2008.02.001

[91] J. Raukola, N. Kuusinen, and M. Paajanen, "Cellular electrets - from polymer granules to electromechanically active films," in *11th International Symposium on Electrets*, Victoria, Australia, Oct. 1–3, 2002, pp. 195–198. [Online]. Available: http://dx.doi.org/10.1109/ISE.2002.1042977

[92] R. Solecki and R. J. Conant, *Advanced Mechanics of Materials*. New York, NY: Oxford University Press, 2003, pp. 167–182.

[93] A. Safari and E. Akdoğan, Eds., *Piezoelectric and Acoustic Materials for Transducer Applications*. New York, NY: Springer, 2008, ch. 2,20.

[94] N. Setter, Ed., *Piezoelectric Materials in Devices : Extended Reviews on Current and Emerging Piezoelectric Materials, Technology, and Applications*. Lausanne, Switzerland: N. Setter, 2002, ch. 1,12,13.

[95] *IEEE standard on piezoelectricity*, ANSI/IEEE Std. 176-1987, 1988. [Online]. Available: http://dx.doi.org/10.1109/IEEESTD.1988.79638

[96] B. A. Auld, *Acoustic Fields and Waves in Solids*, 2nd ed. Malabar, Fla.: R.E. Krieger, 1990, ch. 8.

[97] C. A. Balanis, *Advanced Engineering Electromagnetics*. Hoboken, NJ: John Wiley & Sons, 1989, ch. 2.

[98] A. P. Boresi and R. J. Schmidt, *Advanced Mechanics of Materials*, 6th ed. New York, NY: John Wiley & Sons, 2003, ch. 3,13.

[99] M. A. Dubois and P. Muralt, "Properties of aluminum nitride thin films for piezoelectric transducers and microwave filter applications," *Applied Physics Letters*, vol. 74, no. 20, pp. 3032–3034, 1999. [Online]. Available: http://dx.doi.org/10.1063/1.124055

[100] S. Trolier-McKinstry and P. Muralt, "Thin film piezoelectrics for MEMS," *Journal of Electroceramics*, vol. 12, no. 1/2, pp. 7–17, Jan 2004. [Online]. Available: http://www.springerlink.com/content/t7415r71417825w7

[101] R. Ruby, "FBAR — from technology development to production," in *Proceedings of the 2nd International Symposium on Acoustic Wave Devices for Future Mobile Communication Systems*, Chiba, Japan, Mar. 2–5, 2004, pp. 1–5.

[102] Y. Oshmyansky, J. D. Larson, R. Ruby, and S. Mishin, "Sputtering processes for bulk acoustic wave filters," *Semiconductor International*, Mar. 2003.

[103] S. Tadigadapa and K. Mateti, "Piezoelectric MEMS sensors: state-of-the-art and perspectives," *Measurement Science and Technology*, vol. 20, no. 9, p. 092001, sep 2009. [Online]. Available: http://dx.doi.org/10.1088/0957-0233/20/9/092001

[104] S. Wilson, R. Jourdain, Q. Zhang, R. Dorey, C. Bowen, M. Willander, Q. Wahab, S. Alhilli, and O. Nur, "New materials for micro-scale sensors and actuatorsan engineering review," *Materials Science and Engineering: R: Reports*, vol. 56, no. 1-6, pp. 1–129, Jun. 2007. [Online]. Available: http://dx.doi.org/10.1016/j.mser.2007.03.001

[105] R. Ruby, P. Bradley, Y. Oshmyansky, A. Chien, and J. Larson, "Thin film bulk wave acoustic resonators (FBAR) for wireless applications," in *Proceedings of the 2001 IEEE Ultrasonics Symposium*, vol. 1, Oct. 10, 2001, pp. 813–821. [Online]. Available: http://dx.doi.org/10.1109/ULTSYM.2001.991846

[106] N. Maluf, *Introduction to microelectromechanical systems engineering*, 2nd ed. Boston, MA: Artech House, 2004, pp. 208–211.

[107] M. Madou, *Fundamentals of Microfabrication*. Boca Raton, FL: CRC Press, 1997, pp. 261–272.

[108] S. Franssila, *Introduction to Microfabrication*. Boulder, CO: John Wiley & Sons, 2004, p. 401.

[109] S. Beeby, *MEMS Mechanical Sensors*. Boston, MA: Artech House, 2004, ch. 6.

[110] H. Lee, D. Kang, and W. Moon, "A micro-machined source transducer for a parametric array in air," vol. 125, no. 4, pp. 1879–93, Apr. 2009. [Online]. Available: http://dx.doi.org/10.1121/1.3081385

[111] S. Trolier-McKinstry, R. Smith, S. Krishnaswamy, and C. Freidhoff, "Vibration of micromachined circular piezoelectric diaphragms," *IEEE Transactions on Ultrasonics, Ferroelectrics and Frequency Control*, vol. 53, no. 4, pp. 697–706, Apr. 2006. [Online]. Available: http://dx.doi.org/10.1109/TUFFC.2006.1621496

[112] P. Blanchard, R. Devaney, and G. Hall, *Differential equations*. Belmont, CA: Brooks/Cole Thomson Learning, 2006.

[113] S. A. N. Prasad, Q. Gallas, S. Horowitz, B. Homeijer, B. V. Sankar, L. N. Cattafesta, and M. Sheplak, "Analytical electroacoustic model of a piezoelectric composite circular plate," *AIAA Journal*, vol. 44, no. 10, pp. 2311–2318, Oct. 2006. [Online]. Available: http://dx.doi.org/10.2514/1.19855

[114] J. Merhaut, *Theory of Electroacoustics*. New York, NY: McGraw-Hill, 1981, ch. 1,2,6.

[115] F. A. Fischer, *Fundamentals of Electroacoustics*. New York, NY: Interscience Publishers, 1955, ch. 1.

[116] S. T. Todd and H. Xie, "An electrothermomechanical lumped element model of an electrothermal bimorph actuator," *Journal of Microelectromechanical Systems*, vol. 17, no. 1, pp. 213–225, Feb. 2008. [Online]. Available: http://dx.doi.org/10.1109/JMEMS.2007.908754

[117] A. N. Norris and D. M. Photiadis, "Thermoelastic relaxation in elastic structures, with applications to thin plates," *Quarterly Journal of Mechanics and Applied Mathematics*, vol. 58, no. 1, pp. 143–163, Feb. 2005. [Online]. Available: http://dx.doi.org/10.1093/qjmamj/hbi002

[118] S. G. David S. Bindel, "Elastic PMLs for resonator anchor loss simulation," *International Journal for Numerical Methods in Engineering*, vol. 64, no. 6, pp. 789–818, Oct. 2005. [Online]. Available: http://dx.doi.org/10.1002/nme.1394

[119] S. B. Horowitz, "Development of a MEMS-based acoustic energy harvester," Ph.D. dissertation, University of Florida, Gainesville, FL, Dec. 2005.

[120] B. R. Munson, D. F. Young, and T. H. Okiishi, *Fundamentals of Fluid Mechanics*, 4th ed. New York, NY: John Wiley & Sons, 2002, pp. 352–354.

[121] J. N. Reddy, *Theory and Analysis of Elastic Plates*. Philadelphia, PA: Taylor & Francis, 1999, ch. 1–3,5.

[122] A. H. Nayfeh and P. F. Pai, *Linear and Nonlinear Structural Mechanics*. Hoboken, N.J.: Wiley-Interscience, 2004, ch. 7.

[123] I. Chopra, "Review of state of art of smart structures and integrated systems," *AIAA Journal*, vol. 40, no. 11, pp. 2145–2187, 2002. [Online]. Available: http://dx.doi.org/10.2514/2.1561

[124] Y. T. Antonyak and M. Vassergiser, "Calculation of the characteristics of a membrane-type flexural-mode piezoelectric transducer," *Soviet Physical Acoustics*, vol. 28, no. 3, pp. 176–180, May–Jun. 1982.

[125] Y. B. Evseichik, S. I. Rudnitskii, V. M. Sharapov, and N. A. Shul'ga, "Sensitivity of a metal-piezoceramic bimorph transducer," *International Applied Mechanics*, vol. 26, no. 12, pp. 1174–1181, Dec. 1990.

[126] S. H. Chang and B. C. Du, "Optimization of asymmetric bimorphic disk transducers," *The Journal of the Acoustical Society of America*, vol. 109, no. 1, pp. 194–202, Jan. 2001. [Online]. Available: http://dx.doi.org/10.1121/1.1310669

[127] G. Wang, B. V. Sankar, L. N. Cattafesta, and M. Sheplak, "Analysis of a composite piezoelectric circular plate with initial stresses for MEMS," in *Proceedings of 2002 ASME International Mechanical Engineering Congress and Exposition*, New Orleans, LA, Nov. 17–22, 2002, paper 34337, pp. 339–346.

[128] S. Prasad, B. Sankar, L. Cattafesta, S. Horowitz, Q. Gallas, and M. Sheplak, "Two-port electroacoustic model of an axisymmetric piezoelectric composite plate," in *43rd AIAA Structures, Structural Dynamics, and Materials Conference*, Denver, CO, Apr. 22–25, 2002, AIAA paper 2002-1365.

[129] S. Li and S. Chen, "Analytical analysis of a circular PZT actuator for valveless micropumps," *Sensors and Actuators A: Physical*, vol. 104, no. 2, pp. 151–161, Apr. 2003. [Online]. Available: http://dx.doi.org/10.1016/S0924-4247(03)00006-2

[130] S. Kim, W. W. Clark, and Q. M. Wang, "Piezoelectric energy harvesting with a clamped circular plate: analysis," *Journal of Intelligent Material Systems and Structures*, vol. 16, no. 10, pp. 847–854, Oct. 2005. [Online]. Available: http://dx.doi.org/10.1177/1045389X05054044

[131] C. Mo, R. Wright, W. S. Slaughter, and W. W. Clark, "Behaviour of a unimorph circular piezoelectric actuator," *Smart Materials and Structures*, vol. 15, no. 4, pp. 1094–1102, Aug. 2006. [Online]. Available: http://dx.doi.org/10.1088/0964-1726/15/4/023

[132] C. Mo, R. Wright, and W. W. Clark, "The effect of electrode pattern on the behavior of piezoelectric actuators in a circular diaphragm structure," *Journal of Intelligent Material Systems and Structures*, vol. 18, no. 5, pp. 467–476, May 2007. [Online]. Available: http://dx.doi.org/10.1177/1045389X06067112

[133] M. Deshpande and L. Saggere, "An analytical model and working equations for static deflections of a circular multi-layered diaphragm-type piezoelectric actuator," *Sensors and Actuators A: Physical*, vol. 136, no. 2, pp. 673–689, May 2007. [Online]. Available: http://dx.doi.org/10.1016/j.sna.2006.12.022

[134] M. Papila, M. Sheplak, and L. N. C. III, "Optimization of clamped circular piezoelectric composite actuators," *Sensors and Actuators A: Physical*, vol. 147, no. 1, pp. 310–323, Sep. 2008. [Online]. Available: http://dx.doi.org/10.1016/j.sna.2008.05.018

[135] C.-K. Lee, "Piezoelectric laminates for torsional and bending modal control: theory and experiment," Ph.D. dissertation, Cornell University, Ithaca, NY, 1987.

[136] ——, "Theory of laminated piezoelectric plates for the design of distributed sensors/actuators. Part I: Governing equations and reciprocal relationships," *The Journal of the Acoustical Society of America*, vol. 87, p. 1144, Mar. 1990. [Online]. Available: http://dx.doi.org/10.1121/1.398788

[137] J. N. Reddy, "On laminated composite plates with integrated sensors and actuators," *Engineering Structures*, vol. 21, no. 7, pp. 568–593, Jul. 1999. [Online]. Available: http://dx.doi.org/10.1016/S0141-0296(97)00212-5

[138] *MATLAB Help File*, MathWorks, Natick, MA, 2010, release R2010a.

[139] B. A. Griffin, M. D. Williams, C. S. Coffman, and M. Sheplak, "Aluminum nitride ultrasonic air-coupled actuator," *Journal of Microelectromechanical Systems*, vol. 20, no. 2, pp. 476–486, Apr. 2011. [Online]. Available: http://dx.doi.org/10.1109/JMEMS.2011.2111357

[140] B. A. Griffin, "Development of an ultrasonic piezoelectric MEMS-based radiator for nonlinear acoustic applications," Ph.D. dissertation, University of Florida, Gainesville, FL, May 2009.

[141] K. Tsubouchi and N. Mikoshiba, "Zero-temperature-coefficient SAW devices on AlN epitaxial films," *IEEE Transactions on Sonics and Ultrasonics*, vol. 32, no. 5, pp. 634–644, Sep. 1985. [Online]. Available: http://dx.doi.org/10.1109/T-SU.1985.31647

[142] J. Reddy, *Energy Principles and Variational Methods in Applied Mechanics*. Hoboken, NJ: John Wiley & Sons, Inc., 2002, ch. 4–6,8.

[143] *ABAQUS Help File*, Simulia, Providence, RI, 2008, version 6.8.

[144] A. S. Sedra and K. C. Smith, *Microelectronic Circuits*, 4th ed. New York, NY: Oxford University Press, 1998, p. 21.

[145] D. Johns and K. Martin, *Analog Integrated Circuit Design*. New York, NY: John Wiley & Sons, 2009.

[146] M. Serridge and T. R. Licht, *Piezoelectric Accelerometer and Vibration Preamplifier Handbook*, Brüel and Kjær, Nov. 1987.

[147] E. Bartolome, "Signal conditioning for piezoelectric sensors," *Analog Applications Journal*, no. 1Q, p. 10, 2010. [Online]. Available: http://focus.ti.com/lit/an/slyt369/slyt369.pdf

[148] G. Gautschi, *Piezoelectric Sensorics*. Berlin, Germany: Springer-Verlag, 2002, ch. 11.

[149] K. Kadirvel, "Development of closed-loop interface circuits for capacitive transducers with application to a MEMS capacitive microphone," Ph.D. dissertation, University of Florida, Gainesville, FL, Dec. 2007. [Online]. Available: http://purl.fcla.edu/fcla/etd/UFE0020083

[150] R. T. Haftka and Z. Gürdal, *Elements of Structural Optimization*, 3rd ed. Dordrecht, The Netherlands: Kluwer Academic Publishers, 1992, ch. 1,2.

[151] R. Spencer, B. Fleischer, P. Barth, and J. Angell, "A theoretical study of transducer noise in piezoresistive and capacitive silicon pressure sensors," *IEEE Transactions on Electron Devices*, vol. 35, no. 8, pp. 1289–1298, Aug. 1988. [Online]. Available: http://dx.doi.org/10.1109/16.2550

[152] M. Papila, R. Haftka, T. Nishida, and M. Sheplak, "Piezoresistive microphone design pareto optimization: tradeoff between sensitivity and noise floor," *Journal of Microelectromechanical Systems*, vol. 15, no. 6, pp. 1632–1643, Dec. 2006. [Online]. Available: http://dx.doi.org/10.1109/JMEMS.2006.883884

[153] J. Branke, K. Deb, K. Miettinen, and R. Słowiński, Eds., *Multiobjective Optimization : Interactive and Evolutionary Approaches*. Berlin, Germany: Springer, 2008, ch. 1.

[154] K. Deb, A. Pratap, S. Agarwal, and T. Meyarivan, "A fast and elitist multiobjective genetic algorithm: NSGA-II," *IEEE Transactions on Evolutionary Computation*, vol. 6, no. 2, pp. 182–197, Apr. 2002. [Online]. Available: http://dx.doi.org/10.1109/4235.996017

[155] L. Liberti and N. Maculan, *Global Optimization: From Theory to Implementation*. Berlin, Germany: Springer, 2006, p. 248.

[156] G. G. Stoney, "The tension of metallic films deposited by electrolysis the tension of metallic films deposited by electrolysis ." *Proceedings of the Royal Society of London Series A*, vol. 82, no. 553, pp. 172–175, May 1909. [Online]. Available: http://www.jstor.org/stable/92886

[157] (2010) Services. Dynatex International. [Online]. Available: http://www.dynatex.com/services.html

[158] T. Lizotte, "Laser dicing of chip scale and silicon wafer scale packages," in *IEEE/CPMT/SEMI 28th International Electronics Manufacturing Technology Symposium*, San Jose, CA, Jul. 16–18, 2003, pp. 1–5. [Online]. Available: http://dx.doi.org/10.1109/IEMT.2003.1225869

[159] *Ablebond 84-1LMI*, Ablestik, Jan. 2005.

[160] *Dualbond 707*, Cyberbond LLC, Feb. 2011.

[161] *3145 RTV MIL-A-46146 Adhesive/Sealant*, Dow Corning, Feb. 2011.

[162] *Ultiboard Help File*, National Instruments, Jan. 2007, version 10.0.343.

[163] W. Navidi, *Statistics for Engineers and Scientists*. McGraw-Hill, 2006, ch. 1,5.

[164] W. R. Thompson, "On a criterion for the rejection of observations and the distribution of the ratio of deviation to sample standard deviation," *The Annals of Mathematical Statistics*, vol. 6, no. 4, pp. 214–219, 1935. [Online]. Available: http://dx.doi.org/10.1214/aoms/1177732567

[165] J. Griffin, T. Schultz, R. Holman, L. Ukeiley, and L. Cattafesta, "Application of multivariate outlier detection to fluid velocity measurements," *Experiments in Fluids*, vol. 49, no. 1, pp. 305–317, Jul. 2010. [Online]. Available: http://dx.doi.org/10.1007/s00348-010-0875-3

[166] M. Hubert and S. Van der Veeken, "Outlier detection for skewed data," *Journal of Chemometrics*, vol. 22, no. 3–4, pp. 235–246, Mar.–Apr. 2008. [Online]. Available: http://dx.doi.org/10.1002/cem.1123

[167] S. Verboven and M. Hubert, "LIBRA: A MATLAB library for robust analysis," *Chemometrics and Intelligent Laboratory Systems*, vol. 75, no. 2, pp. 127–136, Feb. 2005. [Online]. Available: http://dx.doi.org/10.1016/j.chemolab.2004.06.003

[168] M. Hubert. (2009, Nov.) LIBRA: A MATLAB library for robust analysis. Robust Statistics Research Group, Katholieke Universiteit Leuven. Leuven, Belgium. [Online]. Available: http://wis.kuleuven.be/stat/robust/LIBRA.html

[169] M. Hubert and E. Vandervieren, "An adjusted boxplot for skewed distributions," *Computational Statistics & Data Analysis*, vol. 52, no. 12, pp. 5186–5201, Aug. 2008. [Online]. Available: http://dx.doi.org/10.1016/j.csda.2007.11.008

[170] S. Woods, "Understanding scanning white light interferometry," *MICRO Manufacturing*, vol. 2, no. 4, pp. 19–21, Winter 2009. [Online]. Available: http://www.micromanufacturing.com/past_editions/pdf/Winter09.pdf

[171] G. S. K. Wong and T. F. W. Embleton, *AIP Handbook of Condensor Microphones*. New York, NY: American Institute of Physics, 1995, ch. 13.

[172] *Measurement Microphones - Part 5: Methods for Pressure Calibration of Working Standard Microphones by Comparison*, International Electrotechnical Commission International Standard CEI/IEC 61094-5:2001, Oct. 2001.

[173] D. Alexander, C. Barnard, M. Sheplak, and B. Griffin, "Characterization of a high-frequency pressure-field calibration method," in *Proceedings of the 159th Meeting of the Acoustical Society of America*, Baltimore, MD, Apr. 19–23, 2010.

[174] *Condenser Microphones and Microphone Preamplifiers for Acoustic Measurements*, Brüel and Kjær, Nærum, Denmark, 1982.

[175] *Agilent 4294A Precision Impedance Analyzer Operation Manual*, 7th ed., Agilent Technologies, Japan, Feb. 2003. [Online]. Available: http://cp.literature.agilent.com/litweb/pdf/04294-90060.pdf

[176] *Impedance Measurement Handbook*, Agilent Technologies, Dec. 2003. [Online]. Available: http://cp.literature.agilent.com/litweb/pdf/5950-3000.pdf

[177] *New Technologies for Accurate Impedance Measurement (40 Hz to 110 MHz)*, Agilent Technologies, Jun. 2009, product note. [Online]. Available: http://cp.literature.agilent.com/litweb/pdf/5968-4506E.pdf

[178] M. Robinson, technical support call, Agilent Technologies, Mar. 2010.

[179] L. N. Virgin, *Introduction to Experimental Nonlinear Dynamics*. Cambridge, UK: Cambridge University Press, 2000.

[180] ——, *Vibration of Axially Loaded Structures*. Cambridge, UK: Cambridge University Press, 2007.

[181] A. Naini and M. Green, "Fringing fields in a parallel-plate capacitor," *American Journal of Physics*, vol. 45, no. 9, pp. 877– 879, Sep. 1977. [Online]. Available: http://dx.doi.org/10.1119/1.11075

[182] G. Servais and S. Brandenburg, "Wire bonding—a closer look," in *17th International Symposium for Testing & Failure Analysis*, Los Angeles, CA, Nov. 11–15, 1991, pp. 525–529.

[183] R. Vispute, H. Wu, and J. Narayan, "High quality epitaxial aluminum nitride layers on sapphire by pulsed laser deposition," *Applied Physics Letters*, vol. 67, no. 11, pp. 1549–1551, Sep. 1995. [Online]. Available: http://dx.doi.org/10.1063/1.114489

[184] F. Martin, P. Muralt, M. Dubois, and A. Pezous, "Thickness dependence of the properties of highly c-axis textured AlN thin films," *Journal of Vacuum Science & Technology A: Vacuum, Surfaces, and Films*, vol. 22, no. 2, p. 361, Mar./Apr. 2004. [Online]. Available: http://dx.doi.org/10.1116/1.1649343

[185] S. Sanchez, "Robust design: seeking the best of all possible worlds," in *2000 Winter Simulation Conference Proceedings*, Orlando, FL, Dec. 10–13, 2000, pp. 69–76. [Online]. Available: http://dx.doi.org/10.1109/WSC.2000.899700

[186] J. S. Han and B. M. Kwak, "Robust optimal design of a vibratory microgyroscope considering fabrication errors," *Journal of Micromechanics and Microengineering*, vol. 11, pp. 662–671, 2001. [Online]. Available: http://dx.doi.org/10.1088/0960-1317/11/6/307

[187] J. Wittwer, M. Baker, and L. Howell, "Robust design and model validation of nonlinear compliant micromechanisms," *Journal of Microelectromechanical Systems*, vol. 15, no. 1, pp. 33–41, Feb. 2006. [Online]. Available: http://dx.doi.org/10.1109/JMEMS.2005.859190

[188] S. Gurav, J. Goosen, and F. van Keulen, "Bounded-but-unknown uncertainty optimization using design sensitivities and parallel computing: Application to mems," *Computers & Structures*, vol. 83, no. 14, pp. 1134–1149, May 2005. [Online]. Available: http://dx.doi.org/10.1016/j.compstruc.2004.11.021

[189] M. Sheplak and J. Dugundji, "Large deflections of clamped circular plates under tension and transitions to membrane behavior," *Journal of Applied Mechanics*, vol. 65, no. 1, pp. 107–115, Mar. 1998. [Online]. Available: http://dx.doi.org/10.1115/1.2789012

[190] B. Griffin, B. Homeijer, M. Williams, B. Sankar, and M. Sheplak, "Large deflections of clamped composite circular plates with initial in-plane tension," in *IMAC XXVI: Conference and Exposition on Structural Dynamics*, Orlando, FL, Feb. 4–7, 2008.

[191] Y.-Y. Yu, *Vibrations of Elastic Plates : Linear and Nonlinear Dynamical Modeling of Sandwiches, Laminated Composites, and Piezoelectric Layers*. New York, NY: Springer, 1996, ch. 1,7.

[192] W. M. Lai, D. Rubin, and E. Krempl, *Introduction to Continuum Mechanics*, 1st ed. New York, NY: Pergamon Press, 1974.

[193] L. E. Malvern, *Introduction to the Mechanics of a Continuous Medium*. Englewood Cliffs, NJ: Prentice-Hall, 1969, ch. 4.

[194] R. L. Panton, *Incompressible Flow*, 3rd ed. Hoboken, NJ: John Wiley & Sons, 2005, ch. 1.

[195] C. L. Dym and I. H. Shames, *Solid Mechanics: a Variational Approach*. New York, NY: McGraw-Hill, 1973, ch. 4,6–8.

[196] A. J. M. Spencer, *Continuum Mechanics*. Mineola, NY: Dover Publications, 2004, p. 83.

[197] C.-Y. Chia, *Nonlinear Analysis of Plates*. New York, NY: McGraw-Hill, 1980, ch. 1,3.

[198] J. N. Reddy, *Mechanics of Laminated Composite Plates : Theory and Analysis*. Boca Raton: CRC Press, 1997, ch. 5.

[199] K. R. Nagle, E. B. Saff, and A. David, *Fundamentals of Differential Equations and Boundary Value Problems*, 3rd ed. Reading, MA: Addison-Wesley, 2000, pp. 187–189, 510–514.

[200] A. King, J. Billingham, and S. Otto, *Differential Equations*. Cambridge, UK: Cambridge University Press, 2003, ch. 3.

[201] H. W. Coleman and W. G. Steele, *Experimentation, Validation, and Uncertainty Analysis for Engineers*, 3rd ed. Hoboken, NJ: John Wiley & Sons, 2009, ch. 1–3.

[202] *Guide to the Expression of Uncertainty in Measurement*, International Organization for Standardization International Standard, 1993.

[203] L. Cattafesta, "Spectral functions," Spring 2007, unpublished.

[204] P. D. Welch, "The use of fast fourier transform for the estimation of power spectra," *IEEE Transactions on Audio and Electroacoustics*, vol. 15, no. 2, pp. 70 – 73, Jun. 1967. [Online]. Available: http://dx.doi.org/10.1109/TAU.1967.1161901

BIOGRAPHICAL SKETCH

Matthew David Williams was born in 1982 in Plano, TX and subsequently lived in Garland, TX, Maryville, TN, and Batesburg-Leesville, SC before graduating from Batesburg-Leesville High School in June 2001. He enrolled at Clemson University (Clemson, SC) in August 2001 and was selected a recipient of the Barry M. Goldwater Scholarship in 2004 before graduating summa cum laude with a bachelor's degree in mechanical engineering in May 2005. In August 2005, Matt enrolled at University of Florida (Gainesville, FL) as a National Science Foundation Graduate Research Fellow, joining Interdisciplinary Microsystems Group in April 2006. Matt received his masters degree in mechanical engineering in May 2008 before serving as a visiting research at the Delft University of Technology from September 2008–September 2009. Upon returning to University of Florida, Matt completed his doctoral degree in mechanical engineering in May 2011. Matt's research interests include the design and optimization of microscale sensors and actuators, in addition to nonlinear mechanics, particular post-buckling and snap-through of multistable electromechanical microstructures.